Florida International University

FIU Digital Commons

11-9-2021

Evaluation and Damage Detection of Highway Bridges with Distinct Vulnerabilities

Mohammad Abedin
mabed005@fiu.edu

Follow this and additional works at: https://digitalcommons.fiu.edu/etd

Part of the Structural Engineering Commons

Recommended Citation

FLORIDA INTERNATIONAL UNIVERSITY

Miami, Florida

EVALUATION AND DAMAGE DETECTION OF HIGHWAY BRIDGES WITH

DISTINCT VULNERABILITIES

A dissertation submitted in partial fulfillment of

the requirements for the degree of

DOCTOR OF PHILOSOPHY

in

CIVIL ENGINEERING

by

Mohammad Abedin

2021

To: Dean John L. Volakis
      College of Engineering and Computing

This dissertation, written by Mohammad Abedin, and entitled Evaluation and Damage Detection of Highway Bridges with Distinct Vulnerabilities, having been approved in respect to style and intellectual content, is referred to you for judgment.

We have read this dissertation and recommend that it be approved.

_____
Atorod Azizinamini

_____
Ioannis Zisis

_____
Pezhman Mardanpour

_____
Armin Mehrabi , Major Professor

Date of Defense: November 9, 2021

The dissertation of Mohammad Abedin is approved.

_____
Dean John L. Volakis
College of Engineering and Computing

_____
Andrés G. Gil
Vice President for Research and Economic Development
and Dean of the University Graduate School

Florida International University, 2021

ii

DEDICATION

I dedicate this dissertation to my wife, who has been a constant source of support and encouragement during the challenges of graduate school and life. I am truly thankful for having you in my life. I also dedicate this dissertation to my parents, who have always loved me unconditionally and whose good examples have taught me to work hard for the things that I aspire to achieve.

ACKNOWLEDGMENTS

I would like to thank my advisor, Dr. Armin Mehrabi, for his guidance, patience, and for his confidence in me. His dynamism, vision, sincerity, and motivation have deeply inspired me. It was a great privilege and honor to work and study under his guidance. I am extremely grateful for what he has offered me. I also thank him for his friendship, empathy, and kindness.

I would also like to thank Dr. Atorod Azizinamini, Dr. Ioannis Zisis, and Dr. Pezhman Mardanpour, as my dissertation committee members, and Dr. Michel Ghosn, Dr. Andrzej S Nowak, and Dr. Antonio Nanni for their sound advice, constructive comments, and kind support.

My appreciation also goes out to my family, friends, and fellow graduate students for their encouragement and support all through my studies. Thanks to the administrative staff at Florida International University for helping out with the departmental and university policies and procedures. Finally, I extend my thanks to all those unnamed individuals whose encouragement and cooperation directly or indirectly contributed to the completion of this dissertation.

ABSTRACT OF THE DISSERTATION

EVALUATION AND DAMAGE DETECTION OF HIGHWAY BRIDGES WITH

DISTINCT VULNERABILITIES

by

Mohammad Abedin

Florida International University, 2021

Miami, Florida

Professor Armin Mehrabi, Major Professor

Bridge failures over the past few decades have shown conventional bridge monitoring is insufficient to effectively evaluate the safety of this important piece of infrastructure. Therefore, new methods for bridge monitoring and special considerations in bridge design are needed to ensure the health of these structures. The objective of this research is to explore new means for detecting damage in bridge members during normal operations that are both accurate and affordable at the same time. To achieve the objective of this research, a two-fold investigation was performed. One was to study the bridge behavior subjected to various damage scenarios and identify possible failure mechanisms. The other was to develop an effective non-destructive method for damage detection based on the bridge behavior after the damage. Two types of bridges were selected and studied for this purpose, twin steel box girder bridges (TSBG) that are classified as fracture critical and prefabricated bridge systems containing cast-in-place joints. The results of the current study confirmed that concrete deck failure is the dominant failure mode of the TSBG bridge after the occurrence of a fracture in one of the girders. Therefore, an improved simple and unified yield line analysis method was developed to determine the bridge deck capacity

and to evaluate the bridge redundancy. Moreover, the TSBG bridge dynamic analysis after damage showed that bridge frequencies are sufficiently sensitive for identifying partial or full-depth girder fracture in the simple span bridges. The results show a significant change in the vibration mode shapes after damage in both simple and continuous span bridges. Investigation on the performance of the full-depth precast-prestressed box-beam bridge shows the vulnerability of such bridge decks to damage at the longitudinal joints. Using the FE analysis and load testing results, a new damage detection method and software for structural health monitoring of bridges with precast deck panels were also developed. This method, applicable to all bridges with modular precast deck units, can effectively identify locations and significance of potential deck joint damage based on the measured changes in bridge response and model updating method.

TABLE OF CONTENTS

LIST OF TABLES

LIST OF FIGURES

CHAPTER 1   INTRODUCTION

The recent collapse of several bridges, such as the Silver Bridge in Ohio in 1967 [1], the I-35 truss bridge in Minneapolis in 2007 (Figure 1-1(a)) [2], the Ponte Morandi cable-stayed bridge in Italy in 2018 [3], FIU pedestrian bridge collapse over a congested road in Miami, FL, in 2018 (Figure 1-1 (b)), and the Nanfang'ao steel single-arch bridge in Taiwan in 2019, have highlighted the importance of bridge design and maintenance. As a result of these events, attention was given not only to inspection frequency but also to potential weak points in a bridge. One of the problems identified was the lack of alternative load paths built into the bridge structural system. The lack of redundancy in bridges left these structures vulnerable to collapse after a failure in an individual member.

| (a) | (b) |

Figure 1-1. Bridge collapse;(a) I-35 W bridge over Mississippi River in 2007 [2], (b) FIU pedestrian bridge in 2018.

After each failure incident, state and federal agencies normally issue instructions for in-depth inspection of all populations of bridges with similar characteristics, imposing huge costs and burdens on the bridge maintenance agencies (Figure 1-2). For example, after the I-35 W Bridge incident, it was required that inspection of steel bridges with fracture critical elements be carried out using an "arms-length" approach at two-year intervals [4,5]. However, inspection of steel bridges, especially near mid-span over a busy roadway, is

costly, time-consuming, and causes traffic disruption and potential safety hazards. It may also take the inspectors as long as two years to detect the fracture, rendering the bridge potentially unsafe for a long duration. Similarly, for concrete bridges where most critical damages could be hidden from the naked eye for a long time, such inspections may not even bear any results.

Figure 1-2. In-depth bridge inspection near mid-span over a busy roadway.

As the many bridge failures over the past few decades have shown, conventional bridge monitoring is insufficient to effectively evaluate the safety of this important piece of infrastructure. New methods for bridge monitoring and special considerations in bridge design are needed to ensure the health of these structures as they continue to age and prevent the possibility of catastrophic collapses from minute and difficult to detect damage. For this purpose, the principal causes of bridge failure, such as deficiencies in design, detailing, construction, and materials [6], need to be investigated, and possible failure mechanisms for each cause need to be identified. Based on that, new approaches in bridge design and monitoring can be developed to reduce the risk of future bridge collapses. Some of these bridges are designed with distinct vulnerabilities that make them more susceptible

2

to certain types of damages. These include steel bridges with fracture critical members that contain fatigue-sensitive details and concrete and steel bridges designed and built using Accelerated Bridge Construction methods containing cast-in-place joints. For such bridges, the notion of developing a rapid yet accurate method of health monitoring becomes even more critical. Such methods would only be positively productive if they are preceded (or, in some cases, followed) by analysis of vulnerabilities of the bridge to determine the level of its redundancy.

1.1   Objective and Methodology

The objective of this research is to explore new means for detecting damage in bridge members during normal operations that are both accurate and affordable at the same time. Timely detection of the onset of fracture or damage will allow the maintenance crew to address the situation before the progress in damage threatens public safety and requires major closures and costs.

To achieve the objective of this research, a two-fold investigation was performed. One was to study the bridge behavior subjected to various damage scenarios and identify possible failure mechanisms. This results in a method for bridge evaluation after damage and determines its level of vulnerability to such damage; in other words, it defines the redundancy and reliability of the structure subjected to such damage. The other was to develop an effective non-destructive method for damage detection based on the bridge behavior after the damage. Two types of bridges are selected for this purpose, twin steel box girder bridges and prefabricated bridge systems.

1.1.1 Twin Steel Box Girder Bridges

In steel girder bridges, fatigue cracking is one of the most important phenomena affecting structural performance and integrity [7]. Development of fatigue cracking may lead in time to a full-depth fracture of one girder without noticeable bridge profile changes. It is critical to ensure that the bridge will have adequate capacity to prevent collapse until the next cycle of inspection discovers the damage. Investigations on the steel bridge collapses show that a failure in an individual member, known as fracture critical members (FCMs), could result in the total collapse of the structure [8]. The AASHTO Bridge Design Specifications [9] classify several types of bridges as fracture critical that require biennial arms-length in-service inspections, including twin steel box girder bridges (Figure 1-3) [10].

Figure 1-3. Twin steel box girder bridge classified as fracture critical.

Several studies on fracture critical bridges revealed examples of steel bridges that survived even after a full-depth fracture in one of the girders [11–13]. The analysis of these bridges demonstrated a high level of internal redundancy and secondary load paths in bridge systems that are not usually considered in the design procedure [14–17]. The US-52 bridge

4

over the Mississippi River, the Neville Island bridge on I-79 in Pittsburgh, and the Brandywine River bridge on I-95 in Wilmington are examples of bridges with a full-depth fracture in one of their girders that remained in service with a static deflection [18,19]. Recent research results indicate that twin steel box girder bridges could be redundant because of their high torsional resistance even after a full-depth fracture of one girder. The most notable study is the series of full-scale tests carried out by the University of Texas at Austin [20–22] that demonstrated a high level of internal redundancy of twin steel box girder bridges even after a full-depth fracture in one of its girders (Figure 1-4(a)). A study on the twin box girder structures in the Marquette Interchange, through non-linear numerical analysis, also demonstrated the high level of internal and structural redundancy of twin steel box girder bridges [23]. Connor et al. [24] have recently developed a series of recommendations and requirements for twin steel box girder bridges to be considered non-fracture critical. The recent study conducted by Van Pham et al. [12] shows that the deck and intact girder together are able to provide stability and reserve load-resisting capability for twin steel box girder bridges even after a full depth fracture of one girder (Figure 1-4(b)). It was concluded that the railings, continuity, and external intermediate cross-frames could further improve the redundancy level in these bridges. Moreover, during the experimental tests, unzipping or progressive failure of shear studs was not observed in the bridge.

<div align="center">(a)   (b)</div>

Figure 1-4. Twin steel box girder bridge tests; (a) University of Texas at Austin, (b) Florida International University.

Several studies have been conducted in the past to study the redundancy of bridge superstructures and substructures and calibrate methods to assess their capability of carrying some live load after damage to one of their main members [25]. Frangopol and Nakib [26] established the load modifier factors that are currently specified in the AASHTO Bridge Design Specifications. Hendawi and Frangopol [27] followed that work and proposed reliability-based redundancy criteria. Similarly, the work of Ghosn and Moses [28] has led to the establishment of the system factors and the step-by-step analysis procedure recommended in the AASHTO Manual of Bridge Evaluation. More recently, Frangopol et al. [29] proposed a new definition of redundancy factor, providing an improved quantification of system redundancy levels in component design. Following a similar rationale, a European-wide study by Strauss et al. [30] has also proposed a set of unified European standards for assessing the safety of existing bridges, including their reliability and redundancy.

Even though some analyses addressed bridges with fatigue fracture [31,32], most of these previous studies evaluated bridge redundancy, assuming complete damage to one of the bridge members, and investigated bridge behavior after severe damage [32]. The analysis approach proposed in the AASHTO guide manual for analyzing fracture critical bridges

[10] specified load factors established according to data provided by Nowak [33] that are based on assuming general bending failure mode for the bridge girders. However, the bridge's behavior and failure after the fracture of one girder do not necessarily follow the general girder bending failure. Therefore, determining the load level that should be used when analyzing twin steel girder bridges with fatigue fractures and establishing appropriate live load factors require further investigation. Questions remain regarding the expected failure modes of damaged twin steel box girder bridges and the methods for assessing bridge performance before these bridges could be removed from the fracture critical list. Moreover, although the use of the new recommendations and new materials and techniques could decrease the risk of bridge failure, there is still a justifiable and strong need to monitor the bridges periodically as aging, and environmental impacts can cause failure sooner and more severely than expected.

1.1.2   *Prefabricated Bridge Deck Systems*

Precast-prestressed concrete box beams offer an efficient alternative to traditional cast-in-place concrete bridge deck construction. The precast system is an economical option because of savings in required field labor and the reduction of on-site construction activities. Prefabrication eliminates the time of concrete deck casting and curing at the bridge site and leaves just a minimal amount of cast-in-place concrete work for securing panel connections at the site (Figure 1-5). Various prestressed panel shapes ranging from multiple stemmed to solid or box-beam slabs have been used for this precast system over time. Adjacent solid slab bridge deck panels are one of the common precast systems built by placing narrow precast panels side-by-side and connecting them with longitudinal shear key joints. Grouting is performed at the joints for connectivity and sealing. When covering

longer spans, the prestressed slab units are thickened, and tubular voids are added, known as side-by-side box-beam bridges, to reduce the self-weight of the superstructure. Moreover, transverse post-tensioning bars, usually at two locations along the span, are added to keep the precast bridge panels transversely in compression and avoid problems such as leaking, cracking, and spalling at the longitudinal joints.

Figure 1-5. Prefabricated bridge system with transverse and longitudinal joints.

Although utilizing the precast system makes the process of field construction faster than the cast-in-place bridge construction, over time, the post-tensioning transverse forces cannot be maintained due to steel relaxation and concrete creep. As a result, the panels may experience differential deflection as the grout in the joint breaks down under heavy traffic loading. This ultimately leads to initiation and/or extension of reflective cracking on the deck surface and leaking at longitudinal joints [34] (Figure 1-6).

Figure 1-6. Reflective cracking on the deck surface of a precast bridge.

The longitudinal reflective cracking along the shear keys in adjacent precast concrete box-beam bridges has been identified as a common problem [35–38]. The reflective cracks allow surface water penetration along the full length of the panels, causing corrosion of prestressing tendons and mild reinforcement. This durability issue is more noticeable for bridges where de-icing salt is used for winter maintenance, and the surface water is often laced with chloride ions [39].

Several attempts in recent years have been made to minimize or eliminate bridge deterioration caused by longitudinal cracking along the shear keys of precast concrete decks. The Precast/Prestressed Concrete Institute (PCI) [40] and Russell [41] collected information on the joint design, fabrication, and construction of precast/prestressed adjacent box-beam bridges. Attanayake and Aktan [42] studied the construction of several side-by-side box-beam bridges in Michigan. They concluded that regardless of the bridge age, longitudinal reflective cracking is one of the prevalent defects among all side-by-side box-beam decks. Researchers have proposed increasing the amount of post-tensioning force in the transverse strands to minimize the reflective cracking [43]. However, information regarding the contribution of the transverse post-tensioned strands is limited

and recent studies have demonstrated that increased transverse post-tensioning may not mitigate reflective cracking [44,45].

Strip closure joint details with steel reinforcement and Ultra-High Performance Concrete (UHPC) have recently been suggested for full-depth and partial depth longitudinal and transverse joints to increase durability and service life [46,47]. The strip closure joints with top and bottom reinforcement provide a continuous connection that transfers shear and moment between panels, eliminating the need for diaphragms, post-tensioning, and cast-in-place concrete topping, resulting in greater construction speed [48]. Nevertheless, there are still several old box-beam bridges in service where the shear key failure has led to leakage. Leakage and consequent deterioration affect the bridge integrity, alter the live-load distribution, and can potentially reduce the load-carrying capacity of the structure, thus posing a safety problem over time.

1.1.3   Structural Health Monitoring

Structural health monitoring (SHM) refers to a wide spectrum of activities and approaches to determining the changes in a structure and therefore determining its integrity and functional adequacy. This may range from routine visual inspection to sophisticated non-destructive evaluation techniques. It can be performed through periodic and on-demand inspection or can be carried out through continuous monitoring systems installed on the structure. One may consider SHM in two major categories; methods for which the structure is installed with sensors (sensor-based SHM) and methods for which the health of the structure is evaluated without a sensor and using external devices (Figure 1-7). Non-destructive evaluation methods, the use of remote non-contact sensors, visual inspection, and other vision-based methods can be considered in the latter group. Contacting sensor-

based SHM system typically has three major subsystems: a sensor (and wirings), a data acquisition, and a diagnosis subsystem. The diagnosis subsystem generally includes data processing, data mining, damage detection and can go further to expand to model updating and structural safety and reliability determination. The accuracy of results is largely dependent on not only the type and sophistication of the sensors and instruments but also on the variety, quantity, and quality of the measured data.

<div align="center">(a)   (b)</div>
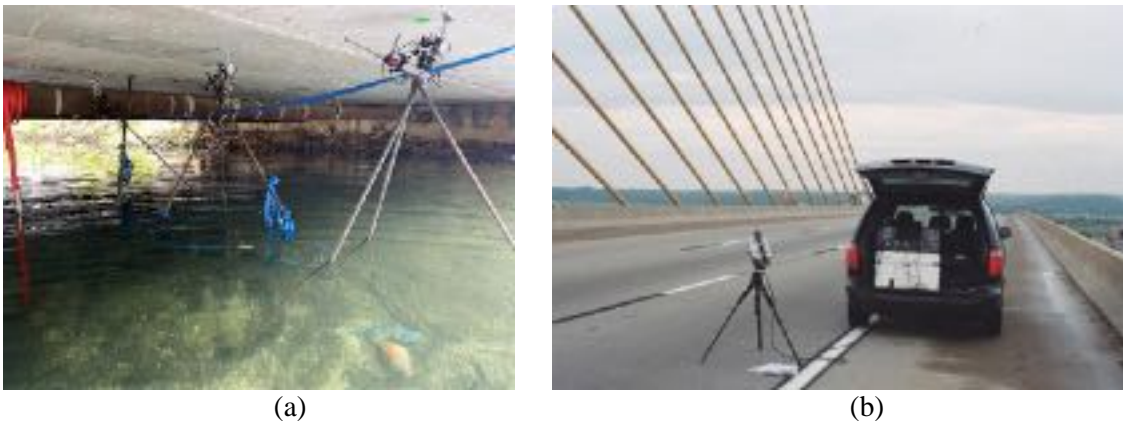
Figure 1-7. Structural health monitoring; (a) Sensor-based technique, (b) Remote non-contact sensor technique.

On a larger scale, optimal sensor placement has been a concern among researchers and has been studied widely. The goal is to improve the ability of the sensor subsystem with the least number of sensors possible [49,50]. The quality of the collected data is also a matter of attention [51]. Inaccurate results could lead to false alarms or to missing the recording of an event, therefore leading to unsafe structure and other consequences. A sensor commonly consists of different elements, including sensing component, transducer, signal-processing, and communication interface module. Malfunction, harsh environment, and normal wear and tear, as well as other factors such as electromagnetic interference, may lead to distortion of results and false data. For damage detection in large-scale and distributed systems, using a large number of sensors is a common trend because it promises more coverage hence a better chance of detection [52]. This, in turn, introduces challenges

for data collection and processing and for meaningful interpretation of the results. Developing a simple, economical, flexible, and at the same time, accurate sensor is very much in demand. Sensor types developed for SHM purposes in recent decades include electric strain gages, piezoelectric sensors, cement-based strain gauges, corrosion sensors, Nano material-based sensors, wireless sensors, accelerometers, inclinometers, acoustic emission sensors [53], wave propagation devices, and various fiber optic sensors (FOS). Additionally, advanced sensor and sensing technologies, such as fiber optics and Bragg grating sensors [54,55] and those based on Global Positioning System [56], have been recently developed for strain, displacement, and other response measurements.

Each of the sensor types has a certain application and works better in certain conditions. Nevertheless, the actual use of these sensors presents some challenges in the real environment. For instance, PZT (lead-zirconate-titanate)-based active and passive damage detection technologies can be used as acoustic emission (AE) sensor, which receives the stress wave signal generated by damage occurred in a structure. A cement-based strain sensor is considered as one appropriate candidate to solve the incompatibility issue. Dispersed sensors have also been used for monitoring purposes. Incorporated with fibers, conductive Nano-particles, magnetized or magnetic metals, PZT, or a combination can give concrete and another medium a sensing ability.

Traditional wired sensors may enable continuous monitoring of the bridge. However, the cost of installing wired sensors for longer-span bridges, providing continuous power, and their maintenance may make them impractical in many cases. To address the shortcomings associated with wired sensors, the use of wireless sensors has offered a valuable alternative. Nevertheless, these sensors typically rely on battery energy sources for operation, and the

cost of periodic battery replacement for large-scale monitoring would constitute a major expense. New developments for "energy harvesting" to feed the sensors could be a potential solution for providing continuous power to permanent sensors. Energy harvesting techniques are mainly based on solar energy, thermal gradients, and vibration energy. Among these techniques, vibration energy, because of providing a high level of energy and the ability to be embedded (as in concrete structures), could be used for continuous large-scale monitoring [57]. As an example, Self-powered piezo-floating-gate (PFG) sensors empowered using piezoelectric transducers through harvesting energy are used for detection of distortion-induced fatigue cracking of steel bridges [58,59].

Non-destructive bridge load testing can also be used for the assessment of damaged or deteriorated in-service bridges [60,61] (Figure 1-8). The information obtained from load testing can be used to reduce uncertainties associated with actual bridge conditions, material properties, and assumptions made during the bridge design. This becomes even more effective when accurate information on design and construction is not available. The verification of the design assumptions can be carried out by comparing the measured structural response and the analytically determined response. Due to a large number of old bridges, interest in the use of non-destructive load testing has increased significantly in recent years to provide a better understanding of the bridge behavior in its actual condition. To date, this method is used for a variety of goals, such as providing better estimates for bridge load rating [62–64], bridge rating using system reliability assessment [65], transverse load distribution of existing bridges [66], redundancy evaluation of damaged bridges [67], residual bridge capacity after damage [68], and performance evaluation of new bridge structural systems [69].

Figure 1-8. Non-destructive bridge load testing for the assessment of damaged bridges.

Bridge monitoring and damage detection through determining changes in the bridge dynamic characteristics have been rising over the years. Many researchers have attempted to detect damage in structures using changes in natural frequencies [70,71], damping ratios [72,73], and mode shapes [74–76]. Monitoring the dynamic bridge responses can be performed through sensors installed on the bridge to record the bridge vibration using normal traffic or bridge load test as excitation [77]. The location of sensors can be optimized such that the maximum response is obtained for the desired sensors for the vibration modes of interest [78]. Most of the typical experimental tests have been carried out using piezoelectric accelerometers and fiber optic sensors [79]. This method has been successfully implemented in many applications, such as cable-stayed bridges and steel highway bridges [80–83]. Nevertheless, bridge load testing and instrumentation require direct access to the bridge and hardwiring from the transducers to the data acquisition system, causing traffic interruption and safety issues [84,85].

Damage detection using static field test measurements is another method utilized by researchers [86]. Mehrabi et al. [87] proposed an analytical procedure, Precursor Transformation Method (PTM), to effectively identify the location(s) and severity of possible damage based on measured changes in structural response parameters in cable-stayed bridges. This method has been used by many researchers as an applicable damage detection approach in axial members [88–90]. The main concept in this method is to measure changes in structural response parameters in time under a specific loading condition, e.g., dead load. For bridges with smaller spans, the dead load level alone is not significant enough to cause noticeable response changes, and live load testing becomes inevitable. Other methods that are based on parameter estimation and model updating will be more closely applicable to the bridges in this study. In these methods, the analytical model of the structure is updated based on available static or dynamic load testing results [91–97]. For these methods to be effective, a number of loading cases/configurations and corresponding measured responses are needed. The more the number of loading configurations, the better will be the accuracy of the model.

1.2 Significance of Study

Bridges are ubiquitous features of the American transportation system, connecting the roadways that link the infrastructure of the United States. Currently, there are over 617,000 bridges in the U.S.; 42% of all bridges are at least 50 years old, and 46,154, or 7.5% of the nation's bridges, are considered structurally deficient, meaning they are in "poor" condition. A recent estimate for the nation's backlog of bridge repair needs is $125 billion [98]. As these figures indicate, the U.S. struggles with significant deficiencies in its most essential infrastructure. However, repairs and replacement are not the only costs associated

with bridges, as monitoring alone requires a significant investment by local, regional, and national authorities as well as causes significant traffic blockages and hazards for both those assessing the damage and the drivers negotiating the roads. There is an urgent need for new ways to advance the United States' response to its current and impending bridge crisis as the structures continue to age. This includes tools both to predict and to monitor needed bridge maintenance, which ultimately reduces high financial costs while increasing public safety.

1.3 Organization of Dissertation

This dissertation is organized into four chapters, as follow:

Chapter 1 (herein) describes the twin steel box girder bridges, prefabricated bridge systems, and available damage detection methods for monitoring these bridges.

Chapter 2 establishes a design target performance and safety level for twin steel box girder bridges consistent with the principles of reliability theory that was previously used for calibrating the current AASHTO LRFD specifications and LRFR manual and outlines a methodology for assessing the redundancy of these bridges. Reliability analysis requires the actual bridge behavior before and after the fracture of one girder as well as the maximum live load expected on the bridge for the time interval used in the reliability calculations. Moreover, this chapter investigates the dynamic and static behavior of twin steel box girder bridges after various damage scenarios and develops a non-contact bridge monitoring technique for fracture critical elements based on the bridge dynamic responses to address issues associated with conventional inspection.

Chapter 3 investigates the performance of a box-beam bridge to understand its behavior after potential damage at the longitudinal joints. This chapter develops a new analytical

procedure to detect the location of the longitudinal joint damage and its relative significance in the bridge based on the measured changes in bridge dynamic and static response parameters and model updating methods.

Chapter 4 summarizes the conclusions, recommendations, and suggestions for future studies.

1.4   Major Contribution of This Dissertation

The research performed for this dissertation has contributed to the body of the knowledge in several aspects:

- Analytical approaches using detailed finite element (FE) modeling methods were developed to simulate the behavior of damaged bridges for calculating the bridge load-carrying capacity and investigating the failure mechanisms after damage considering shear stud failure, support uplift, concrete damage plasticity, dynamic behavior, railing contact, and connection failure.

- A simple and unified yield line analysis model was developed based on the concrete deck damage pattern observed in the FE analysis to determine the load-carrying capacity of twin steel box girder bridges subjected to different trucks configurations after a full-depth fracture of one girder. This model applies to a wide variety of truck loads and configurations.

- Experimental approaches were developed for monitoring of structural behavior, including the use of a non-contact laser vibrometer. This technique addresses the traffic interruption and safety issues associated with the available bridge monitoring methods.

- Damage detection methods were developed and suited to bridges with distinct vulnerabilities. These methods can effectively identify locations and significance of possible damage based on the measured changes in bridge response parameters. These methods followed the general approach for model updating, parameter identification, vibration frequency, and mode shape-based damage detection.

- A damage detection tool was developed for bridges with prefabricated deck panels/girders that is generally applicable to all bridges with distinct vulnerabilities.

These features are discussed in detail in the next chapters.

CHAPTER 2   TWIN STEEL BOX GIRDER BRIDGES

This chapter is divided into two sections; 1) Redundancy of twin steel box girder bridges that establishes a design target performance and safety level for twin steel box girder bridges consistent with the principles of reliability theory that was previously used for calibrating the current AASHTO LRFD specifications and LRFR manual, and outlines a methodology for assessing the redundancy of these bridges, and 2) Health monitoring of steel box girder bridges that investigates the dynamic and static behavior of twin steel box girder bridges after various damage scenarios and develops a non-contact bridge monitoring technique for fracture critical elements based on the bridge responses to address issues associated with conventional inspection.

It is critical to establish the interconnectivity of the two subjects introduced in the above paragraph. The main goal is to develop a rapid and effective damage detection methods for TSBG bridges so that the bridge can be repaired before the damage results in irreparable damage or collapses. However, since these bridges are designated/suspected to be fracture critical and therefore vulnerable to fracture in one girder, it is imperative to establish that they have reserve capacity after the fracturing of one girder. Otherwise, detection of damage that is a cause for total failure or collapse would not make sense.

2.1   Redundancy of Twin Steel Box Girder Bridges

2.1.1   Development of "Equivalent" or Notional Twin Steel Box Girder Bridge

The FDOT sponsored project performed earlier by FIU has developed a preliminary approach to develop an "Equivalent" simple or continuous span bridge that could represent a series of twin steel box girder bridges [13]. This approach and conceptual steps for developing a notional bridge are summarized as follows.

The most reliable method for checking the redundancy of twin steel box girder bridges is conducting a detailed nonlinear finite element model and checking the critical limit states and the minimum load levels that bridges can carry before these limit states are reached. However, checking the redundancy of all twin steel box girder bridges within the inventory of a given state requires a significant amount of financial, labor, and computer recourses. Moreover, future bridges may have different characteristics than the current bridges, and their redundancy needs to be evaluated by developing a new finite element model.

The notional approach proposed by the earlier FIU study suggested reducing the level of efforts by subdividing all twin steel box girder bridges within the state inventory into several groups based on their main characteristics and developing a notional simple or continuous span twin steel box girder bridge that would represent each group. By evaluating the redundancy of the notional bridge using a detailed nonlinear finite element model, all bridges within the group under consideration can also be evaluated. Moreover, the redundancy of any new bridge can be evaluated by comparing its characteristics to the presented notional bridges.

The grouping criteria are determined based on the geometrical characteristics of the bridge, including the type of bridge, designed lane-load number, maximum span length, number of spans, the radius of curvature, and cross-section. Based on these factors, bridges of interest can be categorized into several groups. Once select bridges are categorized into groups, a notional bridge model that can represent all the bridges within each group needs to be developed.

By developing a calibrated finite element model for the notional bridge representing each group, the analysis results such as the ultimate load-carrying capacity and maximum

deflection can be calculated to check against redundancy criteria. As a result, if the notional bridge model satisfies the redundancy criteria and is classified as redundant, all the bridges within that group will also be categorized as redundant. If the criteria are not satisfied, bridges in that group can be divided into smaller subgroups, and the process to find a group that meets the redundancy criteria can be repeated. This approach has the potential ability to classify all the bridges into redundant or non-redundant groups.

2.1.2   *Florida Bridge Inventory*

At the request of FIU researchers, FDOT Research Office provided an inventory of steel box girder bridges in the state of Florida. As it was stated earlier, the functional and geometric parameters of bridges that have an effect on the ultimate load-carrying capacity and maximum deflection need to be considered for developing a notional bridge for each group of bridges in the inventory. As a result, the Florida Bridge Inventory was statistically analyzed to determine the available range of each functional and geometric parameter. According to the Florida Bridge Inventory, as of 2016, there are approximately 12,900 bridges in Florida, including 1200 steel bridges, of which 140 are steel box girder bridges, with the majority being two-box girder bridges. Three hundred ninety steel bridges currently are classified as Fracture Critical. Table 2-1and Figure 2-1 show the distribution of bridges based on the number of box girders that varies from a single girder to nine girders. Single box girder bridges, regardless of their configurations, are classified as fracture critical bridges and are excluded from this study. If a twin steel box girder bridge group is determined to be redundant, bridges with three or more box girders with the same character would be automatically determined to be redundant. Hence, statistical analysis of the inventory in this study will be performed over all available two-box girder bridges.

Table 2-1. Distribution of bridges: Number of the box girder.

No. of Box Girders	1	2	3	4	≥ 5	Total
No. of Bridges	3	85	33	7	12	140
Percentage	2%	61%	24%	5%	9%	
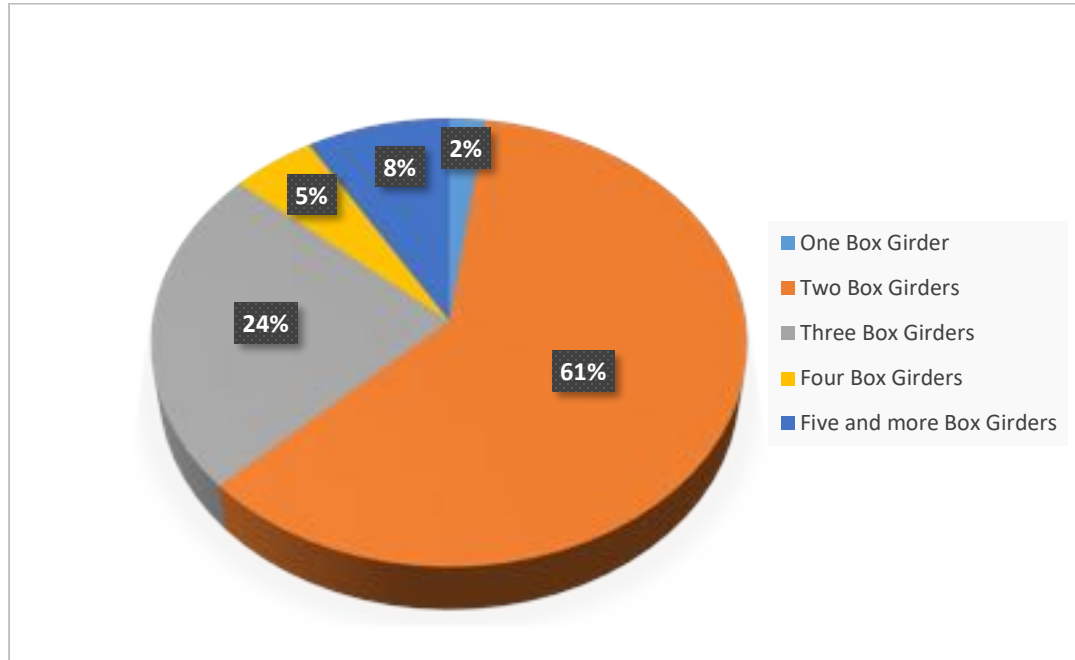
Figure 2-1. Distribution of bridges: Number of box girders.

2.1.2.1 *Maximum Span Lengths and Number of Spans*

The span lengths and the number of spans for a bridge are normally determined in design based on parameters such as the topography of the site, configuration of other roads beneath or around the bridge, environmental issues, architectural plans, structural systems, and construction methods. In a multi-span bridge, span lengths and the number of piers are usually determined for optimum configuration. However, by considering environmental effects and construction difficulties for the piers, longer spans with fewer foundations may be the preferred solution. Figure 2-2 shows the distribution of maximum lengths of span for Florida's twin steel box girder bridges divided into five main groups. The span lengths

vary from 113 ft to 372 ft, with a large majority of bridges having a span between 150~250 ft.

Figure 2-3 shows the distribution of bridges based on the number of spans. As can be seen, most of the bridges have more than three spans, and there are only five simple span bridges of this type in the state of Florida. The number of spans, consequently the continuity of spans, plays a defining role in the maximum deflection and ultimate load capacity of a bridge. This is especially important since one fractured girder in a span within a multi-span bridge can carry the load as a cantilever beam. As a result, the stiffness of continuous bridges after fracture is much higher than simple span bridges with the same characteristics. The worst fracture scenario in a multi-span bridge is a fracture in the middle of the first or last span, i.e., exterior spans. Because in this case, the fractured girder can act as a cantilever beam just on one side. Accordingly, and for simplicity, a two-span continuous bridge can be considered to represent all multi-span bridges conservatively.

	100 ≤Span<150	150≤Span<200	200≤Span<250	250≤Span<300	300≤Span<400
No. of Bridges	10	28	28	15	4

MAXIMUM SPAN LENGTH (FT)
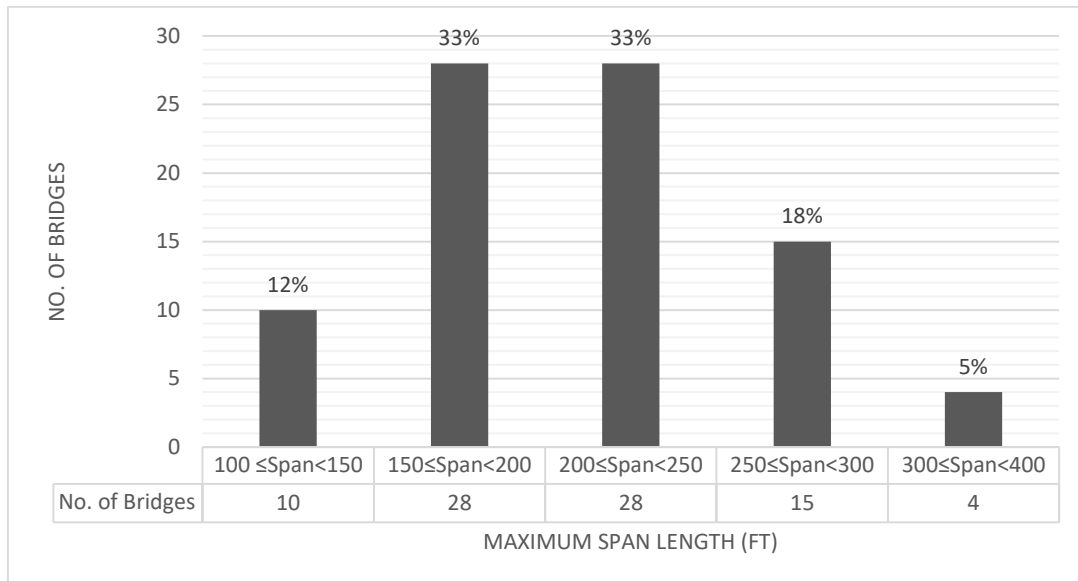
Figure 2-2. Distribution of bridges: Length of max. Span.

23
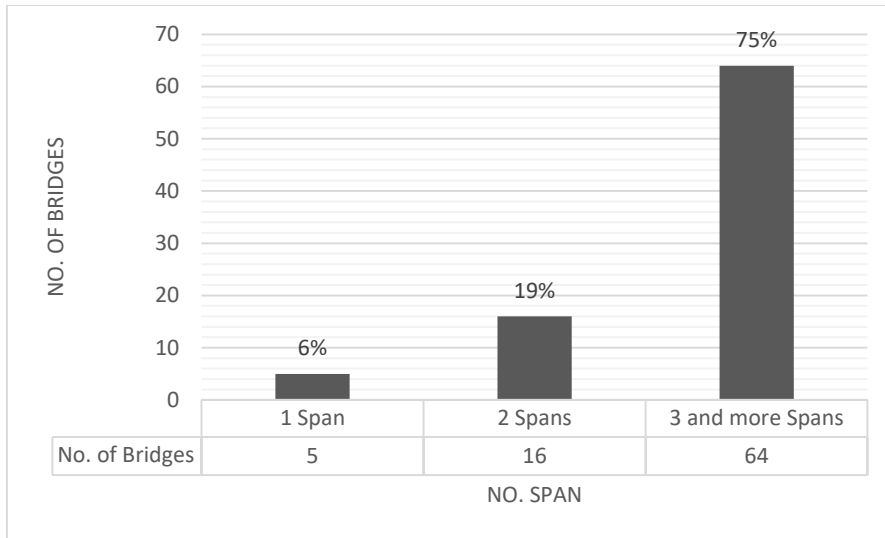
Figure 2-3. Distribution of bridges: Number of the span.

2.1.2.2 *Number of Lanes*

The number of lanes is determined based on parameters such as average annual daily traffic (ADTT), the desired level of service, percent of trucks and peak hour factor (PHF), and the number of lanes in the connecting roadway. Loading configuration for the design and evaluation of a bridge depends on the number of lanes, therefore making it another effective parameter in redundancy evaluation. As shown in Figure 2-4, statistical analysis over the Florida bridge inventory shows that 92% of twin steel box girder bridges have 1 or 2 lanes, which are generally used for overpass roadways. Therefore, because of their lower percentage number, bridges with 3 or 4 lanes, for the time being, are not considered in the grouping criteria. Also, for all the remaining single and double-lane bridges, 2-lane bridges will be used conservatively in the grouping process.

24
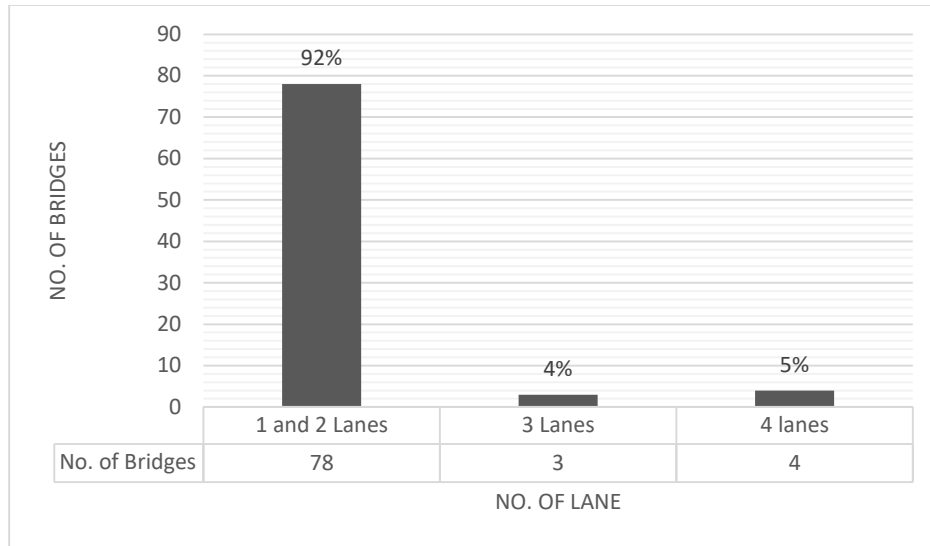
Figure 2-4. Distribution of bridges: Number of lanes.

2.1.2.3 *Deck Width*

The typical lane width is 12 ft; however, the actual width can vary based on the type of roadway, whether it is a principal arterial, rural highway, or residential street, or whether it is in a straight or curved span. Further, the lane closest to a raised median or in a ramp may be extra wide to allow for some distance between the vehicle and the median. Deck width includes the lane widths plus shoulders, curbs, and railings, and the larger the lane width, the more critical will be the effect of eccentric loading (over fractured girder). Road width is normally 2 to 3 ft smaller than deck width. Analysis of inventory bridges shows that the deck width varies within a range for a certain number of lanes. For example, the deck width for a two-lane bridge varies between 40 ft and 50 ft. For this study, the deck width is not considered a parameter (variable). For simplicity, it will be attempted to use in analysis a typical width that would represent the majority of two-lane bridges. It is also realized that the design of a specific bridge, including dimensions and spacing of the

girders, have already taken into account the deck width, therefore renders it to be a dependable variable. Figure 2-5 shows the distribution of bridges based on the deck width.
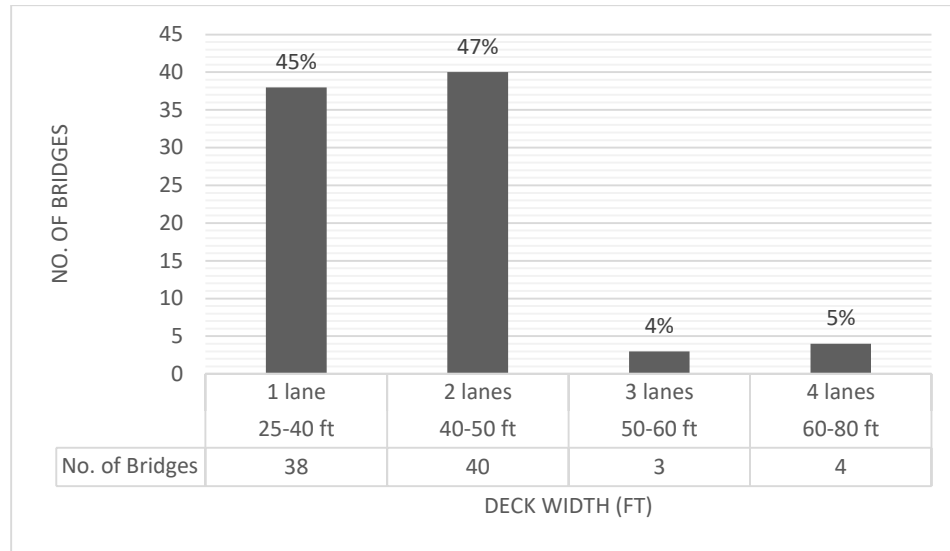
Figure 2-5. Distribution of bridges: Deck width.

2.1.2.4 *Radius of Curvature*

Whilst straight highway bridges are the ideal configuration when the design is concerned; bridge layouts may need to be curved due to the site topology, existing obstacles, and roadway function (ramps). The minimum radius of curvature, as shown in Figure 2-6, is normally determined based on parameters such as design speed, slide friction factor, lateral acceleration, super-elevation, steel constructability, functional adequacy, space availability, etc. As the radius of curvature of a bridge decrease, the torsional moment increases due to the eccentricity of gravity loads relative to the line of support. This torsional moment is significant even for a short-span bridge.

Because of this, steel box girder bridges, because of their high torsional resistance, are mainly used for ramp and curved overpass highway bridges. In cases where one girder is fractured, torsional resistance would decrease significantly; as a result, loading eccentricity

due to curvature will negatively affect the ultimate load capacity and serviceability of the bridge and cannot be ignored.
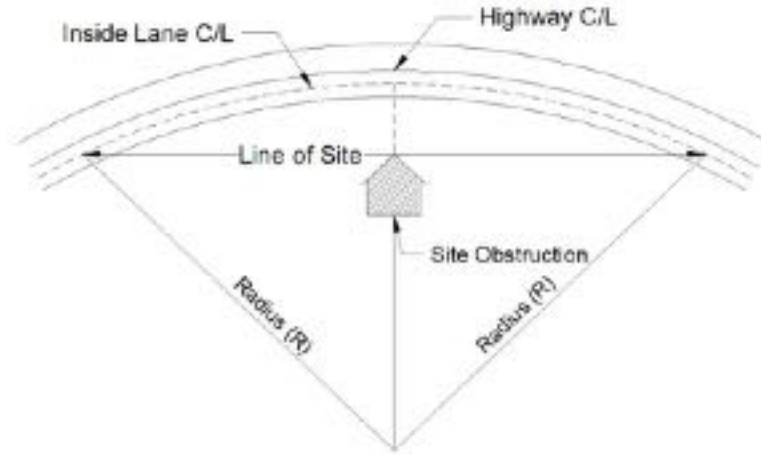
Figure 2-6. The radius of curvature in the bridge layout.

According to the AASHTO LRFD, the horizontal radius of curvature measured to the centerline of the girder web shall not be less than 150 ft. In addition, the radius shall not be less than 1000 ft when the flange thickness exceeds 3.0 in or the flange width exceeds 30.0 in. Table 2-2 shows the available minimum radius of curvature for each span group that would be used for grouping representing the most critical combination of span length and curvature.

Table 2-2. Distribution of loading eccentricity based on bridge curvature.

Length of Max. Span (ft)	100-150	150-200	200-250	250-300	300-400
Available Min. radius of curvature (ft)	175	280	400	490	774

2.1.2.5 *Parameters to Be Considered in Grouping*

Based on analyzing Florida Bridge Inventory, it can be concluded that the only number of spans (single span or two continuous spans), maximum span length, the radius of curvature, and cross-section are the parameters with the highest impact and will be considered for grouping criteria. Other parameters will be assumed constant for notional bridges. In this

research, the deck is assumed to have two lanes, and the width of the deck is assumed to be a typical value most used within the inventory for 2-lane bridges. For this study, skewness at supports will not be considered as one of the parameters, i.e., supports are assumed to be perpendicular to the longitudinal axis of the bridge.

For the initial grouping, all bridges in the inventory are divided into two main groups of simple and two continuous spans. In the latter case, the fractured girder in a multi-span bridge can still carry loads as a cantilever beam from one side; as a result, the stiffness of these bridges after fracture is higher than simple span bridges with the same characteristics. Also, a two continuous-span bridge can represent all other multi-span bridges conservatively. Each of these two main groups can be divided into five subgroups based on the maximum span length presented in Figure 2-2 to form 10 main initial groups. The range of radius of curvature for each span length group can be determined according to the available radius of curvature in the inventory.

Once geometric parameters of the notional bridge for each group are determined, design details of a set of similar inventory bridges will be obtained from FDOT. The notional finite element model for each group could then be developed based on these design details and analyzed to evaluate the ultimate load-carrying capacity and the maximum deflection to span length ratio for the intact bridge. The load-carrying capacity and deflection will be used to define the level of over or under capacity design as well as the deflection to span ratio and to assure that the cross-sections are a true representation for bridge configuration. Finally, the notional finite element model representing each group with the minimum available radius of curvature for that group can be developed for the fractured girder condition. The models can be analyzed under the loading condition obtained from

reliability analysis. The results can be compared to the redundancy criteria (Ultimate limit state and serviceability limit states) to find if a notional bridge with the minimum allowable radius of curvature will meet the redundancy criteria. If the notional bridge representing a group with the minimum radius of curvature satisfies the redundancy criteria, then all bridges in that group will be identified as redundant. Otherwise, the radius of curvature will be increased incrementally until the redundancy criteria are met. Accordingly, the referenced bridge group can be divided into subgroups based on the radius of curvature that would satisfy the redundancy criteria. Since the groups cover wide ranges of span length with different radius of curvature, it is likely that some groups with large spans will not meet the redundancy criteria even for a straight bridge. For such cases, the bridge group can then be divided into subgroups with varying span lengths in each group to determine redundant and non-redundant subgroups based on their span length. Figure 2-7 presents the initial grouping for the notional bridge concept to be considered in the redundancy analysis.
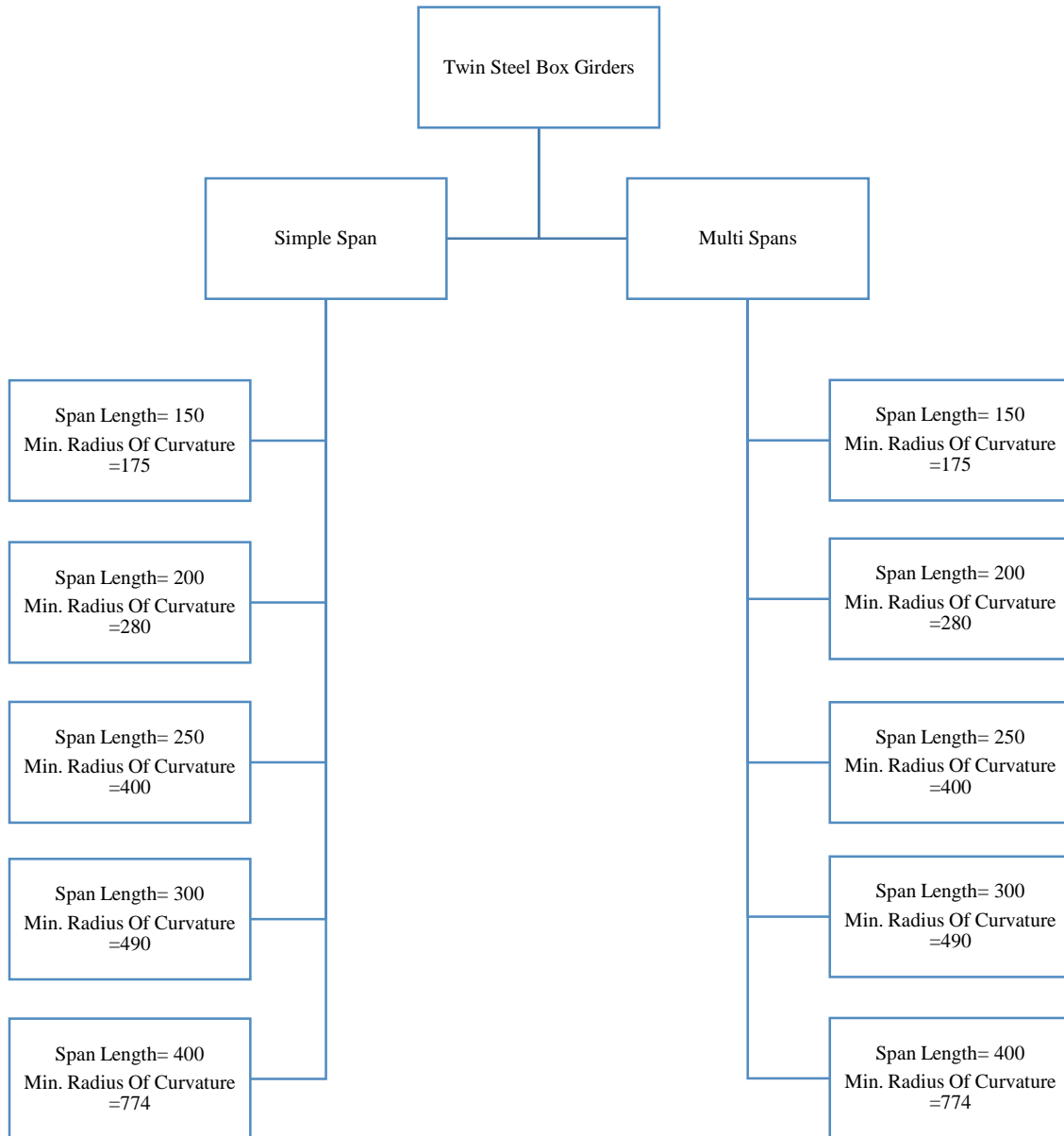
Figure 2-7. The initial notional bridges to be considered in the redundancy analysis.

2.1.3   Development of Loading and Criteria for Redundancy Verification

Several investigations have been conducted for bridge redundancy using different load levels [99–102]. This study attempts to further develop a rational approach to establishing the load level that the damaged bridge should carry using scientific methods and actual data. This involves establishing the target safety level or reliability index [103].

2.1.3.1 *WIM Database*

In the new generation of design codes, safety reserve is provided by means of load and resistance factors determined by the reliability-based calibration process [33]. The code calibration requires the knowledge of statistical parameters of load and resistance. It is important to know the expected maximum load and its statistical parameters. However, these statistical parameters are site-specific dependent on local traffic conditions, the legal limits applicable to the jurisdiction, and the level of enforcement. They also depend on the considered time period and the Average Daily Truck Traffic (ADTT). The load-carrying capacity is also a random variable with corresponding statistical parameters. Therefore, developing criteria for evaluating the redundancy must be based on risk and reliability-based assessment methods before they can be implemented in bridge design and safety assessment codes and standards.

The redundancy criteria must be based on a state-specific bridge live load model that represents the maximum loads expected on the bridge after fracture may have taken place. Since US bridges are inspected every two years, the evaluation period is limited to the inspection period with the understanding that bridge inspectors would be able to detect the fracture during the regular inspection cycle and alert the authorities to take necessary actions. The analysis performed to develop an appropriate live load model for Florida bridges includes weigh-in-motion (WIM) data from 32 stations collected throughout four

years (2013-2016). The truck weight data included relevant information such as, but not limited to, the number of axles, the spacing between axles, axle weights and gross vehicle weight (GVW), and exact time of measurement for each recorded vehicle at each location. The data included 136 million vehicles in total.
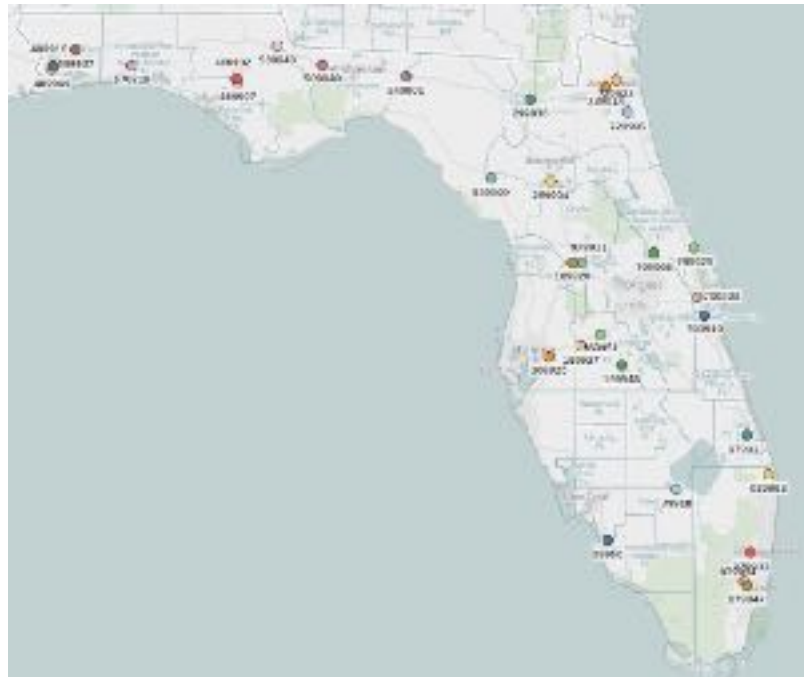
Figure 2-8. Weigh-in-motion (WIM) stations in Florida.

2.1.3.1.1 WIM Data Filtering

Long-term WIM data collection can be affected by errors in recording due to various reasons such as malfunction and improper vehicle positioning on the sensor. More reasons for the need of WIM data filtering are discussed in the literature [104,105]. Some of the errors are inevitable but using the proper filtering criteria can eliminate improper records, thus eliminating the possibility of under or overestimating loads and designs. It was observed that the data obtained from FHWA was filtered through the Traffic Monitoring Analysis System (TMAS) Quality Control (QC) checks [106]. Vehicles with a GVW of

less than 20 kips (9.1 tons) were eliminated from the obtained database as they cause only insignificant damage to bridges and pavements [107].

2.1.3.1.2 Initial Data Analysis

The data left after filtering out vehicles less than 20 kip GVW are used for further analysis. The Cumulative Distribution Function (CDF) of GVWs are plotted on probability paper in Figure 2-9 for the year 2014. Each curve on the plot is data from each WIM station in Florida. Since the controlling criteria in the design are the load effects, i.e., moment and shear created by vehicles. Each vehicle in the database is run over an influence line for the considered span length of 120 ft, and moment and shear are calculated. For a better interpretation of results, the moment and shear produced by each vehicle are divided by the corresponding load effects of the HS-20 design truck. Figure 2-10 shows the CDF plot for the moment ratio of 120 ft span length for the year 2014, and Figure 2-11 shows the corresponding CDF plot for a shear ratio. The CDF of the moment and shear ratios have similar distribution shapes.
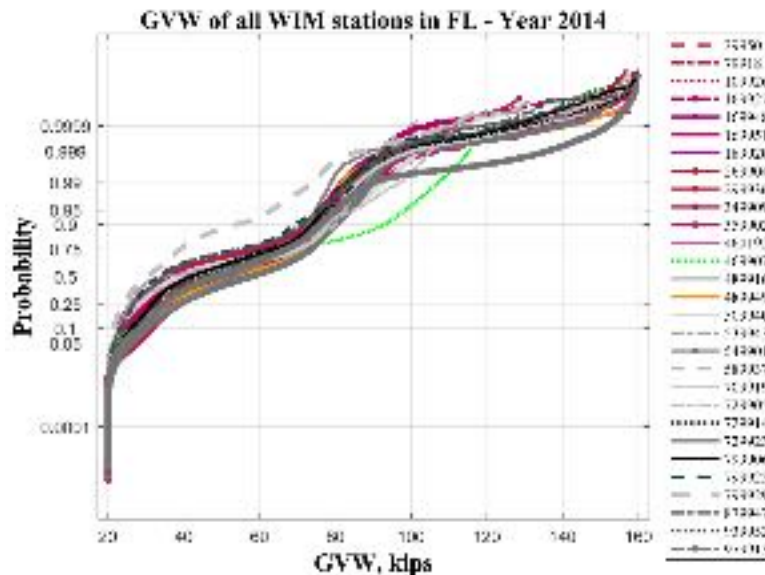
Figure 2-9. CDF plot of GVW of all WIM stations in Florida for the year 2014.
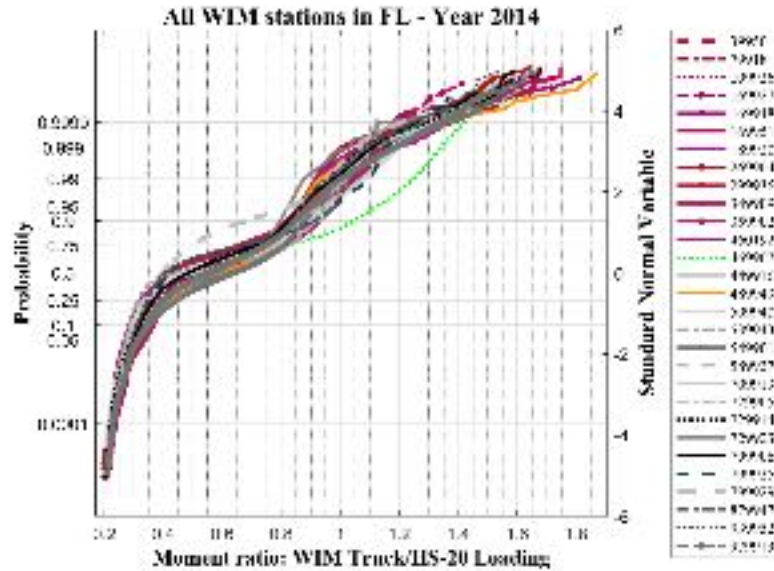
Figure 2-10. CDF plot of the moment ratio of all WIM stations in Florida for the year 2014.
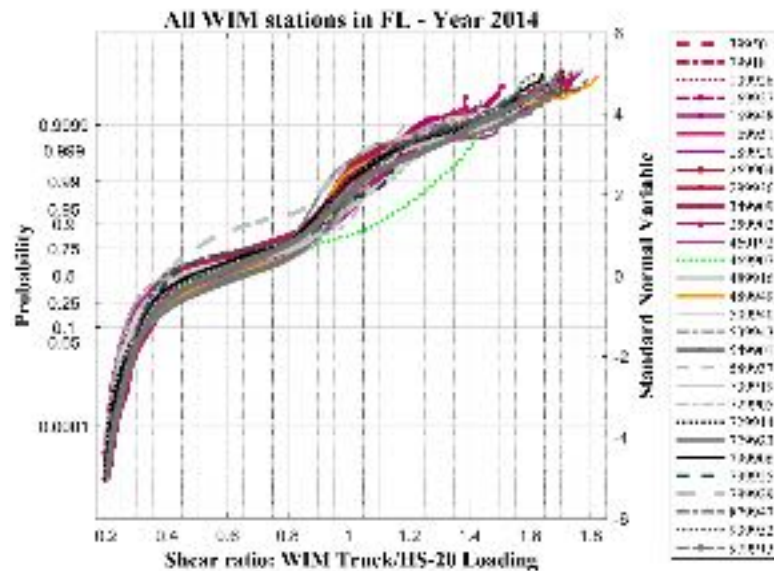
Figure 2-11. CDF plot of the shear ratio of all WIM stations in Florida for the year 2014.

2.1.3.1.3 Maximum Moment for Different Load Periods

The maximum moment is a random variable, and it depends on the period of time considered, ADTT, and span length. In this study, the period of time of two years and a span length of 120 ft is considered. The ADTTs are varied from 250 to 10,000. The mean value of the maximum moment is determined for each WIM station traffic data for different

34

ADTTs. More information about the procedure is discussed in Kulicki, J.M et al. [105].

The vertical coordinates for different ADTT's are shown in Figure 2-12 (a) on a normal

probability scale on the left vertical axis and a standard normal variable scale on the right

vertical axis. For each CDF, the vertical coordinate of the maximum moment (Zmax) is

given by Equation (2-1).

$$Z_{max} = \Phi^{-1}\left(\frac{1}{N}\right) \tag{2-1}$$

where, Φ^{-1} = inverse standard normal distribution function. N = number of records for the

period, T (in days), and certain ADTT as shown in Equation (2-2)

$$N = T * ADTT \tag{2-2}$$

The mean maximum moment can be directly obtained from the graph by reading the

moment ratio (horizontal axis) with the corresponding vertical coordinate for the

considered time period. The values for larger coordinates were projected or extrapolated

as appropriate. For an easier interpretation, the vertical coordinates for different ADTT's

are plotted on the probability paper along with CDF's for the year 2016 in Figure 2-12(a).

The mean maximum moments of each WIM station traffic data for the year 2016 are plotted

on probability paper in Figure 2-12(b).

2.1.3.1.4 Statistical Parameters

It is assumed that 32 WIM stations in Florida have representative truck traffic for Florida.

The statistical parameters of mean maximum and coefficient of variation (COV) of live

load (moment) are shown in Table 2-3. The mean of these maximum values can be

considered as the mean maximum for Florida based live load model. These statistical

parameters can be further used for reliability analysis calculations. In this study, the statistical parameters are calculated only for moments.

(a)

(b)
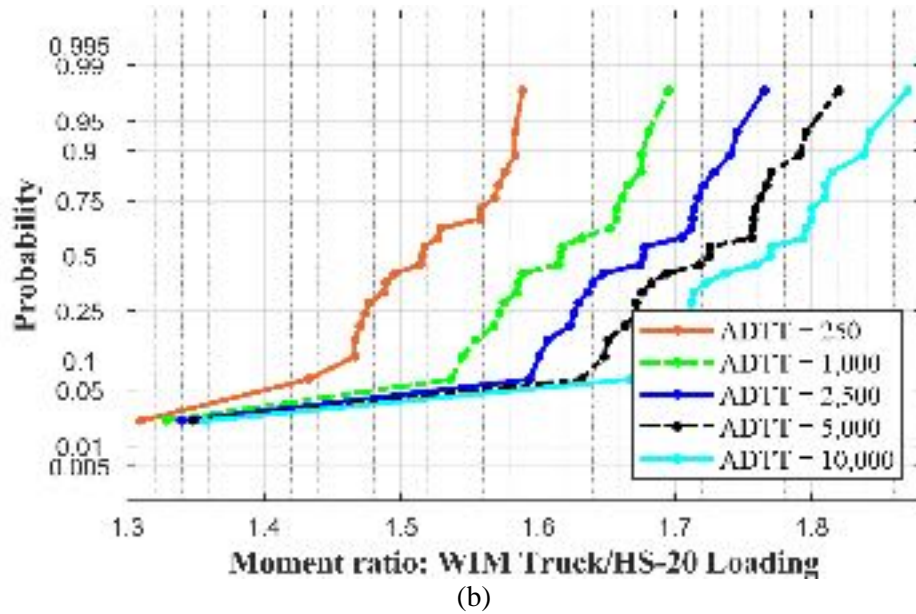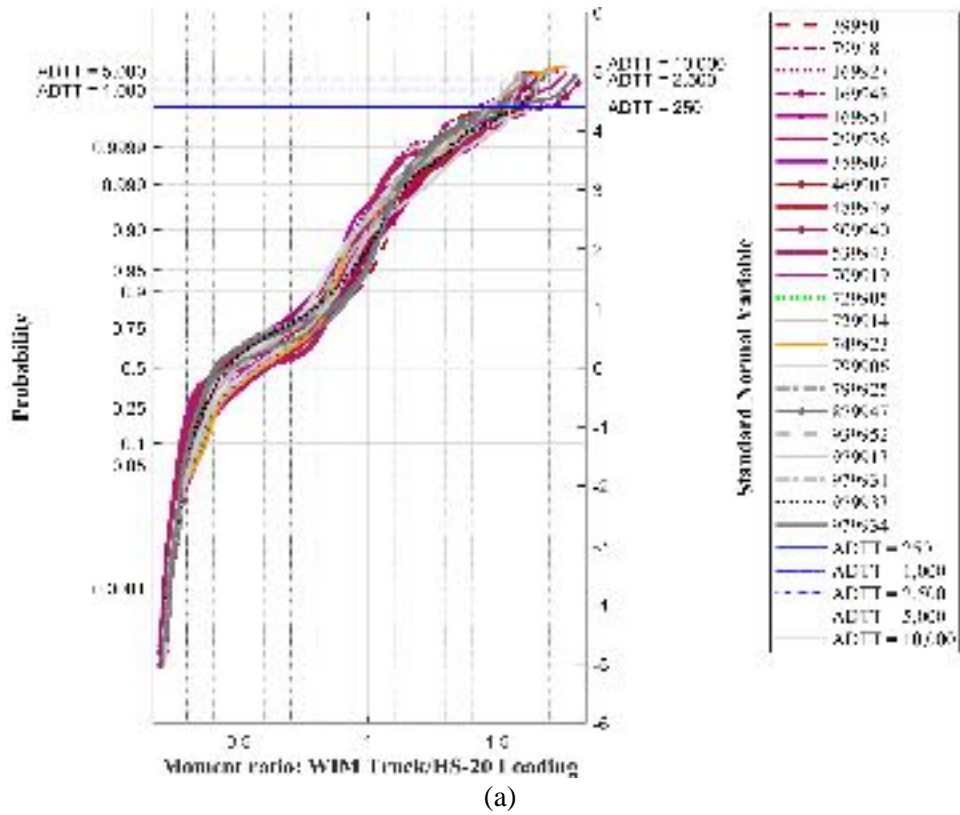
Figure 2-12. CDF plot for the year 2016: (a) Vertical coordinates for different time periods; (b) Mean maximum moment ratios for different ADTT.

Table 2-3. Statistical parameters of live load moments for different ADTT.

ADTT	Year 2013		Year 2014		Year 2015		Year 2016		All years averaged	
	μ	COV	μ	COV	μ	COV	μ	COV	μ	COV
250	1.51	0.07	1.51	0.08	1.50	0.06	1.51	0.04	1.51	0.06
1,000	1.60	0.09	1.61	0.09	1.59	0.07	1.61	0.05	1.60	0.07
2,500	1.66	0.10	1.67	0.10	1.64	0.07	1.66	0.05	1.66	0.08
5,000	1.70	0.11	1.71	0.11	1.69	0.07	1.71	0.05	1.70	0.09
10,000	1.75	0.11	1.76	0.12	1.73	0.08	1.75	0.06	1.74	0.09

2.1.4 Development and Validation of Finite Element Method

Finite element modeling has been recognized as a means for detailed analysis of steel box girder bridges to investigate their redundancy. Construction of a detailed FE model of the bridge and analysis under loading of various configurations is a time-consuming and costly activity. Modeling of every detail in the bridge is neither economic nor always necessary. Additionally, solution methods available for numerical analysis of FE models are numerous and do not always end with proper convergence and accurate results. Hence, the application of FE modeling and analysis can be quite complex and finding an optimum level of refinement and modeling details, as well as the proper solution method, requires performing some experimentation and validation. Validation can be performed by modeling and analysis of bridges that are tested and for which adequate data in the behavior is available. The finite element (FE) model of a twin steel box girder bridge adopted for this study was created in the environment of ABAQUS [108] to simulate the response of the bridge under the fractured box scenario. A generic model is shown in Figure 2-13. The proper modeling techniques, analysis procedure, and material inputs were investigated thoroughly. The details on element types, material properties, and solution method will be discussed later for each of the bridges modeled.

Three bridge specimens for which experimental test results were available were modeled and analyzed for validation of the FE model developed in this study. These bridges are:

- The University of Nebraska–Lincoln Multiple Plate Girder Bridge,

- The University of Texas Twin Steel Box Girder Bridge,

- The Florida International University Twin Steel Box Girder Bridge,

The selected bridges have a steel girder concrete deck composite superstructure.

The University of Nebraska-Lincoln bridge [109] is selected as the first model for validation of the FE models for the elastic and ultimate load tests available for this bridge. Although the Nebraska bridge did not use steel box girders and was not subject to fracture of the girder, however, availability of extensive and accurate experimental test results that included failure modes similar to those expected for twin steel box girder bridges were recognized to provide an excellent source for validating FE modeling and analysis technique and its details in general. The bridge has the same combination of steel girder (I-girder) and concrete deck and included failure modes for the deck such as one-way shear and two-way shear (punching shear) and failure limit states for steel girders.

For the second step, The University of Texas Twin Steel Box Girder Bridge was selected to validate the twin steel box girder model for intact and fractured scenarios. The Texas bridge tests included ultimate uniform loading and point loads in terms of simulating the HS-20 truck for the fractured box scenario. Finally, The Florida International University (FIU) Twin Steel Box Girder Bridge [110] was used to validate the capability of the finite element model for predicting local failure modes such as punching shear and one-way shear in addition to global bridge response. In the FIU bridge tests, a series of elastic tests, a cyclic test, and ultimate load tests were conducted on a small-scale twin steel box girder to

evaluate the redundancy of this type of bridge. The results of the experimental tests revealed that punching shear and one-way shear would be the dominant failure modes for both intact and one-girder fractured twin steel box girder bridges subjected to wheel-simulated loads.

After the model is validated by using experimental results of these three bridges, the twin steel box girder bridge model can then be used for evaluating the redundancy of existing bridges in the state of Florida by analyzing the notional bridges for each group of bridges. The results of these analyses can also be used to determine the dominant failure mode to be considered in the reliability and redundancy analysis.

2.1.4.1 *Modeling Details*

Material nonlinearity for steel and concrete is considered in the models. Traditional metal plasticity is used to represent steel components, and concrete damaged plasticity is used for simulating the cracking and crushing of concrete. Geometric nonlinearity was not deemed to have a significant effect on the results, and for the sake of simplicity, was not included in the modeling. When bridge railing is modeled, Hard contact surface is used for defining the surface contact between the railings. Because there is a gap between each railing segment, there would be no contact between the railing until the gap is closed due to the large deflection of the bridge. In that stage, two sides of the gap will come in contact, and contact force would increase the stiffness of the bridge. As a result, railing contact with a gap needs to be considered in all models. Experimental tests on fractured twin steel box girders show that when there is loading eccentrically over the fractured girder only, torsional moment induced by the loading eccentricity may cause uplift of the intact girder

over the supports. Therefore, to consider the possibility of support uplift during the loading, the contact surface is defined between the girders and supports.

Twin steel box girder bridges consist of steel plate girders, brace members, concrete deck, and bridge railings. According to the structural behavior of each component, various type of elements is used to provide a realistic representation of the twin steel box bridges [111]. Eight-node linear brick elements are used for the concrete deck and the railing with a 2-node linear 3-D truss as the reinforcement embedded into the concrete elements. The Four-node shell element (S4R) is used for modeling steel plate girders and stiffeners; all the brace members for diaphragms are modeled using 2-node linear 3-D truss and beam elements. According to the results of available tests and analyses, shear studs between girders and deck slab may influence the onset of failure in the deck, and therefore shear stud failure is modeled. In this study, the effect of shear stud failure was investigated by comparing the results of FE analysis in the models where shear studs were modeled with the result of analysis where shear studs were not modeled (perfect bond between steel and concrete at the girder to deck slab interface).

Figure 2-13. Typical finite element model of twin steel box girder bridge.

2.1.4.2   *Material*

2.1.4.2.1   *Steel Material Model*

The multi-linear inelastic material model with isotropic hardening is used for the behavior

of steel plates, diaphragms, and reinforcement in both tension and compression [112]. The

linear elastic behavior was defined by the specification of the modulus of elasticity and

Poisson's ratio, which were 29,000 ksi and 0.3, respectively. Yield and ultimate stress of

steel material are considered as the typical value used in the Florida bridges. For the case

of the University of Nebraska–Lincoln bridge, the girders were specified as A36 steel with

the yield strength of 40 ksi (average obtained from tensile testing), and the concrete

reinforcing rebar used in the concrete slab was specified as grade 60 with 60 ksi yield

strength, and for the UT bridge, 50 ksi for the steel plates and 60 ksi for the concrete

reinforcing bars is assumed as the yield strength of steel material. Figure 2-14 shows the

uniaxial representation of the stress-strain relationship for the steel plates and concrete

reinforcement used for the UT bridge. According to von Mises theory, the material yields

when the equivalent stress exceeds the yield criterion.
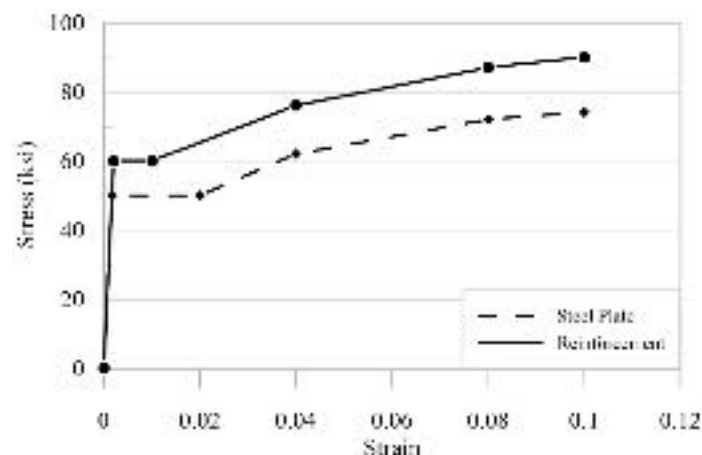
Figure 2-14. Typical steel stress-strain relation.

2.1.4.2.2 Concrete Material Model

A linear elasticity with the concrete damage plasticity is used in the FE models [113]. For the initial elastic behavior, the modulus of elasticity is calculated based on the ACI 318-14 [114] ($E_c = 57,000\sqrt{f_c'}$ (in psi) for normal-weight concrete) and a Poisson ratio of 0.2 was used. The concrete damage plasticity is a continuum, plasticity-based, damage model for concrete. It assumes that the main two failure mechanisms are tensile cracking and compressive crushing of the concrete material, and the uniaxial tensile and compressive response of concrete is characterized by damaged plasticity, as shown in Figure 2-15 [108].
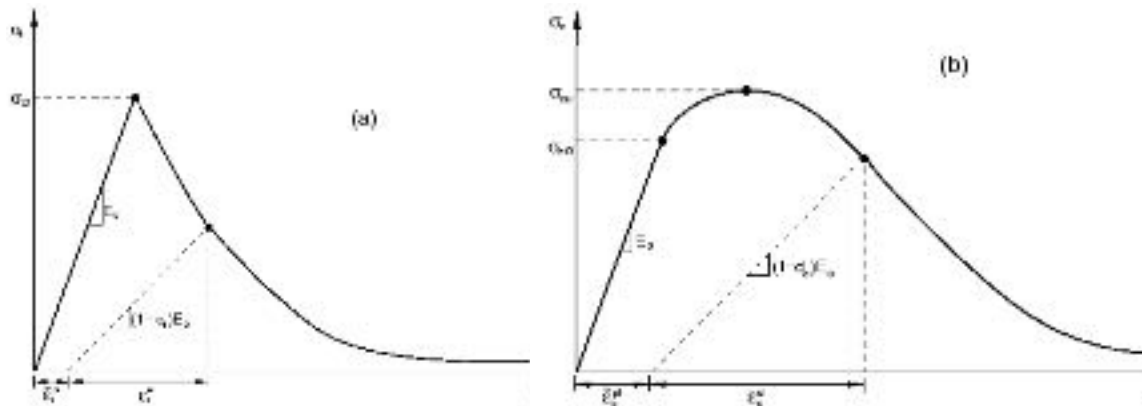
Figure 2-15. Response of concrete to uniaxial loading: (a) in tension; (b) in compression.*[108]*

For uniaxial tension, the stress-strain relationship of concrete is a linear elastic until the point of failure stress, σ_{t0}. After that point, due to micro-cracking in the concrete, tensile resistance decreases with a sharp softening stress-strain response, which induces strain localization in the concrete structure. Under uniaxial compression, the response is linear elastic until the point of initial yield, σ_{c0}. In the plastic regime, the response is typically characterized by stress hardening followed by strain-softening beyond the ultimate stress, σ_{cu}. This representation, although somewhat simplified, captures the main features of the response of concrete.

As shown in Figure 2-15, when the concrete specimen is unloaded from any point on the strain-softening branch of the stress-strain curves, the unloading response is weakened: the elastic stiffness of the material appears to be damaged (or degraded). The degradation of the elastic stiffness is characterized by two damage variables, d_t and d_c, which are assumed to be functions of the plastic strains, temperature, and field variables. The damage variables can take values from zero, representing the undamaged material, to one, which represents the total loss of strength.

2.1.4.3 *Analysis Procedure*

For simulating the bridge behavior during construction, finite element analysis is divided into two main steps: bridge construction and final analysis for live loading. For the first step, an initial implicit static analysis is used to incorporate the loading effect through the erection and construction phase when the concrete is not hardened yet, and the section acts non-compositely with only the girders carrying the dead load. During the bridge construction, only the girders carry the deck, and the dead load deflections in the girders remain locked after the concrete deck hardens. For this reason, the stiffness and mass of the concrete and reinforcing rebar are reduced to a very low value during the construction phase, and an equivalent dead load of the deck is applied on the top flange of the girders based on the tributary area. Moreover, the self-weight of the structural steel of the girder components is applied to the model at this stage. By reducing the stiffness of the deck to negligible, only girders carry the load, and there will be no stress and strain on the concrete deck at the end of the construction phase once the concrete deck has hardened.

The results of the first step will be used as an initial predefined state for the final analysis step. In other words, initial states (stresses, strains, displacements, and forces) for the final

analysis step is the final state at the completion of bridge construction. From this point on, the girder and slab sections act compositely together. Therefore, the initial equivalent uniform dead load of the concrete on the girders considered in the analysis for the previous step is removed and replaced by concrete with its actual stiffness and mass. The concrete damaged plasticity is also activated. Moreover, based on the construction procedure, railing elements are added at this step, which depending on the railing type, can increase the stiffness of the bridge. To model the sudden girder fracture, tie constraints between the elements of the girder web and flange on two sides of the fracture assigned at the first step are removed.

At the final step, the flange and webs of one girder are fractured, and an HS-20 truck loading is applied at the middle of the span over the fractured girder with the maximum transverse eccentricity. At this stage, the bridge experiences large deflection and material damage, and the problem becomes highly nonlinear. Because of this, the implicit static solution method for analysis becomes very sensitive and suffers from numerical instability. As a result, the Explicit dynamic solution method that uses the Euler Central Difference scheme is used for the final analysis steps to prevent convergence problems. In an Explicit solver, the solution at the end of a time increment is computed based on the state of the system at the beginning of the time increment. The stability of the solution is constrained to a small stable time increment and depends on the mass, stiffness, and size of the finite elements used.

In order to compare the results of dynamic analysis with static test experiments, HS-20 truck loading is applied on the deck slowly to minimize the dynamic effect of sudden fracture and loading on the bridge. The equivalent static deflection is then obtained by

averaging the peak dynamic displacements after two periods of oscillation and the maximum. Figure 2-16 shows a typical girder mid-span deflections during dynamic explicit analysis.
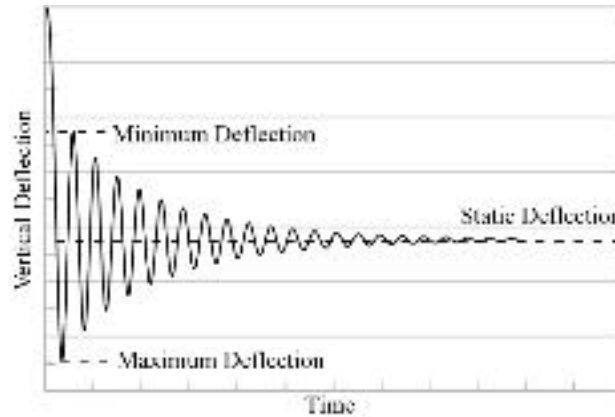
Figure 2-16. Typical dynamic girder deflection due to traffic loading.

2.1.4.4 *Nebraska Bridge Test*

The University of Nebraska bridge, whose test results will be used here for validation of the FE model, is a full-scale simple span bridge with a span length of 70 ft and is 26 ft wide (two lanes). The superstructure consists of three welded steel plate girders made composite with a 7 ½ inches reinforced concrete deck, as shown in Figure 2-17. The girders are spaced 10 feet in the center, and the reinforced concrete deck has a 3 feet overhang. As shown in Figure 2-18, the railing system is a typical Nebraska Department of Road (NDOR) open concrete bridge rail, with 11x11 inch posts spaced 8 feet on center. Although the superstructure in this bridge did not contain steel box girders, due to the availability of reliable and extensive experimental results that included service and ultimate load testing and associate failure modes, modeling of this bridge was thought to provide a good background for validation of the FE modeling method adopted for this study.
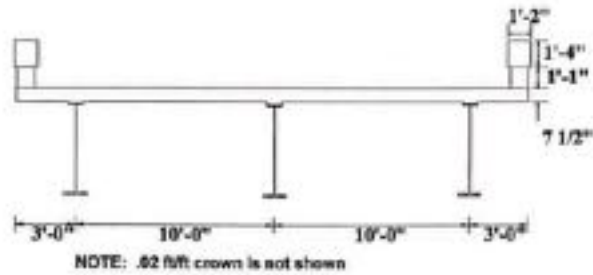
Figure 2-17. The cross-section of the Nebraska test.
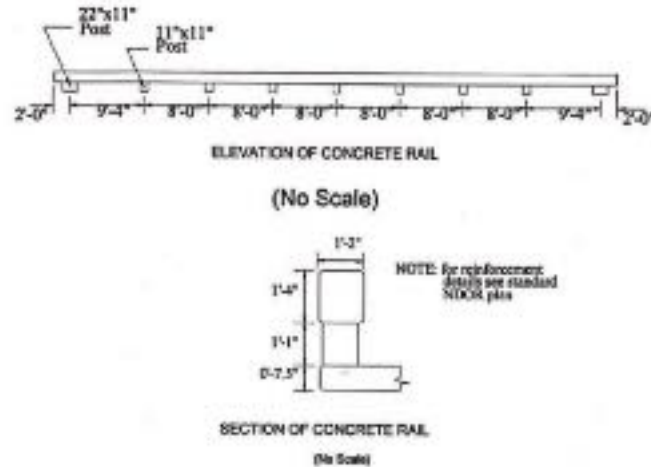
Figure 2-18. Details of standard NDOR open concrete bridge rail.

Live load testing of this bridge consisted of applying cycles of the equivalent of 2.5 times the weight of AASHTO HS-20-44 truck load on each lane of the bridge. Because of the laboratory limitations, the loading pads were placed at twelve and fifteen feet, instead of ASHTO HS-20 typical spacing of 14 feet. To simulate the typical tire contact area, loads were applied through steel plates having the dimensions of 20"×8"×2" and 10"×4"×2" for the rear and front wheels, respectfully.

Several tests were conducted on this bridge to evaluate the effect of diaphragms, elastic behavior, and ultimate load-carrying capacity of the bridge. The ultimate test, which consisted of loading the bridge to collapse, is selected for validating the capability of FE modeling adopted in this study for predicting the elastic behavior and ultimate capacity and failure modes. During the ultimate load test, all diaphragms except those at the ends were

removed to analyze more accurately the response of the steel girder bridge to the applied truck loading. The bridge failure in the laboratory testing is governed by local punching shear failure in the deck under the loading plates. Figure 2-19 shows the loading configuration of the ultimate test.

The strength tests on concrete cylinder samples showed 6000 psi for 221 days after casting, which coincides with the time of ultimate load testing. The steel material used for the girders was specified as A36 steel with the yield strength of 40 ksi, (average obtained from tensile testing), and the concrete reinforcing rebar used in the concrete slab was specified as grade 60 with 60 ksi yield strength. Figure 2-20 shows typical K-frame diaphragms used in the ultimate test for the end supports. Deflection measured at mid-span by potentiometers is used to validate the FE model.
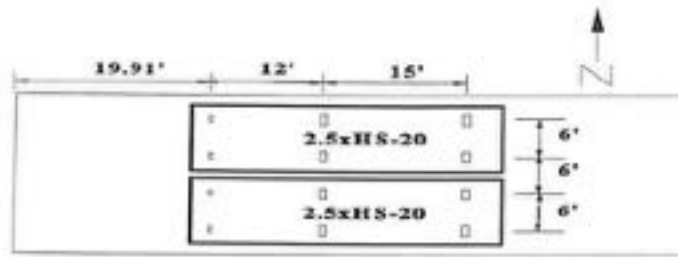
Figure 2-19 The loading configuration of the ultimate Nebraska bridge test.
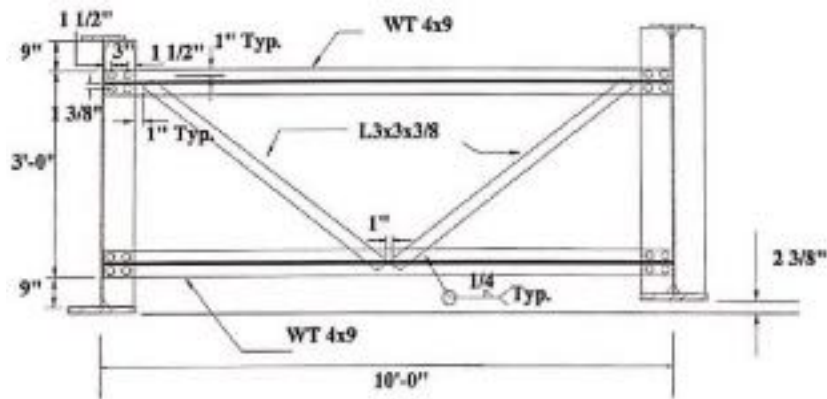
Figure 2-20. Typical K frame detail used in the Nebraska bridge.

The two-step analysis (bridge construction and load application) was carried out to verify the capability of the FE model for predicting the global behavior and the local punching shear failure for the ultimate test. Figure 2-22 and Figure 2-21 show the location and pattern of local punching shear failure that occurred in the experimental test and the FE concrete damage at the top and bottom of the deck, respectively. Figure 2-23 to Figure 2-25 show the comparison of load-deflection curves between experimental and FE results for exterior and interior girders.

Figure 2-26 compares the local cracking in the railing during ultimate load testing for the experimental test and FE model. The results and comparisons show that the FE model can predict the global behavior of the bridge during the elastic and plastic states and simulates the local failure due to punching shear in the deck and cracking in the railing.

(a)   (b)
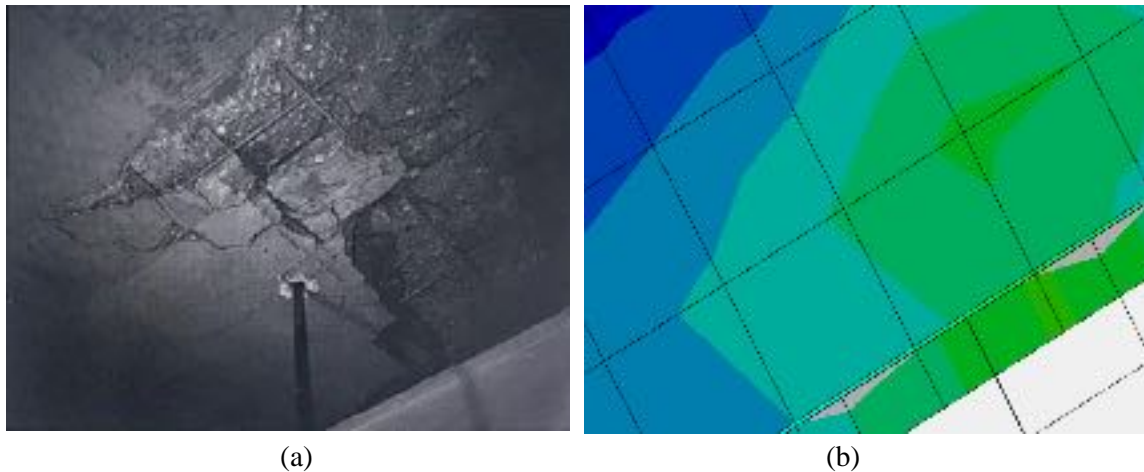
Figure 2-21. Typical punching shear failure: (a) Experimental test; (b) Finite Element Model.
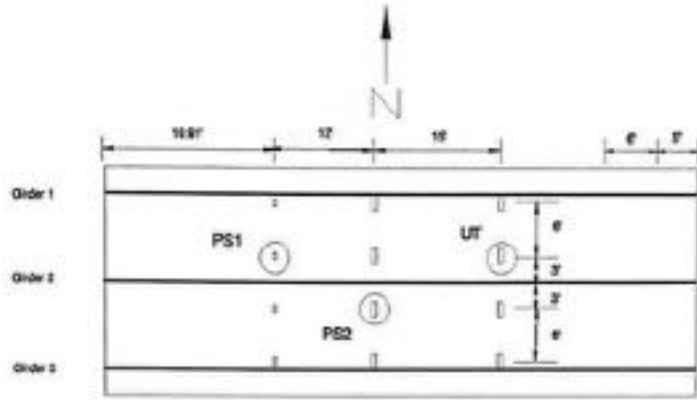
(a)
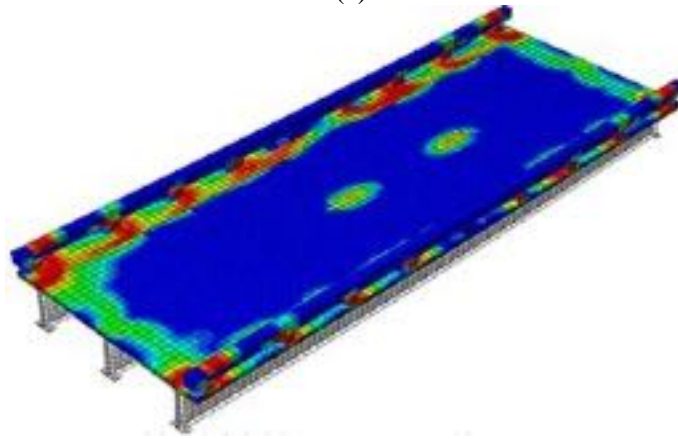
(b)

Figure 2-22. The locations of punching shear failure: (a) Experimental test; (b) Finite Element Model.
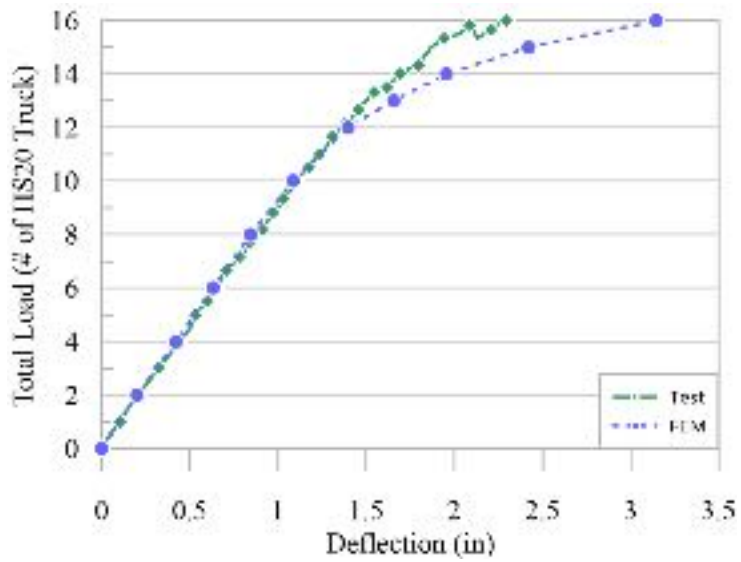
Figure 2-23. Comparison of load-deflection curves for north exterior girder obtained from experiment and FE model.
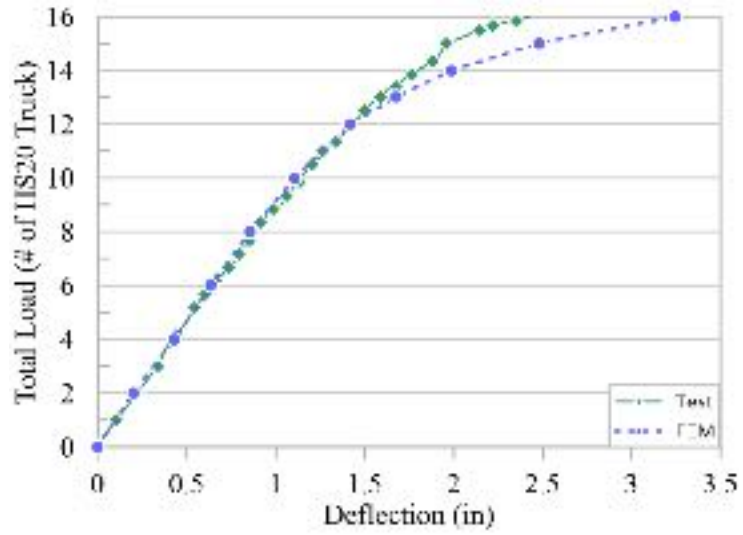
Figure 2-24. Comparison of load-deflection curves for south exterior girder obtained from experiment and FE model.
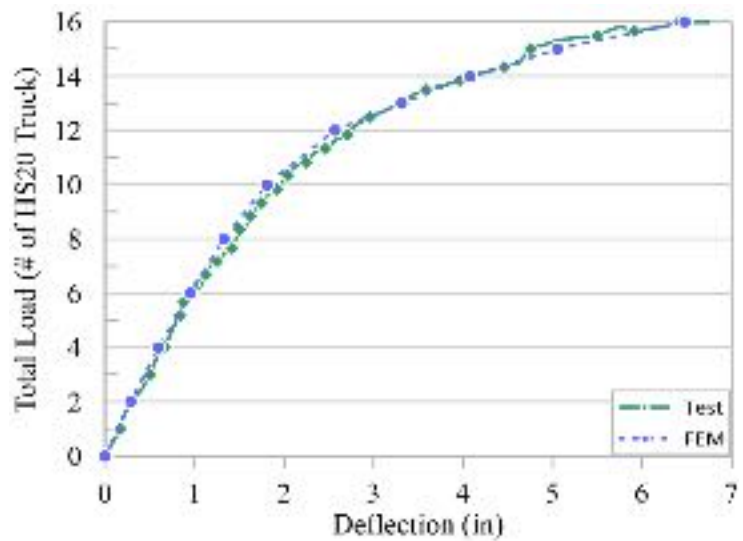
Figure 2-25. Comparison of load-deflection curves for interior girder obtained from experiment and FE model.

<div align="center">(a)   (b)</div>
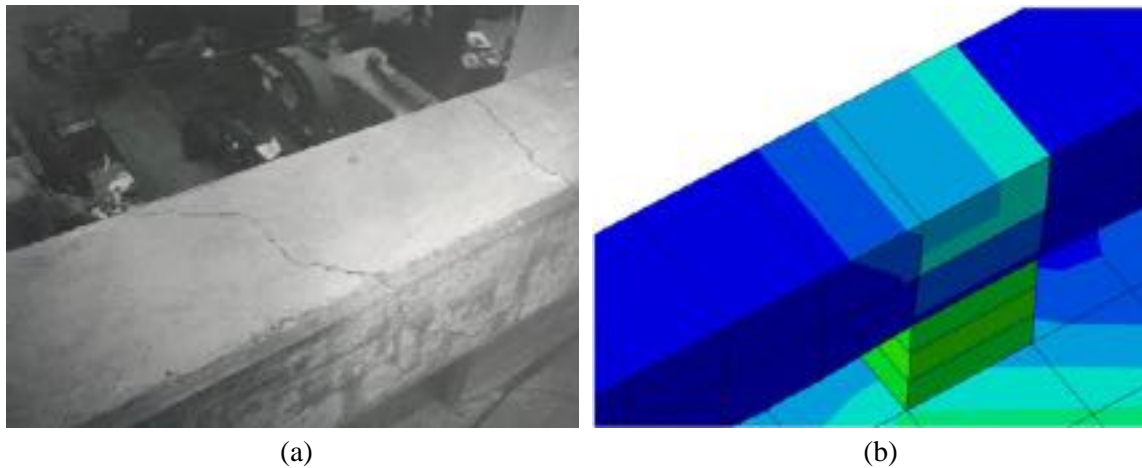
Figure 2-26. Torsional cracks in the rails: (a) Experimental test; (b) Finite Element Model.

2.1.4.5 *The University of Texas Twin Steel Box Girder Bridge*

To further verify the FE model for the case of a bridge with steel box girders, The University of Texas Twin Steel Box Girder bridge was selected. This bridge had been tested in full-scale, with one of its girders having the bottom flange and part of the web fractured, and therefore, offered an excellent opportunity for FE model verification. The UT bridge was a curved 120-ft composite single-span twin box girder bridge. The deck width was 23.3 ft with the radius of curvature of 1,365.4 ft and a deck slab thickness of 8 in. The bridge also used 3 in. concrete haunch above the flange of the steel boxes. Figure 2-27 shows the UT bridge that was tested. The deck in this bridge also had erection diaphragms, end stiffeners, intermediate diaphragms, and horizontal bracings.

Three tests were conducted on the full-scale bridge. The first test was performed to evaluate the behavior of the bridge under loading simulated by the weight of concrete blocks (slightly over HS-20 loading and equal to 76 kips total) after a sudden fracture at the bottom flange of the exterior girder. The second test was conducted by cutting the bottom flange and 83% web of the exterior girder to study the fractured bridge behavior under the same loading as Test 1. And finally, the ultimate load test was performed to investigate the

ultimate load-carrying capacity of the fractured bridge. The ultimate test was performed by increasing a uniform load applied using sand over the HS-20 truck outline area until the bridge collapsed. These three tests were used for verification of the FE model for the fractured bridge scenario.

Figure 2-27. The University of Texas twin steel box girder bridge.

The steel material used for the girders of this bridge was specified with a yield strength of 50 ksi, and the reinforcing rebar used in the concrete slab was specified as grade 60 with 60 ksi yield strength. Based on the compression tests performed on the concrete cylinder samples, 5.37 ksi for the first test and 6.23 ksi for the second and third test was used as the compressive strength of concrete in the deck.

Similar to the earlier analysis, a two-step analysis (bridge construction and load application) was performed with the FE model for simulating the experimental testing on the UT bridge. Figure 2-28 shows the FE model used for validating the results. Hard contact surfaces were used for defining the surface contact at railing gaps, and girders support bearings in this model. Since there is a gap between each railing segment, there is no contact between railing segments until the gap is closed due to the large deflection of the

bridge, as shown in Figure 2-29 with the stress and concrete damage rise at railing contact points. After closing the gap, the contact force increases the stiffness of the bridge. As a result, for the first test, since there is a small deflection, the railing does not increase the stiffness of the system. However, for the second and third tests, surface contact between railings increases the stiffness of the bridge.
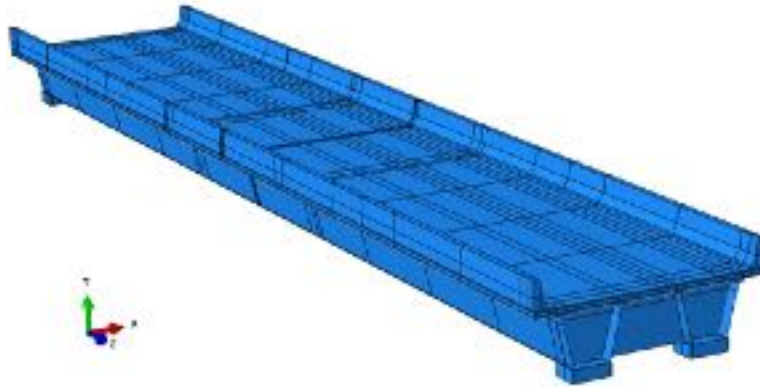
Figure 2-28. The University of Texas FE model.
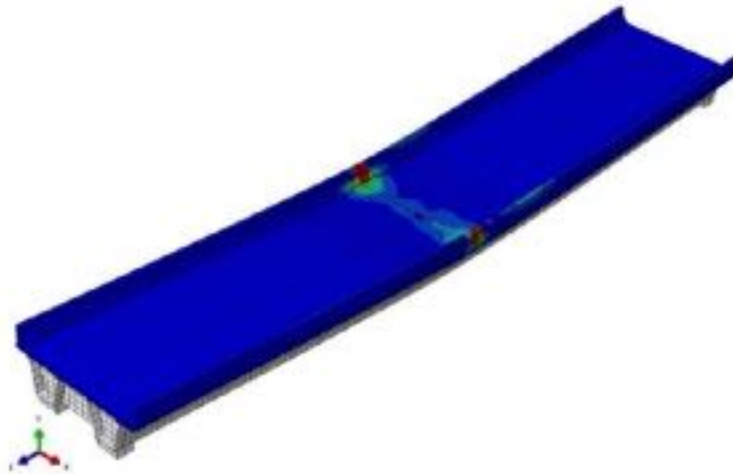
Figure 2-29. Crushing of the railing due to contact surface.

Figure 2-30 and Figure 2-31 show the comparison between experimental and analytical deflection of the fractured girder for the first and second tests, respectively. The horizontal axis in these graphs shows the location along the span, and the vertical axis shows the deflection at the end of the test. As shown in these graphs, the FE model can predict the

deflection of the girder along the bridge for both the first and second tests. One exception is for Test 2 (Figure 2-31) for deflection at the mid-span. A separation between the top flanges of the fractured girder and the concrete deck due to tension cracking of the concrete was observed during the second experimental test, which caused a sudden deflection at the middle of the span. This may, however, be attributed to post-failure local loss of composite action. By defining the concrete damage plasticity, the FE model can predict the cracking and crushing of the deck due to loading within its capabilities.

Experimental results of the University of Texas test show that extensive cracking developed on the top surface of the concrete deck in the second test. The most prominent cracks were located longitudinally above the intact girder due to one-way shear failure, and the cracks extended toward the supports. Furthermore, some transverse cracks were observed starting from the railing of the fractured girder toward the intact girder. Figure 2-32 and Figure 2-33 show the crack pattern on the surface of the concrete deck from both experimental test and FE analysis. As shown, the FE model can predict the transverse and longitudinal crack pattern of the concrete deck due to load distribution after the fracture.
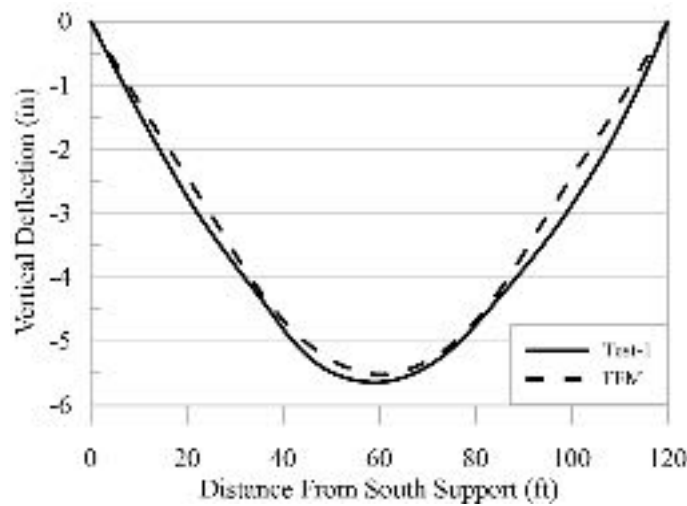
Figure 2-30. Comparison of the deflection curve of the first test for fractured girder obtained from experiment and FE model.
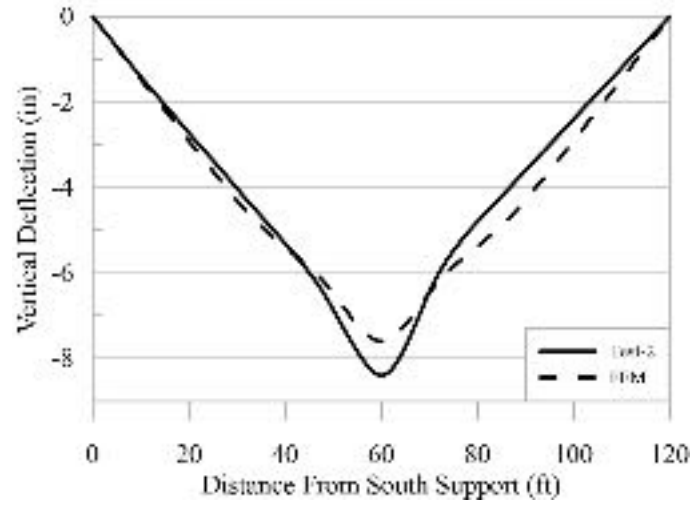
Figure 2-31. Comparison of the deflection curve of the second test for fractured girder obtained from experiment and FE model.

(a)

(b)
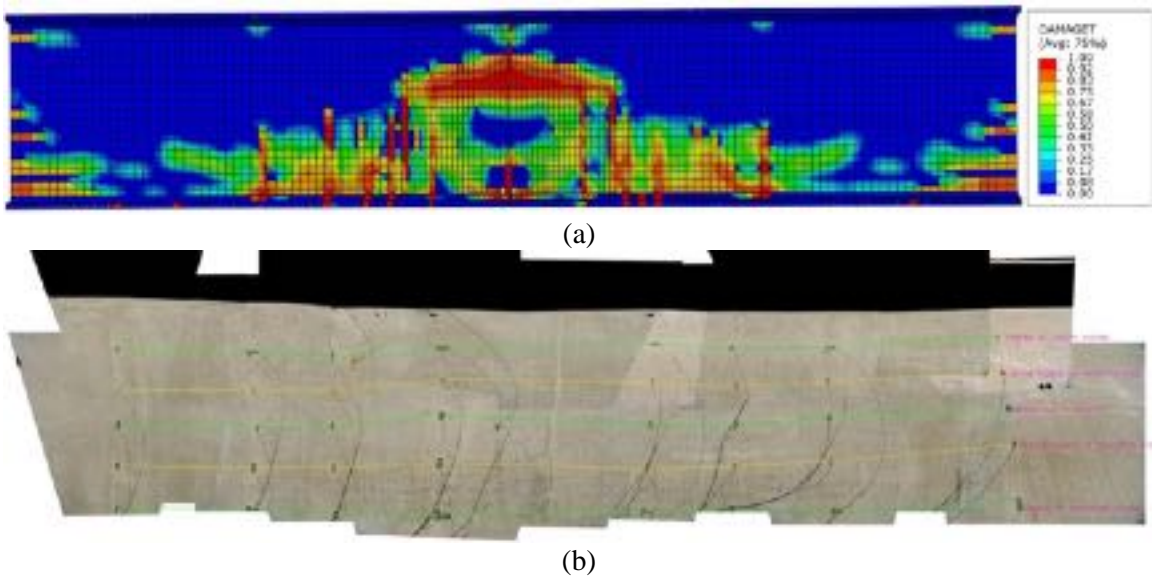
Figure 2-32. Crack patterns on concrete deck; (a) Finite Element Model, (b) Experimental test.

<p style="text-align:center">(a)   (b)</p>

Figure 2-33. Crack patterns above the interior flange of the intact girder: (a) Experimental test; (b) Finite Element Model.

2.1.4.6 *The Florida International University Twin Steel Box Girder Bridge Specimen*

After comparing the results of the FE model with the experimental test results for two full-scale bridges (The Nebraska bridge Test and UT bridge), a twin steel box girder bridge specimen tested by the Florida International University (FIU) (Figure 2-34 and Figure 2-35) was selected to validate the capability of the FE model for predicting local failure modes like punching shear or one-way shear of the concrete slab in addition to predicting the global behavior. The results from the FIU experiments indicate that the bridge with a full fracture in one of the girders has some reserved capacity, and the vertical loads could be transferred to the intact girder through one or more of the railing, continuity, slab, and external cross frames. Moreover, the results show that depending on the loading configuration, the failure mode of the fractured bridge could be punching shear or one-way shear of the deck.

(a)   (b)
Figure 2-34. The FIU test setup: (a) View from the cantilever end; (b) View from the simply supported end.

The FIU bridge was an approximately one-third scale straight version of a typical twin steel box girder bridge. The bridge consisted of two spans to consider the effect of continuity on the bridge redundancy with a total length of 41 ft. and width of 109 in. The thickness of the deck was selected and designed to be 5 in. to provide enough space for four mats of #4 reinforcement bars. A removable railing system, including several railing segments, was used to investigate the effect of railing on the behavior of the fractured bridge. Figure 2-35 shows the cross-section and side view of the bridge, and Figure 2-34 shows the FIU test setup.

All the steel plates of the box girders were ASTM A709 Grade 50, and the steel reinforcements were A706 Grade 60 materials. The concrete used for the deck had a compressive strength of 7.8 ksi at the time of the ultimate tests. Several elastic tests, a cyclic test, and five ultimate tests were conducted on this bridge to investigate the behavior of twin steel box girder bridges in both linear and nonlinear ranges. In order to investigate the failure mode for the fractured bridge, five ultimate tests were performed on the bridge with a full fracture in one of the girders, which are summarized in Table

2-4. Railing segments and continuity were removed for the ultimate tests, and different

load configurations and locations were used to investigate all the possible failure modes

for the fractured bridge.

(a)

(b)

(c)
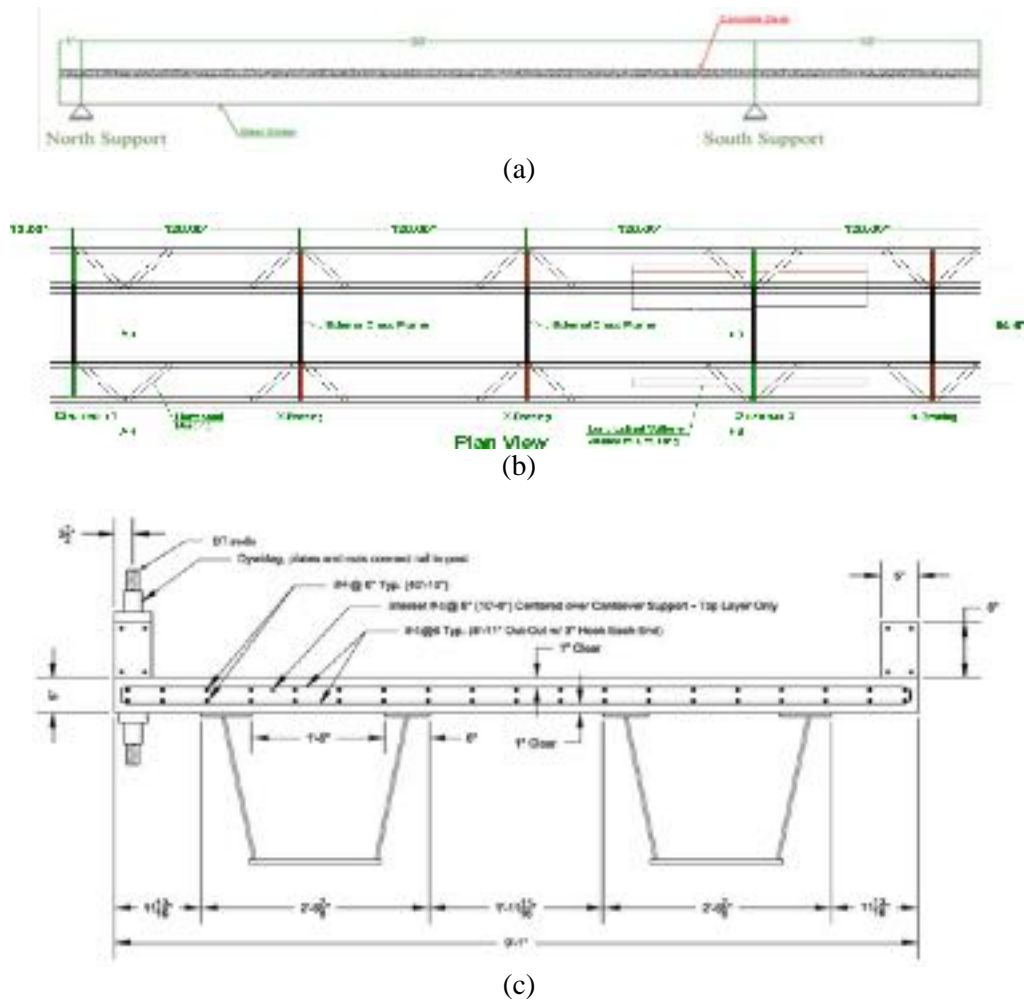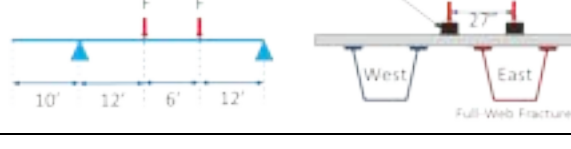
Figure 2-35. The Florida International University bridge: (a) Side view; (b) plan view; (c) cross-section view.

Tests E-1 and E-2 (Table 2-4) of five ultimate tests performed by FIU were modeled to

validate the FE method for predicting local and global failure modes for the one-girder

fractured condition. Test E-1 included loading on top of the fractured girder with a single

loading pad (2×9×36 in.) placed at the mid-span location, and Test E-2 included a single

smaller loading pad (10 in. square) over the fracture in between the steel girder flanges

to investigate the punching shear failure. The overall response of the ultimate Test E-1

illustrated that the fractured bridge had a linear elastic response up to 60 kips. After that,

by extending longitudinal and transverse cracks at the mid-span, the bridge stiffness

greatly reduced, and at the load of 156 kips, the specimen failed due to concrete deck

crushing under the loading pad. The test results indicated that a combination of one–way

shear and two-way shear was the failure mode of the fractured bridge under a large single

loading pad, as shown in Figure 2-37.

Table 2-4. The FIU ultimate load tests.

Test	Loading Configuration		Loading Type
W-1			The load was applied until the plateau in the load-deflection curve was observed. The test was discontinued before the failure.
W-2			The load was applied until the failure occurred
E-1			The load was applied incrementally until failure occurred.
E-2			The load was applied until the failure occurred
E-3			The load was applied through four loading pads until failure occurred.

Since in the ultimate test E-1, the edge of the loading pad was located on the top of the

girder flanges, the ultimate test E-2 was conducted to consider the punching shear failure

between flanges. The results of test E-2 show that the damaged girder responded linearly

up to 30 kips when cracking of concrete started to propagate; however, as shown in Figure 2-36, the intact girder responded linearly for the entire test until the punching shear failure through the loading pad at 83 kips. It is important to note that since this test was conducted after ultimate Tests, W-1 and W-2, and the deck was not reconstructed (only repaired locally), there are some residual deformations in the experimental test results. Therefore, the experimental results of this test are used only for comparing the punching shear capacity predicted by the FE model and the test results.

The FIU bridge specimen was constructed with shoring and then transferred to the test setup. Therefore, the analysis with the FE model was performed only by the application of the load at the loading pad for simulating the experimental testing on the bridge. The displacement control approach was utilized to simulate the test loading by defining a frictionless contact surface between the loading pad and the bridge deck. Figure 2-38 shows the FE model used for the analysis. Experimental tests of this bridge showed that one-way or (punching) two-way shear failure is the failure mode for the bridge with one fractured girder under wheel simulated loading. To simulate this type of failure, the concrete damage plasticity index for cracking and crushing was calculated over the effective area of one-way shear and (punching) two-way shear, as shown in Figure 2-39. The damage index is indicative of the extent of damage occurring at each stage and can be effectively used to signal shear failure over the effective area/line. In the analysis, damage index along the effective lines and within the slab depth were calculated and averaged.

In general, shear strength in reinforced concrete slabs can be checked by two approaches. The first approach is to calculate the beam shear capacity over a certain effective width of the support. The second approach is to calculate the punching shear capacity of the slabs

over the critical perimeter around the load. ACI 318-14 [114] will be utilized in this study to predict the shear resistance of a damaged twin steel box girder bridge that predominantly failed in one-way or two-way shear. It should be noted that these shear resistance expressions are derived based on results from beam tests. For beams, the maximum shear stress is assumed to be uniform over the entire beam width so that the entire width will be used to compute the shear resistance in the beam. For the slabs, however, the shear resistance should not be calculated over its entire width but over a certain effective width (b_{eff}). The effective width of a one-way slab under a concentrated load can be determined using either a fixed width approach or a horizontal load spreading approach. The horizontal load spreading approach is a more popular approach where the effective width is determined by the projected length of the load onto the face of the support. There are a couple of variations of this horizontal load spreading approach being used depending on the local practice and nature of the problem. Based on the ACI 318-14, the one-way and two-way shear capacity of the deck can be calculated using Equations (2-3) and (2-4), respectively.

Figure 2-36. Punching shear failure in the Test E-2 of FIU bridge.

(a)

(b)

(c)

(d)

Shear stress
pulling up

Shear stress
pulling down

Shear stress
pulling up

(e)

Figure 2-37. Damages in the Test E-1 of FIU bridge.

Figure 2-38. The FIU bridge FE model.
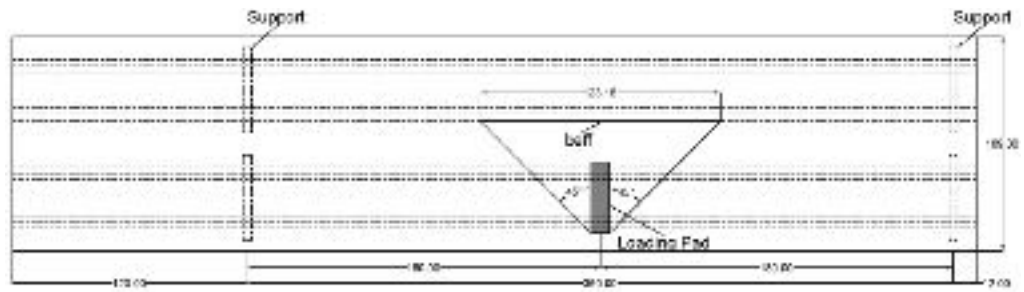
(a)
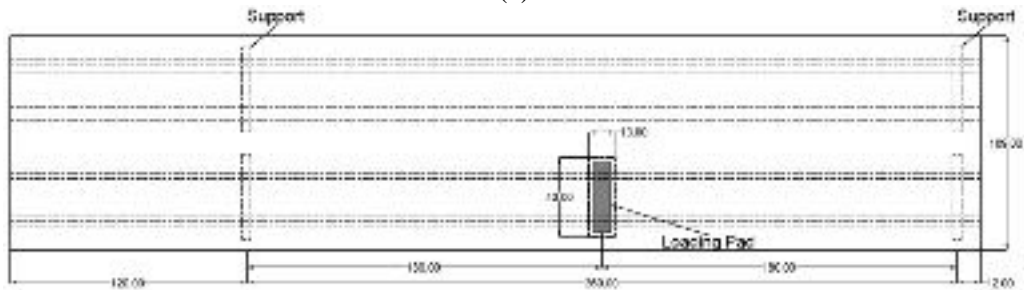
(b)
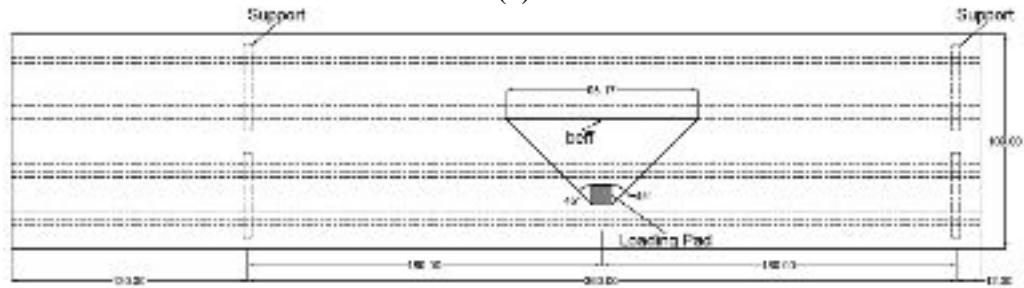
(c)
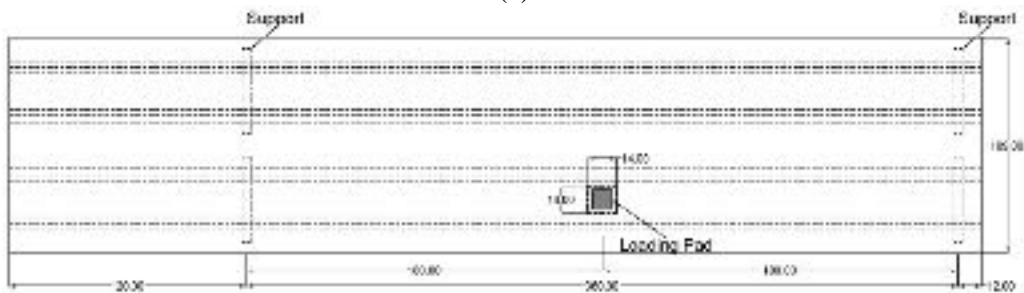
(d)

Figure 2-39. Determination of effective width: (a) One-way shear for Test E-1; (b) Two-way shear for Test E-1; (c) One-way shear for Test E-2; (d) Two-way shear for Test E-1.

$$V_{ACI} = 2\sqrt{f'_c}\,b_{eff}\,d \text{ (psi)} \tag{2-3}$$

$$P_{ACI} = 4\sqrt{f'_c}\,b_o\,d \text{ (psi)} \tag{2-4}$$

These equations were derived from tests on slab-column connections and are also applicable to slabs. The effective width for calculating one-way shear is determined using

45º horizontal spreading from the far side of the load, as shown in Figure 2-39. This method was also found to have a better correlation with the experimental results of Lantsoght's study [115]. When the slabs are subjected to multiple concentrated loads, the effective width can be considered by each wheel load separately or by each wheel axle. In ACI 318-14 code, the punching shear stress is assumed to be twice the maximum shear stress of beams failing in the one-way shear manner. The punching shear resistance of the slabs, according to ACI 318-14, is calculated over a critical perimeter, b_o, located at a distance d/2 away from the loading area. It is important to note that the predictions of the punching shear resistance of the bridge slabs in both Tests W-2 and E-2 would be the same using the punching shear provisions above since the load was applied over the same area of the footprint. However, as observed in the experiment, the punching shear failure load in Test W-2 was more than two times greater than the failure load in Test E-2. This significant difference indicated that the fracture damage had a great influence on the punching shear capacity of the deck slab. Critical perimeter and effective width for Test E-1 and E-2 are shown in Figure 2-39.

As was mentioned above, damage indexes along the effective lines and within the slab depth were calculated and averaged as an indication of one-way and two-way shear failure. The average tension damage index for all elements of the effective width and perimeter, as shown in Figure 2-40 and Figure 2-41, is obtained from the FE model to investigate the one-way and two-way shear failure modes of the model. Figure 2-42 (b, d) illustrates the load-tension damage index curve for Test E-1 and E-2. The average damage index of zero in these graphs shows that there is no damage in the effective area. As damage progresses, the damage index increases toward one that would indicate fully damaged elements and

complete loss of stiffness in tension. For convergence reasons, however, a smaller upper limit of 0.9 was considered. It is also understood that some portions of element thickness toward the bottom of the deck panel could be in compression and therefore not included in damage index calculation, another reason for the average index to be lower than 0.9. As it can be concluded from the results, the effective one-way shear width starts cracking around 32 kips and 45 kips for the Test E-1 and E-2, respectively. Tension cracks start to propagate from the surface of the mid-span and extend to the supports and depth of the deck. By comparing the damage index of the FE model and experimental test results, it can be concluded that when the average damage index of the effective area reaches about 0.7, the section has lost its capacity in carrying more load, a stage that can be considered as the one-way or two-way shear failure. At this point, the maximum tension damage index for all elements of the effective area in tension is reached to signal negligible capacity. Figure 2-42 (b) indicates that both one-way and two-way shear failure occur at the end of Test E-2 around 160 kips loading. However, Figure 2-42 (d) shows that by decreasing the size of the loading pad in Test E-2, the two-way shear capacity of the section was decreased, and therefore, the FE and experimental Test results show that two-way shear is the failure mode for Test E-2 with the capacity of around 83 kips. Table 2-5 compares the results of one-way and two-way shear capacity obtained from the Test, FEM, and ACI 318-14.
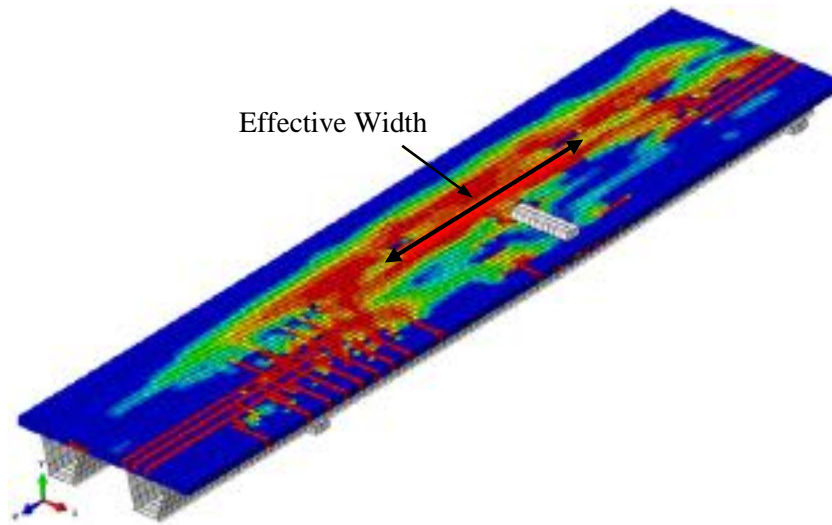
Figure 2-40. One-way shear effective width in the FE model.
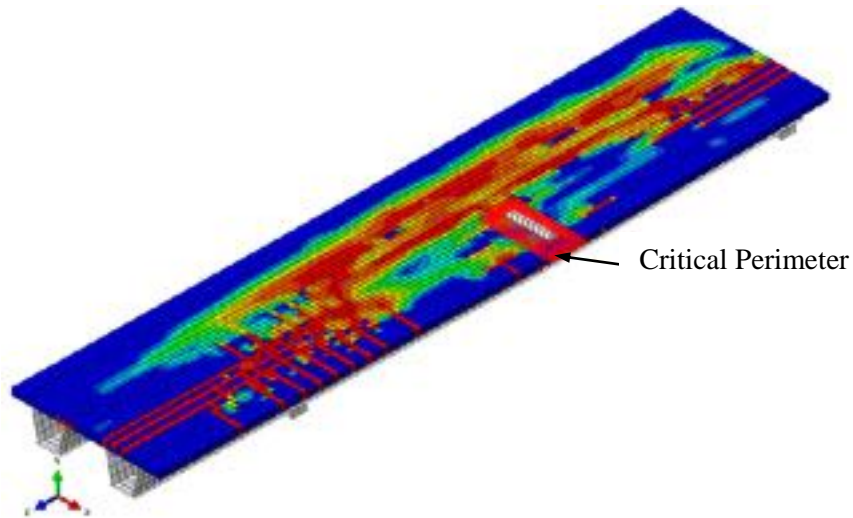
Figure 2-41. Two-way shear critical perimeter in the FE model.

Table 2-5. Comparison of one-way and two-way shear.

| | Test E-1 $f'_c = 7.8\ ksi$ | | Test E-2 $f'_c = 7.2\ ksi$ | |
	One-Way (kips)	Two-Way (kips)	One-Way (kips)	Two-Way (kips)
Test	156	156	-	83
FEM	161.9	168.6	159.8	94.17
ACI	87.03	149.79	66.64	76.03
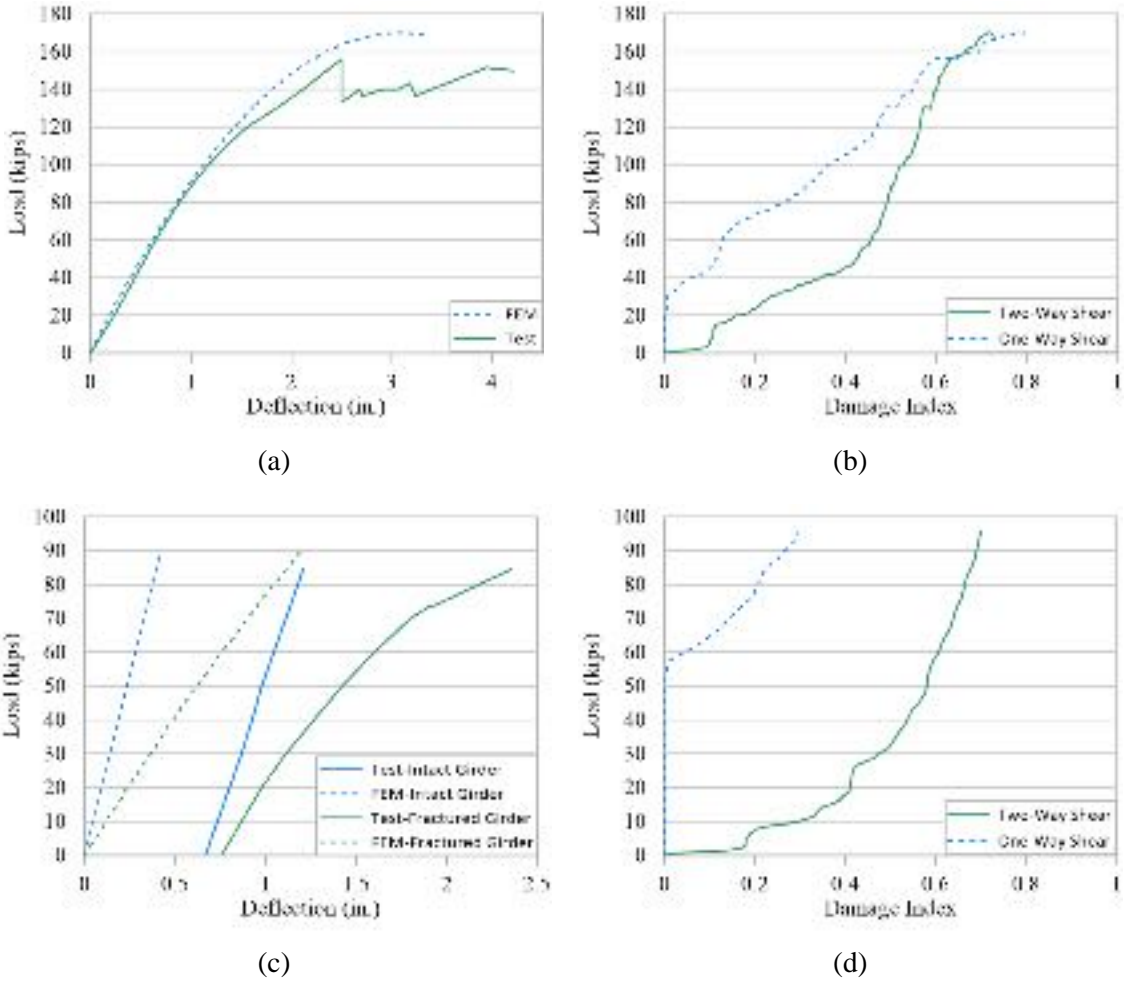
Figure 2-42. Comparison of the FE model with the experimental test: (a) Load-deflection curves of Test E-1; (b) Concrete Damage Plasticity Index of Test E-1; (c) Load-deflection curves of Test E-2; (d) Concrete Damage Plasticity Index of Test E-2.

In order to obtain useful data for local behavior of the fractured bridge under point loads in the FIU test, strain gauges and potentiometers were installed along the length of the specimen at different sections, as shown in Figure 2-43 and Figure 2-44. It is important to note that in addition to predicting the global response, the FE model also needs to be validated for simulating the local behavior of the bridge in the ultimate tests to demonstrate its ability for predicting load transferring mechanism and failure modes. To this end, strain results of the FE model for top and bottom flanges of the intact girder at mid-span section and the strain of intact girder bottom flange at section 5 way from the mid-span for the Test

67

E-1 are compared with the experimental results and shown in Figure 2-45 (minor fluctuation in the FE results is due to utilizing the dynamic solution for the damaged bridge). The comparison of the strain data shows that the FE model could predict not only the global behavior and failure mode but also local behavior and load transferring mechanism.
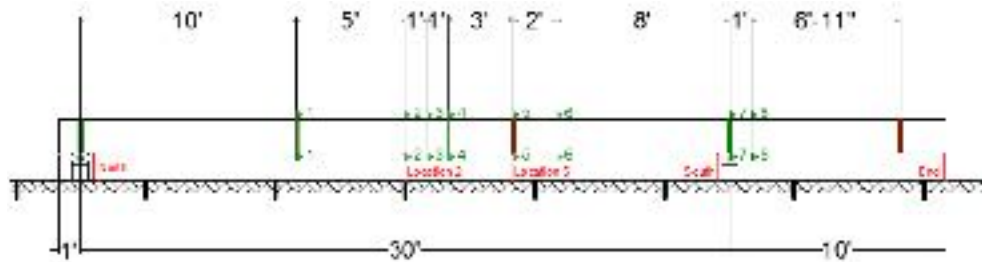
Figure 2-43. Location of strain gauges and potentiometers along the length of the specimen in the FIU test.
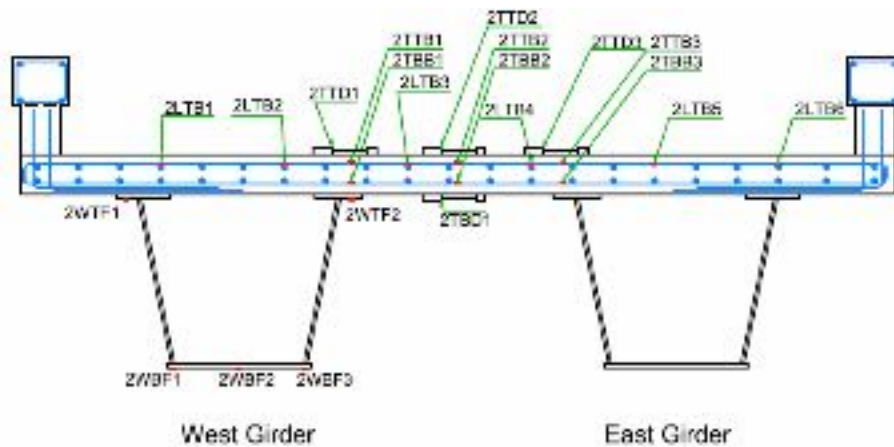
Figure 2-44.Strain gauges in section 2 of the FIU test.
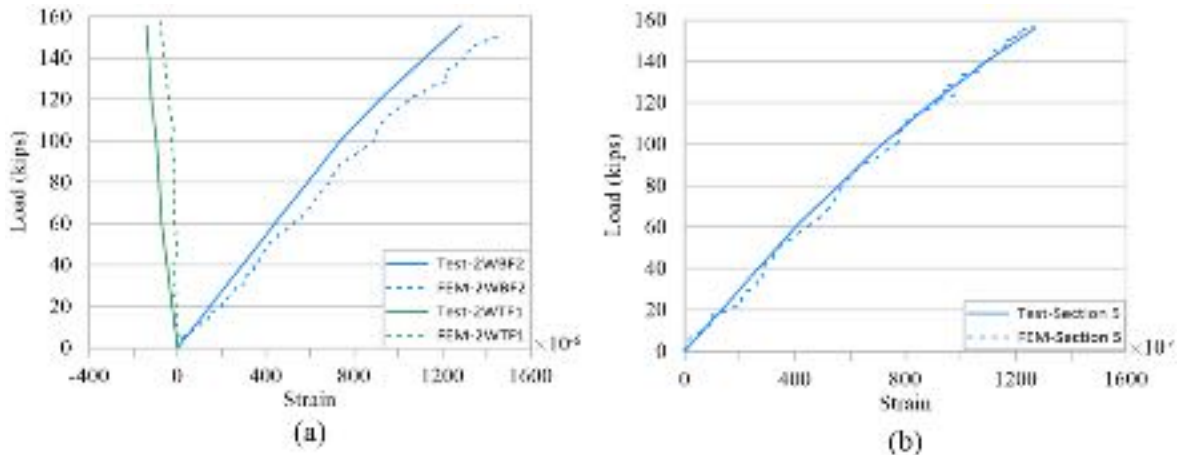
Figure 2-45. Comparison of the longitudinal strain of intact girder: (a) Section 2; (b) Section 5.

2.1.4.7 *FE Analysis for Load-Carrying Capacity of a Baseline Bridge*

After verification of the FE model, The University of Texas bridge was selected as a baseline model for developing information for preliminary reliability analysis of twin steel box girder bridges. The bridge was analyzed for two scenarios of the intact bridge, where both girders are intact, and the fractured scenario, where one of the girders is fully fractured. The goal was to develop the response curve and maximum load-carrying capacity under these scenarios and to investigate the local and global behavior of the twin steel box girder bridge under the HS-20 truck loading. The HS-20 truck loading configuration is shown in Figure 2-46. The distance between the front and middle axles shall be varied between 14 ft and 30 ft to produce the maximum loading effect. The tire contact area is assumed to be a single 10-in. square footprint for the front wheels and a single rectangular with 20 in. width and 10 in. length footprint for the rear wheels. In this study, axle distances were considered to be 14 ft, to produce the maximum positive moment and deflection in the middle of the bridge. The truck load is placed in the middle of the bridge (at a position to produce the maximum moment at fracture location) and only in one lane over the left box girder (fractured) to create the worst scenario, i.e., when there is maximum torsion and bending on the bridge due to eccentric loading caused by

69

distributions. The truck load was increased in terms of multiple HS-20 until the bridge reached its maximum capacity.
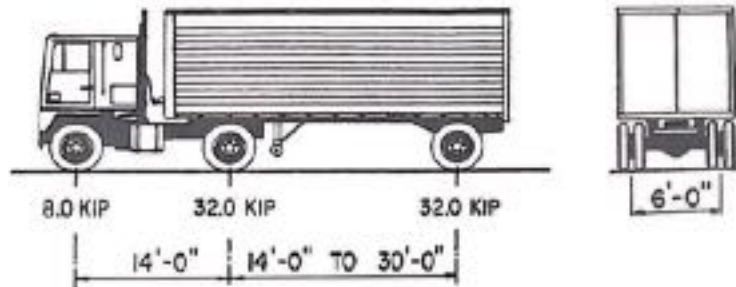
Figure 2-46. Characteristic of the HS-20 design truck.

2.1.4.7.1 Intact Bridge

Figure 2-47 shows the load-deflection curve for the intact bridge scenario at the middle of the span under the center of the girders due to truck loading. The truck loading increased until the load-displacement curve flattened, indicating approaching the maximum load capacity of the bridge. This condition was associated with the development of plastic strain over the entire section of both girders. Before reaching this stage, local failures were in the deck were also observed. The first local failure, as shown in Figure 2-48, was the punching shear pattern under the rear wheels around nine times HS-20, after which one-way shear occurred above the right box. After the local failures, the bridge still continued to carry higher loads until 19 times the HS-20, at which the bridge response (load-deflection curve) plateaued, indicating reaching maximum capacity due to the formation of a hinge in the girders. Figure 2-49 shows the plastic stress over the entire sections at 19 times the HS-20 load.
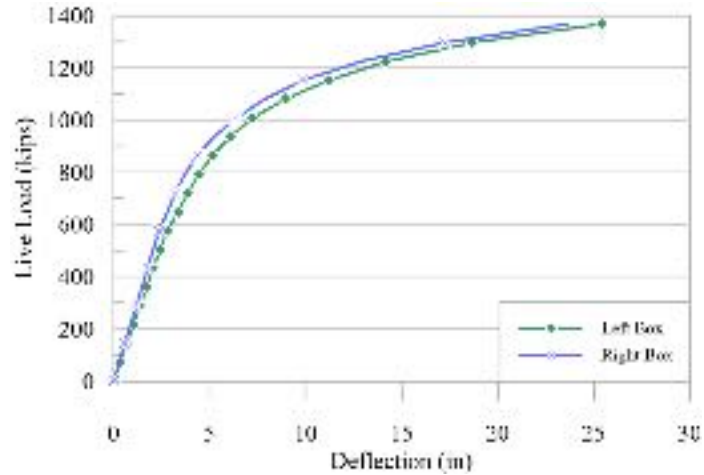
Figure 2-47. Load-deflection curves of intact bridge obtained from the FE model.
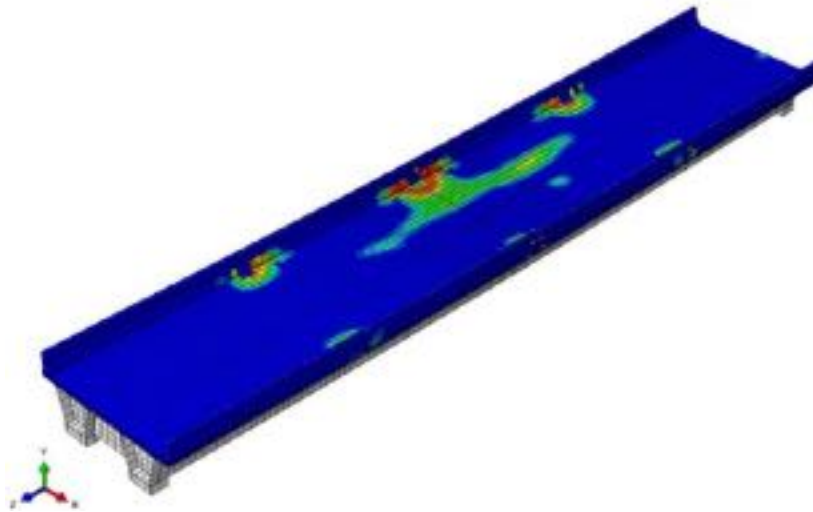
Figure 2-48. The punching shear failure of the concrete deck under 9xHS-20.
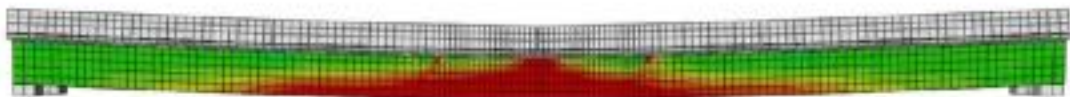
Figure 2-49. Plastic stress of the steel boxes under 19xHS-20.

2.1.4.7.2 Bridge with One Fractured Girder

The FE results of the damaged bridge show that once the sudden fracture happened, the bridge had a 3.1 in. deflection under the self-weight of the bridge at the mid-span of the fractured girder, and the tension stress at the bottom flange of the intact girder reached the yielding stress. After that, the truck loading increased up to 6 times the HS-20 load, where

71

the middle span deflection of the fractured girder reached 11.51 in. At this level (defined here as failure), the concrete deck experienced extensive damage leading to tension stress at the intact girder due to flexural and torsional moment reaching the yielding point. Figure 2-50 (a) shows the yielding of the intact girder under six times HS-20 loading, and Figure 2-50 (b) shows the concrete tension damage at the top of the deck at this load level.

(a)

(b)
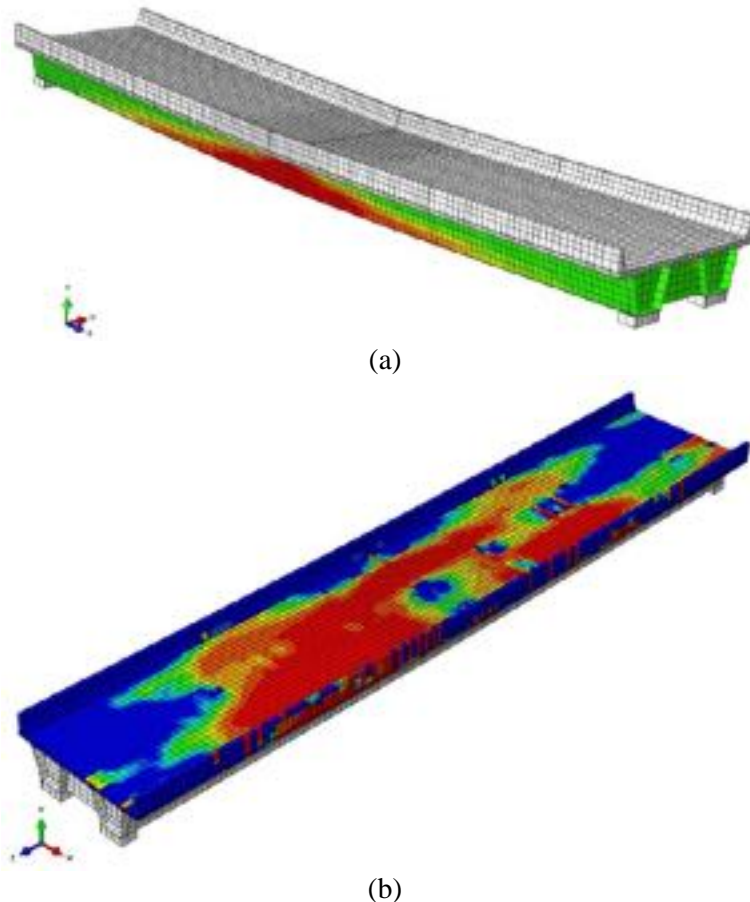
Figure 2-50. Fractured bridge under 6xHS-20: (a) Yielding of the intact girder; (b) Concrete tension damage.

2.1.4.7.3 *Plastic Moment Capacity of UT Bridge Test*

The plastic moment capacity of the UT bridge test for the intact scenario is calculated to compare with the maximum capacity of the bridge obtained from the FE model. The effective flange width of a concrete deck slab in composite or monolithic construction may be taken as the tributary width perpendicular to the axis of the member for determining

cross-section stiffness for analysis and for determining flexural resistances. The slab effective flange width in composite girder and/or stringer systems or in the chords of composite deck trusses may be taken as one-half the distance to the adjacent stringer or girder on each side of the component, or one-half the distance to the adjacent stringer or girder plus the full overhang width.

To determine the plastic moment capacity of composite sections, the following assumptions are made:

- Full interaction between steel, reinforcement, and concrete – this is normal practice for bridge design and assumes no slip between the composite components

- The effective area of the structural steel member is stressed to f_{yd}

- The area of reinforcement in compression is ignored

- The effective area of concrete in compression is stressed to $0.85f_c$

Table 2-6 and Figure 2-51 summarize the section properties of the University of Texas bridge for calculating the plastic moment of one girder. The total flexural capacity of the bridge can be obtained by adding the capacity of two girders. Moreover, the FE model is used for obtaining the bridge plastic moment capacity considering all the details, such as reinforcement, as shown in Figure 2-52. Table 2-7 shows the calculation of the plastic moment for two different concrete compressive strengths and the result obtained from the FE model. The higher plastic moment obtained from the FE model compared to that obtained by hand calculation can be attributed to the contribution of reinforcement in the FE model and the higher concrete compressive strength (6.2 ksi). In addition, the moment-curvature of the bridge section is illustrated in Figure 2-53.
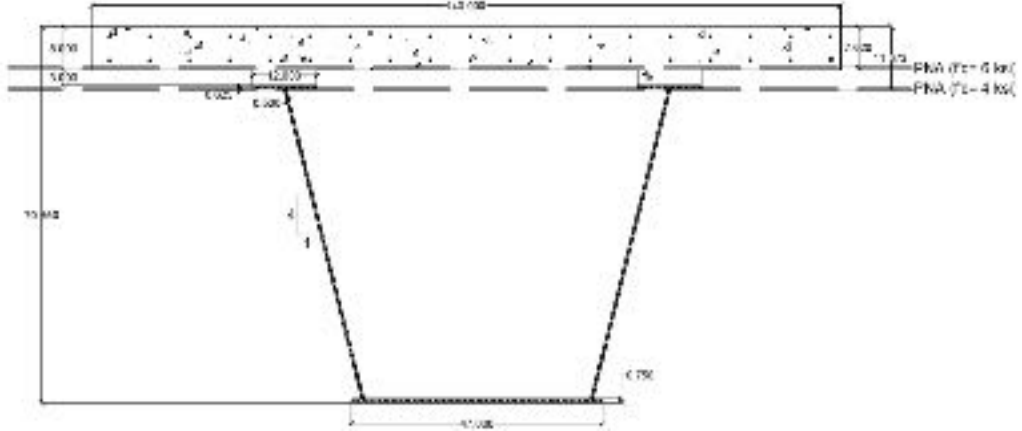
Figure 2-51.University of Texas Bridge Section.

Table 2-6. Section properties of University of Texas bridge.

Parameter	Value	Unit
f'_c	4 or 6	ksi
f_y steel	50	ksi
f_y reinforcement	60	ksi
Slab Thickness	8	in
Slab Effective Flange Width	140	in
Haunch Thickness	3	in
Haunch Width	12	in
Top Flange Thickness	0.625	in
Top Flange Width	12	in
Web Thickness	0.5	in
Web Height	60	in
Web Height Projected	58.17	in
Bottom Flange Thickness	0.75	in
Bottom Flange Width	47	in
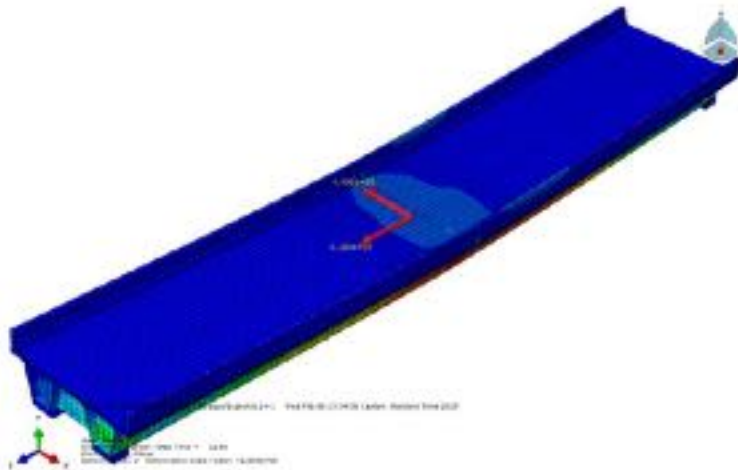
Figure 2-52. Plastic Moment Capacity in FEM.

Table 2-7. Plastic moment capacity.

Compressive Strength of Concrete	P_s kip	P_h kip	P_c kip	P_w kip	P_t kip	Y_{PNA} in	d_t in	d_w in	d_c in	M_p kip. ft
F'c=4 ksi	3808	163.2	750	3000	1687.5	11.6	58.6	29.1	0.3	17972.2
F'c=6 ksi	5712	244.8	750	3000	1687.5	7.6	62.6	33.1	3.7	19026.8
F'c=6.2 ksi-FEM	FEM									20816.7
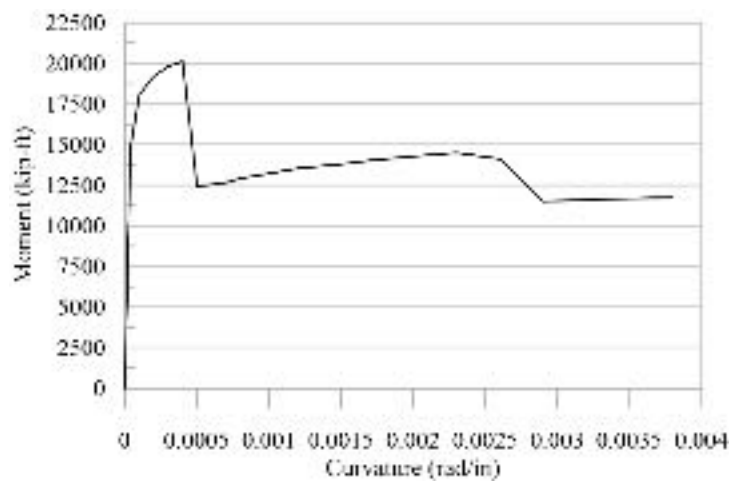
Figure 2-53. Moment curvature curve with nonlinear material properties (f'c=6 ksi).

In order to investigate the effect of railing on the final capacity of the bridge in fracture and intact scenarios, the UT bridge model was loaded until the failure for the intact and

75

fractured bridge considering the effect of the railing. Figure 2-54 shows the results obtained

from the FE models for two conditions of the intact bridge (no fracture in the left girder

under the load) and the fractured condition (fracture of left girder under the load). It can be

concluded from the results that the railing could slightly decrease the maximum deflection

of the fractured bridge at failure load by up to 8%.
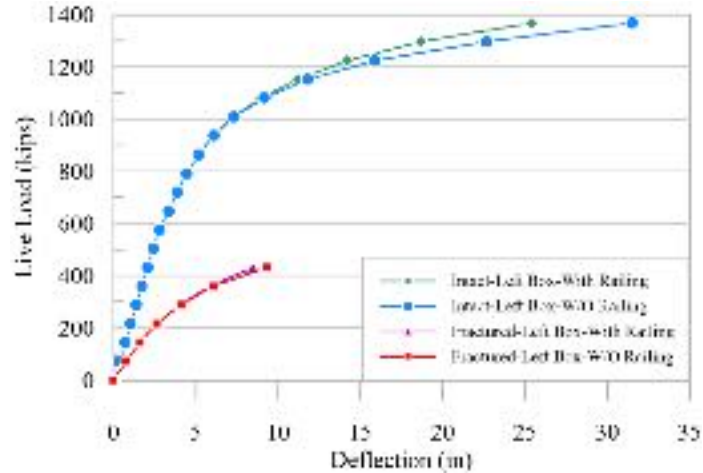
Figure 2-54. The effect of railing on the fractured bridge.

2.1.5 Determining Failure Load Using Simple Analysis for Possible Failure Mechanisms

Based on the finite element analysis and available experimental results, as well as work by

others, it is inferred that the failure after fracture of one girder can be one of; a) one-way

shear failure of the deck, or b) flexural failure of the deck. The failure of the intact girder

under bending and torsion could also be a possible mechanism; however, none of the results

from analysis and experiments nor other sources have indicated the occurrence of such

mechanism before the failure of the deck. One-way shear failure and flexural failure of the

deck are investigated here for the University of Texas bridge.

2.1.5.1 *Sensitivity Analysis for One-Way Shear Transfer in the University of Texas Twin Steel Box Girder Bridge*

The objective of the investigation reported in this section is to perform a sensitivity analysis for one-way shear transfer in the deck slab where the varying parameter is the transverse position of the truck wheels. The main goal is to validate the simple model for one-way shear at the deck in comparison with finite element results and to determine the effective width for the calculation of shear stresses for HS-20 loading. The bridge was loaded in terms of the HS-20 design truck with 14 ft axle spacing positioned at the mid-span over the fractured girder to generate maximum moment at the section with the fracture. Figure 2-55 shows the loading configuration for the parametric study of one-way shear failure. In order to study the effect of truck position on one-way shear effective width and shear stress distribution over the girders, HS-20 truck was positioned in four different locations across the bridge width as shown in Figure 2-56, to constitute four cases, one for each position. Cases 2, 3, and 4 were used for investigating the sensitivity analysis for one-way shear. Case 1, an extraordinary eccentric loading, was used for bending failure investigation later in this report.

Based on the HS-20 design truck location, the shear stress profile was obtained for four sections in the bridge deck slab along the bridge immediately next to the end of steel girder flanges of intact and fractured girders. Figure 2-57 shows the location of shear stress sections. Total shear force transferred longitudinally and transversely was calculated by integrating shear stress profile in longitudinal and transverse across the bridge slab. According to the results, it can be seen that despite the fracture in one girder, a portion of the truck loading is transferred to the fractured girder end supports in the longitudinal direction, and the remaining is transferred transversely to the intact girder. The portion of

live load transferred longitudinally by the fractured girder to its support can be calculated by integrating shear stresses along the sections shown in Figure 2-57, and transverse distribution of the live load from the fractured girder to the intact girder can be calculated by subtracting the longitudinally transferred load from the total live load. The proportion of longitudinal and transverse load transfer will depend on the truck location and bridge configuration, i.e., girder spacing, deck thickness, cross-frame spacing, etc.
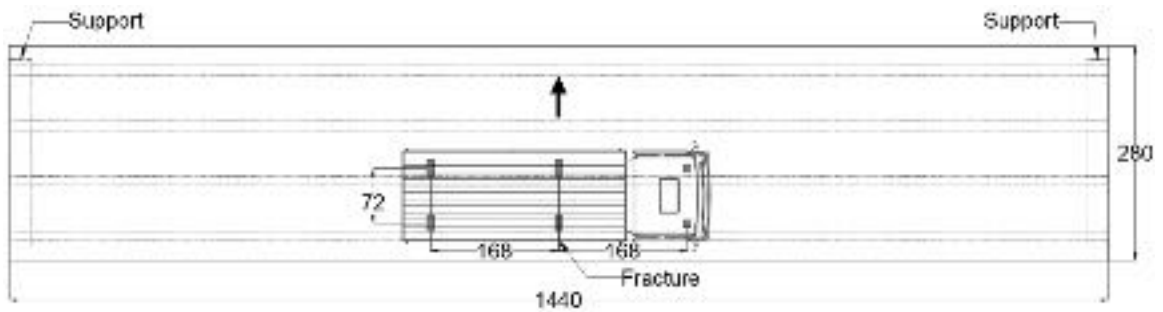
Figure 2-55. Loading Configuration in the one-way shear analysis.
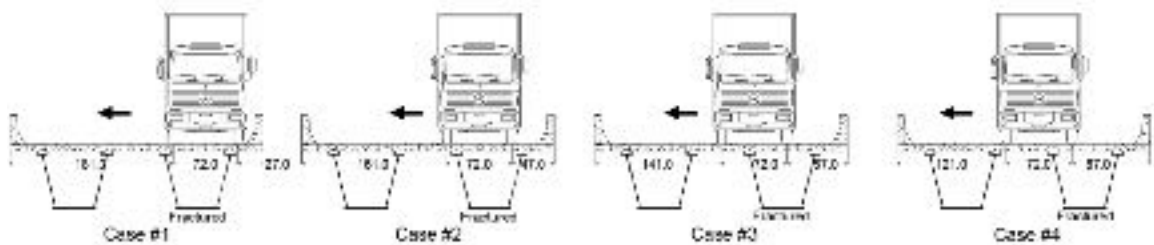
Figure 2-56. HS-20 Truck location in the one-way shear analysis.
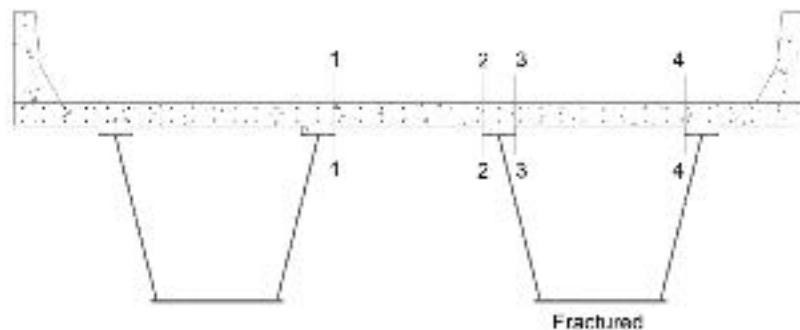
Figure 2-57. Sections in the one-way shear analysis.

For the analysis, the bridge was loaded incrementally until the failure, plateau in the load-deflection curve, and shear stress was captured for all the sections along the bridge in four different truck positions (Cases 1- 4). The results show that shear stress follows a similar pattern for each section and case by increasing the truck loading until the failure stage, where crushing and cracking of the deck changes the initial pattern. Hence, the stress pattern is studied for the failure stage. Figure 2-58 shows the shear stress profile in the slab along the sections for all cases under dead load and twice the HS-20 design truck. Moreover, in order to study the effect of the increasing live load on shear stress pattern and the effective width for one-way shear, shear stress in the slab along Section 1-1 for Case 2 was obtained and is shown in Figure 2-59. The results indicate that by increasing the live load (up to twice HS-20), shear stress follows a similar pattern with negligible changes in one-way shear effective width. Comparison of the shear stress pattern and values in Section 1-1 and Section 2-2 (Figure 2-58(a) and (b)) indicates that the live load positioned between intact and fractured girder is transferred in both longitudinal and transverse directions. Moreover, the analysis shows that after the fracture, the intact girder (Section 1-1) carries more shear stress than the fractured girder (Section 2-2) because of having a higher stiffness.

Shear stress analysis of the live load's distribution between Section 3-3 and Section 4-4 (Figure 2-58(c) and (d)) shows that forces over the fractured girder are mainly transferred transversely to Section 2-2 and then to the Section 1-1 and the remaining is transferred longitudinally to the end supports. Total shear force transferred to the fractured girder was calculated by integrating shear stress along the bridge at each section (Figure 2-58(c) and (d)).
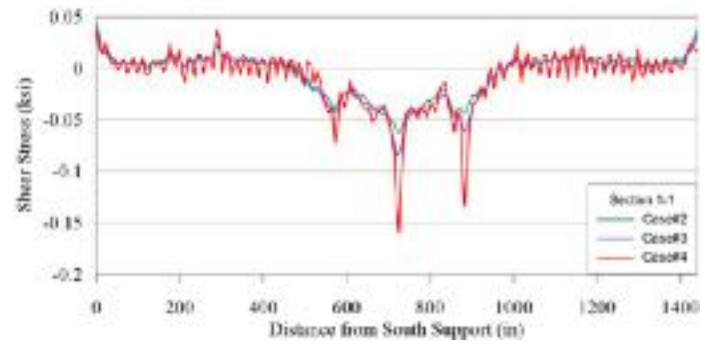
(a)
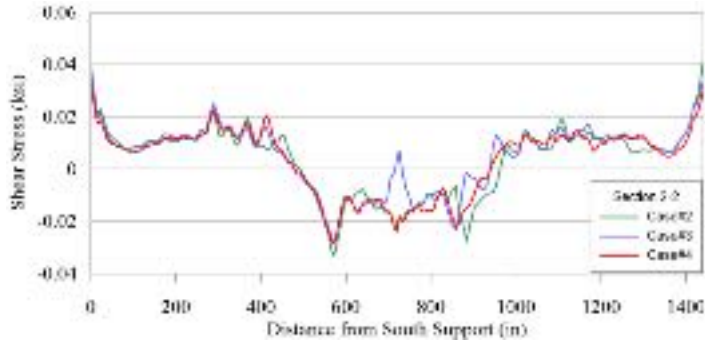
(b)
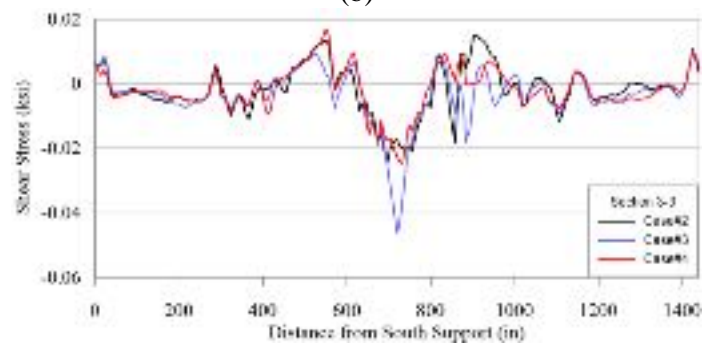
(c)
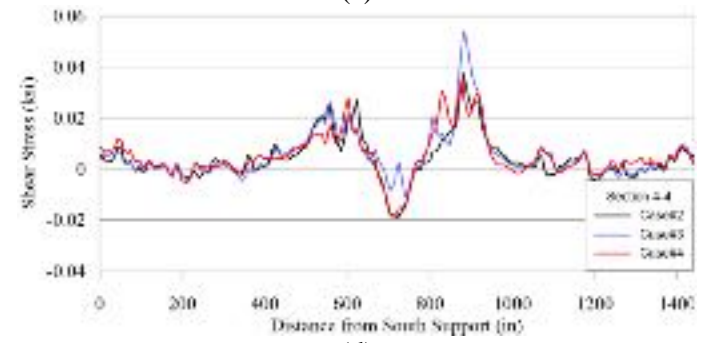
(d)

Figure 2-58. Shear stress in the slab along the faces of the intact and fractured girder for all the cases under dead load and two times HS-20 design truck: (a) Section 1-1; (b) Section 2-2; (c) Section 3-3; (d) Section 4-4.

80
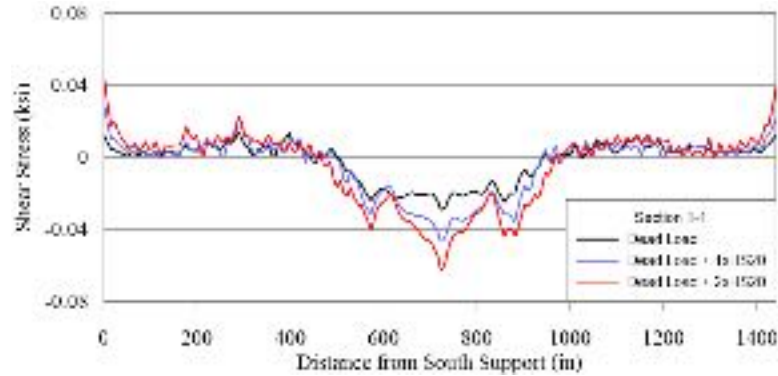
Figure 2-59. Shear stress in the slab along Section 1-1 in case 2 under dead load and increasing HS-20 design truck.

The results reveal that although the local shear transfer is recorded for both Sections 3-3 and 4-4, the total shear force transferred to the fracture girder in the transverse direction is negligible. Therefore, positive and negative shear stress along Section 3-3 and Section 4-4 could be attributed to local deflection after the fracture. The results show pull-out shear forces along Section 3-3 and Section 4-4 in a limited length, which may cause a shear stud failure only at the mid-span. In this region, the bridge deck would not follow the fractured girder deflection at the middle of the span because of its high transverse stiffness, and as a result, pull-out forces will develop between the deck and the fractured girder.

Two methods were used in this study for estimating the effective width and average shear stress transferred transversely to the girders for the approximate simple method (referred hereafter as simple prediction Methods 1 and 2). In the first method (Method 1), the effective width was predicted using 45° spreading lines from the far side of the first and last point loads, and total width was considered as the effective width by ignoring gaps between spreading lines. In the second method (Method 2), the effective width was predicted for each point load separately using 45° spreading line from the far side of each point load. See Figure 2-60 for an illustration of two different effective widths. Furthermore, the effective width for one-way shear was also calculated using the finite

81

element model for Section 1-1 and Section 2-2 by measuring the length of the negative

shear stress to correspond to effective widths estimated using Methods 1 and 2 described

for the simple method.

Figure 2-60 (a) and (b) show effective width estimation for the FE method for Method 2.

The effective width for Method 1 for FE analysis will be the entire length from the first

point on the left to the last point on the right. The effective width for calculating one-way

shear from simple prediction methods was compared to the FEM results, as shown in Table

2-8 and Table 2-9. The prediction value shows a good agreement with the effective width

obtained using the FE model when using Method 1. For Method 1, in all but one case (Case

#4, Section 2-2 in method 1), the approximate effective width is smaller than the FE

calculated, hence providing for more conservative stress calculation. Method 2 results for

simple prediction compare fairly with FE results, the difference to be attributed to the non-

distinct variation of stress in the FE results. As a result, the minimum effective width value

obtained in this study for Section 1-1 based on the critical live load position (Case 4) can

be used for calculating the one-way shear capacity of the fractured bridge.

Table 2-10 and Table 2-11 show the maximum and average stress obtained from FEM and

simple predication Methods 1 and 2 over the effective width under twice the HS-20 design

truck loading. Stresses from the effect of dead load after fracture are subtracted from the

total shear stress to obtain live load shear stresses. The difference between average stress

in FEM and the simple prediction method can be attributed to two sources. First, because

of fracture, in reality, and as captured by FE analysis, the intact girder (Section 1-1) carries

more shear stress than the fractured girder (Section 2-2), i.e., a major proportion of the live

load will be transferred to intact girder from the fractured girder, where, in the simple

predication methods, shear stress is assumed to be transferred only to the intact girder. Moreover, a proportion of live load on fractured girder will be transferred longitudinally to its support, as shown by the FE analysis results. However, in the simple prediction methods, it is assumed that shear stress only will be transferred transversely.

Comparison of results shows that for Method 1 (extended effective width for the entire truck), the average shear stress estimated at Section 1-1 using simple prediction agrees well and is slightly higher than the average shear stress calculated from FE analysis. Results for Method 2 (effective width for individual wheels) show that the average shear stress estimated at Section 1-1 for the rear wheels using the simple prediction method agrees very well with the maximum shear stresses calculated by FE analysis. Method 1 is believed to generate results that are more representative of shear stresses when compared with FE analysis results. The effective length obtained from Method 1 is therefore used for calculating the fractured bridge one-way shear capacity in different cases for comparison with bending yield line results. The maximum shear stress is assumed to be uniform over the entire effective width, and the ACI 318-14 equation for one-way shear is used to compute the shear resistance in the deck (Table 2-14).

Table 2-8. One-way shear effective width for Method 1.

| | One-Way Shear Effective Width (in) | | | | | |
| | Case#2 | | Case#3 | | Case#4 | |
	FEM	Simple Prediction 1	FEM	Simple Prediction 1	FEM	Simple Prediction 1
Section 1-1	506	461	476	421	440	381
Section 2-2	462	381	447	421	418	461
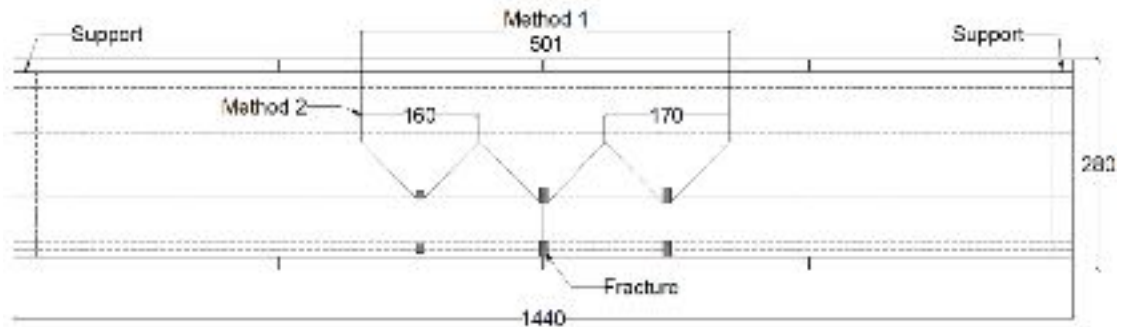
Case #1
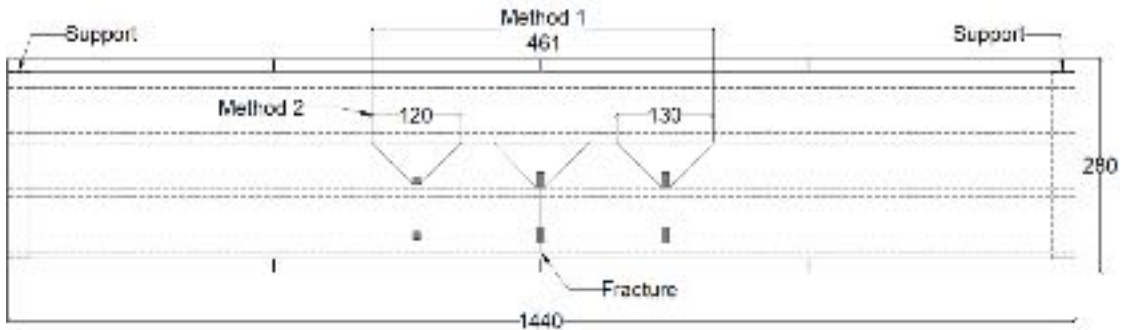
Case #2
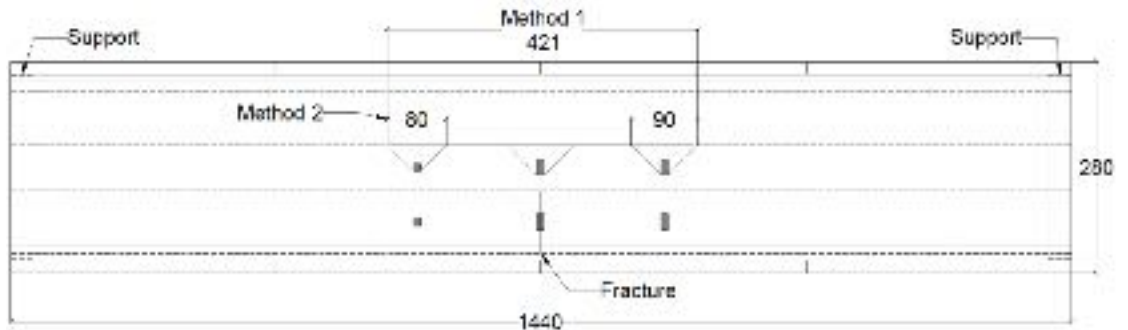
Case #3
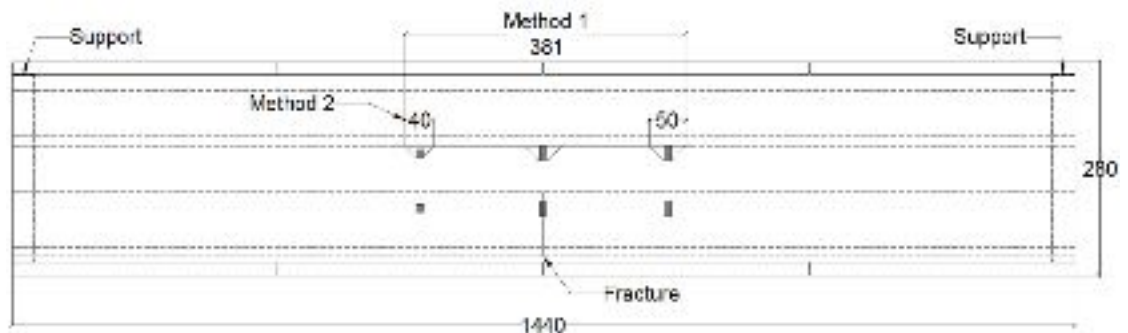
Case #4

Figure 2-60. The effective width for one-way shear using the simple prediction method.

Table 2-9. One-way shear effective width for Method 2 (Front denotes front wheel; Rear denotes rear wheel).

	One-Way Shear Effective Width (in)											
	Case#2				Case#3				Case#4			
	FEM		Simple Prediction 2		FEM		Simple Prediction 2		FEM		Simple Prediction 2	
	R	F	R	F	R	F	R	F	R	F	R	F
Section 1-1	132	139	130	120	139	139	90	80	110	95	50	40
Section 2-2	119	99	50	40	125	139	90	80	154	137	130	120

Note: R= Rear-wheel; F= Front-wheel
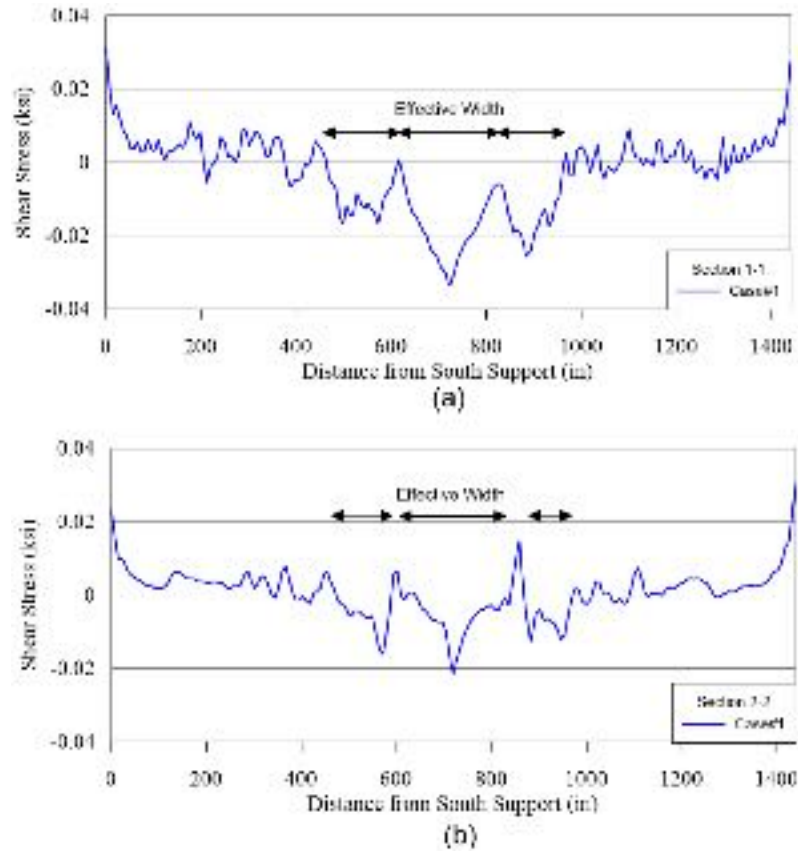
Figure 2-61. The effective width for one-way shear using the finite element model: (a) Section 1-1; (b) Section 2-2.

Table 2-10. One-way shear stress over the effective width under 2xHS-20 for Method 1.

	One-Way Shear Stress (psi)								
	Case#2			Case#3			Case#4		
	FEM		Simple Prediction 1	FEM		Simple Prediction 1	FEM		Simple Prediction 1
	Max.	Avg.	Avg.	Max.	Avg.	Avg.	Max.	Avg.	Avg.
Section 1-1	33.4	14.7	19.5	56.4	18.8	21.4	101.4	20.5	23.6
Section 2-2	21.3	5.76	0	11.3	1.9	0	20.4	5.0	0

Table 2-11. One-way shear stress over the effective width under 2xHS-20 for Method 2.

Section	One-Way Shear Stress (psi)														
	Case#2					Case#3					Case#4				
	FEM			Simple Prediction 2		FEM			Simple Prediction 2		FEM			Simple Prediction 2	
	Max.	Avg.		Avg.		Max.	Avg.		Avg.		Max.	Avg.		Avg.	
		R	F	R	F		R	F	R	F		R	F	R	F
1-1	33.4	15.9	10.9	30.8	8.3	56.4	22.4	11.6	44.4	12.5	101.4	28.3	9.8	80.0	25.0
2-2	21.3	7.5	6.9	0	0	11.3	0.1	3.9	0	0	20.4	7.8	5.9	0	0

Note: R= Rear-wheel; F= Front-wheel

2.1.5.2 *Flexural Failure of the Deck Based on Yield Line Analysis:*

The simple yield line model developed by the University of Texas [22] to capture the bending response of a twin steel box girder is investigated here for estimation of the bending capacity deck in the fractured bridge. The proposed yield line pattern of the University of Texas is based on the overall cracking and crushing pattern from the University of Texas bridge test. The experimental results show that the failure in the deck followed the shape of a half-ellipse. Accordingly, a yield line pattern was developed by the University of Texas using a combination of straight lines. Several assumptions were made for developing the pattern. First, it was assumed that a yield line in the deck between the girders closer to the fractured girder (parallel to the girders longitudinal axis) would not form because the shear studs connecting the fractured girder to the deck will fail due to the pull-out force and the fractured girder would not have any contribution. Second, the yield line consisted of straight lines lying on the perimeter of an ellipse along with two diagonal interior fold lines with the linear deflection to its maximum at the edge of the deck at mid-span. The proposed pattern gives the most conservative estimate of capacity by ignoring the contribution of the fractured girder. The yield line pattern is defined by two major parameters; the angle φ between the inner diagonals and the vertical axis and the horizontal distance from points at the end of outer diagonal lines to the origin (along the outer edge

of the deck over the fractured girder). A series of parametric studies were conducted by the University of Texas to determine these parameters to correspond to minimum capacity under HS-20 truck load.

In the one-way flexural failure of the bridge, plastic hinges will form at the location of the maximum moment, and the hinge lines will rotate plastically with an increase of the load to form the final yield lines. Based on the yield line pattern, the virtual work principle could be used for the calculation of deck bending capacity. The principle of virtual work requires that the external virtual work done by the external forces be equal to the internal virtual work done by the internal forces of each element of a structure. The external virtual work is computed from the summation of the product of the externally applied forces multiplied by the virtual displacement at the load position, which is a function of the assumed virtual displacement. The total internal virtual work due to the virtual displacement is equal to the summation of the product of the bending moment developed at the segment of the yield line multiplied by the hinging rotation of each segment. Figure 2-62 shows the yield line pattern proposed by the University of Texas. It was assumed that a straight yield line would initiate at the interior top flange of the intact girder, and it would extend diagonally to the edge of the deck above the fractured girder. The yield line needs to be completed by assuming two inner diagonal lines from the end of the interior top flange of the intact girder to the edge of the deck above the fractured girder.

A yield line analysis was performed for the four cases discussed above based on the University of Texas yield line pattern. The finite element model was used for estimating the position and length of the outer yield lines by using concrete damage index in the deck as shown in Figure 2-63, and the ultimate capacity of the bridge was calculated for each

case (Table 2-12 and Table 2-13) The yield line obtained from the FE analysis closely compares to the yield line suggested by the University of Texas for a similar loading pattern (Case 1). It should be noted that the actual load carried by the University of Texas bridge under uniform loading in terms of HS-20 was 363 kips (5 times HS-20). According to the Texas yield line (Table 2-14), the maximum capacity of the bridge in case 1 is 4.2 times HS-20, which is slightly conservative when compared to the maximum capacity of 4.5 times HS-20 obtained from the finite element model here in this study. This can be attributed to ignoring the contribution of the fractured girder in the yield line analysis.

Table 2-12. External work calculation of the truck load.

Number of HS-20 Design Truck =							4.2
	P	X_{point}	Y_{point}	r_{Load}	r	Delta	EW
Front Wheel	16.8	14.0	5.9	6.3	22.5	0.3	4.7
Front Wheel	16.8	14.0	11.9	12.3	26.5	0.5	7.8
Middle Wheel	67.2	0.0	5.9	5.9	14.2	0.4	28.0
Middle Wheel	67.2	0.0	11.9	12.0	14.2	0.8	57.0
Rear Wheel	67.2	-14.0	5.9	6.3	22.5	0.3	18.7
Rear Wheel	67.2	-14.0	11.9	12.3	26.5	0.5	31.2
						EW_{Truck}	147.4
						EW_{DL}	33.3
						EW_{Total}	180.7

Table 2-13. Internal work calculation for the Texas bridge.

	L	α	m_l	m_t	m_b	Rotation	dIW
	33.75	0.00	17.86	17.86	17.86	0.07	42.07
Perimeter	19.30	0.77	17.86	17.86	17.86	0.05	15.64
	19.30	1.05	17.86	17.86	17.86	0.05	15.64
	22.00	0.86	22.68	22.68	22.68	0.05	26.13
Diagonals	22.00	0.97	22.68	22.68	22.68	0.05	26.13
						$IW_{Railing}$	55.22
						IW_{Total}	180.82
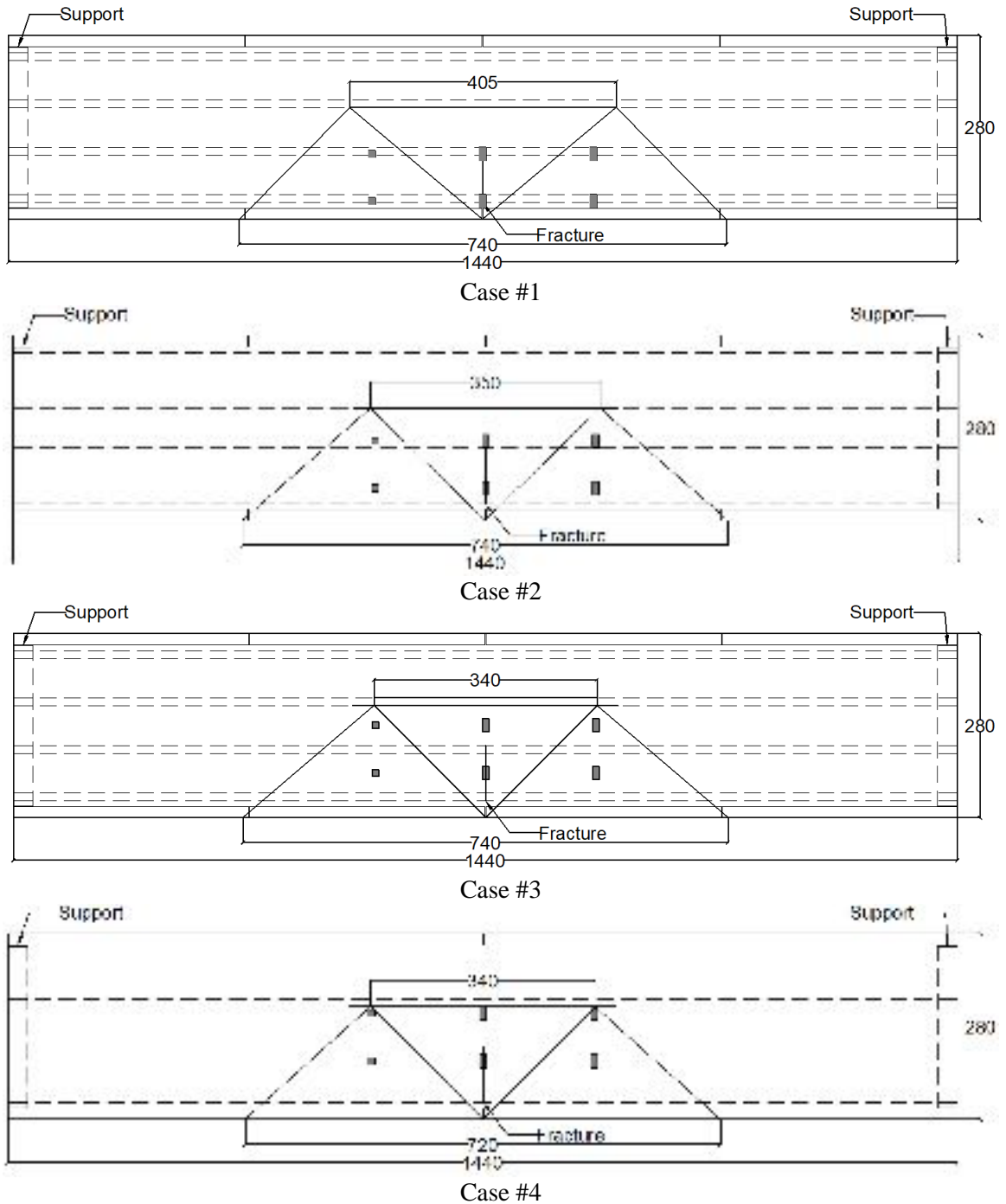
Figure 2-62. The yield line pattern proposed by the University of Texas for cases 1 to 4.

To investigate the effect of shear studs in the load-carrying capacity of the bridge, the interaction between the shear studs and the concrete deck was modeled in the FE analysis. The connector element was utilized for modeling the shear studs. The ultimate shear and

tension capacity for the connector elements were assigned based on the shear and pull-out test conducted by Topkaya [116] and the University of Texas [117]. Once the shear or tension force in the shear stud element reaches its capacity, the element would lose its connection to simulate the pull-out or shear failure. The analysis showed that with the connector elements calibrated based on the available stud tests, failure of the studs occurs along a limited length of the deck immediately over the inner edge of the fractured girder just enough to allow the development of the assumed yield line pattern. For comparison purposes, FE analysis was performed on Texas bridges with and without modeling the shear studs. The case of without shear studs assumes perfect composite action with no failure in the studs. Figure 2-63 shows a comparison between the load-displacements curves for Case 1 loading with and without modeling the studs. The response curves are in close agreement until the applied load of about three times HS-20, where the pull-out failure of shear studs begins at the middle of the span over the fractured girder. Stud pull-out extends over a limited length until the maximum capacity is reached. Table 2-14 shows the maximum capacities obtained from FE analysis with stud modeling. For comparison purposes, the maximum capacity for Case 1 is also reported from FE analysis without modeling the shear studs, i.e., assuming full composite action between deck slab and girders.

Another bridge feature influencing the deck bending failure mechanism is the bridge railing. In the normal bridge operation, the concrete bridge railing is not considered to be a structural component because of the gap between railing segments for expansion joints. When a bridge is subjected to large deflections due to severe damage, two sides of the gap will eventually come into contact, and contact force would increase the stiffness of the

90

bridge. However, in the Finite element model, the railing segments were modeled with no contact force between the segments to eliminate the uncertainty of the railing gap and the force between the railing after a large deflection. On the other hand, the simplified yield line model utilized by the University of Texas takes into account the contribution of the railing in the bending resistance along the yield lines wherever applicable.

The finite element analysis incorporating the shear studs shows that the pull-out of studs occurs along a limited length at the mid-span allowing the yield lines to form in a pattern similar to the University of Texas. Moreover, the bridge deflection in the finite element model matches with the proposed pattern when considering the pull-out shear stud failure. Although the yield line pattern proposed by the University of Texas is conservative due to ignoring the contribution of the fractured girder, it can estimate a lower bound capacity for the fractured bridge.

Figure 2-64 (a) and (b) show the yield line pattern obtained from the finite element model using concrete damage plasticity index in the top and bottom view of the deck, respectively. Positive and negative bending lines can be observed in the bottom and top views of the deck. Figure 2-65 shows the vertical deflection of the deck at the failure in the finite element model and the deflection based on the yield line pattern. It can be seen from the deflected FE model that the bridge deflection in the failure region is approximately linear from the edge of the intact girder to its maximum value at the edge of the deck above the fractured girder at the middle of the span, and the deflection reflects the half-ellipse shape that is the basis for determining the yield line pattern.
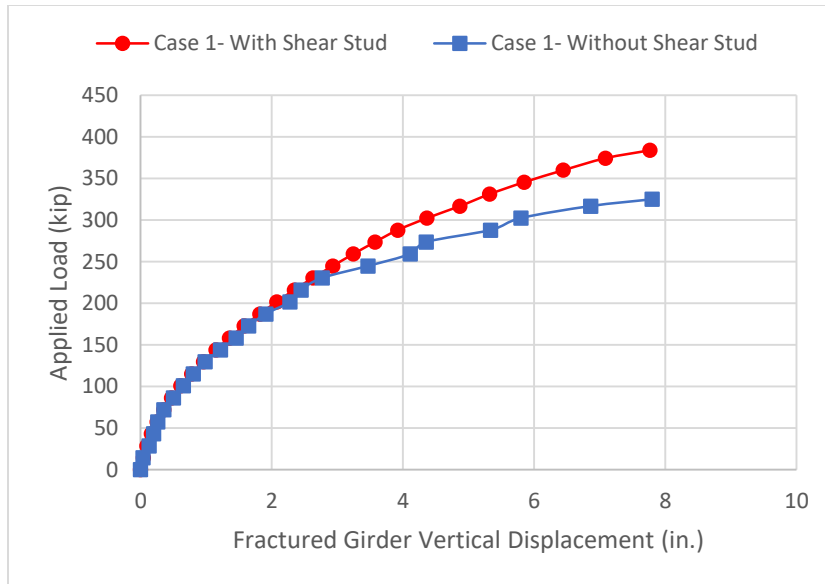
Figure 2-63. Comparison between the load-displacements curves for Case 1 loading with and without modeling the studs.

According to the results shown in Table 2-14, one-way shear is the critical failure mode for Cases 3 and 4 (closest to intact girder), and flexural failure of the deck at the yield lines is the failure mode for Cases 1 and 2 (farthest from intact girder). Accordingly, it can be inferred that the ultimate capacity of the bridge with one fractured girder under HS-20 design truck using simplified method is the smaller value between one-way shear capacity in Case 4 and the deck bending capacity using yield line method in Case 1. Figure 2-66 shows the suggested effective width and yield line pattern for calculating one-way shear and yield line analysis. One-way shear capacity can be estimated using Equation (2-5) for using the effective width shown in Figure 2-66 (a), and the yield line bending capacity can be estimated using the yield line pattern shown in Figure 2-66 (b) as per the procedure described earlier and shown in Table 2-12 and Table 2-13.

$$V_{ACI} = 2\sqrt{f'_c}b_{eff}d \text{ (psi)} \tag{2-5}$$

92
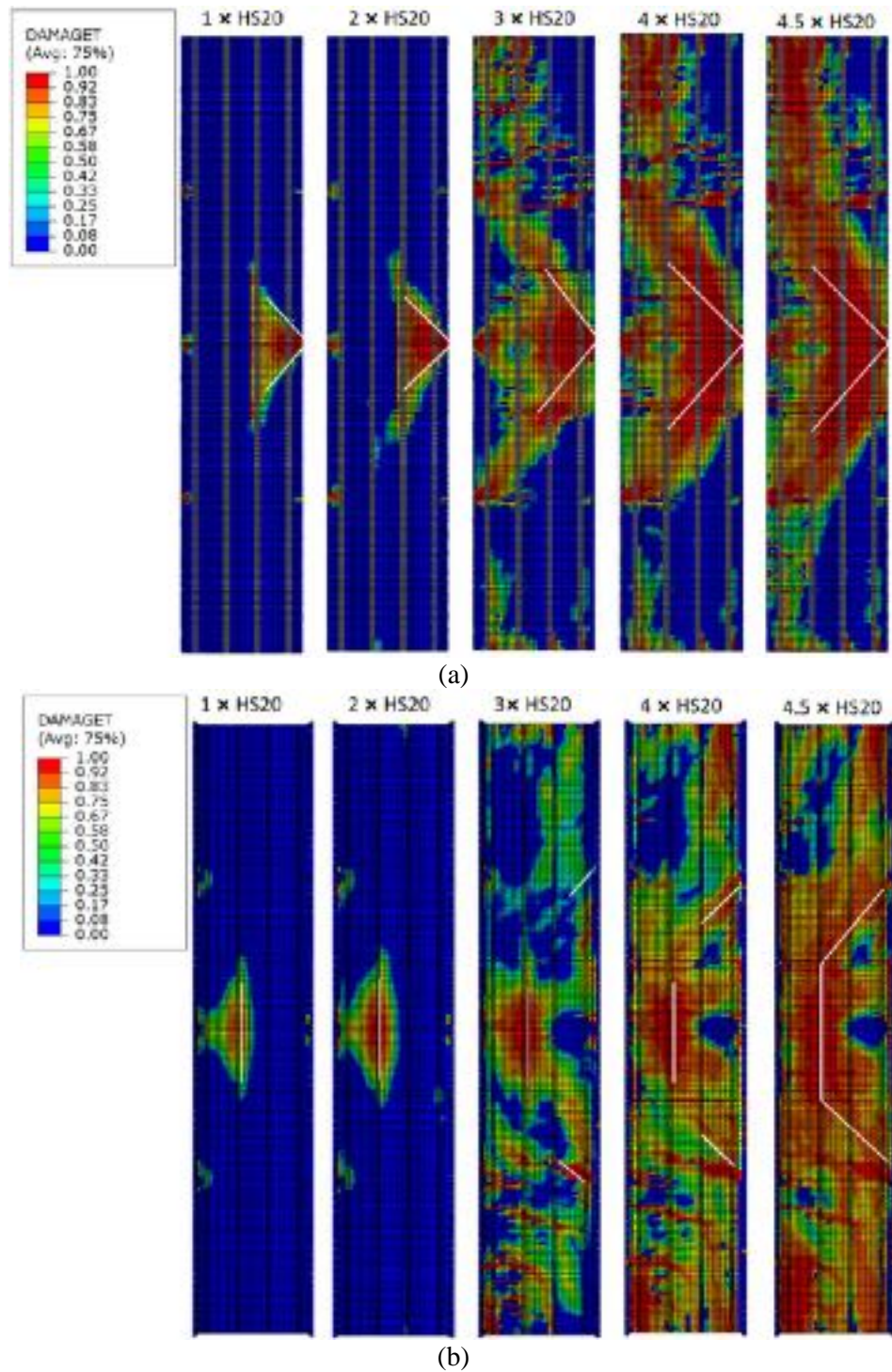
Figure 2-64. The yield line pattern of the deck in the Finite Element Model for Case 1: (a) Bottom view of the deck where positive bending yield lines are shown; (b) Top view of the deck where negative bending yield lines are shown (white lines are added to reflect the idealized yield lines used in simple analysis).

(a)

(b)

(c)

(d)
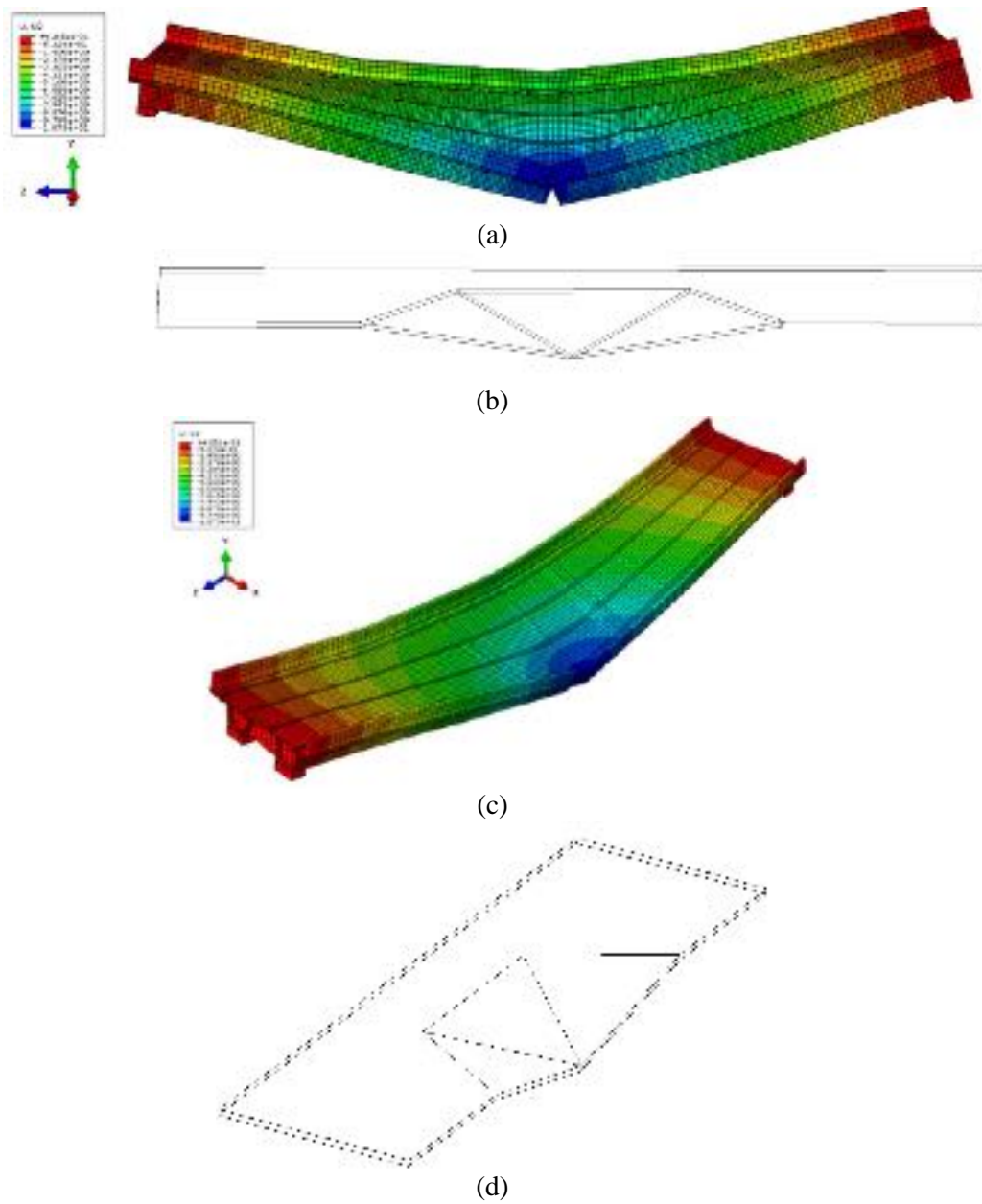
Figure 2-65. Yield line pattern of the deck: (a,c) Deck deflection contour in FEM; (b,d) Deck deflection based on yield line pattern.
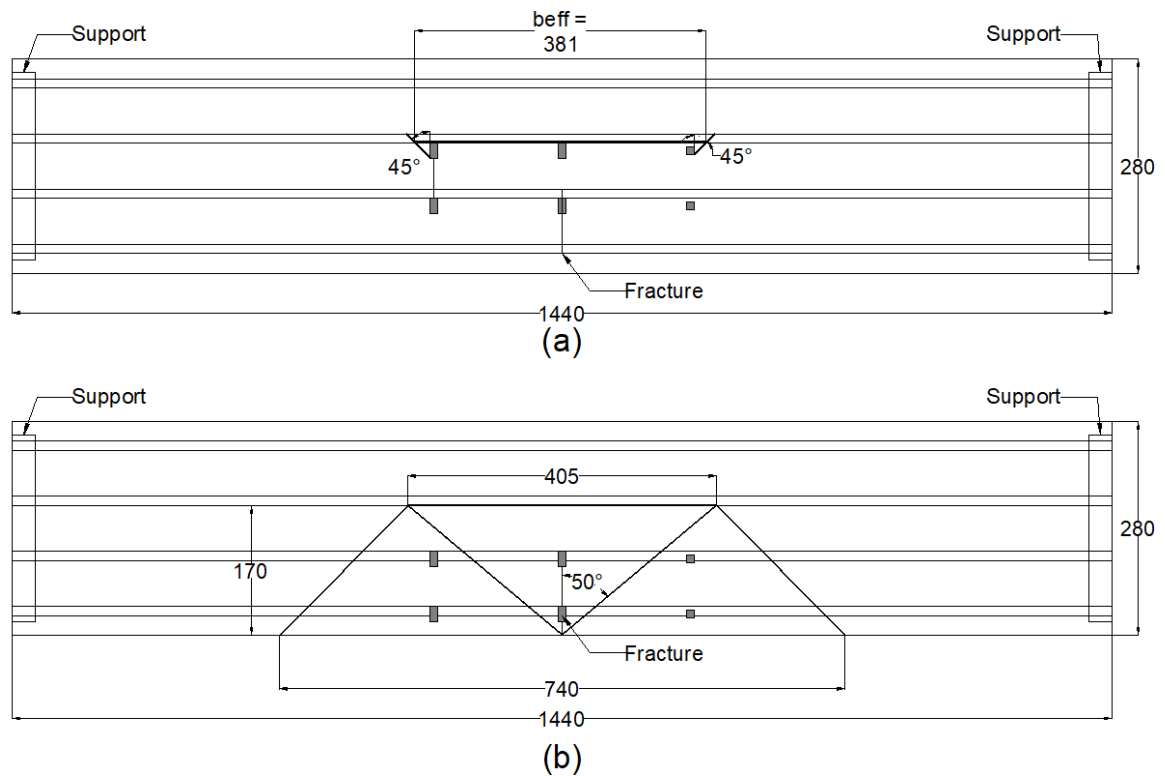
Figure 2-66. The University of Texas bridge failure mechanisms; (a) One-way shear in Case 4, (b) Yield line failure in Case 1.

Table 2-14. Bridge capacity for cases 1 to 4.

Case	One-Way Shear Capacity (kips)	Bending Yield Line capacity (kips)	Max. Capacity from FE analysis- shear studs are modeled (kips)
1	448.7	**301.7**	320
2	412.9	**362.2**	329
3	**377.1**	474.5	335
4	**341.2**	563	340

2.1.5.2.1 Sensitivity Analysis for the Concrete Compressive Strength in the University of Texas Twin Steel Box Girder Bridge

Variation in the bridge configuration and material properties, i.e., concrete compressive strength and steel ultimate strength, may result in different failure modes and, therefore, different reserve capacities. In this section, sensitivity analysis for the deck concrete compressive strength is conducted to investigate its effect on the ultimate failure strength and mode.

95

In the previous analysis, the concrete compressive strength was taken as 6.2 ksi as per reported test results. Accordingly, two other concrete compressive strengths were assigned to the deck in the FE models to investigate the behavior of the bridge with fractured girder under various concrete strengths.

The concrete material parameters used in the presented analyses are: the modulus of elasticity E_0 that is calculated based on the ACI 318-14 [114] ($E_c = 57,000\sqrt{f_c'}$), the Poisson's ratio ν, and the compressive and tensile strengths. The concrete damaged plasticity model was considered in the models. The dilation angle ψ was considered as 36°, the shape factor, $K_c = 0.667$, the stress ratio $\sigma_{b0}/\sigma_{c0} = 1.16$, and the eccentricity $\varepsilon = 0.1$.

Concrete in compression was modeled with the Hognestad parabola [118] (see Figure 2-67). The assumed stress-strain behavior of the concrete under uniaxial compressive loading could be divided into three domains. The first one represents the linear-elastic branch, with the initial modulus of elasticity. The linear branch ends at the stress level of σ_{c0}. The second segment describes the ascending branch of the uniaxial stress-strain relationship for compression loading to the peak load at the corresponding strain level. The third part of the stress-strain curve shows the strength descending part after the peak stress and until the ultimate strain ε_u. Concrete damage was assumed to occur in the softening range in both tension and compression. In compression, the damage was introduced after reaching the load corresponding to the strain level, ε_0.

The uniaxial stress-strain response of concrete in tension is linear elastic up to its tensile strength, f_t'. After cracking, the descending branch is modeled by a softening process, which ends at a tensile strain ε_u, where zero residual tensile strength exists (see Figure

2-68). Sensitivity analyses for the concrete compressive strength for the University of Texas Twin Steel Box Girder bridge were conducted using three different concrete compressive strengths of 4 ksi, 5 ksi, and 6.2 ksi. It should be noted that the concrete compressive strength for the University of Texas bridge at the time of its ultimate test (32 months after casting the deck) was 6.2 ksi and had an average strength of 4.8 ksi at the age of 28 days.

Table 2-15 shows the ultimate bridge capacity obtained from the FE analysis and simplified methods for one-way shear and bending yield line capacity. The results show that by increasing the concrete strength capacity of the deck, the one-way shear capacity increases by the square root of concrete compressive strength according to Equation (2-5). Moreover, section bending capacity increases by increasing the concrete compressive strength. For example, the section capacity along the yield lines with concrete compressive strength of 4 ksi and 5 ksi is 20 kip. ft/ft and 21.3 kip. ft/ft, respectively. The FE results indicate a similar trend.
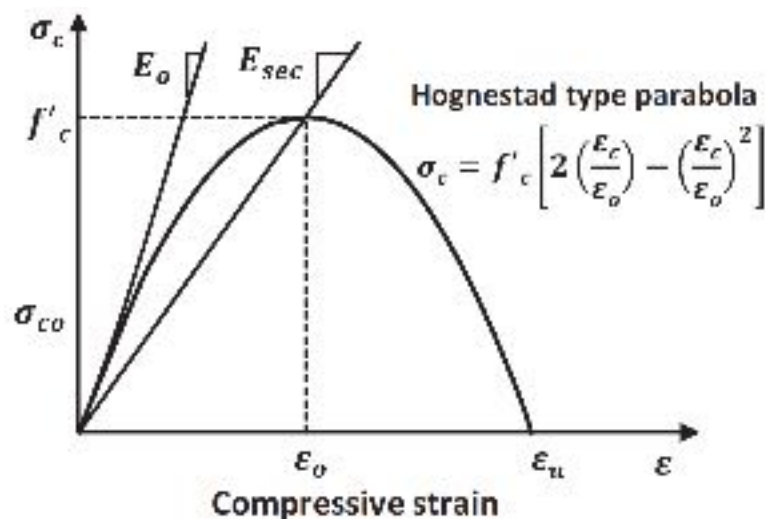
Figure 2-67. The uniaxial compressive stress-strain relationship for concrete.
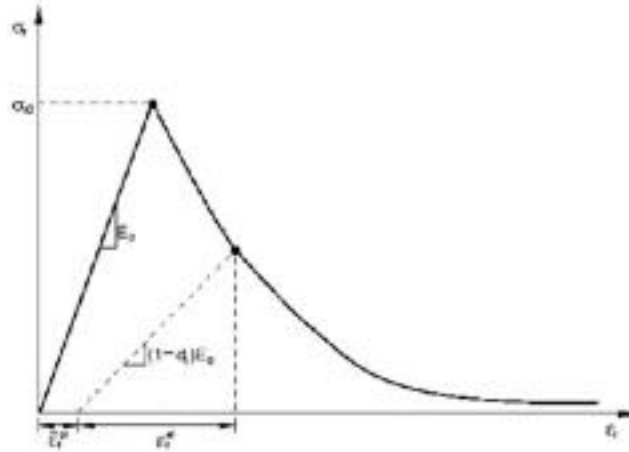
Figure 2-68. The uniaxial tensile stress-strain relationship for concrete.

Table 2-15. Bridge capacity for cases 1 and 4 with different concrete compressive strengths.

Case	concrete compressive strength (ksi)	One-Way Shear Capacity (kips)	Bending Yield Line capacity (kips)	Max. Capacity from FE analysis- shear studs are modeled (kips)
	6.2	448.7	301.7	320
1	5	403.0	288.0	316
	4	360.4	273.6	310
	6.2	341.2	563	340
4	5	306.5	532	335
	4	274.1	506	327

2.1.5.2.2 Sensitivity Analysis for the Truck Loading in the University of Texas Twin Steel Box Girder Bridge

The first edition of AASHTO's Standard Specification for Highway Design in 1931, which was based on the 1924 committee report, contained a representation of a design truck and/or a group of trucks with a single unit weighing up to 40 kips, which was known as the H20 truck, and a lane load to be used in specific circumstances. For the HS-20 design truck loading, this consisted of a uniform load of 0.64 kip/ft and a moving concentrated load or loads. A concentrated load of 26 kips was used for shear and for reaction, two 18-kips concentrated loads were used for the negative moment at support and were positioned in two adjacent spans, and a single 18-kips load was used for all other moment calculations.

In the early 1940s, the design truck was extended into a tractor–semi-trailer combination, known in the 1944 Standard Specifications as H20-S16-44 and commonly referred to as simply the HS-20 truck. This vehicle weighed a total of 72 kips and was comprised of a single steering axle weighing 8 kips and two axles that supported the semi-trailer, each weighing 32 kips. The axle spacing on the semi-trailer could vary from 14 to 30 ft, and it was assumed that there was 14 ft between the steering axle and the adjacent axle that formed part of the tractor. The HS-20 design truck is an idealization and did not represent any particular truck. The truck configuration, i.e., axle spacing and weights, is represented to produce moments and shears in the bridge longitudinal direction based on actual truck loading. However, for the fractured bridge in which most of the loads are being transferred transversely, and the failure mode could be one-way shear or flexural failure of the deck, the HS-20 truck may not represent the worst-case scenario for one-way mechanisms. Therefore, sensitivity analysis for truck loading needs to be conducted for different loading configurations.

In order to consider the effect of truck loading configuration on the bridge failure mode as well as the effect on yield line pattern and one-way shear effective width, three trucks with loading configurations other than the HS-20 truck were selected as shown in Figure 2-69. Florida legal loads and emergency vehicles are used for this purpose. The C5 truck that is one of the Florida legal loads, weighs a total of 80 kips and with a total length of 36 feet that is longer and heavier than the HS-20 design truck configuration used in this study. EV3 truck loading is one of the Florida emergency vehicles with a total weight of 86 kips (14 kips heavier than HS-20 Truck) and a total length of 19 feet (9 feet shorter than the HS-20 truck configuration used in this study) that creates larger longitudinal and transverse

bending moment in the bridge. Moreover, WIM data in the state of Florida was also used for selecting a typical truck, which creates a larger moment and shear for a 120 feet simple span bridge. The selected truck, which is called here WIM Data-FL, has a gross vehicle weight of 120 kips distributed over seven axles (Class 13 based on FHWA vehicle category classification). The ratio of the selected truck moment and shear to HS-20 truck is 1.58 and 1.56, respectively.

It should be noted that in all models studied in this section, concrete compressive strength was considered as 6.2 ksi, and the trucks were positioned over the fractured girder in two different locations across the bridge width, to constitute Case 1 for studying the one-way flexural bending failure of the deck and Case 4 for one-way shear failure. In these cases, where most of the truck loading is being transferred transversely to the intact girder, the center of gravity of trucks was positioned at the mid-span for all cases.

Table 2-16 indicates the results of sensitivity analysis for the truck loading. The one-way shear capacity was calculated using the method mentioned in the previous section (The effective width was predicted using 45° spreading line from the far side of the first and last point loads, and total width was considered as the effective width by ignoring gaps between spreading lines.) and the bending yield lines for each case, as shown in Figure 2-70 and Figure 2-71, were captured from the finite element models using the damage indexes, as explained in the previous sections. The bridge yield line capacity and one-way shear capacity were calculated for each case using the yield line pattern and the proposed method for the shear, and the results were compared in Table 2-16 and Table 2-17 to the bridge ultimate load capacity obtained from the finite element model.
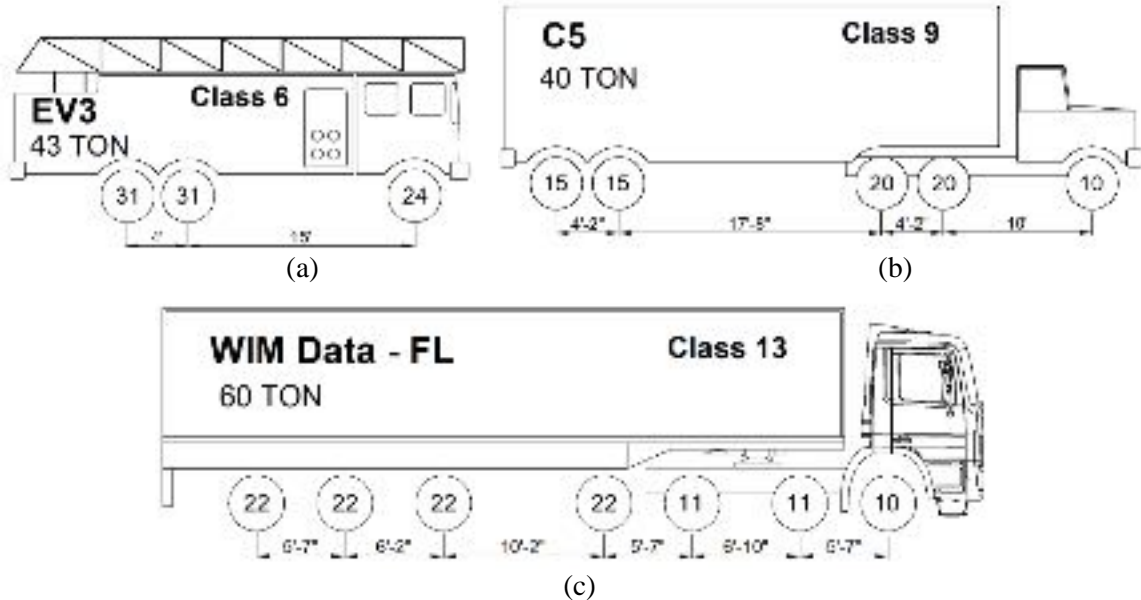
Figure 2-69. Vehicle loading configuration: (a) Florida emergency vehicle (EV3); (b) Florida legal load (C5); (c) Florida typical truck (WIM Data –FL).

The results show that the bending yield line failure is the failure mode for all the truck configurations in Case 1, where the truck position transversely is farthest from the intact girder, and one-way shear is the failure mode in Case 4, where the trucks were positioned closest to the intact girder. Moreover, the proposed bending yield line can conservatively predict the bridge ultimate load capacity in Case 1 by ignoring the effect of the fractured girder and diaphragms. It is worth mentioning that only for the EV3 truck configuration where the truck length is very short, and the truck weight (86 kips) is much heavier than the HS-20 design truck, the one-way shear capacity of the bridge in Case 4 (243.6 kips) is less than its bending yield line capacity in Case 1 (309.6 kips). In all other truck loadings, Case 1, with the largest eccentricity of loading, is the governing case with the bending yield line as the dominant mode of failure.

EV3
(a)

C5
(b)
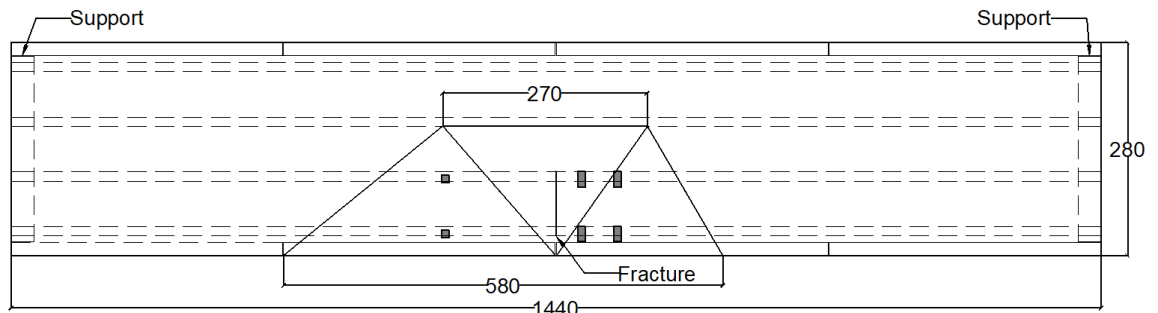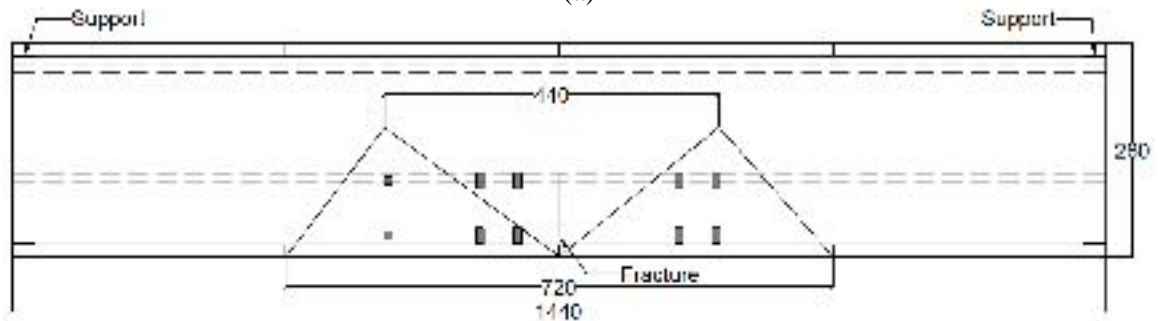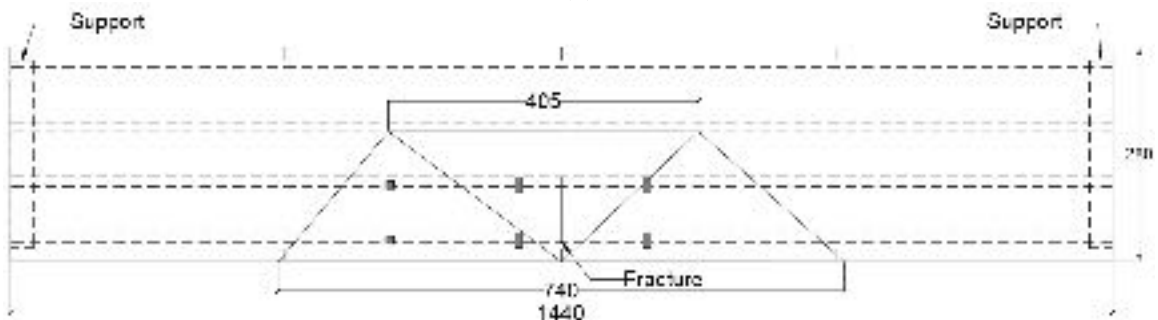
HS-20
(c)
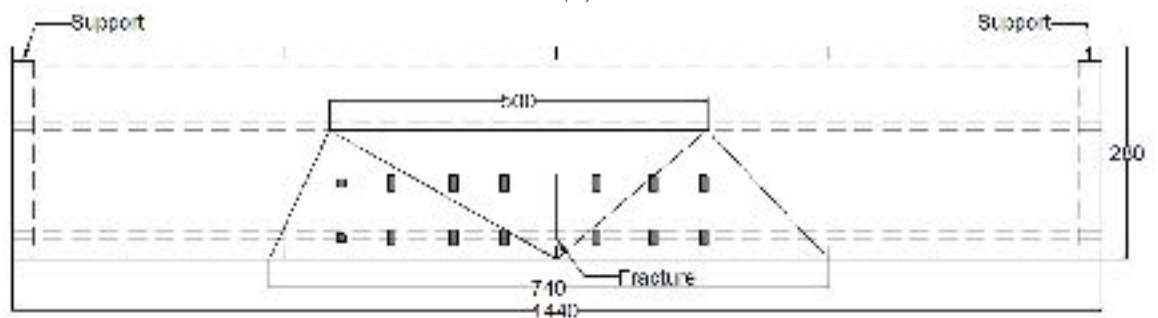
WIM-Data-FL
(d)

Figure 2-70. University of Texas Bridge Yield Line Failure in case 1 for Different Truck Loading: (a) EV3; (b) C5; (c) HS-20; (d) WIM-Data-FL.

EV3

(a)

C5

(b)

HS-20

(c)
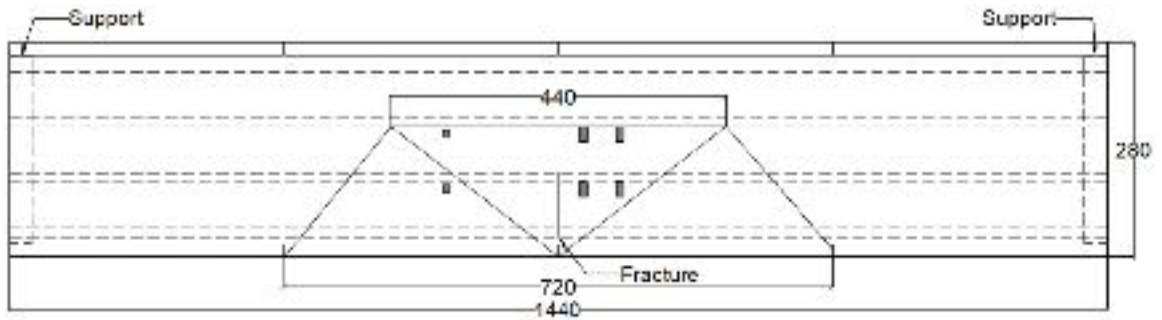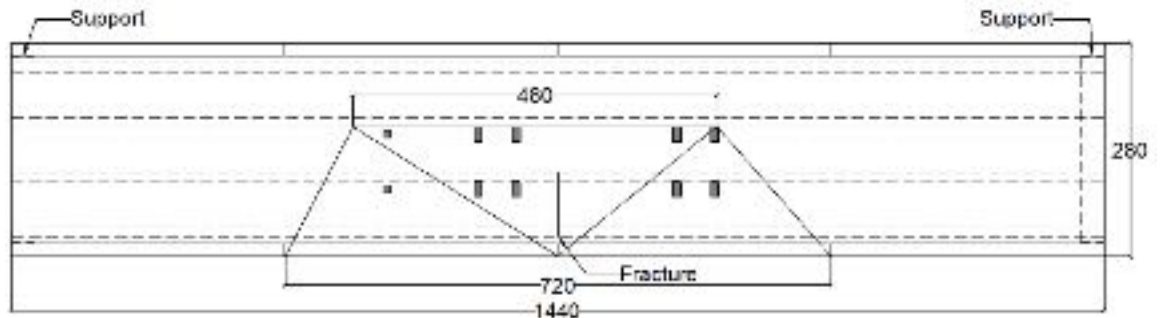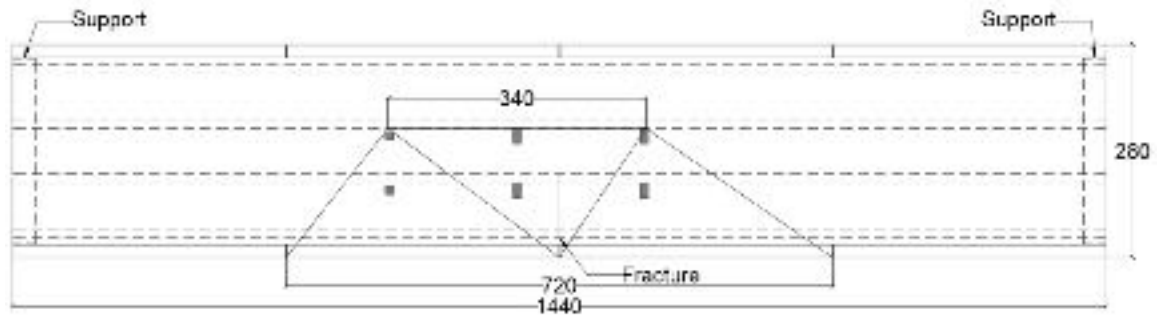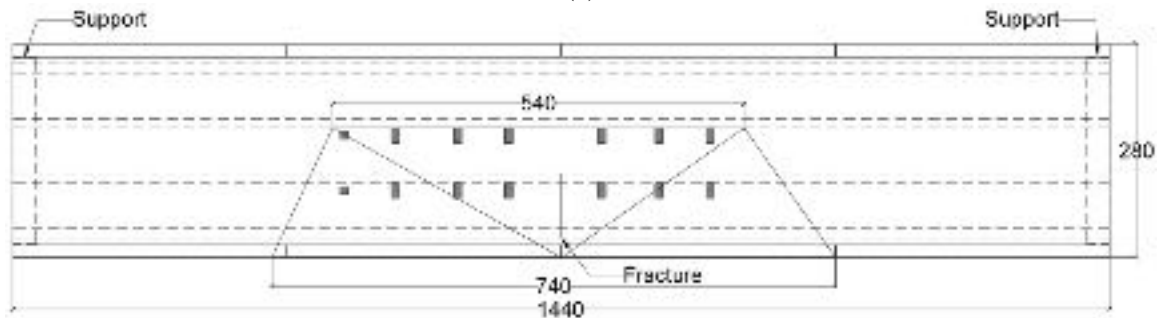
WIM-Data-FL

(d)

Figure 2-71. The University of Texas bridge yield line failure in case 4 for different truck loading: (a) EV3; (b) C5; (c) HS-20; (d) WIM-Data-FL.

Table 2-16. Bridge capacity for Cases 1 and 4 with different truck configurations.

Case	Truck	One-Way Shear Capacity (kips)	Bending Yield Line capacity (kips)	Max. Capacity from FE analysis- shear studs are modeled (Kips)
1	C5	534.7	**288**	300
	HS-20	448.7	**286.6**	318
	EV3	351.1	309.6	333
	WIM-Data	577.7	**330**	374
4	C5	427.2	620	350
	HS-20	341.2	563	340
	EV3	**243.6**	524	352
	WIM-Data	470.2	668	402

In all the above cases, the yield line configuration was determined using the specific finite element damage pattern for each case. Using these results, a unified and simplified method can be developed for predicting the yield line pattern in the deck of a twin steel box girder with one fractured girder for different loading configurations.

Table 2-17. Minimum bridge capacity for all cases with different truck configurations.

Truck	Min. One-Way Shear Capacity (kips)	Min. Bending Yield Line capacity (kips)	Capacity from FE analysis (Kips)
C5	427.2	**288**	300
HS-20	341.2	**286.6**	318
EV3	**243.6**	309.6	333
WIM-Data	470.2	**330**	374

2.1.5.3 *A Unified Simple Model for Predicting the Reserved Capacity of Twin Steel Box Girder Bridges with A Fracture in One Girder*

2.1.5.3.1 Simplified Yield Line Pattern for Different Loading Configurations

The results presented in the previous section indicated that the dominant mode of failure for the twin steel box girder bridge considered in this study after a fracture in one girder in all but one case was the bending yield line failure. The exception was the case of EV3, where one-way shear for Case 4 was smaller than bending yield line failure for Case 1 for

the same truck. However, even in this case, the capacity indicated by bending yield line failure was noticeably smaller than the capacity obtained from finite element analysis. Also, the simple method adopted in this study for one-way shear failure seems too conservative for the shorter and more compact trucks. Hence, from now on, the simple model based on bending yield line failure will be considered for reliability and redundancy analysis applicable to all truck configurations.

The characteristics and geometry of the yield line pattern for each case have been deducted from the detailed finite element analysis conducted for that specific case (truck loading and position). To simplify the process and avoid the need for FE analysis for each loading case, a simple and unified method of determining the yield line pattern becomes instrumental. This unified pattern, however, has to agree well with the results obtained using FE analysis to satisfy the complex load distribution after the fracture of one girder. Therefore, a parametric analysis was conducted for developing a simplified yield line pattern to be used for calculating the bridge capacity based on the bending yield line failure that would be applicable to different loading configurations. The parametric study on the truck loading configuration shows that when the bridge is loaded over the fractured girder far from the intact girder (Case 1), the deck starts to first crack over the intact girder due to the one-way bending mechanism of the bridge deck. By increasing the load, cracks in the deck will extend along the span, and four diagonal cracks will form to complete the failure mechanism in the deck (Figure 2-70). A comparison between the yield line patterns obtained from the FE analysis for different loading configurations shows that the longitudinal crack over the intact girder extends up to about the truck length in all configurations. Internal diagonal cracks will follow a regular pattern connecting the end of

the longitudinal crack to a point on the edge of the deck at the fracture location. However, external diagonal cracks form with different angles from the end of longitudinal cracks to the railing, depending on the loading configuration (see Figure 2-70).

Considering the FE analysis, a simplified yield line pattern was developed, as shown in Figure 2-72. In this pattern, the truck is positioned closest to the railing, where its center of gravity coincides with the mid-span over the fracture. The length of the longitudinal crack is considered equal to the truck length. To find the angle of the diagonal lines (α in Figure 2-72), a parametric analysis was conducted with varying angles. The goal was to find an angle that results in capacity in agreement with previous results using FE-derived patterns and capacity obtained from FE analysis. Table 2-18 summarizes the parametric analysis for yield line patterns with different angles varied from 30° by 5° increments. The ratio of the simplified bending yield line capacity to the bridge capacity obtained from the FE analysis is shown in the table for each angle. The results show that the simplified method with the 35° gives the best average capacity ratio (0.92) compared to the bending yield line capacity and ultimate bridge capacity obtained from the FE analysis, and no case produces capacity above the capacity obtained from FE analysis. By decreasing the angle to 30°, the bending yield line analysis gives a higher capacity than the ultimate bridge capacity from FE analysis, and the results for 40° and 45° are too conservative.

Table 2-18. Parametric results on the suggested simplified yield line pattern for different loading configurations.

Truck	Bending Yield Line capacity-FEM (kips)	Ratio	Bending Yield Line Capacity-Simplified Method (kips)										Capacity from FE analysis (Kips)
			α=30	Ratio	α=35	Ratio	α=40	Ratio	α=45	Ratio		
C5	288	0.96	329.6	1.10	**300.2**	**1.00**	281.6	0.94	263.2	0.88		300
HS-20	286.6	0.90	329.7	1.04	**298.4**	**0.94**	278.6	0.88	251.6	0.79		318
EV3	309.6	0.93	351.1	1.05	**310.4**	**0.93**	279.1	0.84	254.6	0.76		333
WIM-Data	330	0.88	325.6	0.87	**301**	**0.80**	282.7	0.76	265.2	0.71		374
Average		0.92		1.02		**0.92**		0.85		0.79		
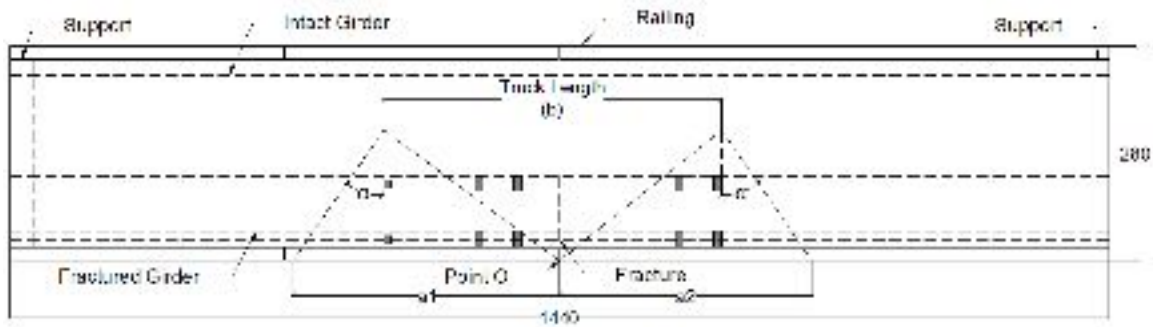
Figure 2-72. Simplified yield line pattern for different loading configurations.

The yield line pattern can be defined for each loading configuration based on the proposed pattern, and the virtual work can be used for computing the fractured bridge capacity. Using fundamental trigonometric relationships, displacement of point loads (Equation (2-6)), the center of gravity of railing, and the concrete deck triangles (for self-weight) are obtained for calculating the external virtual work (Equations (2-7, 2-8, and 2-9)). In order to calculate the internal virtual work by the bridge deck, including the deck and railing, the length and rotation of each yield line are calculated using the failure pattern geometry (Equations (2-10) and (2-11)). Railing can contribute significantly to the ultimate bridge capacity. After a fracture in one of the girders, the railing acts as an edge beam for carrying the loads. The internal work by the railing depends on the type of railing, the location of

the hinge lines, and the gaps between railing segments. In the railing system with expansion joints (gap), two sides of the gap will come in contact after a large displacement and increase the internal work depending on the gap size. However, due to uncertainty of gaps size and to be conservative, virtual work by the railing at the gap (assumed in this study at the fracture location) is not considered in the calculations of the simplified method. Nevertheless, the virtual work by the railing is considered where the yield line intersects the railing by two external diagonal lines.

$$\delta_{load} = r_{load} \cdot \Delta/r \tag{2-6}$$

$$EW_{Railing} = A_{Railing} \cdot (a_1 + a_2) \cdot 0.15 \cdot \Delta/2 \tag{2-7}$$

$$EW_{Deck\ Triangles} = A_{Deck\ Triangles} \cdot t \cdot 0.15 \cdot \Delta/3 \tag{2-8}$$

$$EW_{Truck\ load} = \sum (load. \delta_{load}) \tag{2-9}$$

$$IW_{Deck\ Triangles} = \sum (m_b \cdot l \cdot \theta_{Deck\ Rotation}) \tag{2-10}$$

$$IW_{Railing} = \sum (m_b \cdot \theta_{Railing\ Rotation}) \tag{2-11}$$

Where δ_{load} = Displacement of point loads; r_{load} = Distance from the point load to Point O (see Figure 2-72); r = Distance from Point O to the yield line (passing from the point load); m_b = Bending capacity.

2.1.5.3.2 *Evaluation of the Simple Model for Various Deck Thickness and Concrete Compressive Strength*

The proposed yield line patterns and analysis were used for calculating the ultimate bridge capacity under various truck loading for different concrete deck thickness and compressive strengths separately. The concrete deck thickness varied from 7.5 in. to 8.5 in., and the concrete compressive strength varied from 4 ksi to 7 ksi. Note that for the concrete deck thickness sensitivity analyses, the compressive strength was assumed 6.2 ksi, and for the

concrete compressive strength analyses, 8 in. thickness was assumed for the deck. Table

2-19 and

Table 2-21 summarizes the results of sensitivity analysis for the concrete deck thickness

and compressive strength, respectively. Moreover, FE analyses were used for comparing

the bridge ultimate load-carrying capacity obtained from the FE model and the simple

method, as shown in Table 2-20 and Table 2-22.

Table 2-19. Ultimate bridge capacity obtained using the yield line analysis for different concrete deck thicknesses (ksi).

	Truck	Concrete Deck Thickness (in)										
		7.5	7.6	7.7	7.8	7.9	8	8.1	8.2	8.3	8.4	8.5
Ultimate Bridge Capacity (kips)	EV3	292	295.8	299.4	303.2	306.7	310.4	314	317.5	321.3	324.9	328.7
	C5	279.4	283.7	287.7	292	296	300.2	304.2	308.5	312.5	316.7	320.8
	WIM	279.7	283.9	288	292.3	296.6	301	305.2	309.5	313.4	317.8	322.1
	HS-20	279.5	283.3	287.1	290.9	294.7	298.4	302.5	306.3	310	313.8	317.7

Table 2-20. Comparison of the ultimate bridge capacity obtained using the simple and FE analysis methods.

		Concrete Deck Thickness (in)			
	Truck	Yield Line Analysis			FEA
		7.5	8	8.5	8
Ultimate Bridge Capacity (kips)	EV3	292	310.4	328.7	333
	C5	279.4	300.2	320.8	300
	WIM	279.7	301	322.1	374
	HS-20	279.5	298.4	317.7	318

Table 2-21. Ultimate bridge capacity obtained using the yield line analysis for different concrete compressive strengths (ksi).

		Concrete Compressive Strength (ksi)							
	Truck	4	4.5	5	5.5	6	6.2	6.5	7
Ultimate Bridge Capacity (kips)	EV3	287.4	293.4	298.8	303.9	308.3	310.4	312.5	316.3
	C5	273	280.2	286.7	292.6	297.9	300.2	302.8	307.2
	WIM	272.8	280.2	286.9	293	298.4	301	303.6	308
	HS-20	274	280.3	286.2	291.7	296.4	298.4	301	304.8

Table 2-22. Comparison of ultimate bridge capacity obtained using simple and FE analysis methods.

		Concrete Compressive Strength (ksi)					
	Truck	Yield Line Analysis			Finite Element Analysis		
		4	5	6.2	4	5	6.2
Ultimate Bridge Capacity (kips)	HS-20	274	286.2	298.4	308	314	318

It should be pointed out that the amount of reinforcement in the deck was kept the same (#5 bar with 6 inches spacing (Figure 2-73)) for all deck thicknesses. As shown in Figure 2-74, the external/internal work (used in the simple method) and the ultimate bridge capacity in the yield line analysis varies with the section moment capacity, loading configuration, and the yield line patterns. The results indicate that the bridge ultimate load capacity is directly proportional to the deck section moment capacity and deck thicknesses and varies nonlinearly with the concrete compressive strength.

Figure 2-74(a) and (b) show the moment capacity and the external/internal work (used in yield line analysis) obtained using the simple method for various truck configuration and variation of the deck thickness, where Figure 2-74 (c) and (d) show the same for variation of concrete compressive strength. The results show that the slope of the ultimate bridge capacity and external/internal work varies with each truck because of the difference in the loading configurations and yield line pattern.

Moment capacity analysis using the simple model (Figure 2-74(c) and (f)) shows that an increase in deck thickness or concrete compressive strength results in an increase in the positive and negative moment capacity. Since the deck configuration used in this study, as shown in Figure 2-73 (#5 bar with 6 inches spacing), is under-reinforced, the rebar reaches yield strain before the concrete reaches crushing strain for all the studied thicknesses. Therefore, increasing the section thickness linearly increases the positive and

negative moment capacity of the deck. However, the effect of concrete compressive strength in the section moment capacity is nonlinear.
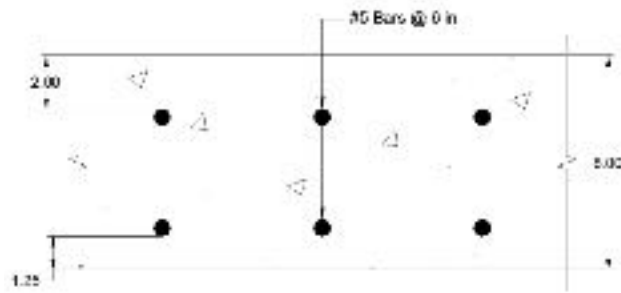
Figure 2-73. The concrete deck section.
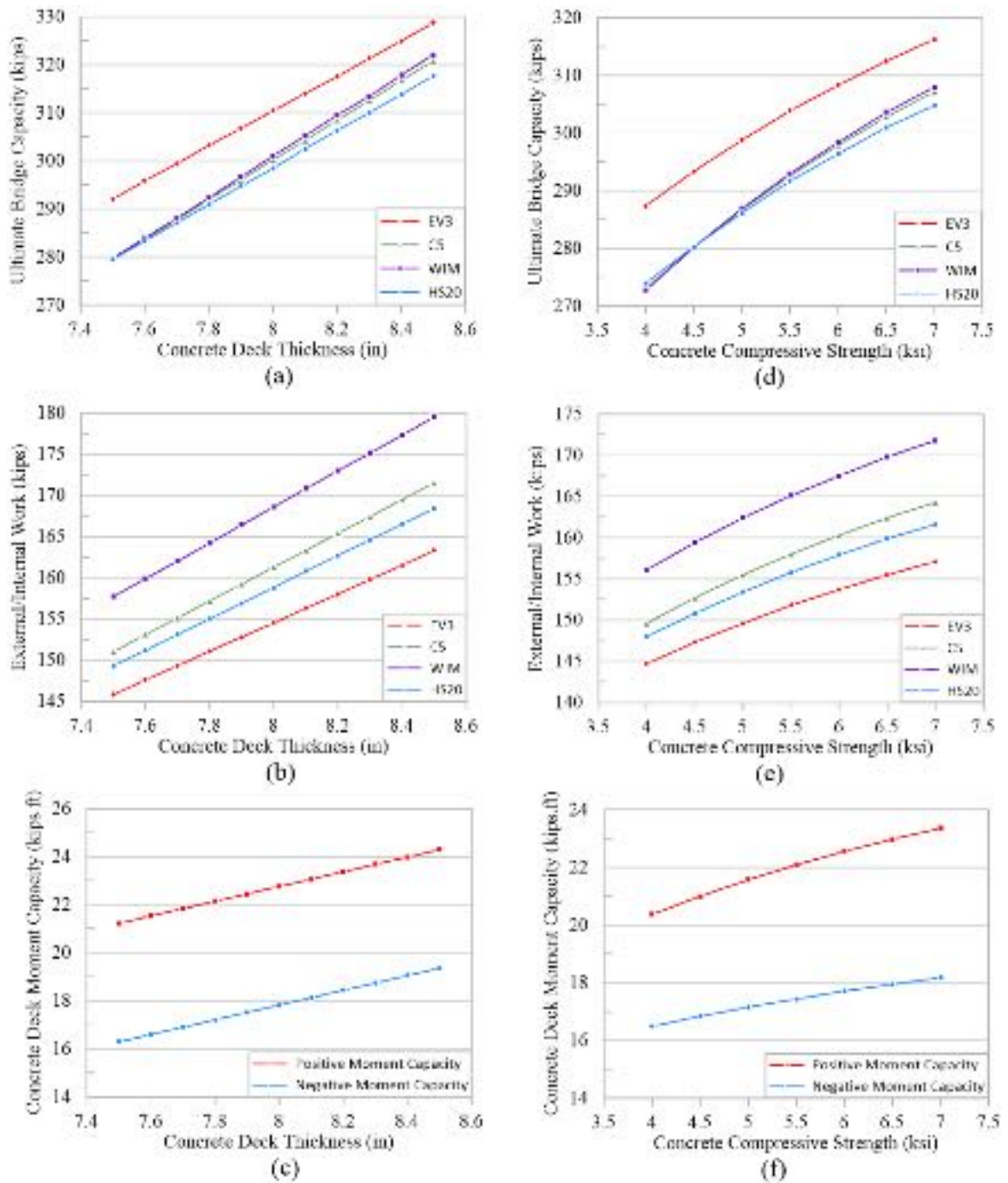
Figure 2-74. Sensitivity analysis of concrete deck thickness: (a-c) and concrete compressive strength; (d-f) using the yield line analysis.
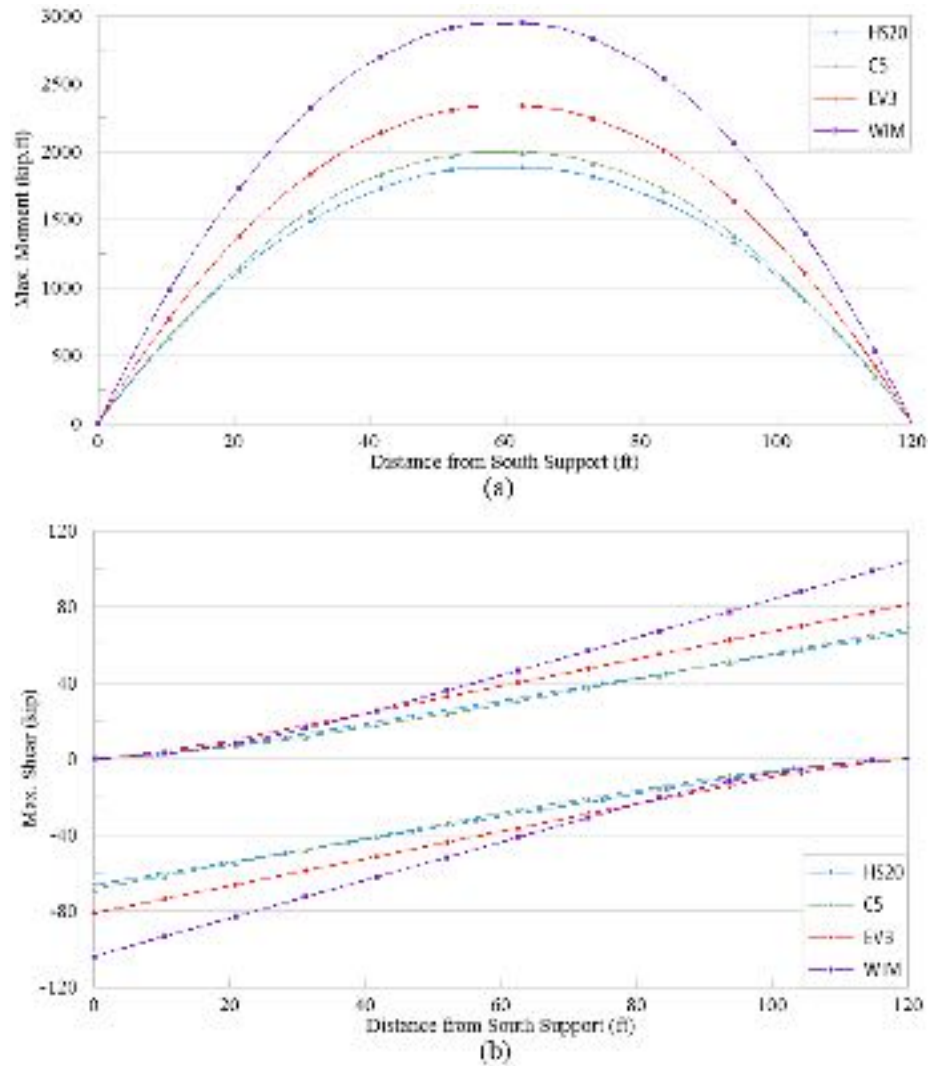
Figure 2-75. Moment and shear diagram in a simple 120 ft span bridge for different truck loading: (a) Maximum moment; (b) Maximum shear.

Table 2-23. Maximum moment and shear in a simple 120- ft span bridge for different truck loading.

| Truck | Moment | | Shear | |
	Maximum (kip.ft)	Location (Distance from support) (ft)	Maximum (Kip)	Location (Distance from support) (ft)
WIM	2944.3	57.8	103.8	
EV3	2339.3	58.6	81.2	0 and 120
C5	1994.8	57.7	68.5	
HS20	1883.8	57.6	66.4	

113

2.1.5.4 *Load Distribution Analysis in the University of Texas Twin Steel Box Girder Bridge*

A series of analyses are conducted on the bridge to investigate the behavior of the bridge in intact and damaged scenarios under dead and increasing live load. The goal is to determine the distribution of dead and live loads before and after the fracture of one girder. One way to determine the load distribution is by comparing the support reactions of the girders. Unsymmetrical bridge loading like Case #1 in this study creates additional torsional moment over the bridge section that is supported at the bearing as coupling forces (upward and downward forces (T)), which can change the total reaction forces. Depending on the loading eccentricity, bridge configuration, and condition, the torsional force could even lead to uplift at the supports. In the twin steel box girder bridges, since after a fracture in one of the girders, the intact girder needs to transfer the torsional moment created by eccentric loading to the supports, the uplift forces are more pronounced. To this end, the reaction forces at the supports for the intact and damaged bridge subjected to the 1×HS-20 loading (Figure 2-77 and Figure 2-78) are obtained from the FE analysis as shown in Table 2-24 and Table 2-25.

The results show that after the fracture in the loaded girder, the reactions at the intact girder supports would increase. However, the girder reactions are affected by both vertical load (R) and an eccentricity torque (T), as shown in Figure 2-77 and Figure 2-78. The torque reduces the total reactions on the right girder and increases the total reaction of the left/loaded girder. The torque is understood to be even larger after fracture when the centroid would move closer to the intact girder. The results show that after a fracture of one girder, a larger portion of the dead load and live load would transfer transversely to the intact girder near the mid-span. A significant portion of the transferred force, however,

returns to the fractured girder through the deck and cross-frames that are away from the fracture zone (yield line pattern) therefore reducing the reaction forces on the intact girder to balance the torque.

Table 2-24. Bridge support reaction for the intact bridge obtained from FE analysis.

	Left Girder (Loaded)				Right Girder			
	North	South	Girder Reaction	Ratio to Total	North	South	Girder Reaction	Ratio to Total
Dead Load (R) (kips)	124.7	124.4	249.1	0.50	124.7	124.4	249.1	0.50
1xHS-20 (R) (kips)	30.9	30.5	61.4	0.85	2.3	8.3	10.6	0.15
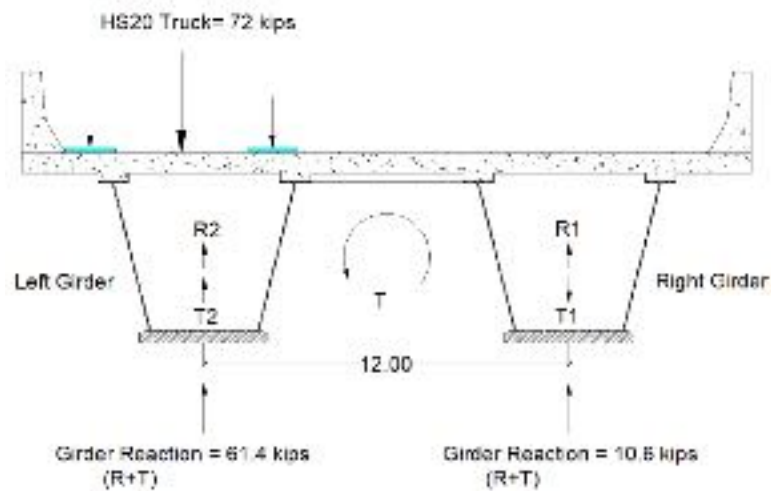
Figure 2-76. Bridge support reaction for the intact bridge obtained from FE analysis.

Table 2-25. Bridge support reaction for dead and live loads after the full-depth fracture obtained from the FE analysis.

	Left Girder (Loaded-Fractured)			Right Girder		
	North	South	Girder Reaction	North	South	Girder Reaction
Dead Load (R+T) (kips)	115.3	116.9	232.2	132.5	133.5	266
1xHS-20 (R+T) (kips)	26.4	30.2	56.6	6.2	9.2	15.4

115
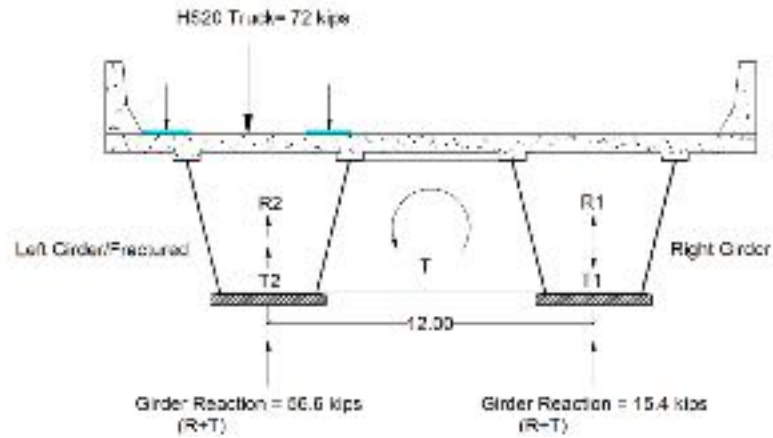
Figure 2-77. Bridge support reaction after the full-depth fracture.

As an alternative way to estimate the live and dead load transfer/distribution to the intact girder after a fracture, shear stress profiles for a section at the face of the intact girder (Figure 2-78) were extracted from the FE analysis. The total shear force from the concrete deck and intermediate cross-frames along the span for the intact and damaged bridge subjected to the dead load and the live load was obtained as shown in Table 2-26 and Table 2-27, respectively. It is also realized that the proportion of load transferred due to the fracture of a girder would increase as the level of load increases. This can partly attribute to the damages at the deck to the girder interface (shear studs) and the deck itself, as well as increased torque due to shifting the bridge centroid. To demonstrate this, the damaged bridge was analyzed under 3.2×HS-20 that is closer to the bridge capacity.

Table 2-27 shows the transfer of loads because of fracture through shear at the deck and cross-frames from fracture of one girder at Section 1-1.

116
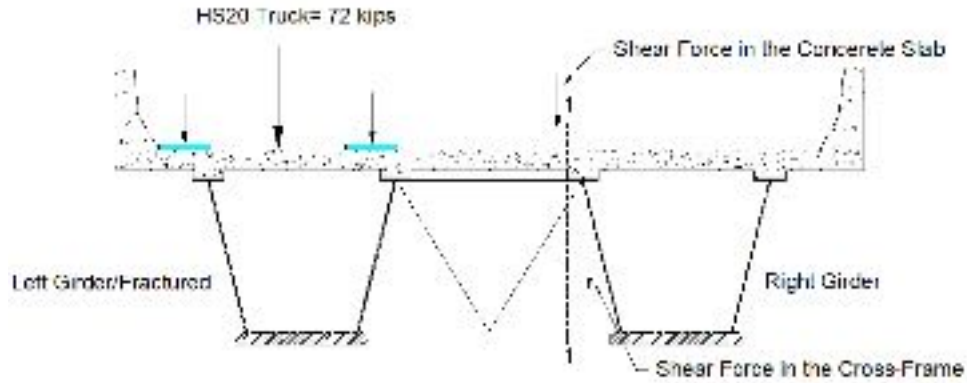
Figure 2-78. Shear force in Section 1-1.

Table 2-26. Shear forces transferred to the right girder under dead load and 1 x HS-20 design truck for the intact bridge at section 1-1.

	Shear Forces		
	Concrete Slab	Cross-Frames	Transfer Total
Dead Load (kips)	16.1	0.3	16.4
1x HS-20 (kips)	10.4	15.6	26

Table 2-27. Shear forces transferred due to fracture to the right girder under dead load and 3.2 times HS-20 design truck.

	Shear Forces			
	Concrete Slab	Cross-Frames	Transfer Total	Ratio to Total live load
Dead Load (kips)	31.7	27.8	59.5	
3.2xTime HS-20 (kips)	71.5	85.0	156.5	0.68

The results show that for 3.2×HS-20, 68% of the total live load will be transferred to the intact girder after the fracture of the loaded girder through the concrete deck and cross-frames. Another way for simple estimation of shear transfer is based on the yield line analysis where the live load is assumed to be transferred as shear stress to the intact and fractured girder through the outside yield lines, as shown in Figure 2-79. The live load distribution to the intact and fractured girder for the HS-20 truck loading according to the suggested yield line pattern was calculated as 70% and 30%, respectively; that is a good estimate compared to the FE analysis (68%).

117
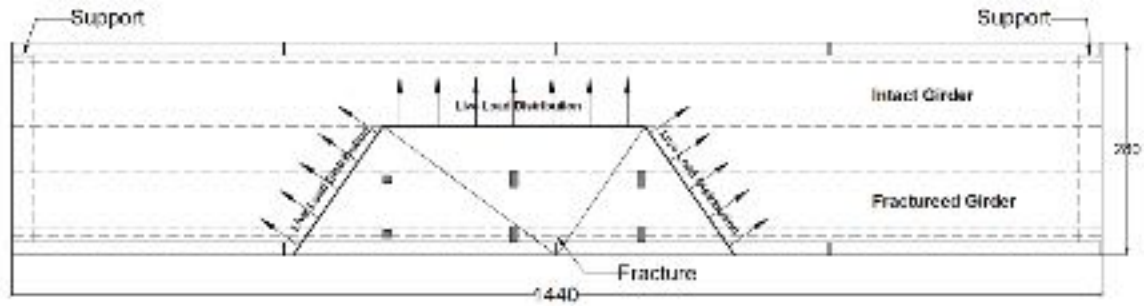
Figure 2-79. Live load distribution based on the yield line analysis for HS-20 loading.

When a fracture occurs, and the deck fails under increasing live load, for the bridge not to collapse, the intact girder has to be able to carry the loads transferred to it, i.e., the intact bridge, to have adequate moment capacity. Accordingly, moment analysis was conducted on the bridge subjected to dead and live load at the middle of the span where the bridge is damaged. Table 2-28 shows sectional moments extracted from finite element analysis for the intact and damaged bridge. According to the results, the dead load moment of each girder in the intact bridge is about 3538.7 kip-ft. However, the moment on intact girder increases by about 50 percent once a fracture occurs in the loaded girder (5618.8 kip. ft). The fractured girder has a very small stiffness at the middle (one can assume hinge or very weak spring), so it attracts only a negligible moment (893 kip. ft) compared to the intact girder.

The live load moment analysis for the intact bridge shows that the left girder (loaded) carries 60%, and the right girder carries 40% of the live load. However, after the fracture, the right girder (intact) carries most of the live load (66%) because of a decrease in stiffness of the fractured girder. Nevertheless, the fractured girder is undamaged through most of its length. Since the truck loads are applied through its wheel footprints, and rear and front wheels are at a distance from the middle, the fracture girder can transfer some portion of

118

live load (34%) through those segments as a cantilever beam. Unlike the live load, the dead load is distributed along the bridge, and the fractured girder is able to transfer a noticeable portion through its undamaged end segments.

In the bridge with one girder fractured, the total moment at the middle of the bridge is not the same as the intact bridge since the girders (or the bridge) cannot be assumed anymore to be separately simply supported. There is a complex interaction between the intact and fractured girder away from the fracture point that can only be simulated with the FE analysis. It should also note that the percentages calculated represent the changes of the moment at mid-span due to the fracture and do not necessarily give a picture of how the load is distributed.

Table 2-28. Moment analysis of the bridge under HS-20 loading (FEM).

	Moment (kip-ft)					
	Bridge Section		Right Girder Section		Left Girder Section	
					Fractured Girder	
	Dead	Dead+ 3.2 HS-20	Dead	Dead+ 3.2 HS-20	Dead	Dead+ 3.2 HS-20
Intact Bridge	7079.6	12636.0	3538.7	5801.7	3541.0	6834.3
Damaged Bridge	6512.2	10792.8	5618.8	9560.7	893.4	1232.1

2.1.6   Continuous Curved Twin Steel Box Girder Bridge

A continuous curved bridge was analyzed to demonstrate the capability of the finite element modeling methods proposed in Section 2.1.4 of the dissertation. The possible failure mechanisms and the applicability of the simplified methods presented in Section 2.1.5.3 for calculating the bridge ultimate load-carrying capacity will also be investigated. Suggestions will also be made for future work to adapt the methods developed in this study for simple spans to continuous spans.

2.1.6.1   Bridge Description

A three-span continuous bridge located in Miami, FL, was selected to represent continuous twin steel box girder bridges in this study. The bridge was built in 2005 and had an overall length of 682.4 ft. and out to out width of 33.6 ft. carrying one traffic lane. The first and last span length is 210 ft., and the middle span length is equal to 262.4 ft. The first and second spans have a radius of curvature of 492.1 ft., while the last span is straight, as shown in Figure 2-80. The bridge superstructure has an 8.5 in. slab deck, diaphragms at supports, and horizontal and vertical bracing along the bridge for stability, similar to the University of Texas bridge. The steel-box section consists of two web plates with a thickness of 0.7 in., each sloped at 4:1 grade. The thickness of the bottom flange varies from 0.6 in. to 2.4 in. along the bridge, with a total width of 59 in., and the thickness of the top flange varies from 0.8 in. to 2.8 in., with a width of 17.7 in. and 23.6 in. varies along the span. The total depth of the box girder is 86.6 ft.

(a)

(b)
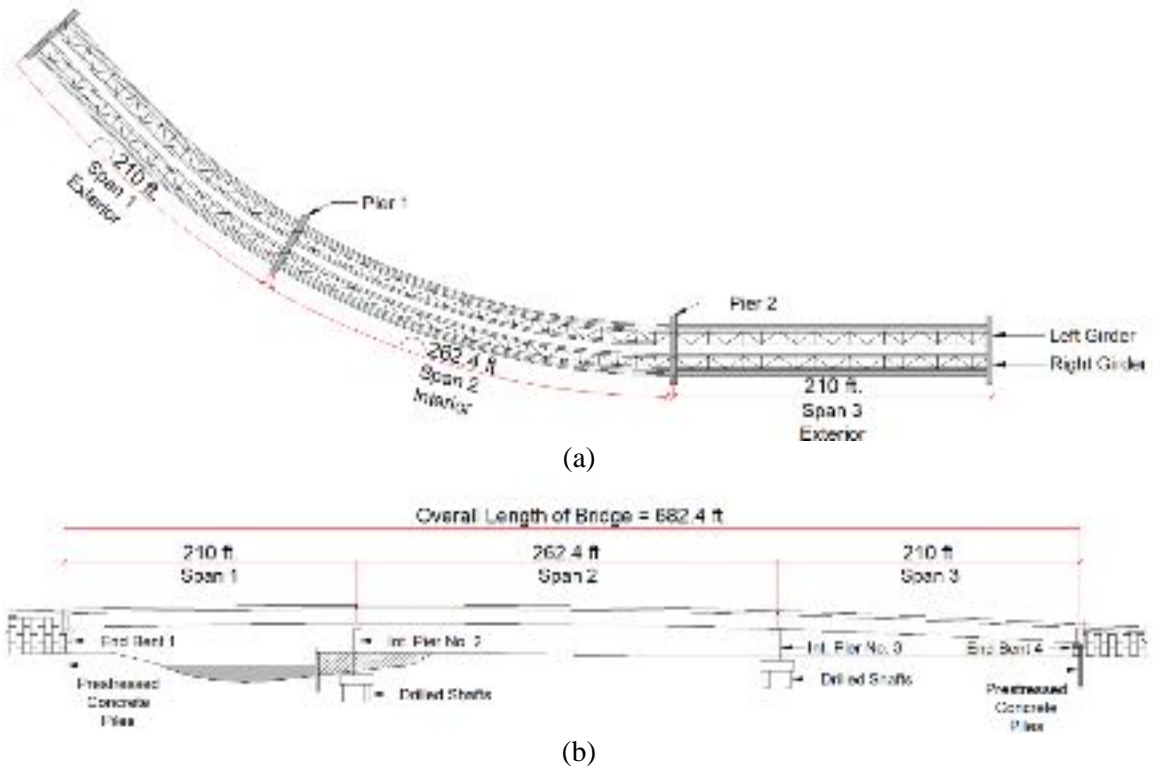
Figure 2-80. Continuous span bridge; (a) Plan view, (b) Elevation view.

2.1.6.2 *Finite Element Analysis*

A finite element model of the bridge was developed to study the bridge behavior after a full-depth fracture at the middle of Span 1 (Figure 2-81). Material properties, contact surfaces, and analysis procedures were assumed the same as the simple span model. In addition to the deck failure mechanisms discussed in this report, a possible failure mechanism in the continuous span bridges is the failure of the intact girder when the bridge is loaded over the fractured girder due to torsion and bending.

In interior spans, two sides of the fracture girder will behave as cantilever beams carrying a large portion of the dead and live load; however, in exterior spans, only one side of the fractured girder can carry the load as a cantilever beam. Therefore, in general, for an equal span length, exterior spans are the critical span for the continuous span bridges, and the only failure in the side span was studied in this report. Since the last span does not have a

121

curvature and has the same length as the first span, the finite element model was developed

to consider the fracture in the first span. For the model, a full-depth fracture was assigned

to the interior girder (left girder) at the middle of the span, and an increasing load in terms

of the HS-20 design truck similar to the simple span bridge was applied over the fractured

girder up to the bridge failure.
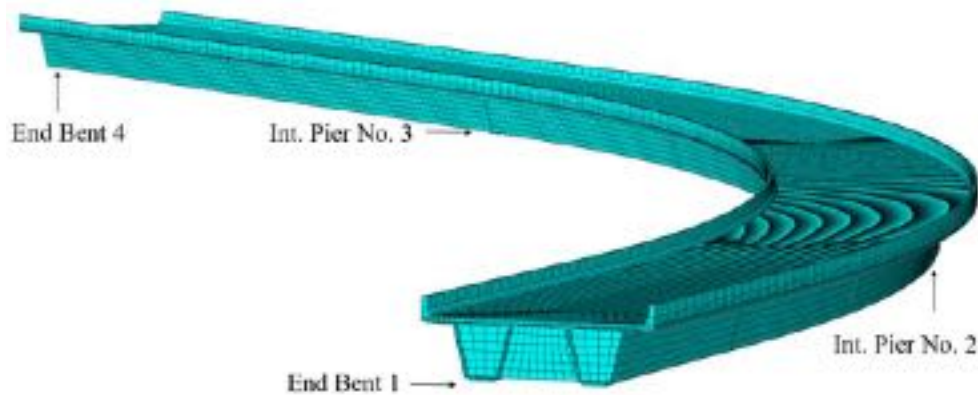
Figure 2-81. Finite element model of the three-continuous span bridge.

2.1.6.3 *Intact Girder Failure Mechanism*

The results show that the intact girder at the middle of Span 1 reaches its plastic moment

under dead load and eight times HS-20 design truck loaded over the fractured girder due

to a portion of dead load and live load being transferred to the intact girder after the fracture.

Moreover, due to the curvature and loading eccentricity, the effect of torsion is more

significant in this bridge compared to a straight bridge. Figure 2-82 shows the failure of

the intact girder under dead and live loading. Moreover, the results indicate that because of

the girder continuity, the fractured girder also carries a large portion of dead load and live

load as a cantilever beam more pronounced on the continuous side. This contribution is

relatively significant since under eight times HS-20 loading when the intact girder is failed,

the stress at the bottom and top flange and a portion of the web of the fractured girder

122

reaches 50 ksi (negative moment). The stress contours in Figure 2-83 show the contribution of the fractured girder in carrying a portion of the loads as a cantilever beam. The FE results also show that after the failure of the intact girder at the middle of Span 1 and with a large deflection, the fractured girder is the only element carrying the load up to the failure at the support due to the negative moment.
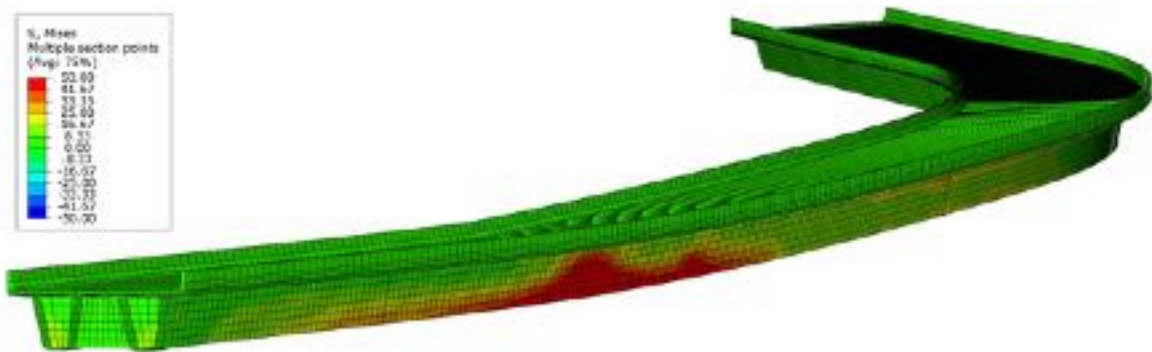
Figure 2-82. Intact girder failure under dead load and eight times HS-20 design truck at the middle of Span. 1.
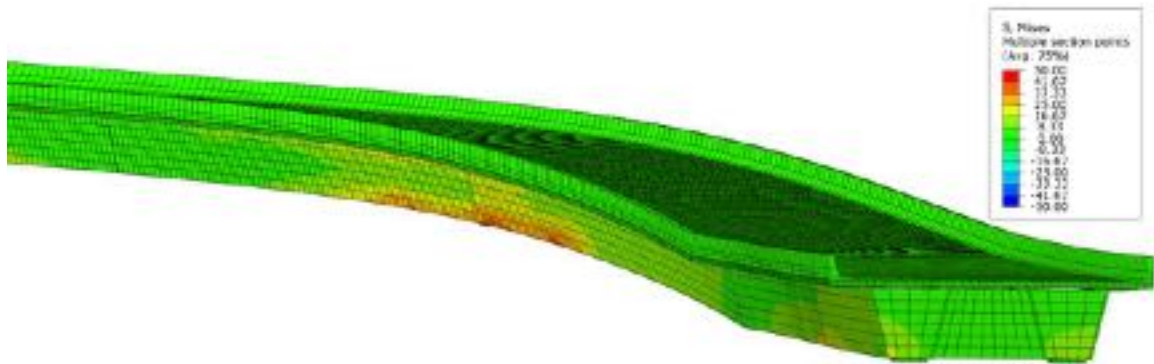
Figure 2-83. Contribution of the fractured girder in carrying a portion of the loads as a cantilever beam.

2.1.6.4 *Deck Failure Mechanism*

Investigation on the deck failure after the fracture using concrete damage plasticity model shows that first cracks will form over the middle supports. After the fracture of one girder, negative moment over the support will increase dramatically since the fractured girder can only carry the load as a cantilever beam (negative moment and partially toward simple

123

support), and some portion of the dead load and live load will transfer to the intact girder which increases the positive moment at the middle of the span and the negative moment over the middle support in the intact girder. Therefore, negative moments over the support will increase for both girders and tension cracks will appear on the top of the deck, as shown in Figure 2-84.

By increasing the live load, longitudinal cracks will form along the intact girder at the middle of the span, and the transverse cracks at the support will be extended. Finally, diagonal cracks will form the half-ellipse failure of the deck, similar to the simple span bridge. Nevertheless, because of the continuity and the contribution of the fractured girder, the angle of the diagonal crack on the continuous span side is much wider than the simple span bridge. Moreover, the fractured girder at the yield line needs to be yielded, as shown in Figure 2-83. (Bottom and a portion of the web in the fractured girder is yielded at the yield line and the support). Therefore, the combination of these factors would result in a higher yield line capacity in the continuous bridge compared to the simple span bridge.
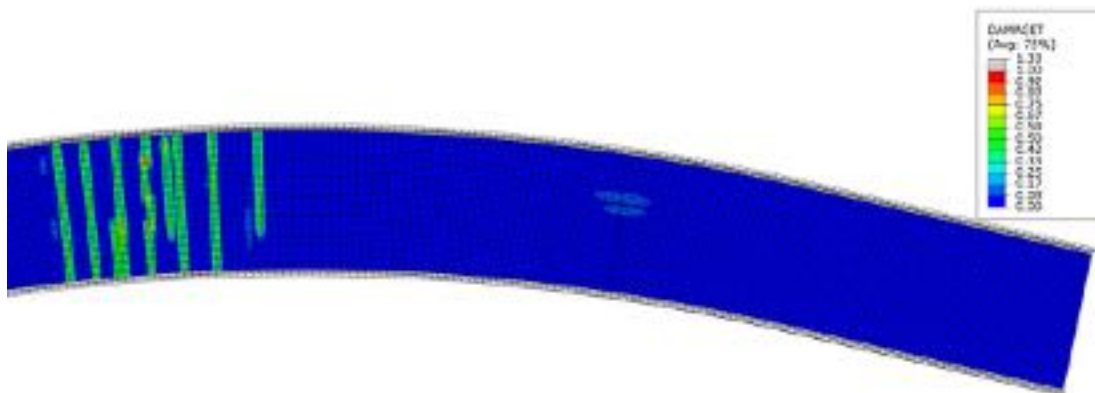
Figure 2-84. Deck crack pattern after a full-depth fracture of one girder in the continuous bridge in Span 1.

The results of the deck failure show that the yield lines will form at dead load plus six times HS-20 before the failure of the intact girder due to the bending and torsion at eight times

HS-20 design truck. Figure 2-85 shows the yield line pattern obtained from the FE analysis, which is compared to the proposed yield line pattern for the simple span bridges in Figure 2-86. It is evident from the FE results that the continuity of the span has significantly altered the yield line pattern when compared to the simple yield line model developed for simple span bridges. However, it is useful to compare the deck capacity using the simple yield line pattern for comparison purposes only.

(2×HS-20 Design Truck)

(4×HS-20 Design Truck)

(6×HS-20 Design Truck)
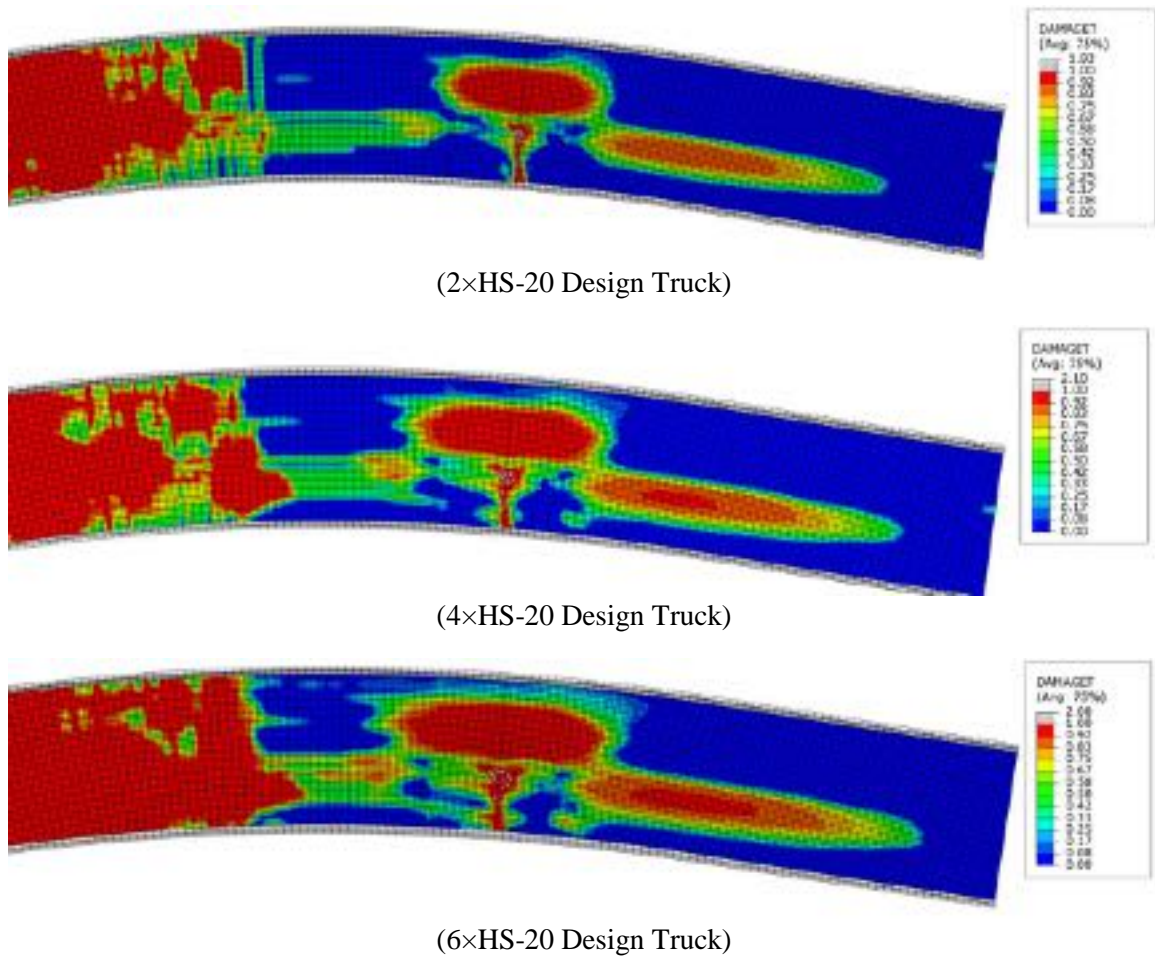
Figure 2-85. The yield line pattern of the deck in the Finite Element Model of the continuous bridge in Span 1.

The simplified yield line analysis proposed in Section 2.1.5.3 for simple span bridges is used to calculate the continuous bridge capacity, as shown in Figure 2-86, Table 2-29, and Table 2-30. This bridge has an 8.5 in. deck reinforced longitudinally using two layers of

#5 bars with a spacing of 12 in. and 10 in. for top and bottom layers, respectively. In the transverse direction, two layers of #4 with a spacing of 5 in are used for both layers. Noted that the deck moment capacity (concrete only) in this bridge is less than the simple span bridge studied in Section 2.1.5.3. (#5 bars with a spacing of 6 in. is used for the simple span bridge for both layers and directions)

In the yield line analysis, only concrete deck capacity was considered in the internal work calculation, and the effect of the fracture girder (continuity) was ignored for simplicity and comparison with Section 2.1.5.3. The bridge yield line capacity was obtained as 1.9 times HS-20 design truck, much less than the capacity obtained from the FE model as six times HS-20 when the yield line pattern formed because of ignoring the girder continuity. Therefore, these results show that the simplified method as deducted for simple span bridges should not be used for continuous span bridges unless modified to account for the effect of girder continuity in future studies.
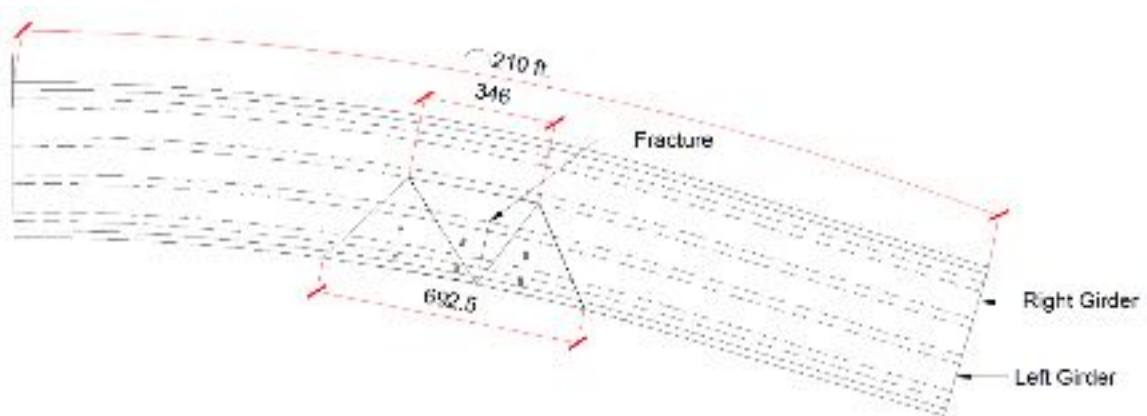
Figure 2-86. The yield line pattern for the continuous span bridge subjected to HS-20 design truck.

Table 2-29. External work calculation of the HS-20 truck load in the continuous span bridge.

	P	X_{point}	Y_{point}	r_{Load}	r	Delta	EW
Number of HS-20 Design Truck =**1.9**							
Front Wheel	7.7	18.7	8.4	6.9	27.3	0.3	2.0
Front Wheel	7.7	18.7	2.4	11.4	30.3	0.4	2.9
Middle Wheel	30.9	4.7	8.4	13.1	22.6	0.6	17.9
Middle Wheel	30.9	4.7	2.4	21.9	27.1	0.8	25.0
Rear Wheel	30.9	-9.3	8.4	7.0	19.5	0.4	11.1
Rear Wheel	30.9	-9.3	2.4	11.1	20.8	0.5	16.5
						EW_{Truck}	75.4
						EW_{DL}	41.1
						EW_{Total}	116.57

Table 2-30. Internal work calculation for the continuous span bridge.

	L	α	m_l	m_t	m_b	Rotation	dIW
Perimeter	28.80	0.00	19.70	16.81	16.81	0.05	24.31
	25.30	0.96	12.99	16.81	14.24	0.04	13.21
	25.00	0.96	12.99	16.81	14.24	0.05	18.65
Diagonals	27.30	0.79	15.05	19.70	17.37	0.04	19.04
	22.10	1.12	15.05	19.70	15.94	0.03	11.68
						$IW_{Railing}$	29.68
						IW_{Total}	116.57

2.1.6.5 *Plastic Moment Capacity*

The plastic moment capacity of the bridge for the intact scenario is calculated for the maximum capacity of the bridge. The effective flange width of a concrete deck slab is taken as the tributary width perpendicular to the axis of the member for determining cross-section stiffness for analysis and for determining flexural resistances. The slab effective flange width is taken as one-half the distance to the adjacent girder plus the full overhang width. The cross-section in this bridge varies along the spans based on the demand moments. The plastic moment of one girder at the middle of Span 1 is calculated as 28257 kip. ft. (Figure 2-87). The total flexural capacity of the bridge can be obtained by adding the capacity of two girders.
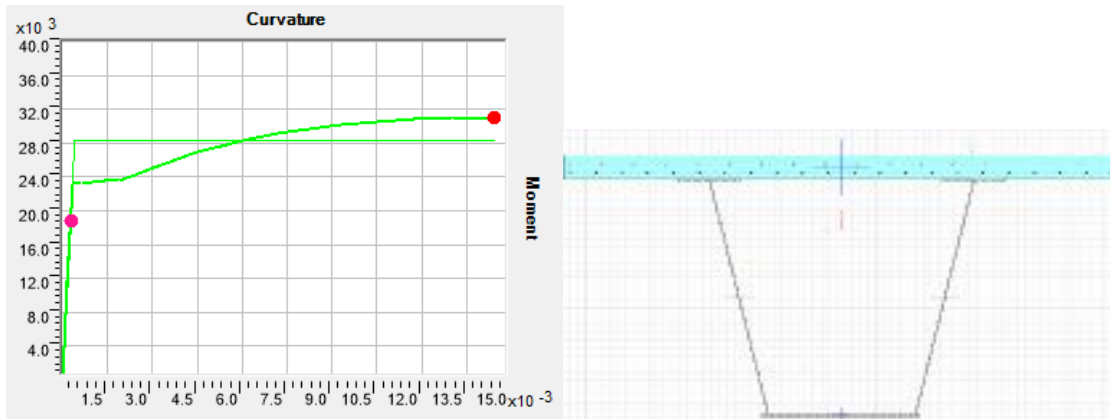
Figure 2-87. Moment curvature curve of one girder at the middle of span 1.

Based on a 3D analysis of the continuous bridge for load condition resulting in the maximum positive moment in the side span, the moment capacity calculated above corresponds to dead load plus 7.2 times HS-20 design truck or 3.1 times HL-93 (Uniform lane load+HS-20 design truck).

2.1.7 *Simplified Reliability Analysis of Fracture-Critical Twin Steel Box Girder Bridge*

This section presents a simplified reliability analysis to develop minimum criteria that the deck and girders of a twin steel box girder bridge should satisfy in order to ensure that it can safely carry a certain level of load when one of the girders sustains a severe fracture. The reliability calculations performed in this section are based on the response of the 120-ft bridge as obtained from the nonlinear finite element analysis described in Section 2.1.4 and the weigh-in-motion data used for projecting the maximum live load effects that a 120-ft Florida bridge may be subject to over different service periods.

Note: The reliability analysis described in this section was performed by Dr. Michel Ghosn from the City College of New York in collaboration with this dissertation author using the live load model and FEA results developed in this study.

2.1.7.1   Overview of Reliability Analysis Methodology

The aim of structural reliability theory is to account for the uncertainties in the evaluation

of the safety of structural systems and in the calibration of load and resistance factors for

structural design and evaluation codes. Load and resistance are treated as random variables,

and they are defined by the type of distribution and statistical parameters. In practice, it is

convenient to use non-dimensional parameters such as bias factor, λ, that is, the ratio of

mean to the nominal value, and coefficient of variation, COV, that is the ratio of standard

deviation and the mean value.

Structural performance can be considered as satisfactory or non-satisfactory. A

mathematical formula that describes the boundary between satisfactory or non-satisfactory

performance is called a limit state function. If R represents resistance and S represents the

load, then the simplest form of a limit state function, Z, is

$$Z = R - S = 0 \tag{2-12}$$

For a limit state function $Z = R - S$, where R and S are independent normal variables, the

reliability index, β, is obtained from:

$$\beta = \frac{\overline{Z}}{\sigma_Z} = \frac{\overline{R} - \overline{S}}{\sqrt{\sigma_R^2 + \sigma_S^2}} \tag{2-13}$$

where $\overline{Z}$ is the mean safety margin, σ_Z is the standard deviation of the safety margin, $\overline{R}$ and

$\overline{S}$ are the mean values, and σ_R and σ_S are the standard deviations of R and S.

The reliability index, β, defined in Equation (2-13) provides an exact evaluation of the

probability of failure if R and S are normal distributions. Although β was originally

developed for normal distributions, similar calculations can be made if R and S are

lognormally distributed (i.e., when the logarithms of the basic variables follow normal distributions). In this case, the reliability index can be calculated as:

$$\beta = \frac{\ln\left(\frac{\overline{R}}{\overline{S}}\sqrt{\frac{1+V_S^2}{1+V_R^2}}\right)}{\sqrt{\ln\left[\left(1+V_R^2\right)\left(1+V_S^2\right)\right]}}$$

(2-14)

Which, for small values of V_R and V_S on the order of 20% or less, can be approximated as:

$$\beta = \frac{\ln\left(\frac{\overline{R}}{\overline{S}}\right)}{\sqrt{V_R^2 + V_S^2}}$$

(2-15)

When R and S are functions of several underlying random variables or when the safety margin equation is not linear, the evaluation of the reliability index β becomes more complicated [33,103]. The approximate nature of Equation (2-15) notwithstanding, several previous studies have shown that Equation (2-15) is sufficiently accurate to produce reliability index values very close to those obtained using FORM algorithms and Monte Carlo Simulations when analyzing the reliability of short to medium span bridges [119]. As observed from this short introduction, evaluating the reliability of bridges requires probabilistic models for all the random variables that control the safety of bridge structures. These can be assembled into three groups: Live loads, Permanent Loads, and Member Resistance.

2.1.7.2 *Live Load Reliability Model*

The factored nominal live load models used in the design and load capacity evaluation of bridges take the form of deterministic simplified formats that do not explicitly include all the parameters that control the effects of live loading on the bridge, nor do the models

explicitly reflect the random nature of the live load. A more realistic representation of live load effects on bridge members would take the form [104,119]:

$$LL_T = L_{max} \times L_{HS20} \times IM_{fact} \times \lambda_{max} \times \lambda_{site-to-site} \times \lambda_{data} \qquad (2\text{-}16)$$

Where LL_T = total live load effect on the bridge member or on the bridge system, L_{max}= maximum projected load due to the random trucks on the bridge presented in the function of the number of HS-20 equivalent trucks, L_{HS-20} is the load effect of the HS-20 truck used as the baseline for analysis, IM_{fac}= dynamic amplification factor of the total load effect, λ_{Lmax} is a variable that reflects the uncertainties in estimating the maximum load effect calculated using the live load projection methodology performed in this study, $\lambda_{site-to-site}$ is a variable representing the variation in the projected live load between data collected at different WIM sites, λ_{data} is a variable representing the effect of limitations in the approach taken to perform the live load simulation and the extreme value projection technique utilized.

The live load model presented in Equation (2-16) can be used to perform reliability calculations of bridge members or systems. Statistical data related to the random variables of Equation (2-16) are obtained from three sources: a) the analysis of large numbers of WIM data sets assembled from various parts of the state of Florida, b) the data used in NCHRP 368 during the calibration of the AASHTO LRFD as described in NCHRP 368 by Nowak [33], c) The analysis of large numbers of WIM data sets assembled from various parts of the US as described by Sivakumar and Ghosn [120] in the web-based report NCHRP 20-07 Task 285.

2.1.7.2.1 *Maximum Load Effects*

The analyses performed in this study have shown that the failure of fractured twin steel box girder bridges is dominated by loading in the lane closest to the fractured box when the deck slab reaches its limiting capacity, which restricts its ability to transfer the entire load to the other intact box girder. Therefore, the load simulations performed in this study provided projections for the expected maximum load effect in a single lane obtained based on projections of truck traffic data collected at a number of Florida weigh-in-motion (WIM) sites. The simulations have shown that generally speaking, the maximum moment on the 120-ft simply supported bridge approaches a normal distribution with a ratio between the simulated maximum moment as compared to the effect of the AASHTO HS-20 design truck that varies between 1.50 to 1.75 depending on the site and the projection period (Table 2-3). The simulations show that if one lane of traffic on a 120-ft (36.58 m) bridge shows an Average Daily Truck Traffic ADTT=1250 (thus a total ADTT=2500 on the plots presented in this study), the heaviest trucks on the bridge will produce an expected maximum two-year load effect equivalent to the effect of 1.66 times that of the AASHTO HS-20 truck. A five-year projection of the loads on a bridge whose ADTT=2000 will lead to a maximum moment effect equal to 1.76 times that of the HS-20 design truck.

The AASHTO Manual of Bridge Evaluation [5] was calibrated using projections assuming a rating period equal to 5 years, while as mentioned earlier, the inspection cycle is two years. Thus, for the purposes of this study, the results were compared when the variable L_{max} in Equation (2-16) will take the value of 1.76 for a five-year period to the value equal to 1.66 times the HS-20 for a period of two years. The variability in this estimated load

effect is on the average equal to 9%. Thus, λ_{Lmax} in Equation (2-16) is assumed to be a random variable with an average value equal to 1.0 and a COV=8%.

2.1.7.2.2 *Variability in Results of Simulations*

In addition to the expected maximum load effect from the simulation, the reliability analysis requires the consideration of the uncertainties in the maximum load estimate. These uncertainties are represented by the variables λ_{data} and $\lambda_{site\text{-}to\text{-}site}$. Previous sensitivity analyses such as those performed in NCHRP 683 by Sivakumar et al. [104] have indicated that λ_{data} can approximately have a COV on the order of 2% to 5%. These variabilities, for example, represent the differences obtained when comparing the data collected over different periods of time from the same site. A value of 5% is adopted in this study. Finally, the variability in the results between different data collection sites having the same ADTT but accounting for different truck weight histograms is represented by $\lambda_{site\text{-}to\text{-}site}$, which in NCHRP Report 20-07 Task 285 have shown variations in COV with a conservative estimate on the order of 20%, which is the value adopted in this study [120].

2.1.7.2.3 *Variability in Dynamic Amplification Factors*

The AASHTO LRFD [9] specifies that a nominal dynamic amplification IM=1.33 be used on the truck load effect to account for the increased stresses due to the vibrations of the bridge under moving loads. However, it has been well established that this value is a conservative upper bound. On the average, Nowak [33] indicates that heavily loaded trucks usually produce lower values of dynamic amplification (mean value of $IM_{fact} = 1.17$ and a COV of V_{IM}=9%) than the nominal value. For simultaneous crossings in multi-lanes, the average is IM_{fact}=1.10, and the COV is V_{IM}=5.5%.

2.1.7.3 *Permanent Load Model*

Following the approach adopted by Nowak [33], the total permanent load effect, *DL* is divided into the dead load of pre-fabricated members, DC_1, the dead load of cast-in-place members, DC_2, and the dead load of the wearing surface, *DW*, such that the mean total dead load is given by:

$$\overline{DL} = \overline{DC}_1 + \overline{DC}_2 + \overline{DW}$$

(2-17)

The standard deviation of the total dead load, σ_{DL}, is expressed as a function of the standard deviations of each dead load component:

$$\sigma_{DL} = \sqrt{\sigma_{DC_1}^2 + \sigma_{DC_1}^2 + \sigma_{DW}^2}$$

(2-18)

Following Nowak [33], the dead load effects are assumed to follow normal probability distribution where the mean values and the COV's of each dead load component are given as:

$$\overline{DC}_1 = 1.03DC_1 \qquad V_{DC_1} = 8\%$$

$$\overline{DC}_2 = 1.05DC_2 \qquad V_{DC_2} = 10\%$$

(2-19)

$$\overline{DW} = DW \qquad V_{DW} = 25\%$$

Where DC_1, DC_2, and *DW* are respectively the nominal values of the dead load of pre-fabricated members, cast-in-place members, and wearing surface.

The example bridge analyzed in this study has a cast-in-place concrete slab and composite steel box girders where the steel is pre-manufactured and the concrete is cast in place. Because the weight of the concrete dominates, a bias equal to 1.05 and a COV=10% are used for the effects of all permanent loads.

2.1.7.4 *Load Carrying Capacity Model*

The traditional methods used to calculate the moment and shear capacities of bridge members have been found to lead to conservative estimates of the actual capacities. The data used by Nowak [33] to account for the biases and the variability in the existing current member analysis methods assuming that the member capacities follow lognormal distributions are summarized as follows:

Bending capacity of composite steel beams; $\quad \bar{R} = 1.12 R_n \quad V_R = 10\%$

Bending of prestressed concrete beams; $\quad \bar{R} = 1.05 R_n \quad V_R = 7.5\% \quad$ (2-20)

Bending of reinforced concrete beams; $\quad \bar{R} = 1.14 R_n \quad V_R = 13\%$

The statistical parameters in Equation (2-20) are for structural member capacities in bending. There is very little data that provide probabilistic models for the variability and biases between actual bridge system capacities and those estimated using advanced finite element analyses. For the purposes of this study, it is assumed that the biases and COV's listed for composite steel members are also valid for steel box girder bridges. Therefore, a bias equal to 1.12 and COV equal to 10% are adopted for the box girders to illustrate the proposed reliability analysis methodology assuming that the mode of failure is related to exceeding the bending capacity of composite members. For the analysis of the failure of the concrete slab in bending, a bias equal to 1.14 and a COV=13% are adopted.

2.1.7.5 *Reliability Analysis of the Twin Steel Box Girder Bridge*

Based on the finite element analysis and available experimental results, as well as work by others, it is inferred that the failure after fracture of one girder can be either; a) flexural failure of the deck or b) failure of the intact girder. Therefore, a reliability analysis was performed for these two failure mechanisms. It is noted that none of the results from the

analysis of actual bridges or experimental investigations have indicated the failure of the intact girder before the failure of the deck. Nevertheless, this is a possible failure mode when the bridge girders may have deteriorated over time or when the deck is so overdesigned that it could resist very high loads.

While the main box girders of the bridge in its intact configuration are expected to safely carry the applied maximum single-lane and two-lane loadings, the question that arises is whether a box girder bridge will be able to safely withstand the total loads should one of the box girders fracture. To perform the reliability analysis, the load distribution observed from the finite element analysis performed in this study was used. The finite element analysis performed for the 120-ft simply supported bridge shows that if one of the two boxes is fractured, the remaining intact girder is expected to carry a significant portion of loads that were originally carried by the fractured girder.

To verify that a bridge whose members are designed to satisfy the current AASHTO strength limit state will be able to sustain the maximum live load expected on the bridge during a 5-year service period, a reliability analysis was conducted assuming that the box girders were designed to exactly satisfy the AASHTO strength limit state. The analysis is performed for a 5-year load because a fractured bridge must survive in its damaged configuration for a period of time until the fracture is detected and corrective actions are undertaken. The five-year period is consistent with the rating period used for the AASHTO LRFR calibration [120,121]. The calculations are also repeated for a two-year service period, which would be consistent with the two-year biennial inspection cycle.

When studying the loads on the bridge system, the maximum live load is obtained using the live load modeling procedure performed in this study. The maximum live loads for

different projections are shown in Table 2-3 in terms of HS-20 equivalents. For one-lane loading on the 120-ft simple span bridge, the expected maximum moment will be equivalent to 1.74 HS-20 trucks for a 5-year service period assuming an ADTT=2000 trucks per day, which is equivalent to an ADTT=10,000 as set in Table 2-3. The calculations also show that the expected maximum live load will be associated with a COV for λ_{Lmax}=9%. A variation in the estimate with a COV λ_{data}=5% is also used as recommended by Sivakumar et al. [104] to reflect variations in the expected maximum load associated with the load projection method and the number of data points used to perform the projection. Also, based on previous work by Sivakumar et al. [104], who studied a large number of WIM data sites, it is estimated that the variations due to changes in the WIM data can be associated with $\lambda_{site-to-site}$ on the order of 20%. Furthermore, the dynamic load allowance has an average value $\overline{IM}_{fact}$=1.17 and a COV of V_{IM}=9% for individual truck crossings based on Nowak [33].

The WIM data from Florida was not analyzed for multiple lane loading. Therefore, in this analysis, it was assumed that the observations regarding the relation between one lane and two-lane loadings during the calibration of the AASHTO specifications are valid. Nowak [33] found that when two lanes of the bridge are loaded, each lane will carry 0.85 of the maximum expected load projected for a single lane loading. The 0.85 factor accounts for the lower probability of having two very heavy trucks side-by-side on the bridge as compared to having a single heavy truck. Also, Nowak [33] uses a mean dynamic allowance for two-lane loading equal to 1.10 with a COV=5.5%. The lower mean dynamic amplification for two lanes is due to the lower probability that trucks moving

simultaneously in multiple lanes will have their maximum dynamic components occur at the same instant of time.

The analysis of the fractured bridge considering the failure of the intact girder was performed, assuming that the load distribution follows the nonlinear FE analysis conducted in this study. Table 2-31 gives the LRFR Inventory Rating Factors required for the box girder members to ensure that the bridge will be able to sustain the fracture of one box girder and yet be able to support sufficient live loading over a two-year or a 5-year service period until the damage is detected and necessary rehabilitation actions are undertaken. In this case, an Inventory Rating on the order of R.F.=1.00 is required to meet a target reliability index β_{target} on the order of 1.25. A target $\beta_{target} = 2.50$ would require an inventory rating on the order of 1.34 to 1.38.

The bridge analyzed in this study has an LRFR Inventory Rating of R.F.=2.05. Thus, the intact box girder is capable of sustaining a significant level of live loads as well as a large proportion of the dead loads that were originally carried by the fractured girder, and that the bridge failure is expected to be due to the failure of the deck as explained earlier. It should be noted that in simple span steel bridges, service limit states are normally the governing design limit states, and the strength LRFR Inventory Rating is considerably greater than one and on the same order of magnitude as observed for the bridge considered in this study.

Simplified reliability analysis of the deck is also performed to estimate the minimum criteria that the deck should satisfy in order to ensure that it will be able to transfer a minimum level of the load from the fractured box girder to the intact box. The calculations

are performed assuming that the load-carrying capacity of the deck is modeled using the yield line analysis approach proposed in this study.

Table 2-31. LRFR inventory rating factors for the fractured bridge to meet different target reliabilities.

Target Reliability index, β_{target}	R.F. Inventory Rating for 5-year service life	R.F. Inventory Rating for 2-year service life
3.50	1.74	1.69
3.00	1.55	1.51
2.50	1.38	1.34
2.25	1.30	1.27
2.00	1.23	1.19
1.75	1.15	1.12
1.50	1.08	1.05
1.25	1.01	0.98
1.00	0.95	0.92

In these reliability calculations, the yield line pattern was adopted for the Florida C5 load rating truck. This truck is selected because semi-trailer trucks are known to represent the vast majority of trucks on US highways. It is herein assumed that the maximum 5-year truck load and the maximum 2-year truck load are due to trucks having the C5 truck configuration.

The analysis of the capacity of the yield line to carry the applied load is based on the moment capacity of the reinforced concrete deck. No statistical data is currently available on the moment capacity of concrete decks. Therefore, in this analysis, the bias and COV used by Nowak [33] during the calibration of the AASHTO LRFD specifications were adopted, which for Bending of reinforced concrete beams have a mean value $\overline{R} = 1.14R_n$ and a COV $V_R = 13\%$.

Table 2-32 gives the different live load factors necessary to achieve different reliability levels for the deck. Results for both a five-year rating period and a two-year bridge inspection cycle are given. To achieve the target reliability, in addition to applying the

recommended live load factor, γ_{LL} given in Table 2-32, the yield line analysis implies the application of a dynamic amplification factor IM=1.33, a dead load factor γ_{DL}=1.25 and a moment resistance factor for the concrete deck equal to ϕ=0.9.

The analysis of the bridge deck studied in this paper indicates that the bridge deck in its current configuration and specified concrete strength, and ignoring the possible contribution of the railings to help carry some of the load, will fail at a live load factor γ_{LL}=1.71. This indicates that its reliability index is on the order of β=2.0 for a five-year service period, or slightly higher than that for a two-year service period.

Table 2-32. Live load factors for deck analysis necessary to meet different target reliabilities

Target Reliability index	5-year live load factor, γ_{LL}	2-year live load factor, γ_{LL}
3.50	2.69	2.61
3.00	2.32	2.26
2.50	2.00	1.94
2.25	1.85	1.79
2.00	1.71	1.65
1.50	1.44	1.39
1.00	1.21	1.16

2.2   Health Monitoring of Steel Box Girder Bridges

The reliability analysis presented in the previous section demonstrated that even simple-span TSBG bridges might have significant reserve capacity after a fracture of one girder in full depth. Therefore, this presents a great opportunity for a rapid and effective damage detection to spot the initiation and progression of the damage before it forces the bridge closure and causes irreparable damage. This section investigates the dynamic and static behavior of twin steel box girder bridges after various damage scenarios and develops a non-contact bridge monitoring technique for fracture critical elements based on the bridge dynamic responses.

To achieve the objective of this section, the simple span bridge for which the results of experimental load testing were available and the continuous three-span twin steel box girder bridge were selected. For the latter, a series of field tests were conducted to study the feasibility of using non-contact sensors to capture the bridge dynamic response during bridge normal operation. Also, detailed finite element models of the bridges were developed and validated using the field test and available experimental test results. To address cost, traffic interruption, and safety issues associated with conventional inspection, the bridge dynamic responses after various damage scenarios were studied to develop a new non-contact bridge monitoring technique to detect the damage type, severity, and location along the bridge.

2.2.1 Field Test

The natural frequencies of the continuous span bridge were captured using a laser vibrometer to investigate the feasibility of utilizing non-contact sensors for bridge health monitoring and validating the finite element model of the bridge. A laser vibrometer was stationed under the bridge without traffic interruption to the bridge itself and the roadway below without a need for direct access to the bridge. The bridge vibration at the middle of the second (longest) span was recorded under normal traffic passing the bridge, as shown in Figure 2-88 and Figure 2-89. The frequency spectra of the bridge were obtained using Fast Fourier Transform (FFT) and are shown in Figure 2-89(b). Based on the result, the main bridge natural frequencies were obtained as 1.15, 1.54, 2.17, and 2.42 Hz. The first three mode shapes in this bridge correspond to the vertical bending, and mode 4 corresponds to the torsional mode shape of the bridge. The amplitude of bending mode shapes excited by traffic at the middle of Span 2 is maximum which is captured using the

laser vibrometer. Nevertheless, it is difficult to distinguish the torsional modes due to their

low amplitudes.

Figure 2-88. Field test using a laser vibrometer on the three-span continuous bridge.

(a)

(b)
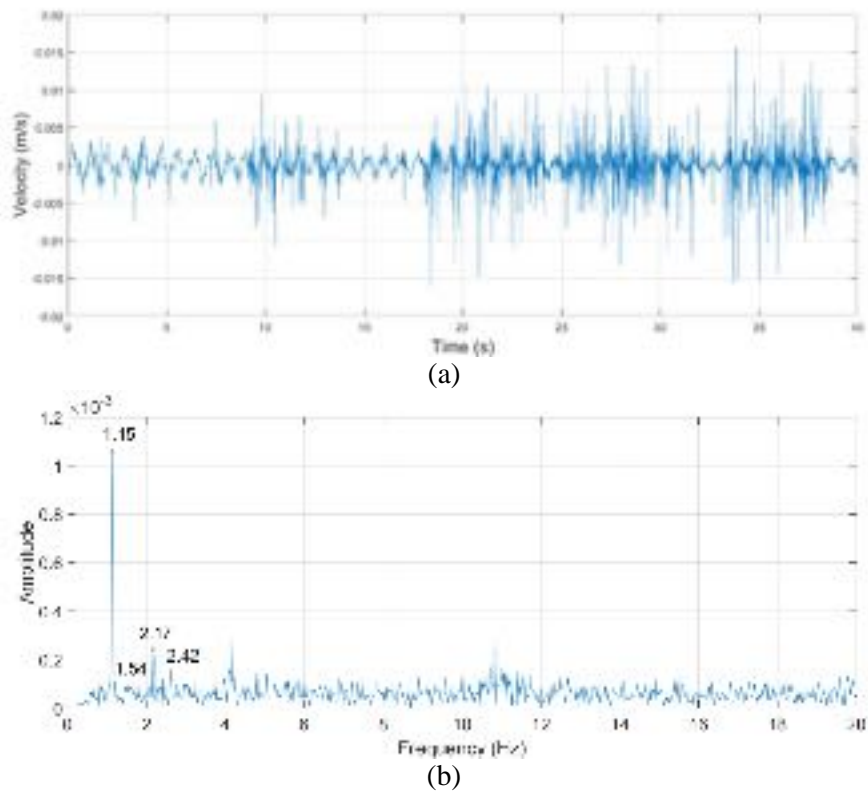
Figure 2-89. Bridge vibration; (a) Time series, (b) Frequency spectrum.

2.2.2 Model Dynamic Validation

The dynamic results of the experimental tests by the University of Texas at Austin and the dynamic bridge field test in this study were used to validate the FE models for single and continuous span bridges. Figure 2-90 shows the longitudinal strain as a function of time at the centerline of the bottom flange of the intact girder at a location 6 ft. away from the middle of the simple span bridge. This dynamic strain response was obtained during the second bridge test of the University of Texas at Austin [21]. In this test, 83% of one of the girders was cut, and concrete blocks representing 76,000 lb design truck were placed on the deck over the fractured girder. The bridge natural frequency from the dynamic strain response was obtained as 1.72 Hz for the damaged bridge. To validate the dynamic behavior of the simple span bridge model, the second test of the University of Texas at Austin was simulated, considering the mass of concrete blocks and the main bridge natural frequency was calibrated using the test result as 1.72 Hz. The bridge natural frequencies obtained from the field test also were used to validate the continuous span bridge model (Table 2-33). The results show that the models can predict the bridge dynamic behavior and natural frequencies.
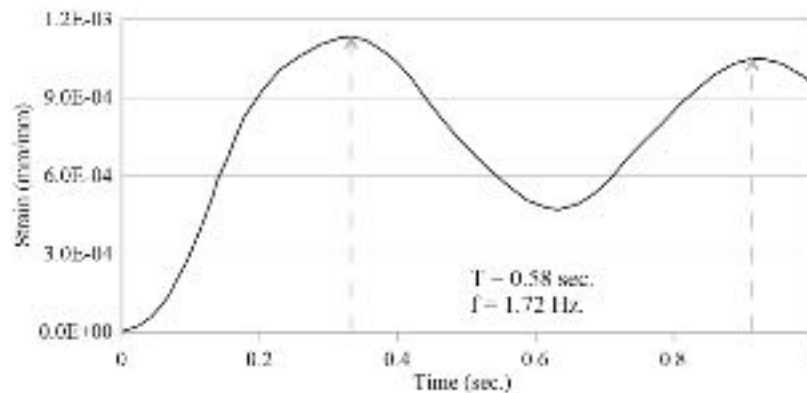
Figure 2-90. Dynamic strain response for the simple span bridge *[21]*.

Table 2-33. FE model validation for the continuous span bridge.

	Frequency (Hz)			
	Mode 1	Mode 2	Mode 3	Mode 4
Field Test	1.15	1.54	2.17	2.42
FEM	1.15	1.53	2.15	2.43

2.2.3 Bridge Dynamic Responses for Different Damage Scenarios

The validated finite element models were used to investigate the simple and continuous span bridge dynamic behavior after various damage scenarios, including bottom flange, partial and full–depth fracture of one of the girders at the middle of each span, and the failure of the vertical bracing connecting two girders near the middle of spans. Figure 2-91 illustrates the damage scenarios investigated in this study. For each damage scenario, the bridge natural frequencies and mode shapes were obtained from the detailed finite element models and compared to the bridge's intact condition. To simulate the girder fracture in the FE models, tie connections between two sides of the girders were removed. The full-depth girder fracture in the middle of the span is considered the worst-case scenario (major structural damage) where the deck, intact girder, and vertical bracing are the only elements transferring the dead and live loads over the fractured girder to the supports. In the bracing failure scenario, connections of the bracing elements to the steel girders near the middle of the span were removed to simulate minor damage to the structural system. The partial-depth fracture scenario where half of the girder is fractured was considered to study the bridge behavior before the progress of damage leads to the full-depth fracture.

Note that some damage in steel bridges may not cause permanent deformation in the deck, and their effects are not significant enough to be detected by untrained inspectors. Moreover, major damage in large structures (continuous span bridges) may not be noticed by the public between inspection periods. Therefore, affordable and accurate damage

144

detection methods are required for these bridges to detect damage at an early stage in between inspection periods.
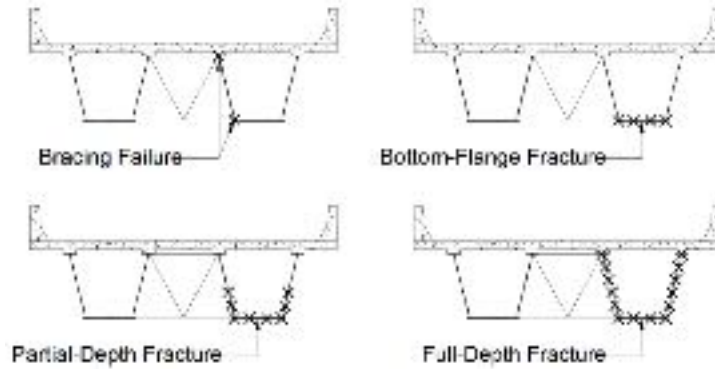
Figure 2-91. Damage scenarios.

2.2.4 Damage Detection Theory

The method presented here is designed to yield information on the location and severity of damage directly from measured changes in modal characteristics of the bridges. The modal characteristics of interest here are natural frequencies and mode shapes.

2.2.4.1 Frequency-Based Damage Detection

The change in the bridge natural frequency of mode i ($\delta\omega_i$) due to local damage is a function (f) of the reduction in bridge stiffness (δK), and the position vector (r) showing the damage location across the bridge. Thus [122]

$$\delta\omega_i = f(\delta K, r) \tag{2-21}$$

For the intact bridge, the stiffness parameters would be zero ($\delta K = 0$); however, for the damaged bridge, depending on the severity of the damage, this parameter will not be zero. To expand Equation (2-21) about the intact condition, a first-order Taylor series expansion is used for linearizing by neglecting higher-order terms

$$\delta\omega_i \approx f(0,r) + \delta K\, S\,(0,r) + \text{higher-order terms} \tag{2-22}$$

145

$$S_i = \partial f / \partial(\delta K) \tag{2-23}$$

Since there is no frequency changes without damage, $f(0,r) = 0$ for all r. Therefore,

$$\delta\omega_i \approx \delta K \, S_i \, (r) \tag{2-24}$$

Similarly, for the mode j

$$\delta\omega_j \approx \delta K \, S_j \, (r) \tag{2-25}$$

Thus, provided that the change in stiffness is independent of the bridge frequency [74],

$$\delta\omega_i / \delta\omega_j = S_i(r)/S_j(r) = h(r) \tag{2-26}$$

Equation (2-26) shows that the ratio of frequency changes in two modes is a function of the damage location.

2.2.4.2 *Mode-Shape-Based Damage Detection*

Assuming an Euler-Bernoulli beam model because the bridges consist of two box girders, the modal sensitivity (i.e., the fraction of modal energy) of mode i and element j between two locations $(x_j, x_j+\Delta x_j)$ can be computed by [123]:

$$F_{ij} = \int_{x_j}^{x_j+\Delta x_j} EI\{\phi_i''(x)\}^2 dx/K_i; \quad K_i = \int_0^L EI\{\phi_i''(x)\}^2 dx; \tag{2-27}$$

$$K_{ij} = K_j \int_j EI\{\phi_i''(x)\}^2 dx \tag{2-28}$$

Where E is the elastic modulus, I is the second moment of area, L is the bridge span length, and $\phi_i(x)$ is the *i*th mode shape function.

For the damaged bridge $(F_{ij}{}^*)$

$$F_{ij}{}^* = F_{ij} + \delta F_{ij} \tag{2-29}$$

The term δF_{ij} represents the variation of the fraction of modal energy at the *j*th member and for the *i*th mode.

On differentiating Equation (2-29), the quantity δF_{ij} is given by:

$$\delta F_{ij} = K_{ij}/K_i \left[\delta K_{ij}/K_{ij} - \delta K_i/K_i \right] \tag{2-30}$$

Equation (2-29) can be further simplified by assuming $K_i \gg K_{ij}$:

$$\delta F_{ij} \cong \delta K_{ij}/K_i \tag{2-31}$$

Assuming the bridge is damaged in ND multiple locations, $\delta K_{ij}/K_i$ can be approximated by the fractional change in the ith eigenvalue due to damage by [124]:

$$g_i = \delta K_{ij}/K_i \cong 1/ND \, (\delta \omega_i^2/\omega_i^2) \tag{2-32}$$

Kim et al. [74] provide a more detailed explanation and discussion of this approximation. It is necessary to obtain the changes in the bridge natural frequencies and mode shapes compared to the intact condition, which can be obtained by periodic bridge monitoring using the proposed laser-based method. In this study, a finite element model was used to simulate various damage scenarios at different locations along the bridge with different severity to compute the changes in the natural frequencies and mode shapes.

2.2.5   Results and Discussion

2.2.5.1   Bridge Dynamic Characteristics

Table 2-34 summarizes the first four bridge natural frequencies of the simple-span twin steel box bridge for different damage scenarios. For this bridge, modes 1 and 4 correspond to the bridge vertical bending, mode 2 is the bridge torsional bending, and mode 3 relates to the bridge horizontal bending, as shown in Figure 2-92. Note that the FE model was validated using the bridge frequency of 1.72 Hz obtained from the experimental test result of the bridge with a nearly full-depth fracture loaded using concrete blocks. The mass of the concrete blocks decreases the bridge natural frequency compared to the frequency of 1.87 Hz for the full-depth fracture scenario extracted from the FE model.

Table 2-34. Bridge natural frequency changes for different damage scenarios for the single-span bridge.

Mode	Frequency (Hz)				
	Intact Condition	Bracing Failure	Bottom-Flange Fracture	Partial-Depth Fracture	Full-Depth Fracture
1	2.34	2.34	2.32	2.11	1.87
2	6.64	6.57	6.63	6.53	6.43
3	7.55	7.55	7.55	7.53	7.50
4	8.11	8.11	8.11	8.10	8.09

The results show that minor damage to the structural system, such as a failure of the vertical bracing or the bottom-flange fracture of one girder, has a negligible effect on the bridge dynamic responses. In this case, the failure of the vertical bracing connections near the middle of the span decreases the torsional frequency (Mode 2) by only 1.1%, and the bottom-flange fracture decreases the first bending mode (Mode 1) by 0.9%. Nevertheless, major structural damage, in this case, the partial or full-depth fracture of one girder, could significantly change the bridge natural frequencies. The FE results indicate that both torsional and bending bridge frequencies were decreased after such damage due to a noticeable change in the bridge stiffness. For this bridge, the first bending mode was decreased by 9.8% and 20.1% after the partial and full-depth girder fracture, respectively, which could be captured using the laser vibrometer investigated in this study. Note that Mode 4 is not sensitive to damage at the middle of the span where the vibration amplitude is zero, as shown in Table 2-34. Nevertheless, this mode is indicative for all other locations through the bridge.

Mode 1   Mode 2

Mode 3   Mode 4
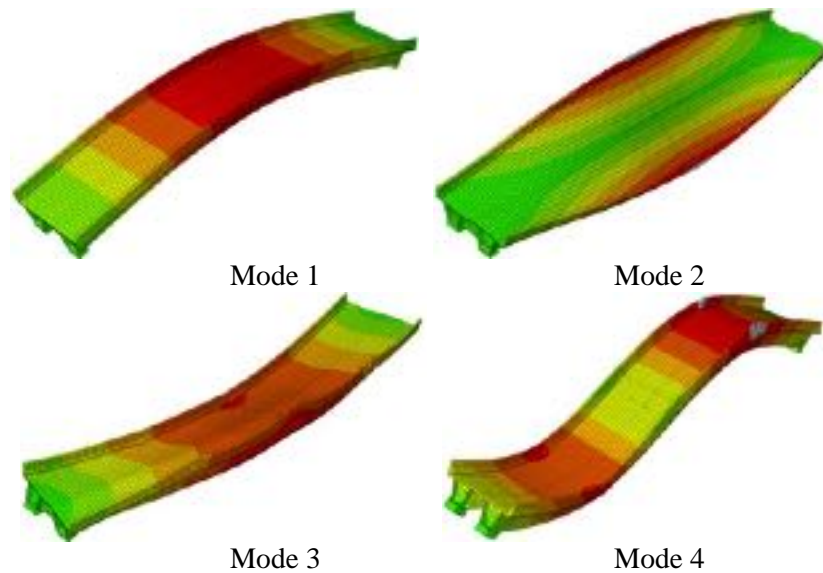
Figure 2-92. The first four mode shapes of the intact simple span bridge.

The results of the bridge frequencies after various damage scenarios for the continuous span bridge are shown in Table 2-35. This table compares the first five bridge frequencies after damage in each span. The first three modes in this bridge correspond to the vertical bridge bending and modes 4 and 5 are related to the torsional bending of Span 1 and Span 3, respectively. The results show that a bracing failure (minor damage) decreases the torsional stiffness of the bridge at that span. Consequently, the bridge natural frequency corresponds to the torsional bending of the span will be decreased. The effect of partial or full-depth girder fracture in the continuous span bridge is less than the single-span bridge since all the spans contribute to the bridge bending and torsional modes, and damage in one of the spans has less effect on the bridge dynamic behavior. For example, a full-depth fracture at Span 1 decreases the first and second frequency modes by 3.48% and 3.92%, respectively, compared to the simple span bridge that the same damage scenario decreases the bridge frequency by 20.1%. Note that the bottom flange fracture does not change the first five bridge frequencies; however, the effect of this damage can be seen in higher modes that are not presented in Table 2-35.

149

Table 2-35. Bridge natural frequency for different damage scenarios for the continuous span bridge

Mode	Intact	Span 1			Span 2			Span 3		
		Bracing Failure	Partial Fracture	Full Fracture	Bracing Failure	Partial Fracture	Full Fracture	Bracing Failure	Partial Fracture	Full Fracture
1	1.15	1.15	1.13	1.11	1.15	1.15	1.15	1.15	1.13	1.11
2	1.53	1.53	1.5	1.47	1.53	1.51	1.49	1.53	1.53	1.53
3	2.15	2.15	2.15	2.15	2.15	2.14	2.13	2.15	2.13	2.11
4	2.43	2.42	2.37	2.37	2.43	2.43	2.43	2.43	2.43	2.43
5	2.84	2.84	2.84	2.84	2.84	2.84	2.84	2.83	2.78	2.77

The header row above "Frequency (Hz)" spans all damage columns.

Table 2-36 shows the bridge frequency changes compared to the bridge intact condition for the bracing failure, partial and full-depth fracture scenarios investigated in this study. The results indicate a clear pattern in the frequency changes for each damage scenario. For example, the first mode corresponding to the vertical bending would change after severe damage in Span 1 and 3, while the second mode depends on the girder damage in Spans 1 and 2. A similar pattern can be seen for changes in Mode 3 that are related to Spans 2 and 3. The bracing failure would only change the torsional modes of the bridge (Modes 4 and 5) corresponding to that span. The severity of the girder damage (partial or full-depth fracture) can be identified by comparing the level of change in the corresponding bridge frequencies, e.g., the frequency changes in modes 1 and 2 after the partial-depth fracture of one girder in Span 1 is almost half of the changes due to the full-depth fracture, while the frequency changes in mode 4 corresponding to torsional bending is similar for both partial and full-depth fracture scenarios.

Table 2-36. Bridge natural frequency changes for different damage scenarios for the continuous span bridge.

Mode	Frequency Change (%)								
	Span 1			Span 2			Span 3		
	Bracing Failure	Partial Fracture	Full Fracture	Bracing Failure	Partial Fracture	Full Fracture	Bracing Failure	Partial Fracture	Full Fracture
1	0.00	1.74	3.48	0.00	0.00	0.00	0.00	1.74	3.48
2	0.00	1.96	3.92	0.00	1.31	2.61	0.00	0.00	0.00
3	0.00	0.00	0.00	0.00	0.47	0.93	0.00	0.93	1.86
4	0.41	2.47	2.47	0.00	0.00	0.00	0.00	0.00	0.00
5	0.00	0.00	0.00	0.00	0.00	0.00	0.35	2.11	2.46

Table 2-37 shows the ratio of frequency changes in two bending modes for major damage (i.e., partial or full-depth fracture) in the simple and continuous span bridges. It is observed that according to Equation (2-26), the ratio of corresponding frequency changes is a function of the damage location along the bridge. For example, the ratio of frequency changes in Mode 1 and 2 is equal for both partial and full-depth fracture scenarios at the middle of Span 1 of the continuous span bridge and differs from the damage at other locations showing that this ratio is the only function of the damage location. This pattern can be used to detect the damage type, severity, and location along the bridge. A supervised machine learning approach [86] can be utilized for continuous bridge monitoring using the bridge natural frequencies obtained from the non-contact laser-based approach introduced in this study to detect the severity and location of the possible damage in the bridge system based on the pattern of the frequency changes.

Table 2-37. The ratio of frequency changes in two modes for partial and full-depth fracture scenarios in the continuous span bridge.

	Continuous span bridge			Simple span bridge
	Span 1	Span 2	Span 3	
	$\delta\omega_1/\delta\omega_2$	$\delta\omega_2/\delta\omega_3$	$\delta\omega_1/\delta\omega_3$	$\delta\omega_1/\delta\omega_4$
Partial-Depth Fracture	0.7	2.0	1.0	24.6
Full-Depth Fracture	0.7	2.0	1.0	24.5

The most appealing feature associated with using changes in frequency for damage detection is that bridge natural frequencies are relatively simple to measure using the laser-based method proposed in this study. However, significant damage such as partial girder fracture may cause very small changes in natural frequencies, particularly in continuous span bridges, as shown in Table 2-36, and these damages may go undetected by being masked within the measurement resolution and accuracy. Moreover, variation in the mass of the bridge due to the traffic or measurement temperature could introduce uncertainties in the measured frequency changes. Nevertheless, this method could be used successfully for simple span bridges where the natural frequencies are sensitive to significant damage, as shown in Table 2-34.

2.2.5.2 *Bridge Mode Shapes*

To address difficulties with low sensitivity of vibration frequencies to damages, changes in mode shapes could be used as an alternative for damage detection. The appealing feature is that mode shapes are much sensitive to local damages when compared to natural frequencies. Nevertheless, extracting the bridge mode shapes requires sensors installed along the bridge, and the number of sensors and the choice of sensor coordinates may have a crucial effect on the accuracy of the damage detection procedure.

To investigate the changes in the mode shapes of the twin steel box girder bridges after various damage scenarios, bridge mode shapes of the simple and continuous span bridges were extracted from the FE models and compared to the intact condition. Figure 2-93 shows the first four mode shapes of the simple span bridge with a full-depth fracture at the middle of the span. The results indicate the changes in the first three mode shapes in the vicinity of the damage. For the continuous span bridge, the results show a significant

change in the mode shapes after a partial or full-depth fracture similar to the simple span

bridge. Figure 2-94 compares the mode shape changes due to a full-depth fracture at the

middle of Span 1 and 2.

Mode 1   Mode 2

Mode 3   Mode 4
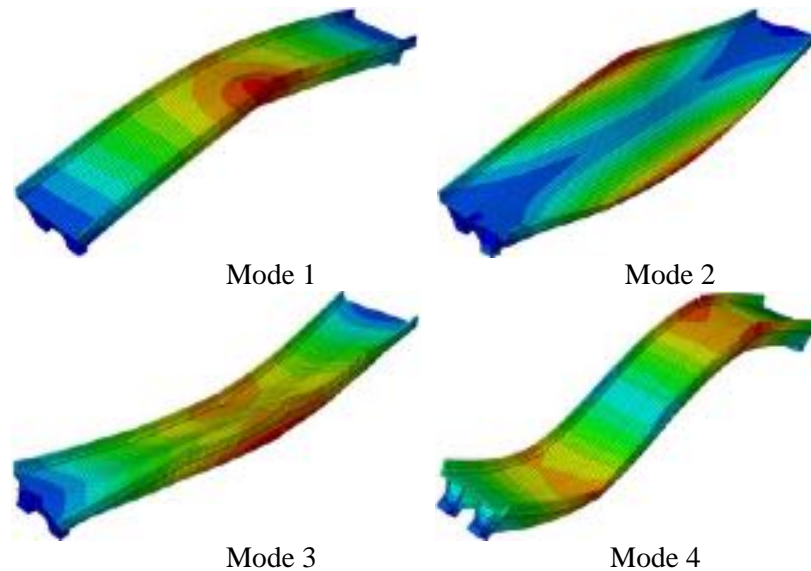
Figure 2-93. The first four mode shapes of the simple span bridge with a full-depth fracture at the
middle of the span with distinct changes at damage location.

The intact mode shapes of the simple and continuous span bridge were compared to the

post-damage mode shapes in Figures 2-95 to 2-97. Note from the figures that the amplitude

changes in the mode shapes are sensitive enough to detect damage at the inflicted locations.

These changes are more pronounced for a full or partial-depth fracture at the middle of the

span and less for minor damage such as bracing failure and bottom-flange fracture in the

simple span bridge. The results show that minor damage in a large bridge, e.g., continuous

span bridges, would not influence mode shapes of the lower modes that are usually

measured. These minor damage may influence the higher modes that are difficult to

measure using the sensors. Nevertheless, Figure 2-96 shows that the mode shapes are

sensitive enough to monitor the significant damage in the continuous steel girders

compared to the frequency changes that these damages may cause very small changes in

the bridge natural frequencies, as shown in Table 2-36. Figure 2-97 compares the first two mode shapes of the continuous span bridge in intact condition versus a full-depth fracture at the middle of each span. The comparison shows that damage at different locations along the bridge has different amplitude changes in the mode shape that could be used to localize the damage.

Mode 1: Intact Condition

Full-Depth Fracture

Mode 1: Full-Depth Fracture at Span 1

Mode 2: Intact Condition

Full-Depth Fracture

Mode 2: Full-Depth Fracture at Span 2
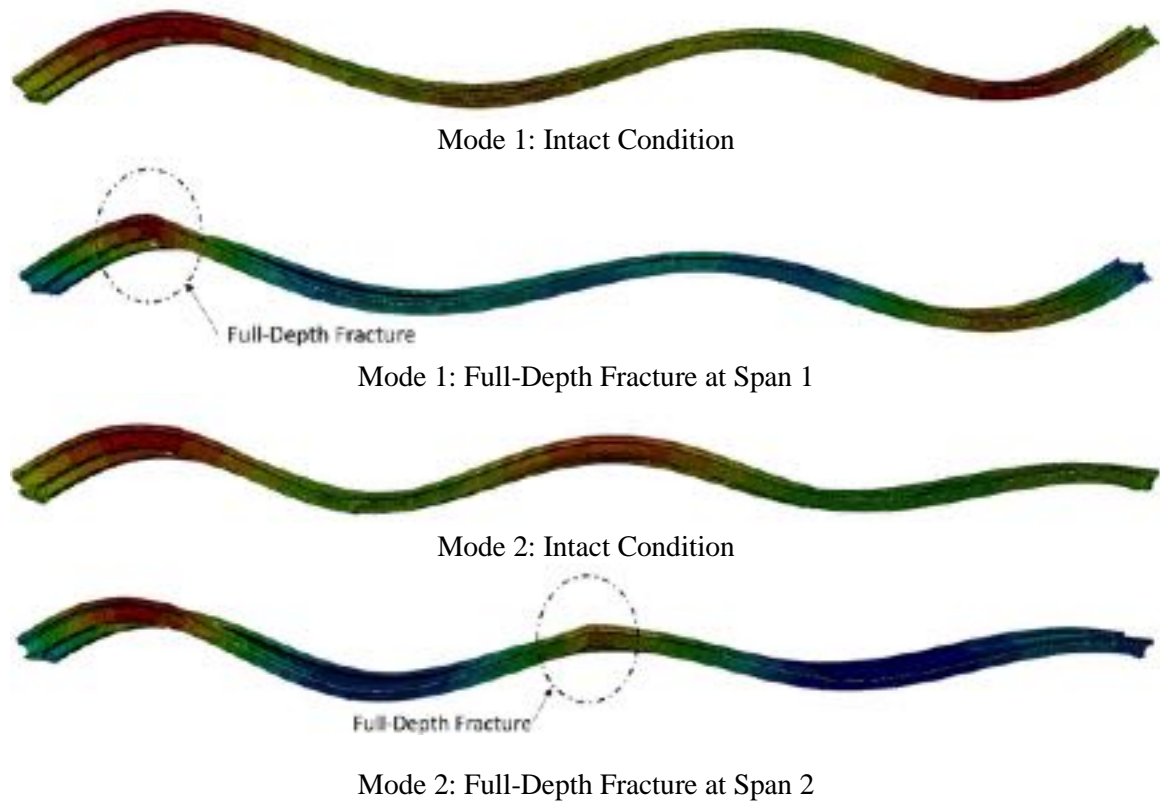
Figure 2-94. The changes in the mode shapes of the continuous span bridge.

(a)

(b)
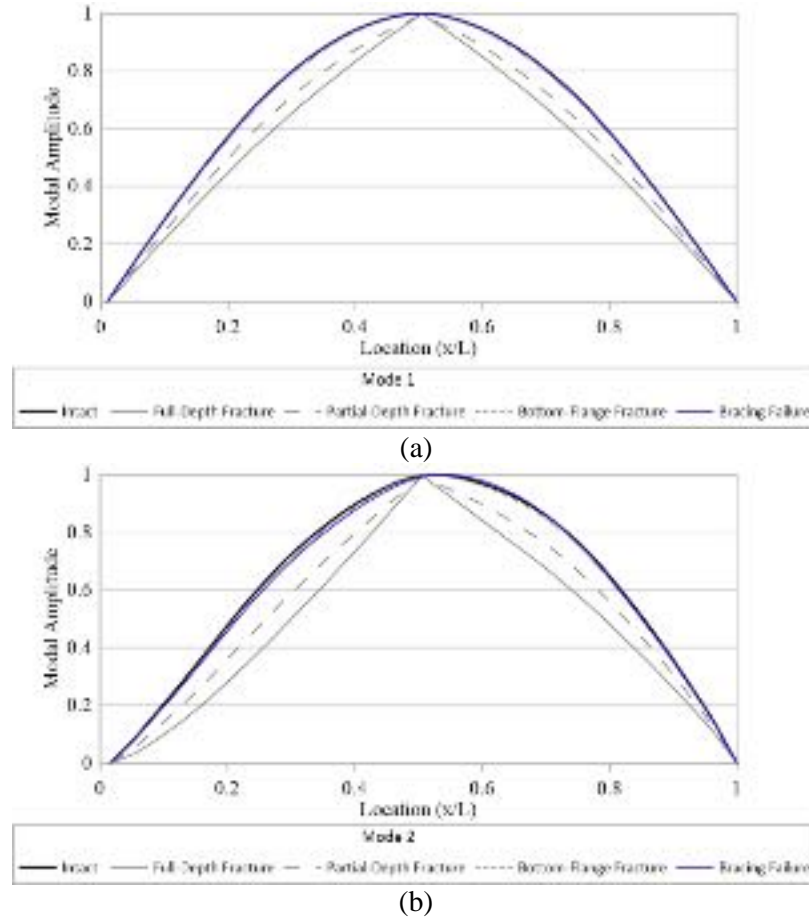
Figure 2-95. Comparison of mode shapes in the simple span bridge: Intact vs. damage scenarios; (a) Mode 1, (b) Mode 2.

The curvature $\phi_i''(x)$ of the mode shapes were generated for the first two bending modes of the simple span (i.e., Modes 1 and 4) and the first three modes of the continuous span bridges (i.e., Modes 1,2, and 3) via spline interpolation functions. Figure 2-98 and Figure 2-99 show the normalized modal sensitivity of the intact simple and continuous span bridges, respectively, using Equation (2-28) normalized by dividing it to $(\phi_{Max.}'')^2 EI$.
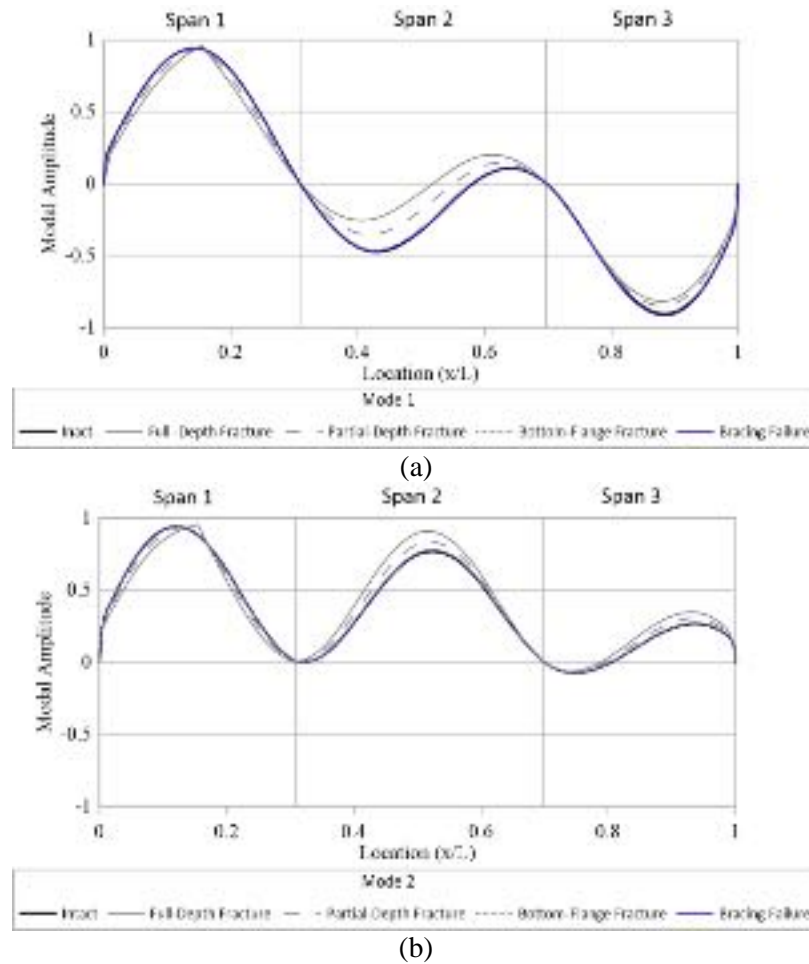
Figure 2-96. Comparison of mode shapes in the continuous span bridge: Intact vs. damage scenarios at Span 1; (a) Mode 1, (b) Mode 2.

It is observed that for the simple span bridge, the first mode is sensitive enough to monitor and localize damage near the middle of the span where the mode shape amplitude is maximum, and Mode 4 can be utilized for damage detection near the quarter-span. Therefore, either the individual modal sensitivities (Mode 1 or Mode 4) or the combined sensitivities (Mode 1+ Mode 4) are indicative for most locations throughout the span except for both ends of the simply supported bridge, as shown in Figure 2-98. Figure 2-99 indicates that in the continuous span bridge, the combination of the first three bending modes is indicative for all the locations through the bridge. The maximum sensitivity of

156

the combined modes is at the middle of Span 1 and 3 and at the middle supports, where

tension cracks may occur on the deck due to the negative moments.
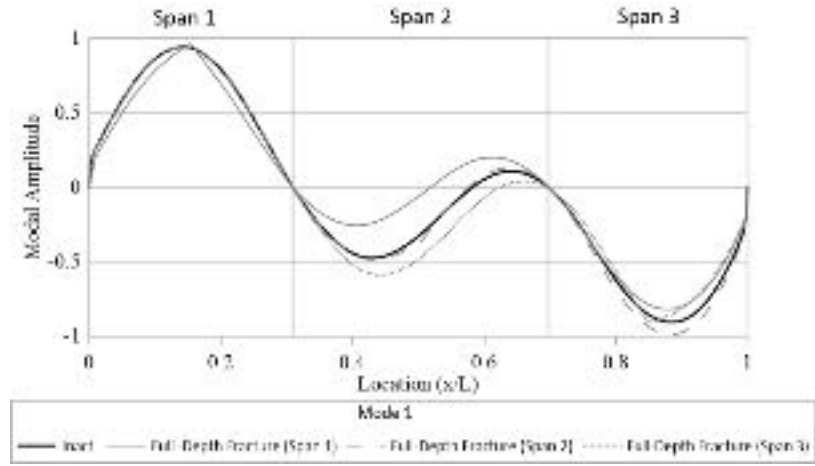
(a)
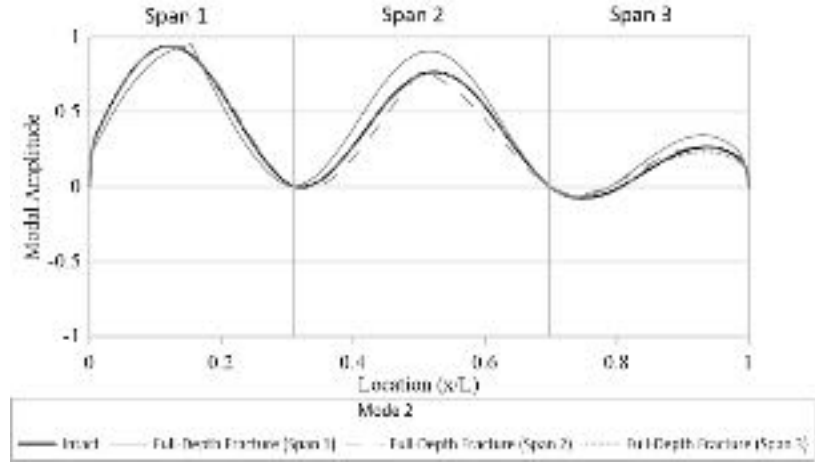
(b)

Figure 2-97. Comparison of mode shapes in the continuous span bridge: Intact vs. Full-depth fracture at the middle of each span; (a) Mode 1, (b) Mode 2.
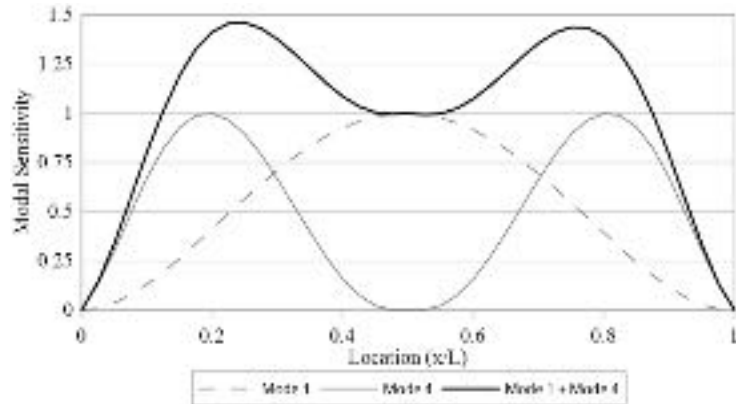
Figure 2-98. Modal sensitivities of the simple span bridge.
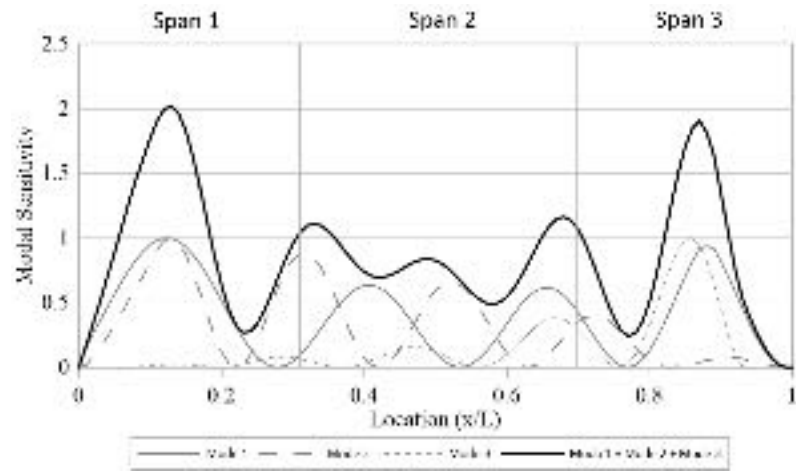
Figure 2-99. Modal sensitivities of the continuous span bridge.

CHAPTER 3   PREFABRICATED BRIDGE SYSTEMS

The purpose of this section was to investigate the performance of a box-beam bridge to understand its behavior after potential damage at the longitudinal joints. To this end, a series of static and dynamic load tests, FE analysis, and inspections were conducted on a bridge that had been in service for more than 50 years. A new analytical procedure has been developed to detect the location of the longitudinal joint damage and its relative significance in the bridge based on the measured changes in bridge dynamic and static response parameters and model updating methods. Although the case study here is a box-beam bridge, the results presented and the damage detection method and tool developed will be applicable to all bridges using modular girders with longitudinal closure joints, including decked steel and concrete girders, box girders, solid slab girders, etc.

Note: The bridge instrumentation and load testing were performed in collaboration with Dr. Antonio Nanni and his team from the University of Miami.

3.1   Bridge Description

The College Drive Bridge (CDB) located at the University of Miami campus was the subject of this study. This bridge is a simple span structure with an approximate length equal to 16.7 m (55 ft) that has been in service for more than 50 years (Figure 3-1). The bridge superstructure consists of 0.55 m (21.7 in.) deep by 1.2 m (48 in.) wide precast-prestressed concrete box beams supported on two abutments with pile foundations. The bridge section consists of a 6.3 m (20 ft 8 in.) vehicular travel lane with 95 mm (3.7 in.) asphalt overlay, and a 0.5 m (18 in.) wide raised curb, and a 3.4 m (11 ft 3 in.) raised sidewalk with a total width of 10.9 m (33 ft 6 in.) as shown in Figure 3-2. The bridge railing

consists of 100 mm (4 in.) thick architectural panels extending to the bottom of the concrete

deck connected to the bridge slab units using steel angles [125].

(a)   (b)

Figure 3-1. College Drive Bridge. (a) Top view; (b) Bottom view.
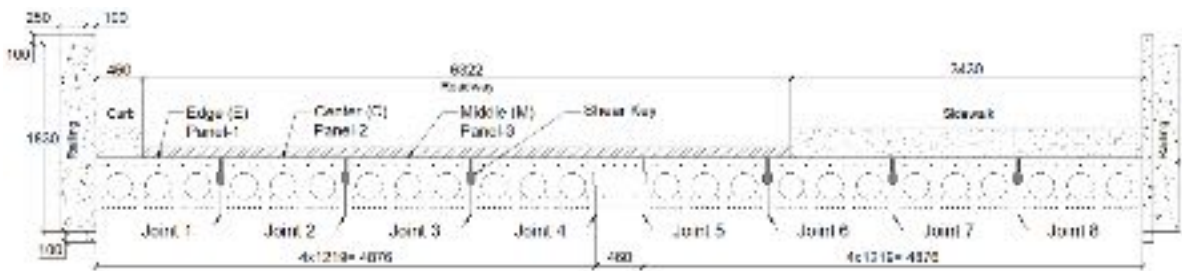
Figure 3-2. College Drive Bridge Section.

Since no design and construction records were available (the bridge is not included in the

United States National Bridge Inventory (NBI)), a series of site inspections were conducted

using non-destructive testing (NDT) such as ground-penetrating radar (GPR), as shown in

Figure 3-3. Given that historical information and site inspections were not sufficient to

confirm the type of cross-section of the slab units of the bridge, an excavation at the

adjacent twin pedestrian bridge was performed by the University of Miami team to expose

the end of the edge precast concrete slab unit. During this process, four core samples were

also extracted to evaluate the strength of the concrete, as illustrated in Figure 3-4. The twin

pedestrian bridge is identical to the CDB selected for this study.

<center>(a)   (b)</center>
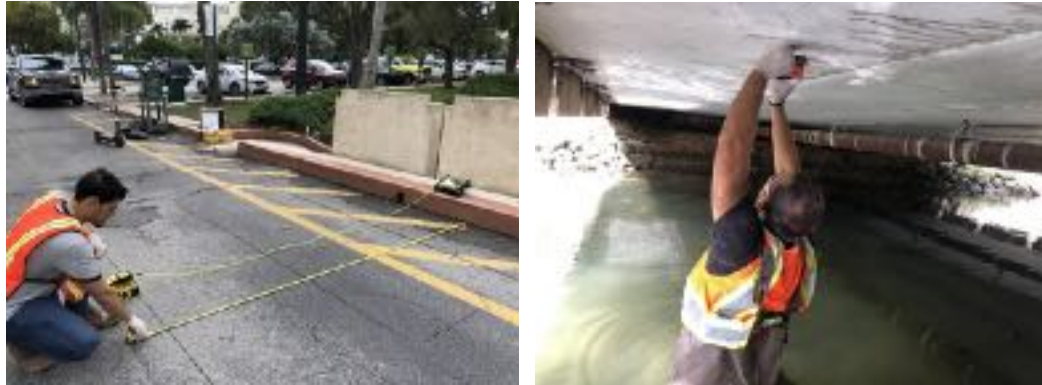
Figure 3-3. Use of NDT at the bridge as part of the preliminary evaluations; (a) Top of the deck, (b) Bottom of the deck.

The excavation allowed identification of the position, number and size of prestressing strands and reinforcing bars as well as the concrete strength. Based on this, it was possible to determine that the precast concrete slab is prestressed with three rows of 7-wire, 12.7 mm (0.5 in.) diameter strands, symmetrically positioned. The compression (top) row has 6 strands, while the tension (bottom) rows have 6 + 20. Figure 3-5 shows a photograph of the end of the exposed concrete slab and the drawing corresponding to the cross-section with details of reinforcement and dimensions. Since it was not possible to test strands and reinforcing bars to determine their mechanical characteristics, Grade 250 SR with the minimum tensile strengths of 1725 MPa (250 ksi) for strands and Grade 40 with the minimum yield strength of 275 MPa (40 ksi) for reinforcing bars are assumed for the analysis in this study based on the typical material properties at the time of the bridge construction [34]. For the prestressed slab unit, the average concrete compressive strength based on three sample cores tested according to ASTM C39 [126] was equal to 36.4 MPa (5.28 ksi).

<center>161</center>

Figure 3-4. Extraction of concrete cores from the end of the precast concrete slab; (a) Sample extraction; (b) Core samples.
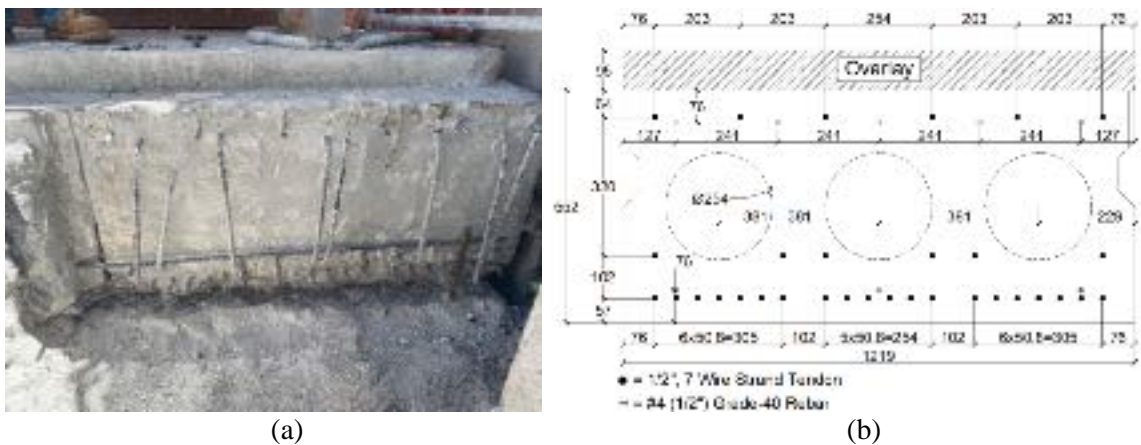
Figure 3-5. Cross-section of the exterior panel. (a) Excavation to the end face of the panel. (b) Cross-section detail.

3.2   Bridge Instrumentation and Load Testing

Vertical deflection of deck panels was recorded during the bridge diagnostic load test. Measurements were evaluated for the first three precast concrete slab units closest to the South edge of the bridge. These slab units were selected since they were directly under the truck wheels, which formed the roadway portion of the bridge. These slab units are considered most critical. Their monitoring also allows for the evaluation of shear transfer among them. The slab units, as represented in Figure 3-6, are herein identified as Panel-1 (Edge (E)), i.e., the panel on the South edge of the bridge with a 0.46 m curb on top of it; Panel-2 (center (C)), the panel next to the edge panel; and Panel-3 (Middle (M)) that is the panel next to the center panel in the middle of the roadway.

162

Three types of instruments were employed during the evaluation of the bridge diagnostic load test: i) Dial gauges; ii) Linear variable displacement transducers (LVDT), and iii) Total-station and its targets. Figure 3-6 and Figure 3-7show the relative location of the instruments.

- Dial Gauges (DGs): Six dial gauges with a travel length of 50 mm (2 in.) and a precision of 0.025 mm (0.001 in.) were used. Three gauges (DG1, DG2 and DG3) were positioned at the south-east end of the bridge mounted onto the vertical pile cap wall at the geometric center width of the concrete slab units under evaluation. The remaining three gauges (DG4, DG5 and DG6) were placed at the mid-span (center of the bridge) at the geometric center width of the concrete slab units under evaluation (Figure 3-7 (a))

- Linear Variable Displacement Transducers (LVDTs): Three high-accuracy direct voltage output displacement transducers were used with an overall travel length of 100 mm (4 in.) and a 0.2% linearity with a precision of 0.025 mm (0.001 in.). The LVDTs were placed at mid-span (center of the bridge) at the geometric center width of the three concrete slab units under evaluation (next to the corresponding DG).

- Total-Station: The Total-Station tracked and measured the position of five different targets (T1 to T5 in Figure 3-7 (b)). The targets were positioned in between the architectural parapet panels, mounted directly on the south side of Panel-1 (Edge (E)).
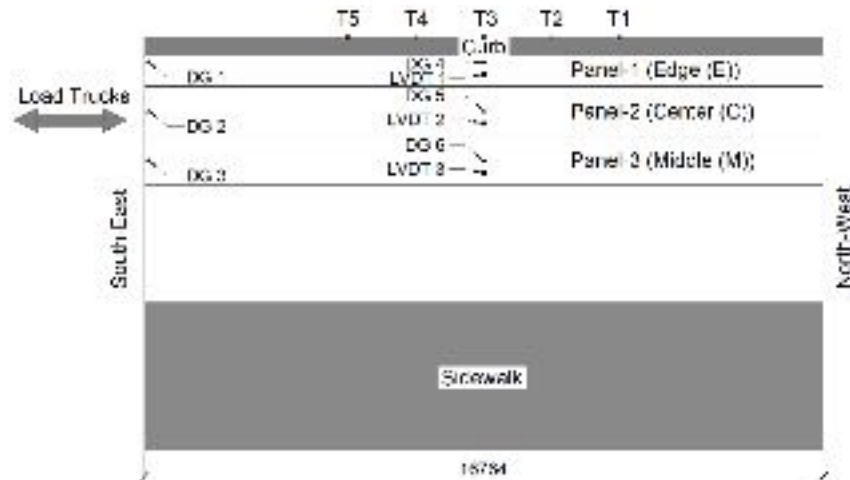
Figure 3-6. Position of instrumentation and targets used to measure displacements during and after the load test.

| (a) | (b) |

Figure 3-7. Installed instruments. (a) Dial gauges 4 to 6 and LVDTs 1 to 3; (b) Total-Station and targets T1 to T5.

3.2.1 Loading Procedure

Loading was applied by means of a three-axle dump truck with an additional (optional) drop axle, as depicted in Figure 3-8. Note that the wheels of the additional third rear-axle were never engaged during the load test. For the bridge investigated in this study made of 0.55 m (21.7 in.) thick precast prestressed panels, flexural strength and serviceability limit states are critical. Additionally, damage at longitudinal panel joints (i.e., the focus of this study) influences the flexural behavior and vertical displacement of the deck. Therefore, the shear strength limit state was not critical.

164
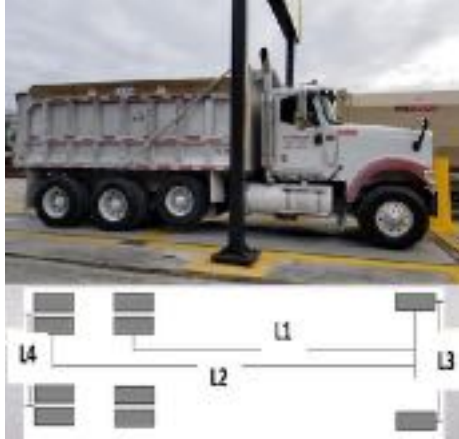
Figure 3-8. Truck dimensions' nomenclature. (See Table 3-1)

The truck weight was measured immediately prior to the load test in three different ways at a certified and accredited weigh station. The first weight measurement was the front (steer) axle only, the second was the rear (drive) double axle only, and the third was the total gross weight. Refer to Table 3-1, which reports the different weights as well as the geometrical dimensions of the truck for reference purposes.

The truck made four different passes driving across the bridge in both North/West and South/East bound directions; refer to Figure 3-9.

- Pass 1: the truck moved from South/East to North/West driving next to the curb, with one set of wheels directly on Panel-1.

- Pass 3: the truck moved from South/East to North/West with one set of wheels directly over mid-width on Panel-2.

- Passes 2 and 4 were the reverse of passes 1 and 3, respectively.

For each pass, three different stops were made on the bridge. Measurements of vertical deflection were then recorded with all instruments at each stop. Figure 3-10 shows a sketch of the stops relative to the bridge span; based on this, passes 1, 2 and 3,4 are mirror images of each other.

165

- Stop 1 was with the rear double axle just outside the bridge span, the remainder of the truck on the bridge.

- Stop 2 was with the rear double axle center at the mid-span for maximizing the positive moment (considered the worst load condition).

- Stop 3 with the front axle just outside the opposite side of the bridge span, and the remainder of the truck on the bridge.

Table 3-1. Trucks specifications.

Truck Weight (kg)			Truck Dimensions* (m)			
Steer Axle	Drive Axle	Gross Weight	L1	L2	L3	L4
8119	23197	31316	4.5	5.9	2.2	1.9

Note: *Refer to Figure 3-8 *for length reference (1.0 kg = 2.2 lb.; 1.0 m = 39.4 in.)*

(a)   (b)

Figure 3-9. Location of the truck on bridge relative to pass number, (a) Pass 1; (b)Pass 2.
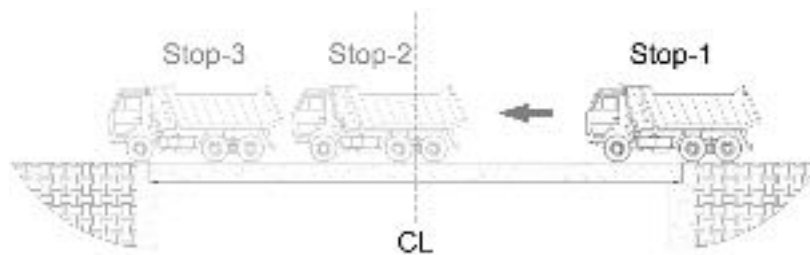
Figure 3-10. Truck stops relative to the bridge span.

166

3.2.2 Measured Bridge Response

3.2.2.1 Dial Gauges and LVDTs

Table 3-2 summarizes the results of the bridge load test. Note that Stop 2 in all the measurements corresponds to the worst-case scenario, as the center of the rear double axle was located at the bridge mid-span. The other stops provide additional information on the overall performance of the bridge.

Table 3-2. Summary results of net vertical deflections at mid-span

Instrument	Slab Unit	Pass-Stop Number- Deflection (mm)											
		11	12	13	21	22	23	31	32	33	41	42	43
LVDT	Panel-1	1.57	6.53	3.10	1.24	6.35	6.71	1.14	4.65	2.49	1.09	4.95	2.62
	Panel-2	1.35	6.45	2.84	1.14	6.73	6.27	1.02	5.21	2.54	1.12	5.21	2.74
	Panel-3	2.31	5.97	2.59	1.02	5.89	5.84	0.84	5.33	2.57	0.97	5.23	2.82
Dial Gauge	Panel-1	0.56	6.73	4.11	0.76	6.78	4.34	0.69	5.00	2.87	0.53	4.85	2.49
	Panel-2	0.58	6.65	4.09	0.76	6.60	3.78	0.69	5.46	3.15	0.69	5.28	2.67
	Panel-3	0.69	3.53	1.32	0.66	3.40	3.25	0.71	5.56	3.25	0.66	5.21	2.62

Note: 1.0 mm = 0.04 in.

Measurements prior to truck loading were taken in order to establish a zero benchmark (reference). Note that for each pass and stop, LVDT measurements started recording prior to the truck movement and continued to record for a minimum of 30 seconds after the truck had made a full stop as part of the data collection process.

The dial gauge measurements were used to further validate and confirm LVDT data, providing the vertical deflection at each point for each slab unit, pass, stop and truck loading. Also, dial gauges were used to record possible support settlements. Results from the LVDTs located at the mid-span of each slab unit under evaluation matched dial gauges. Figure 3-11 shows the panel deflection under the truck in passes 1 and 3. LVDTs recorded in real time the deflection of each slab unit while the truck moved from one position to the next; thus, providing additional information that can aid in the analysis of the bridge. Figure

3-12 shows a representative mid-span vertical displacement (for each slab unit) versus a

time graph for each stop during pass 4. It should be noted that LVDT 2 and 3 (Panel-2 and

Panel-3) recorded the highest level of deflection (green and red lines overlap).

The results of the bridge load test shown in Figure 3-11(a) clearly indicate that the

deflection of Panel-3, which is not directly loaded during truck Passes 1 and 3, is

significantly lower than those of the other two panels. This non-monolithic deflection

pattern could be attributed to the damage at the joints and non-composite action among the

panels. This inference is verified later in this study using the FE analysis. Moreover,

observation of existing reflective longitudinal cracks and leakage along the bridge joints

indicate the presence of damage at the joints.

(a)   (b)
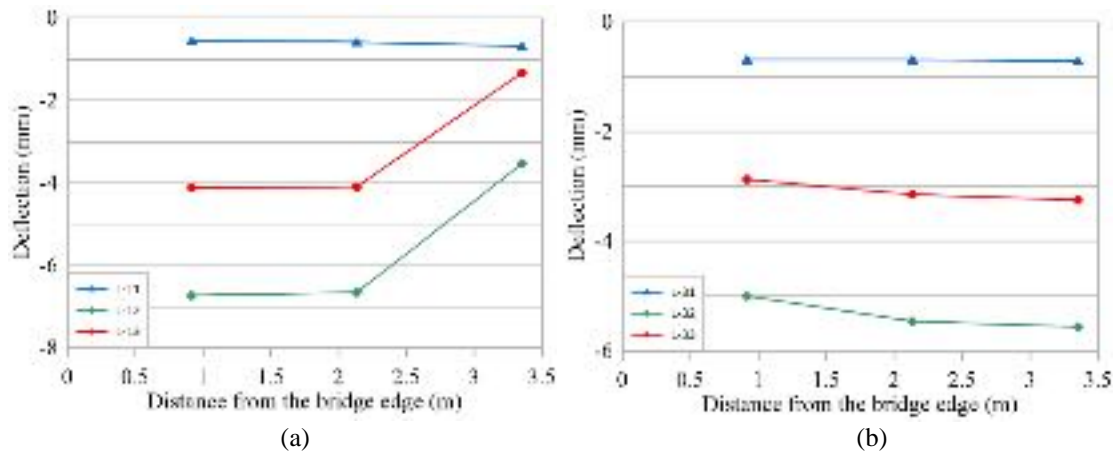
Figure 3-11. Dial Gauge displacement measurements for the three instrumented panels relative to
pass number, (a) Pass 1;(b) Pass 3. (1.0 mm = 0.04 in.).

168
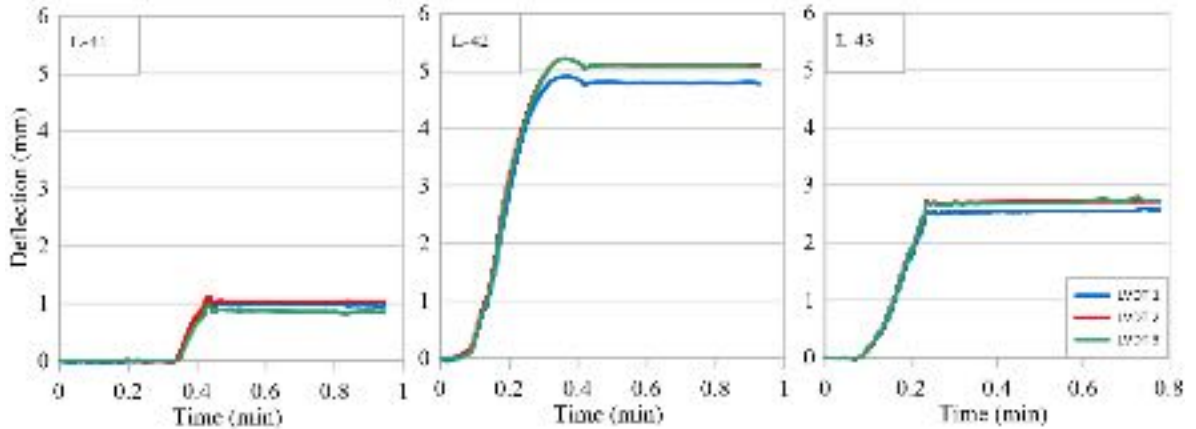
Figure 3-12. Representative vertical displacement versus time during the load test for pass 4-stop 1 (left), pass 4-stop 2 (middle), and pass 4-stop 3 (right). (1.0 mm = 0.04 in.).

The vertical deflections recorded by dial gauges DG 1 through DG 3 show a negligible support settlement under the heavy truck. The maximum deflection at mid-span is recorded as 6.78 mm equal to Span/2,500 at Panel-1 for Pass 2-Stop 2. In this load configuration, the truck was positioned next to the curb at the mid-span resulting in the maximum torsion and bending moments. It should be noted that the deflection limit for concrete bridges under vehicular and pedestrian loads is suggested as Span/1,000 by AASHTO LRFD [9], which is far greater than the bridge deflection recorded during the load test.

3.2.2.2 *Total-Station*

The Total Station was included as a supplemental instrument during the load test. The precision of the instrument was validated by comparison with the dial gauge and LVDT measurements. At each stop, every target position was measured ten times, and the average value was used to calculate the final position of each target and then used to compute the vertical deflections. Figure 3-13 shows the bridge deflection at the railing of Panel-1 subjected to the truck for passes 1 and 3. The results show the maximum deflection of 7.8 mm at the bridge railing for Pass 1-Stop 2. Since the bridge is subjected to eccentric loading, deflection at the edge of the bridge is more than that in the middle width of Panel-

169

1 due to torsional effects. The deflections recorded by the dial gauges and LVDTs for the same load configuration at the middle width of Panel-1 are 6.73 mm and 6.53 mm, respectively, which is expectedly lower than the Total-Station measurement. In this specific bridge, the deflections of individual panels were not recorded by the Total-Station due to the lack of direct view to individual panels. However, if individual panels are visible, the Total-Station could be a good alternative to other measuring sensors.

(a)

(b)
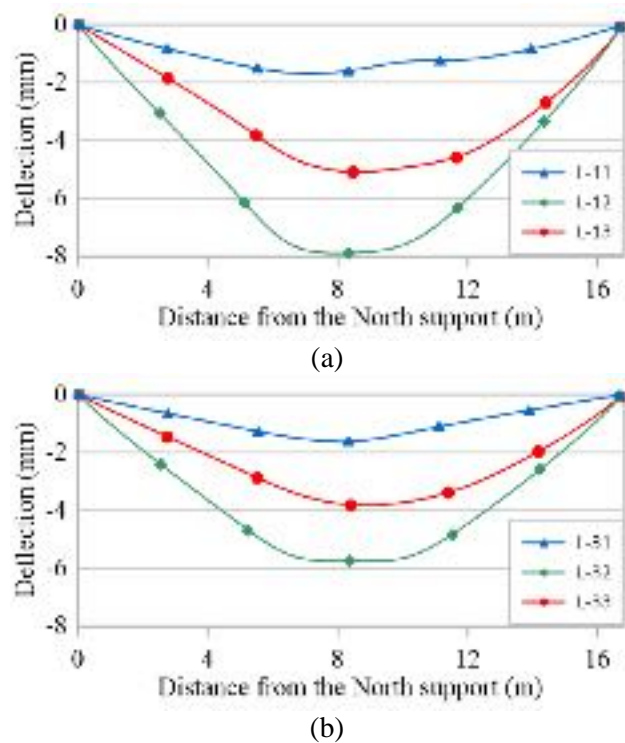
Figure 3-13. Total-Station bridge deflection measurements along the span relative to pass number, (a) Pass 1;(b) Pass 3. (1.0 mm = 0.04 in.)

3.2.3 Dynamic Load Test

To investigate the dynamic behavior of the bridge and provide the bridge modal frequencies for long-term monitoring, a series of dynamic tests were conducted on the bridge. A laser vibrometer, as shown in Figure 3-14, was simply stationed near the bridge with no need for direct access to the bridge. In addition, an accelerometer was located at mid-span over the curb. The bridge vibration at mid-span was captured under moving

170

traffic loading. Figure 3-15 shows the time history and frequency spectrum of bridge acceleration obtained from the dynamic test. Based on the results, the first three bridge frequencies were obtained as 3.53 Hz, 5.39 Hz and 8.18 Hz.

Figure 3-14. Laser vibrometer used for recording bridge vibration during the dynamic load test.

| (a) | (b) |
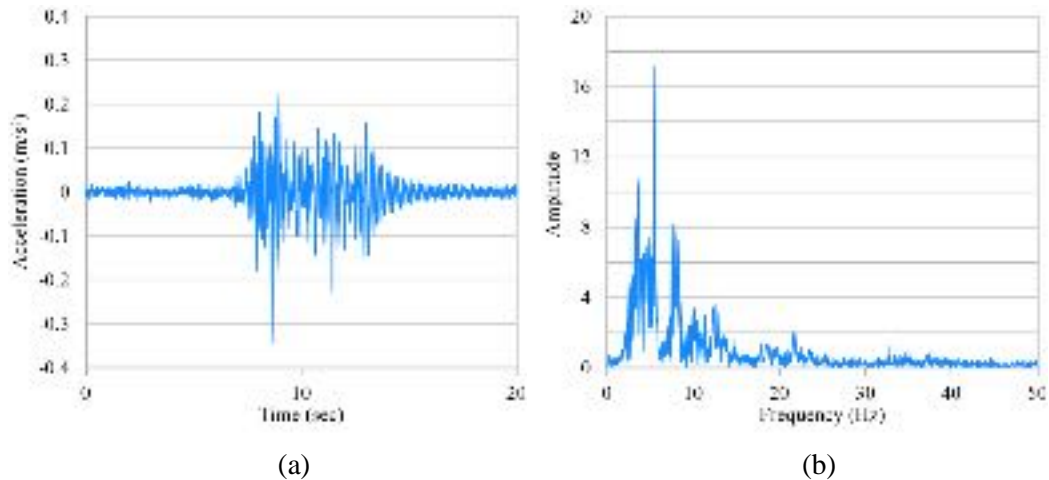
Figure 3-15. Bridge vibration subjected to truck loading, (a) Time history, (b) Frequency spectrum.

3.3 FE Modeling and Analysis

A detailed FE model was developed for the bridge superstructure in the environment of ABAQUS [108] with the objective of contributing to the analysis of the experimental results as well as investigating the behavior of the panel joints. In the FE analysis, steel reinforcement and strands were modeled using a multi-linear inelastic material with isotropic hardening in both tension and compression. The steel materials were specified as

Grade 250 SR with the minimum tensile strengths of 1725 MPa (250 ksi) for strands and Grade 40 with the minimum yield strength of 275 MPa (40 ksi) for reinforcing bars based on the typical material properties at the time of the bridge construction. The modulus of elasticity of reinforcing bars and strands were assumed to be 200,000 MPa (29,000 ksi) and 186,000 MPa (27,000 ksi), respectively, with a Poisson's ratio of 0.3. The initial prestress load for each strand was assumed to be 112 kN (25 kips) with a total prestress loss of 19 kN (4 kips) based on a lump sum estimation as per the Florida Department of Transportation (FDOT) Structures Design Standard [34]. Concrete strength of 31.8 MPa (4.5 ksi) was assigned to the sidewalk and curb, and the concrete strength of the slab units was assumed to be 36.4 MPa (5.3 ksi) as per the average strength of the core samples. For the initial concrete elastic behavior, the modulus of elasticity was calculated based on the ACI 318-14 [114] (for normal-weight concrete) and a Poisson ratio of 0.2 was used.

According to the behavior of each structural component, different element types can be selected to provide a realistic representation of the prestressed concrete bridge. For this study, eight-node linear brick elements were used for the concrete deck, whereas two-node linear 3-dimensional truss elements were used for the strands and the reinforcement embedded in the concrete slab units. The FE model of the bridge is shown in Figure 3-16. Visual inspection of the asphalt overlay surface and pedestrian concrete sidewalk shows reflective longitudinal cracks and leakage along the bridge that match the locations of the slab unit edges. Moreover, non-monolithic panel deflection in the load test (Figure 3-11) indicates joint damage that affected the bridge integrity. To this end, two models were developed to consider joint damage. In the first model, a perfect bond connection was assumed for the joints between adjacent slab units assuming no damage at the joints.

However, in the second model, longitudinal joints connecting adjacent slab units were modeled as elements with a different modulus of elasticity (stiffness) to simulate partial loss of shear transfer between the panels. In this model, based on the levels of joint damage, different stiffness can be assigned to each joint to simulate damaged joint behavior. Although each joint may have a different level of damage along the span, in this study, for simplicity, a single level of damage was assigned to each joint along the entire span.
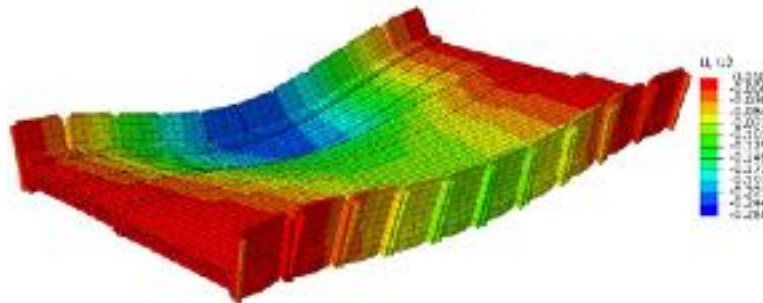
Figure 3-16. Finite Element Model of the college drive bridge. (Contour units are in inch)

3.3.1   First Model Without Considering Joint Damage

The FE model considering perfect shear transfer between panels was developed and analyzed for different truck loading configurations according to the load test. The results were compared to panel deflections measured using LVDTs. Moreover, frequency (modal) analysis was conducted on the bridge for the purpose of bridge long-term health monitoring through detection of changes in bridge natural frequencies due to damage. Structural damage in the bridge, like cracks and joint damage, would change the bridge dynamic characteristics and could be detected by monitoring the bridge modal frequencies over time. The first three natural modal frequencies of the bridge considering no joint damage were extracted from the modal analysis to be 3.82 Hz, 8.44 Hz and 14.7 Hz, as shown in Figure 3-17. Note that the first three mode shapes obtained from the FE analysis correspond

to the classical first three modes for a plate supported at two ends [127], and there are no additional modes between the modes extracted from the FE analysis.

(a)   (b)   (c)
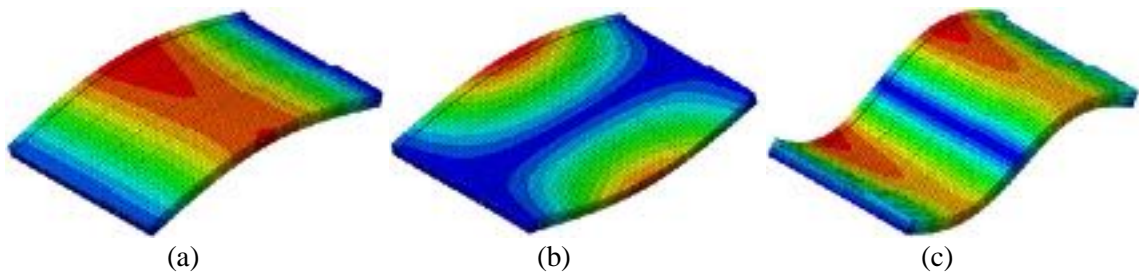
Figure 3-17. The first three mode shapes of the bridge in the first model. (considering no joint damage). (a) 3.82 Hz, (b) 8.44 Hz, (c) 14.70 Hz.

A comparison between the panel deflection obtained from load tests and FE analysis shows that the measured bridge deflection is much more than the model without considering joint damage (up to 60% for the loading configuration considered in this study), and the actual panel deflection is non-monolithic compared to the model where a perfect bond was modeled for the joints. Moreover, the first two modes extracted from the bridge dynamic field test using laser vibrometer were 3.5 Hz and 5.4 Hz. Nevertheless, the bridge modal analysis shows frequencies of 3.82 Hz and 8.44 Hz as the first two modes. It should be noted that modes one and three obtained from FE correspond to the bridge bending mode shapes. Since the bending stiffness of the panels are similar, and mode shapes do not require differential movements in adjacent panels, joint damage has virtually no effect on these two modes. These modes could have small frequency changes because of different stiffness of the sidewalk and curb, and other modeling approximations. However, the second mode corresponds to the torsional mode of the superstructure that is quite sensitive to the damage at the joints. These types of damage could decrease the bridge section torsional stiffness and consequently would decrease the second bridge natural frequency. As a result, the second natural frequency of 5.4 Hz obtained from the field test is another sign of considerable joint damage in the bridge superstructure.

3.3.2   Second Model Considering Joint Damage

Considerable panel joint damage can be inferred through observation of reflective longitudinal cracks and leakage along the bridge joints, non-monolithic panel deflection under heavy truck loading, and the frequency changes. Hence, the second FE model was developed in order to simulate the partial shear transfer between the panels due to the damage at the joints. In this model, panels were connected at joints with elements whose stiffness (modulus of elasticity) could be varied to indirectly simulate various levels of damage. Therefore, intact joints with no damage along the span were assigned a stiffness equal to that of the adjacent panels, and a completely deteriorated joint with no shear capacity was assigned zero stiffness. Using this method, different stiffness between zero and that of the panel can be assigned to each joint based on the level of damage at the joint, and a damage index (ΔD_{JOINT}) can be defined for each joint as Equation (3-1)[128].

$$\Delta D_{JOINT} = 1 - (E_{Damaged}/ E_{Intact}) \tag{3-1}$$

where for an intact joint $\Delta D_{JOINT} = 0$ and for a fully deteriorated joint $\Delta D_{JOINT} = 1$.

The purpose of this section is to find a unique set of damage indexes for the joints that result in a bridge deflection matching with the experimental load test for all the truck loading configurations. Although for each loading configuration, different sets of damage indexes could be found to match the panel deflection, a unique set of damage can be found which satisfies all the loading configurations. To this end, a new model updating method is developed to find the damage index for each joint in precast-prestressed concrete box-beam bridges. In this method, deflections of selected bridge panels are measured using a static load test, and a FE model of the bridge is used to compare the analytical responses and the bridge measured responses. The joint damage indexes are then updated until the

175

differences are minimized to a predefined threshold. It should be pointed out that if an initial response measurement were available for the bridge immediately after construction with supposedly undamaged joint conditions, then the comparison could be made between the current and the initial measurement. For the purpose of this study, and in the absence of initial measurements, the analytical responses from a calibrated FE model replaced the initial measurement.

3.4   Parameter Identification

From the structural analysis viewpoint, the joint damage indexes (here modeled as the level of stiffness change) can be updated/adapted such that structural response parameters (in this case, deflection of panels) obtained from analytical models for various loading configurations are predicted with acceptable accuracy. The solution will therefore involve the application of optimization methods. The identified changes in the panel deflections are used to determine whether or not there is any deterioration in the joints.

The basic force-displacement relationship for bridge panels at mid-span can be written as

$$[F]=[K][v] \tag{3-2}$$

Where F is the vector of applied forces, K is the stiffness matrix, and v is the vector of nodal displacement. The selected measured parameter may be panel deflection, strain, stress, or any other quantity of interest at mid-span (P). These measured parameters are related to nodal displacement by the following equation:

$$[P]=[B][v] \tag{3-3}$$

Where the transformation matrix B relates the response parameter to nodal displacement.

Since only some response parameters are measured through load tests, Equation. (3-2) is partitioned into measured [v_a] and unmeasured [v_b] response parameters:

$$\begin{bmatrix} f_a \\ f_b \end{bmatrix} = \begin{bmatrix} k_{aa} & k_{ab} \\ k_{ba} & k_{bb} \end{bmatrix} [v_a/v_b]$$ (3-4)

Equation (3-4) is reduced to Equation (3-5) by condensing out the unmeasured response parameters:

$$[f_a] = \left[[k_{aa}] - [k_{ab}][k_{bb}]^{-1}[k_{ba}]\right][v_a] + [k_{ab}][k_{bb}]^{-1}[f_b]$$ (3-5)

Matrices related to forces ([f_a] and [f_b]) and measured response parameters [v_a] can be obtained from the load test results, and the analytical stiffness matrices are functions of joints and panels stiffness (p) that depends on joint damage index. An error vector is defined as Equation (3-6) to identify the stiffness parameters [91]:

$$[E(p)] = \left[[k_{aa}] - [k_{ab}][k_{bb}]^{-1}[k_{ba}]\right][v_a] + [k_{ab}][k_{bb}]^{-1}[f_b] - [f_a]$$ (3-6)

For the intact bridge, the stiffness parameters (here, damage indexes) would be zero; however, for the damaged bridge, this parameter will not be zero. To adjust the stiffness parameter [p] in [E(p)], a first-order Taylor series expansion is used for linearizing the error matrix [E(p)] by neglecting higher-order terms and a scalar performance error function is defined as following [91]:

$$[E(p + \Delta p)] \approx [E_p] + [S_p][\Delta_p] + higher\ order\ terms$$ (3-7)

$$[S_p] = [\partial\{E(p)\}/\partial\{p\}]$$ (3-8)

$$J(p + \Delta p) = [E(p + \Delta p)]^T [E(p + \Delta p)]$$ (3-9)

By minimizing the Equation (3-9) with respect to the unknown parameters [p] [91].

$$\partial J(p + \Delta p)/\partial\{p\} = \{0\}$$ (3-10)

Equation (3-11) is derived from Equations (3-7 to 3-10) [91]

$$-[S_p] [\Delta p] = \{Ep\} \tag{3-11}$$

For the case of deck made of precast panels,

E(p) ~ changes in displacements due to change in joint stiffness

$[\Delta p] \approx [\Delta D_{Joint}]$= factor of damage indexes or change of stiffness of joints

$-[S_p] = C$ sensitivity matrix

Hence:

$$[C] \{\Delta D_{Joint}\} = \{E(p)\} \tag{3-12}$$

Sanayei and Saletnik [92,93] presented a similar parameter estimation method to identify the structural element stiffnesses and changes in cross-sectional properties for truss and frame structures using subsets of static applied forces and strain measurements and they provide more detail on the algorithms available for model updating. Equation (3-12) will be the basis of model updating used in this study.

3.4.1 *Implementation of The Damage Detection Procedure*

The detailed FE model considering eight joint elements connecting adjacent panels (see Figure 3-2) is used to calculate the sensitivity matrix C for a particular loading configuration. To do this, deflection of the panels at mid-span can be obtained from FE analysis for the intact bridge as a selected measured parameter (i = joint number from 1 to n, j = panel number for which midpoint displacement is measured from 1 to m). Then, by applying full damage (zero stiffness) to each joint (Joint j), while keeping the other joints intact, these deflections are recalculated at i points. The change of displacements at mid-span with one joint damaged compared to the intact bridge for all panels, will form the column j of the desired sensitivity matrix C (n×m) can be derived. Therefore, each column

of matrix C represents a pattern in state change associated with full damage ($\Delta D_{JOINT} = 1$) at a certain joint. The change of state in the bridge can be obtained through instrumentation and response monitoring of the structure compared to the intact condition. The monitoring can be conducted in a continuous manner by installing permanent measuring devices to monitor the bridge deflection under traffic passing by or can be carried out periodically using load test results. Having C and $\{E(p)\}$, the vector of damage indexes ΔD_{JOINT} can be calculated provided that the sensitivity matrix is non-singular.

3.4.2 Sources of Errors

In general, measurement errors in the bridge load test procedure could corrupt $\{E(p)\}$, resulting in a false ΔD_{JOINT}. To reduce random errors, more load cases can be performed during tests, or the same test should be repeated several times (average measurement), or more response parameters than unknown damage need to be recorded. Moreover, modeling approximations related to material properties, bridge geometry and boundary conditions always exist in developing a FE model of the bridge.

The damage detection method developed in this study for the case of longitudinal joints can be modified to also include other damage types. To accomplish this, the pattern of bridge response changes due to those damage types should be established and included in developing the C matrix. Damage sources other than those included in the C matrix could potentially result in an error in damage identification. Nevertheless, because not detected during inspection, the inclusion of other damage types for the case under consideration was not implemented.

3.4.3 Damage Detection Procedure for Deck Panel Joints

Based on the basic relationship introduced for this method, the number of damage indexes and measured response must be the same. However, if the number of response parameters is larger than the number of damage indexes, the problem is over-determinant. In this case, rather than directly solving Equation (3-12) for the unknown damage indexes, an optimization procedure can be utilized. The problem can be restated as an optimization problem to minimize the error. If the number of unknown (n) is larger than the number of response parameter (m), the problem is under-determinant and different load cases are required from the load testing (truck position) to derive the damage from the limited number of measurement; this case can also be restated as an optimization problem to find the best damage indexes matches different load cases.

To validate the proposed joint damage detection method, the results of the bridge load test are used for detecting possible damage in the joints. The bridge has eight longitudinal joints (unknown) connecting bridge panels. However, only the deflections of three panels were measured during the load test (measured response). Since the number of unknowns is larger than the measured responses (the problem is under-determinant) and errors related to measurements exist in the problem, two different loading configurations were used, and the problem was restated as an optimization problem to find the best damage indexes matching measured bridge responses.

The deflection of the panels at mid-span measured with LVDT was used as the bridge measured responses in this section. To this end, two different load cases of L-12 and L-42 corresponding to the worst-case scenario, with the center of the rear double axle at the bridge mid-span, were selected. Changes in the structural response of the three measured panels (LVDT results including random measurement errors) to the intact condition

obtained from the first FE model were determined and utilized as "measured responses"

for the two load cases as follow:

$$\Delta_{\text{MEASURED-L-12}}= \begin{bmatrix} -2.0 \\ -2.3 \\ -2.3 \end{bmatrix}, \Delta_{\text{MEASURED-L-42}}= \begin{bmatrix} -0.9 \\ -1.4 \\ -1.7 \end{bmatrix}$$

By combining these two matrices, Δ_{MEASURED} can be obtained as: $\Delta_{\text{MEASURED}}= \begin{bmatrix} -2.0 \\ -2.3 \\ -2.3 \\ -0.9 \\ -1.4 \\ -1.7 \end{bmatrix}$

The FE model was used to calculate the transformation matrix C for each of the load cases

(L-12 and L-42) by applying full damage to each joint while keeping other joints intact.

The results showed that the effect of damage at joints 7 and 8 are negligible in the

considered load cases (see Figure 3-2). Therefore, for simplicity, the effect of these two

joints was ignored. Here, as mentioned above, to obtain better accuracy for results, the

number of equations is increased from 3 to 6 by combining the results for two load cases.

For the combined C and Δ_{MEASURED}, the first three rows of the matrix correspond to L-12,

and the last three rows correspond to L-42 loading configuration. Hence, C and ΔD_{JOINT}

can be obtained as:

$$C= \begin{bmatrix} -6.4 & -3.0 & -5.0 & -3.2 & -2.7 & -1.8 \\ 1.2 & -3.5 & -5.4 & -3.5 & -3.0 & -1.9 \\ 1.1 & 0.9 & -5.9 & -3.8 & -3.2 & -2.1 \\ 3.4 & -2.7 & -2.2 & -3.4 & -2.9 & -1.9 \\ -1.2 & -3.3 & -2.6 & -3.8 & -3.2 & -2.1 \\ -0.9 & 0.7 & -3.1 & -4.2 & -3.5 & -2.3 \end{bmatrix}$$

The basic relationship can be introduced as $[C] \ [\Delta D_{\text{JOINT}}] = [\Delta_{\text{MEASURED}}]$

where $\Delta D_{\text{JOINT}} = \begin{bmatrix} d1 \\ d2 \\ d3 \\ d4 \\ d5 \\ d6 \end{bmatrix}$ corresponds to the damage of each joint (see Figure 3-2)

The basic relationship can be restated as an optimization problem:

$$[C] \, [\Delta D_{JOINT}] - [\Delta_{MEASURED}] = [M] = 0 \qquad (3\text{-}13)$$

The target function for this problem is to minimize $\Sigma(M_i)^2$ while $0 \leq d_i \leq 1$. Solving the

optimization problem results in damage indexes for each joint as follow: $\Delta D_{JOINT} = \begin{bmatrix} 0.01 \\ 0 \\ 0.31 \\ 0.15 \\ 0 \\ 0 \end{bmatrix}$

3.5   Results and Discussion

In the FE model, corresponding damage indexes obtained from the model updating were

assigned to the joints as a reduction in stiffness. The results are compared and validated in

the following sections.

3.5.1   *Comparison of Results and Validation of Damage Indexes*

Panel deflections at mid-span subjected to load cases L-12 and L4-2 for intact and damaged

bridge models were plotted and compared to the bridge responses measured through the

load test for the first three panels, as shown in Figure 3-18. The results show that the bridge

deflections predicted by the FE model considering damage in the joints agree well with the

actual bridge response under two different loading configurations.

In order to validate the damage indexes obtained from the proposed method, bridge

responses for other load cases obtained through the load test (L-21 and L-41) were

compared to the bridge deflection predicted by the FE model, as shown in Figure 3-19. The

results show that the model considering joint damage can predict the bridge response for

different loading configurations. Note that small deviations in these figures could be

attributed to errors in bridge response measurement, FE modeling, or ignoring other

sources of damage. In this study, for simplicity and proof of concept, an average damage index was assigned for each joint along the span. However, each joint may have different levels of damage along the span that could change bridge responses subjected to different load cases. Variation in damage level can also be introduced by assigning damage indexes to link elements connection panels along the span. The results prove that the proposed method not only can predict the damage location but also is able to predict the level of damage at each joint. The results can be interpreted such that joints 3 and 4 have lost 31% and 15% of their stiffness (proportional to their structural integrity) due to damage, respectively.
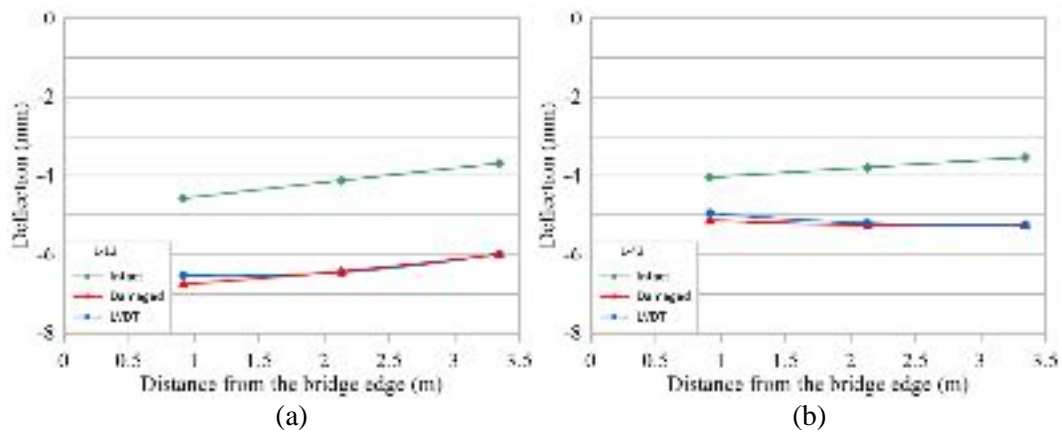
Figure 3-18. Finite Element Models (Intact and Damaged bridge models) to load test comparison for the truck at Stop 2; (a) Pass 1 (b) Pass 4. (1.0 mm = 0.04 in.)
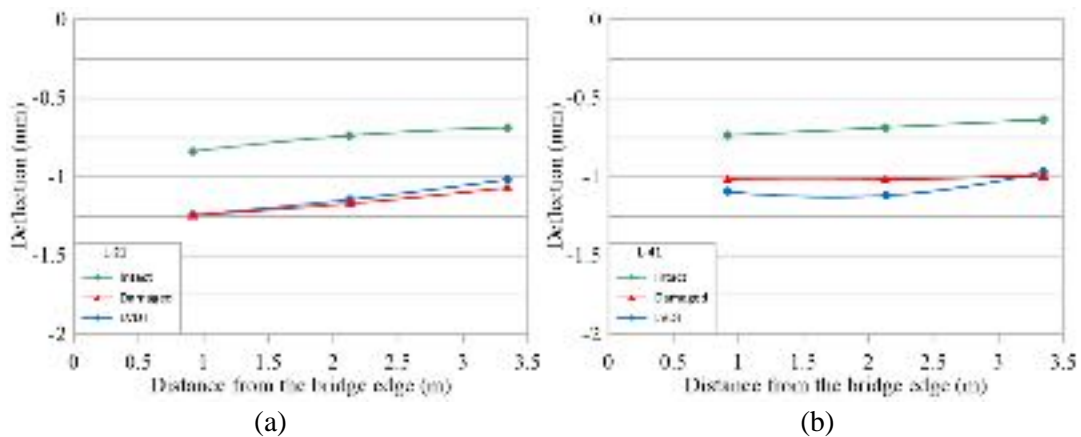
Figure 3-19. Finite Element Models (Intact and Damaged bridge models) to load test comparison for the truck at Stop 1; (a) Pass 1 (b) Pass 4. (1.0 mm = 0.04 in.)

3.5.2 Examination of Damage Indexes Using Dynamic Test Results

Three first bridge natural frequencies for the damaged bridge were extracted from the FE model as shown in Figure 3-20 to investigate the possibility of joint damage detection through changes in bridge dynamic characteristics. After the damage, the bridge first natural frequency (Figure 3-20(a)) decreased from 3.82 Hz to 3.76 Hz, as was expected; since all the panels have the same bending stiffness, joint damage has a negligible effect on the bending frequency (first mode) of the bridge. However, in the torsional mode of the bridge (second mode), longitudinal joints play an important role by transferring shear forces between adjacent panels, and possible damage at the joints could considerably change the bridge natural frequency by reducing the bridge torsional stiffness. The results indicate that after damage, the bridge torsional frequency (second mode) decreased from 8.44 Hz to 5.45 Hz (35% change in the frequency) and also, some new modes were formed due to the damage (Figure 3-20(c)).

Table 3-3 summarizes the bridge natural frequencies obtained from the FE models and the field measurements during the dynamic load test. According to the results, the first two bridge natural frequencies obtained through the field test (3.53 Hz and 5.39 Hz) were predicted by the damaged FE model that validates the accuracy of the proposed damage detection method. The third bridge natural frequency (8.18 Hz) can be referred to the second shape mode of the intact bridge when the truck has passed the bridge, and friction forces in the longitudinal joints can transfer full shear forces between panels due to the bridge free vibration. Therefore, the bridge natural frequencies obtained through the dynamic test agree better with the frequency obtained from the damaged model considering joint damage indexes obtained from the abovementioned analysis. Differences in the range

184

noted in Table 3-3 can be expected because of the approximations and error sources described above.

(a)   (b)   (c)
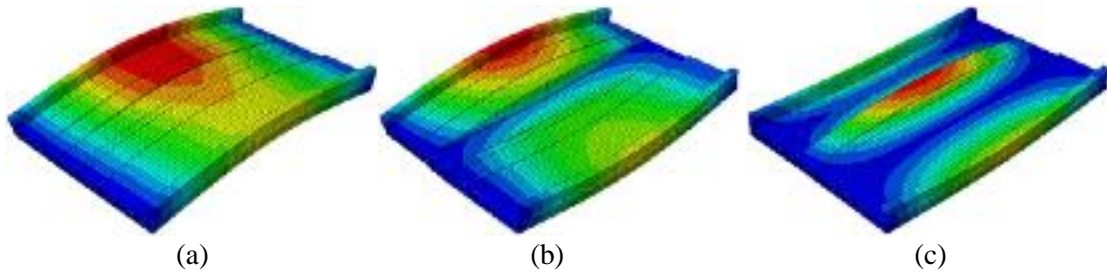
Figure 3-20. The first three mode shapes of the damaged bridge in the second model. (considering joint damage); (a) 3.76 Hz, (b) 5.45 Hz, (c) 12.31 Hz.

Table 3-3. Summary results of the bridge natural frequencies.

Bridge Condition	Bridge Natural Frequency (Hz)		
	First Mode	Second Mode	Third Mode
Intact Model	3.82	8.44	14.70
Damaged Model	3.76	5.45	12.31
Experimental Result	3.53	5.39	8.18

3.5.3 Live Load Distribution on the Panels

Mid-span longitudinal stress at the bottom of the bridge panels at the worst positions (L-12 and L42) obtained from finite element analysis are plotted in Figure 3-21. Load distribution comparison for the intact and damaged bridge.; (a) L-12, (b) L-42 (1.0 MPa = 0.145 ksi) to compare stress distribution over the panels for the intact and damaged bridge. The results show that in the intact bridge, stress varies gradually and almost linearly over the panels, and all the panels contribute to load-carrying capacity. However, the results show that the damage in the joints causing partial shear transfer between the panels demonstrates a highly non-linear curve over the bridge panels with minimal contribution from farther unloaded panels. The maximum bending stress of the damaged bridge under live load increases by 33% in both loading configurations compared to the intact bridge that shows a significant reduction in the bridge load-carrying capacity. Moreover, the

185

maximum bridge deflection increases by 63% and 45% for L-12 and L-42 truck loading, respectively (Figure 3-19).

When the truck load is combined with the dead load and prestressing, the results show that maximum tensile stress in the panels for the load configurations considered in this study reaches 0.7 MPa that is less than the tensile stress limit at service load.
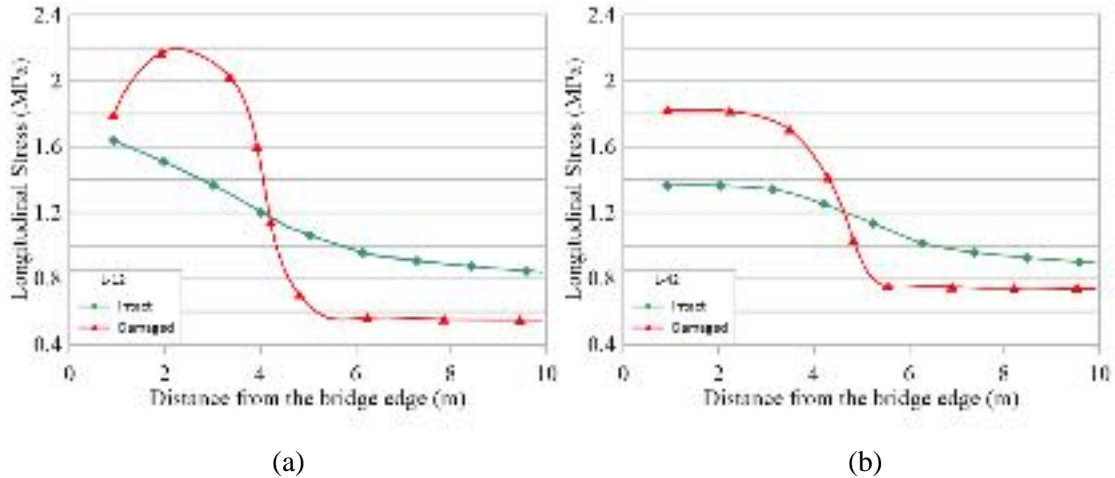
(a) (b)

Figure 3-21. Load distribution comparison for the intact and damaged bridge.; (a) L-12, (b) L-42
(1.0 MPa = 0.145 ksi)

3.6   Structural Joint Damage Detector Tool

Based on the mentioned theory in Section 3.4, a software tool was developed using MATLAB App Designer [129] to detect the location and severity of possible damages in the bridge joints, including superstructure and substructure joints. This tool relies on comparing bridge responses like deflection, strain, vibration, etc., to its initial undamaged responses subjected to the same static or dynamic loading configuration to identify the damages. In this tool, bridge configuration, measured changes in the bridge response, loading configurations, and joints sensitivity matrix is used as input parameters to detect the location of the joint damage and their relative significance in the bridge using optimization algorithms to consider the errors associated with modeling, measurement and ignoring other sources of damage (Figure 3-22). Additionally, this tool can detect damage

186

in joints and connections of any other structures other than bridges that use prefabricated elements. It can also detect damage at joints of conventional structures.

In this method, a detailed finite element model is used to calculate the sensitivity of joint damages in the bridge response parameters for a particular loading configuration, and the change of state in the bridge can be obtained through instrumentation and response monitoring of the structure compared to the intact condition. The monitoring can be conducted in a continuous manner by installing permanent measuring devices to monitor the bridge deflection under traffic passing by or can be carried out periodically using load test results. Then, the bridge response changes and joint damage sensitivity can be used as an input in the Structural Joint Damage Detector Tool to detect the location of the joint damage and their relative significance in the bridge. This tool can be connected to the installed sensors to get the structure measured responses automatically and detect damage in the joints. In the case of the dynamic responses, i.e., natural frequency and mode shapes, the tool can detect the damage in the joint using the normal traffic passing the bridge; however, for the case of using deflection, stress, or strain as the measured responses, a specific loading configuration is required to be performed periodically to detect the damage in the joint. Note that changes in the static responses are more sensitive to the joint damage compared to the dynamic responses, as explained in this study. This approach allows for more frequent and cost-effective methods of bridge performance monitoring, ensuring that structural issues are addressed at shorter intervals, a remarkable feat as it can detect potential failures leading to collapse long before an incident arises.
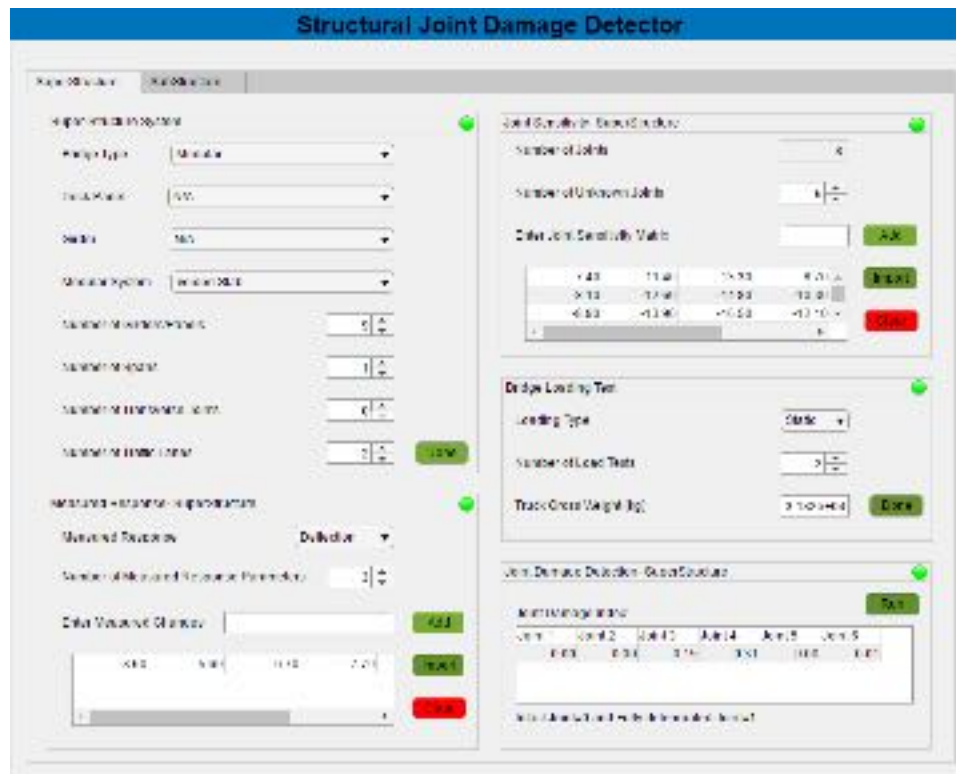
(a)
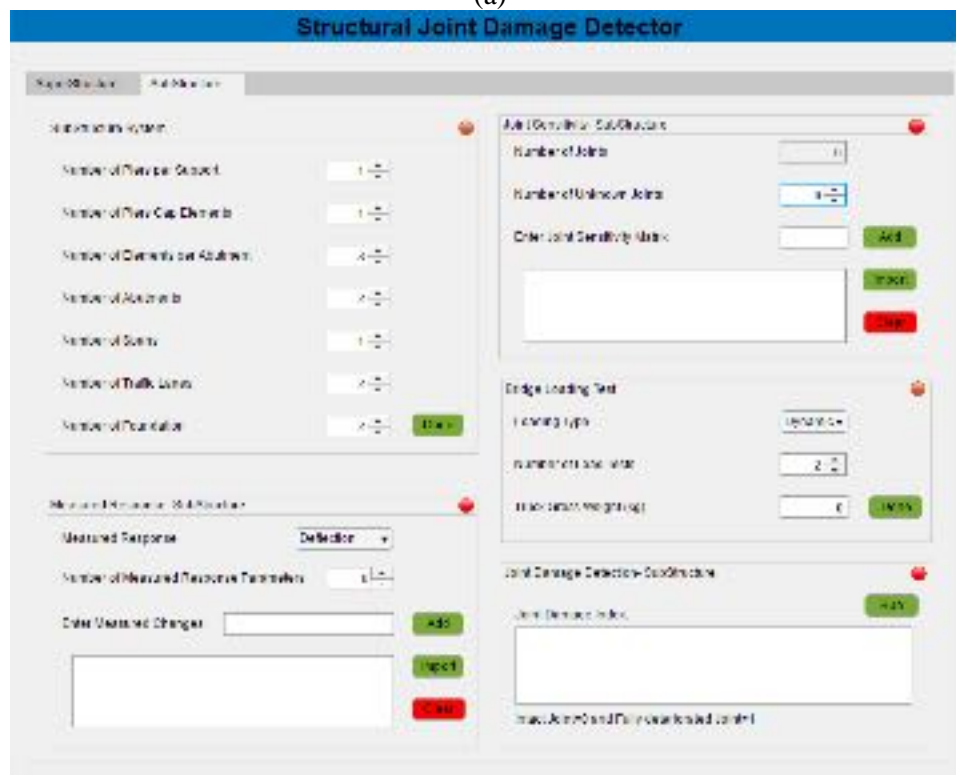
(b)

Figure 3-22. Structural joint damage detector tool; (a) Superstructure, (b) Substructure.

This tool uses superstructure system information, including bridge type, deck panel system, girder type, modular system, number of girders/panels, number of spans, number of transverse joints, and number of traffic lanes to calculate the number of the structural joints and their configurations. Moreover, the tool uses the type of the measured responses, the number of measured responses parameters and measured response changes as the inputs parameters to develop E(p) matrix (Changes in bridge responses due to change in the joint stiffness). Finally, the joint sensitivity matrix needs to be obtained using a detailed finite element model as the input in the Structural Joint Damage Detector tool to detect the location and severity of possible damages in the bridge joints (Figure 3-23). This tool also has the ability to detect damage in the joints of the substructure, including foundations, piers, pier caps, and abutments. Figure 3-22(a) shows the input and output data for the studied bridge in Section 3.4.3 as an example.
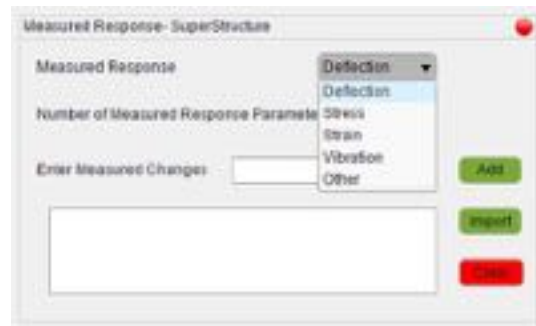
Figure 3-23. Structural joint damage detector tool; (a) Deck panel, (b) Girder, (c) Modular system, (d) Measured response.

CHAPTER 4   SUMMARY AND CONCLUSIONS

Onset and progression of damage in bridges of various types are not always visually detectable.   There have been instances that hidden damages have caused catastrophic collapses costing life and money. Steel bridges with fracture critical elements, cable-supported bridges, and pre-tensioned bridges are among vivid examples of such cases. After each failure incident, state and federal agencies normally issue instructions for in-depth inspection of all populations of bridges with similar characteristics, imposing huge costs and burdens on the bridge maintenance agencies. For example, after the I-35 W Bridge incident, it was required that inspection of steel bridges with fracture critical elements be carried out using an "arms-length" approach at two-year intervals. However, inspection of steel bridges, especially near mid-span over a busy roadway, is costly, time-consuming, and causes traffic disruption and potential safety hazards. It may also take the inspectors as long as two years to detect the fracture, rendering the bridge potentially unsafe for a long duration. Similarly, for concrete bridges where most critical damages could be hidden from the naked eye for a long time, such inspections may not even bear any results. As the many bridge failures over the past few decades have shown, conventional bridge monitoring is insufficient to effectively evaluate the safety of this important piece of infrastructure. New methods for bridge monitoring and special considerations in bridge design are needed to ensure the health of these structures as they continue to age and prevent the possibility of catastrophic collapses from minute and difficult to detect damage. For this purpose, the principal causes of bridge failure, such as deficiencies in design, detailing, construction, and materials, need to be investigated, and possible failure mechanisms for each cause need to be identified. Based on that, new approaches in bridge design and monitoring can be developed to reduce the risk of future bridge collapses. Some

191

of these bridges are designed with distinct vulnerabilities that make them more susceptible to certain types of damages. These include steel bridges with fracture critical members that contain fatigue-sensitive details and concrete and steel bridges designed and built using Accelerated Bridge Construction methods containing cast-in-place joints. For such bridges, the notion of developing a rapid yet accurate method of health monitoring becomes even more critical. Such methods would only be positively productive if they are preceded (or in some cases, followed) by analysis of vulnerabilities of the bridge to determine the level of its redundancy.

The objective of this research was to explore new means for detecting damage in bridge members during normal operations that are both accurate and affordable at the same time. Timely detection of the onset of fracture or damage will allow the maintenance crew to address the situation before the progress in damage threatens public safety and requires major closures and costs. However, to make any damage detection method effective and efficient, the behavior of intact and damaged bridges needs to be investigated, preferably using simple analytical models.

Therefore, to achieve the objective of this research, a two-fold investigation was performed. One was to study the bridge behavior subjected to various damage scenarios and identify possible failure mechanisms. This results in a method for bridge evaluation after damage and determines its level of vulnerability to such damage; in other words, it defines the redundancy and reliability of the structure subjected to such damage. The other was to develop an effective non-destructive method for damage detection based on the bridge behavior after the damage. Two types of bridges were selected and studied for this purpose, twin steel box girder bridges, and prefabricated bridge systems.

4.1 Twin Steel Box Girder Bridges

In steel girder bridges, fatigue cracking is one of the most important phenomena affecting structural performance and integrity. In general, fatigue cracks are the result of out-of-plane distortion or other unanticipated secondary stresses at low fatigue resistance members. Development of fatigue cracking may lead in time to a full-depth fracture of one girder without noticeable bridge profile changes. It is critical to ensure that the bridge will have adequate capacity to prevent collapse until the next cycle of inspection discovers the damage. Bridges that a failure in an individual member could result in the total collapse of the structure are classified as fracture critical by AASHTO. It is required that inspection of these bridges be carried out using the "arms-length" approach, which is costly and is a drain on the state's total bridge budget.

Currently, twin steel box girder bridges are classified as bridges with fracture critical members. However, recent research results indicate that these bridges could be redundant because of their high torsional resistance even after a full-depth fracture of one girder. The most notable studies were the series of tests carried out by the University of Texas-Austin and the Florida International University that demonstrated a high level of internal redundancy of twin steel box girder bridges. The main question as to what load level should be used and established using a scientific approach still remains a task to be accomplished. Further, many questions remain on the expected failure mode of the damaged twin steel box girder bridges and the methods for assessing the bridge performance before these bridges could be removed from the non-redundant list. Moreover, new methods for bridge monitoring are needed to ensure the health of these structures as they continue to age and prevent the possibility of catastrophic collapses from minute and difficult to detect damage.

193

The objective of this section was to establish a design target performance and safety level for twin steel box girder bridges, and outline a methodology and approach for assessing the redundancy of these bridges of simple and continuous spans. Moreover, a non-contact bridge monitoring technique for fracture critical elements was developed based on the bridge dynamic responses to address issues associated with conventional inspection and to that end:

- The Florida Bridge Inventory was statistically analyzed to determine the available range of each functional and geometric parameter

- Weight-in-Motion (WIM) data from 32 stations collected throughout four years (2013-2016) in the state of Florida was used to develop a live load model the bridge would be subjected to during two-year inspection intervals.

- A detailed finite element model of the University of Texas bridge was developed and validated to simulate the local and global behavior of the bridge.

- In order to study the effect of truck position on the failure mode and the ultimate load-carrying capacity, the HS-20 truck was positioned in four different locations across the bridge width at the mid-span over the fractured girder.

- The results showed that concrete deck failure is the governing failure mode of the damaged bridge subjected to truck loading at different positions.

- The results showed that variation in material properties and truck loading configuration would not change the dominant mode of failure for the twin steel box girder bridge considered in this study after a fracture in one girder.

- A simple and unified yield line analysis based on the concrete deck damage pattern observed in the FE analysis was developed to determine the bridge load carrying capacity subjected to different truck configurations.

- A series of analyses were conducted on the bridge to investigate the behavior of the bridge in intact and damaged scenarios under dead and live load. The results showed that the dead load moment on the intact girder increases by about 50 percent once a fracture occurs.

- The live load moment analysis for the intact bridge shows that the left girder (loaded) carries 60%, and the right girder carries 40% of the live load. However, after the fracture, the right girder (intact) carries most of the live load (66%) because of a decrease in stiffness of the fractured girder.

- Simplified reliability analysis of a twin steel box girder bridge superstructure and its deck was presented to estimate the minimum criteria that a deck should satisfy in order to ensure that it can transfer a minimum level of load between the box girders, which one of the girders sustain a severe fracture.

- Based on the analysis, a list of live load factors was provided for different target reliability levels for the case of the two-year service period.

- The reliability analysis indicates that the bridge deck in its current configuration and concrete strength and ignoring the possible contribution of the railings to help carry some of the load will fail at a live load factor $\gamma_{LL}=1.71$. This indicates that its reliability index is on the order of $\beta=2.0$ for a five-year service period, or slightly higher than that for a two-year service period.

- The results show that an LRFR Inventory Rating on the order of R.F.= 1.34 to 1.38 is required to meet a target reliability index β_{target}=2.50 when one of the two box girders fractures.

4.1.1 Reliability and Safety Analysis

The objectives of this study included developing a simple analytical method for estimating the capacity of twin steel box girder bridges following the fracture of one girder and estimating the reliability index associated with the system after the fracture of one girder. The methodology described here uses one particular case study. It should be noted that aspects of the methodology described below are universal and apply to all twin steel box girder bridges. As it is described in the dissertation, the methodology involves three major steps as elaborated below;

Application of the methodology for the reliability analysis of twin steel box girder bridges was achieved using the following ten steps;

1. As-built drawings for the bridge under consideration were obtained and reviewed.

2. Information on truck live loading was gathered, and CDFs per GVW were developed. Representative truck configuration was identified and translated the CDF for a multiple of representative truck weights that would produce equivalent bending moments. Mean and coefficient of variation for various ADTT for a two-year interval were calculated (Section 2.1.3).

3. Using the simple analysis method developed in this study for yield line bending capacity, the bridge deck capacity after fracture of one girder was estimated for the representative truck configuration (Section 2.1.5.3).

4. Using AASHTO LRFD factors, the live load factor that would result in the failure of the deck was calculated.

5. Using the reliability analysis method, as described in Section 2.1.7 of the dissertation, the reliability index controlled by the bridge deck capacity was calculated.

6. The critical loading configuration was determined for the moment along the span in the bridge in the form of single or multiple truck loading, or truck and uniform loading in each lane, and/or truck in one lane or multiple lanes transversely.

7. It was assumed that after the fracture of one girder, the intact girder has to carry its self-weight and all the live load or a refined analysis can be used for the load distribution after the fracture, and calculated the moment acting on the intact girder.

8. The reliability index for the intact girder after one girder fracture was calculated using the procedure described in Section 2.1.7.5 of the dissertation.

9. The least of reliability index between the index for the intact girder (calculated in Item 8) and that for the deck capacity (calculated in Item 5) is controlling.

10. In this case, the controlling reliability indexes are deemed to be indicating the bridge will be safe after the fracture of one girder until the next inspection period, and the bridge can be taken as redundant or not fracture critical.

The steps described above are also illustrated in Figure 4-1.
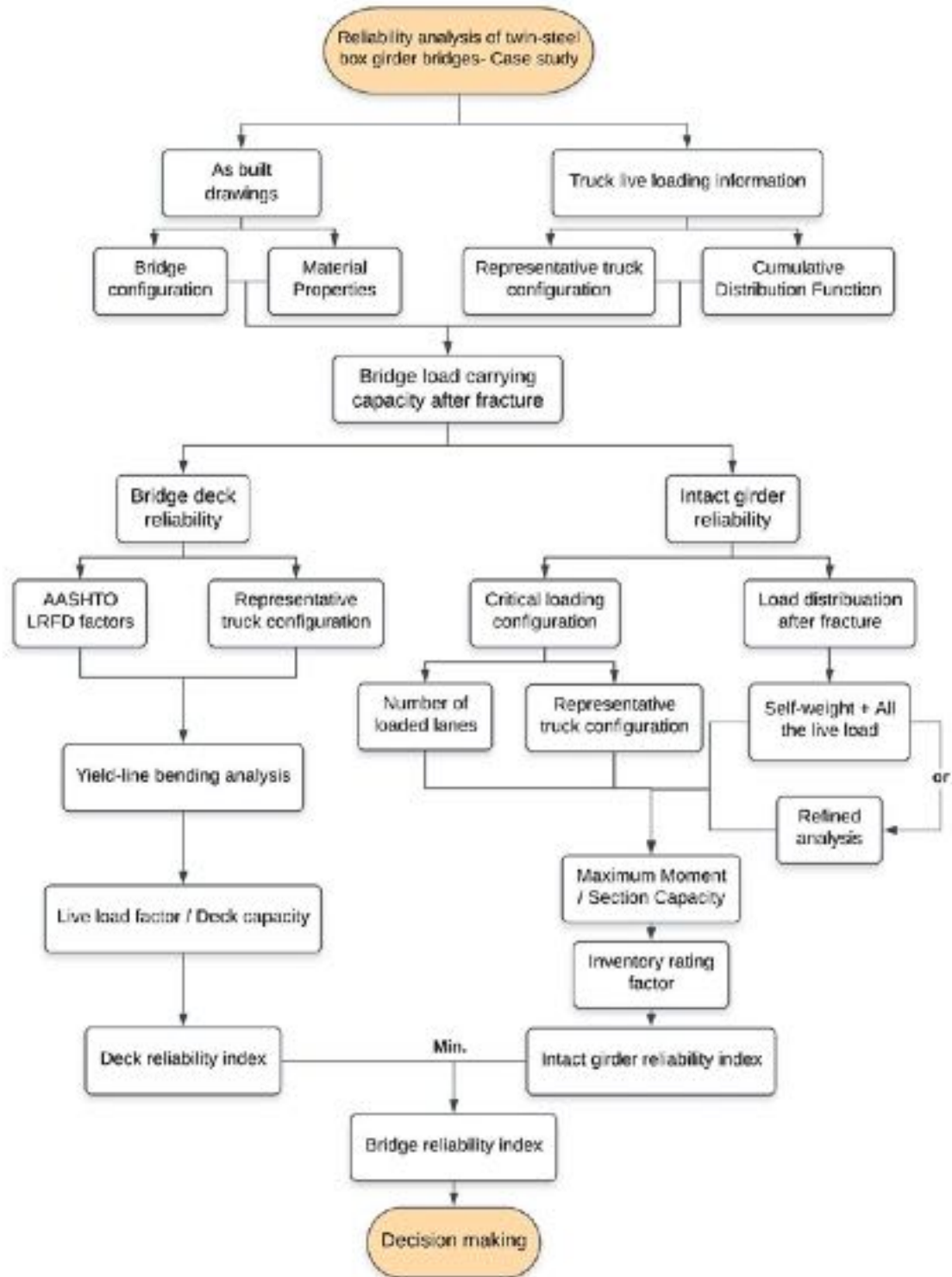
Figure 4-1. Reliability and safety analysis of twin steel box girder bridges with one fractured girder: A case study.

4.1.2   *Health Monitoring of Steel Box Girder Bridges*

The dynamic behavior of simple and continuous span twin steel box girder bridges after various damage scenarios including, bracing failure, partial and full-depth fracture of one girder, was also investigated. To this end:

- A series of field tests were conducted to study the feasibility of using non-contact sensors to capture the bridge dynamic responses during bridge normal operation.

- Detailed finite element models of the bridges were developed and validated using the field test and available experimental test results.

- The bridge field test in this study demonstrated the feasibility of using a non-contact laser vibrometer as an alternative to sensor-based techniques for bridge monitoring. This technique addresses the traffic interruption and safety issues associated with the available bridge monitoring methods.

- The bridge dynamic analysis after damage showed that bridge frequencies are sufficiently sensitive for identifying partial or full-depth girder fracture in the simple span bridges. The results showed that the ratio of frequency changes in two bending modes for major damage is a function of the damage location along the bridge. However, these significant damages may cause very small changes in natural frequencies of continuous span bridges and may go undetected by being masked within the measurement resolution and accuracy.

- The results show a significant change in the mode shapes after damage in both simple and continuous span bridges. The mode shapes are sensitive enough to detect damage at the inflicted locations, in most cases with better resolution when

compared to the frequency changes. These changes are more pronounced for a full or partial-depth fracture at the middle of the span and less for minor damage.

- The comparison of the intact and damaged bridge mode shapes indicates that damage at different locations along the bridge has different amplitude changes in the mode shape that could be used to point to the location of the damage. Moreover, the analyses show that either the individual modal sensitivities or combined sensitivities are indicative for most locations throughout the span except for both ends of the bridge that are not critical.

- The results indicated a clear pattern in the frequency and mode shape changes for each damage scenario that can be used to detect the damage type, severity, and location along the bridge.

4.2   Prefabricated Bridge Systems

Load testing of a precast and prestressed concrete box-beam bridge that has been in service for more than 50 years was conducted to better understand its current behavior and to assess the effect of possible damage to the, among others, longitudinal joints. To this end:

- A series of site inspections, such as non-destructive testing (NDT) and excavation at the adjacent twin pedestrian bridge, were conducted to extract the bridge cross-section details.

- Vertical deflections of the first three precast concrete units closest to the South edge of the bridge were recorded using three different types of instruments during the static load test.

- The bridge vibration was recorded using a laser vibrometer and accelerometers located at mid-span to extract the bridge natural frequencies.

- A detailed FE model was developed with the objective of contributing to the analysis of the experimental results as well as investigating the behavior of the panel joints.

- A comparison between the results of the FE model without considering damage (bridge deflection and frequencies) and actual bridge response and reflective cracking and leaking in the surface of the deck at longitudinal joints indicated that the joints were damaged.

- A new damage detection method using model updating for structural health monitoring of these bridges was introduced. This method can effectively identify locations and significance of possible joint damage based on the measured changes in bridge response parameters.

- The FE model was utilized to derive a behavior matrix that transforms the bridge state changes to corresponding joint damage.

- This method relies on comparing bridge responses to its initial undamaged responses subjected to the same static loading configuration to identify the damage.

- In the absence of initial measurements, the FE model was used to estimate undamaged responses.

- The proposed method was implemented on the bridge to identify the level of damage at each joint using the bridge measured responses through the load test, and the results show a good agreement with the field test for different loading configurations.

- The proposed method could effectively be used for structural health monitoring of new bridges where the initial response measurements are recorded immediately

after bridge construction as a benchmark, and bridge response is monitored periodically to detect the progress of potential damage over time.

- Other damage sources, such as prestress loss (in the longitudinal or transverse direction) and material defects in the precast panels, could also affect the overall bridge performance and influence the initiation and progression of joint damages. In that way, their influence is indirect and already present in the damage detected for the joints. Therefore, the proposed method is capable of detecting joint damage with acceptable accuracy even if multiple sources of distress are present and indirectly contribute to the joint damage.

- The bridge used for validating this method was inspected thoroughly, and the prevalent damage was the longitudinal joint damage potentially from causes such as defective or deteriorated grout at the joints and uneven overload. In particular, there was no evidence of corrosion nor concrete deterioration

- The bridge dynamic analysis shows that modal parameters in slab panel bridges are sufficiently sensitive for identifying joint damage. In these bridges, longitudinal joints play an important role by transferring shear forces between adjacent panels, and possible damage at the joints could considerably change the bridge natural frequency by reducing the bridge torsional stiffness, which can be detected using vibration-based modal analysis techniques.

- A tool is developed to detect the location and severity of possible damages in the bridge joints, including superstructure and substructure joints.

- In this tool, bridge configuration, measured changes in the bridge response, loading configurations, and joints sensitivity matrix will be used as input parameters to

detect the location of the joint damage and their relative significance in the bridge using optimization algorithms to consider the errors associated with modeling, measurement and ignoring other sources of damage.

- This tool can detect damage in joints and connections of any other structures other than bridges that use prefabricated elements. It can also detect damage at joints of conventional structures.

4.3 Main Contributions of This Dissertation

The research performed for this dissertation has contributed to the body of the knowledge in several aspects:

- Analytical approaches using detailed finite element (FE) modeling methods were developed to simulate the behavior of damaged bridges for calculating the bridge load-carrying capacity and investigating the failure mechanisms after damage considering shear stud failure, support uplift, concrete damage plasticity, dynamic behavior, railing contact, and connection failure.

- A simple and unified yield line analysis model was developed based on the concrete deck damage pattern observed in the FE analysis to determine the load-carrying capacity of twin steel box girder bridges subjected to different trucks configurations after a full-depth fracture of one girder. This model applies to a wide variety of truck loads and configurations.

- Experimental approaches were developed for monitoring of structural behavior, including the use of a non-contact laser vibrometer. This technique addresses the traffic interruption and safety issues associated with the available bridge monitoring methods.

- Damage detection methods were developed and suited to bridges with distinct vulnerabilities. These methods can effectively identify locations and significance of possible damage based on the measured changes in bridge response parameters. These methods followed the general approach for model updating, parameter identification, vibration frequency, and mode shape-based damage detection.

- A damage detection tool was developed for bridges with prefabricated deck panels/girders that is generally applicable to all bridges with distinct vulnerabilities.

4.4 Recommendation for Future Studies

In this study, the behavior of two types of bridges with distinct vulnerability, including twin steel box girder bridges and prefabricated bridge systems containing cast-in-place joints, was investigated, and new damage detection methods and a tool were developed for these bridges. Future studies to extend this research could include the following:

- The focus of this research was limited to two types of bridges. A future study can investigate the after damage behavior of other types of bridges such as cable-stayed bridges, arch bridges, and truss bridges to develop a damage detection method suited to these bridge systems.

- The methodology and simple analytical model for the reliability analysis of twin steel box girder bridges were developed based on limited test and analysis results of one particular simple span bridge. Therefore, it is recommended to investigate the behavior of simple and continuous span twin steel box girder bridges with different configurations, i.e., span length, curvature, width, and lanes.

- The use of fiber-reinforced polymer (FRP) decks has the potential to extend the life of the bridge deck exposed to corrosion. FRP deck offers many advantages,

including low weight, high strength, and significant durability advantages. Nevertheless, damage in the FRP deck will reduce the deck stiffness that is not visually detectable, and the progress of damage may cause a brittle failure of the deck. Therefore, a future study can investigate the effect of damage in FRP decks on changes in the bridge dynamic responses (mode shapes and frequencies) to detect and localize the damage.

- The proposed damage detection method for bridges with prefabricated deck panels/girders is designed to detect damage at the bridge longitudinal joints. The method developed is not expected to cover all types of damage; however, this method can be modified to also include other damage types such as changes in support conditions and longitudinal prestress losses, if the pattern of bridge response changes can be established for those damages.

- Accordingly, the structural joint damage detector tool can be modified to detect damage in joints and connections of any structures other than bridges that use prefabricated elements.

- The current version of the structural joint damage detector tool requires finite element software to calculate the joint sensitivity matrix separately. Therefore, the tool should be improved to include a built-in finite element package or linkage compatible with an existing finite element software.

REFERENCES

[1] Lerose C. The collapse of the Silver Bridge. West Virginia Hist Soc Q 2001;15:1.

[2] Feldman BJ. The Collapse of the I-35W Bridge in Minneapolis. Phys Teach 2010;48:541–2.

[3] Morgese M, Ansari F, Domaneschi M, Cimellaro GP. Post-collapse analysis of Morandi's Polcevera viaduct in Genoa Italy. J Civ Struct Heal Monit 2020;10:69–85.

[4] AASHTO and AWS. AASHTO/AWS D1.5M/D1.5: Bridge Welding Code, 2015.

[5] AASHTO. The Manual for Bridge Evaluation. Am Assoc State Highw Transp Off 2nd Ed Washington, DC 2011.

[6] Wardhana K, Hadipriono FC. Analysis of recent bridge failures in the United States. J Perform Constr Facil 2003;17:144–50.

[7] Yu J, Ziehl P, Zrate B, Caicedo J. Prediction of fatigue crack growth in steel bridge components using acoustic emission. J Constr Steel Res 2011;67:1254–60. https://doi.org/10.1016/j.jcsr.2011.03.005.

[8] Scheffey CF. PT pleasant bridge collapse-conclusions of federal study. Civ Eng 1971;41:41.

[9] AASHTO. AASHTO LRFD Bridge Design Specifications (8th ed.). Washington, D.C.: American Association of State Highway and Transportation Officials; 2017.

[10] AASHTO. AASHTO Guide Specifications for Analysis and Identification of Fracture Critical Members and System Redundant Members (1st ed.). Washington, D.C.: American Association of State Highway and Transportation Officials; 2018.

[11] Conner RJ, Dexter RJ, Mahmoud H. Inspection and management of bridges with fracture-critical details: A synthesis of highway practice. vol. 354. Transportation Research Board; 2005.

[12] Van Pham H, Yakel A, Azizinamini A. Experimental investigation of redundancy of twin steel box-girder bridges under concentrated loads. J Constr Steel Res 2021;177:106440.

[13] Pham H, Gull JH, Mohammadi A, Azizinamini A. Managing Florida's fracture critical bridges-phases 1 and 2 2016.

[14] Irfaee M, Mahmoud H. Mixed-Mode Fatigue and Fracture Assessment of a Steel Twin Box-Girder Bridge. J Bridg Eng 2019;24:4019056.

[15] Lin W, Yoda T, Kumagai Y, Saigyo T. Numerical study on post-fracture redundancy of the two-girder steel-concrete composite highway bridges. Int J Steel Struct 2013;13:671–81.

[16] Lin W, Yoda T, Taniguchi N, Lam H, Nakabayashi K. Post-Fracture redundancy evaluation of a twin box-girder shinkansen bridge in Japan. IABSE Conf. Guangzhou 2016 Bridg. Struct. Sustain. - Seek. Intell. Solut. - Rep., vol. 106, Guangzhou, China: International Association for Bridge and Structural Engineering; 2016, p. 675–82. https://doi.org/10.2749/222137816819259077.

[17] Idriss RL, White KR, Woodward CB, Jauregui D V. Evaluation and testing of a fracture critical bridge. NDT E Int 1995;28:339–47.

[18] Fisher JW, Pense AW, Roberts R. Evaluation of fracture of Lafayette Street bridge. J Struct Div 1977;103.

[19] Quiel S. Forensic analysis of the steel girder fracture in the I-95 Brandywine River Bridge. Res Exp Undergraduates Report, Univ Notre Dame 2003.

[20] Neuman BJ. Evaluating the Redundancy of Steel Bridges: Full-Scale Destructive Testing of a Fracture Critical Twin Box-Girder Steel Bridge. University of Texas at Austin (Doctoral Dissertation), TX, USA, 2009.

[21] Kim J, Williamson EB. Finite-element modeling of twin steel box-girder bridges for redundancy evaluation. J Bridg Eng 2015;20:4014106.

[22] Samaras VA, Sutton JP, Williamson EB, Frank KH. Simplified method for evaluating the redundancy of twin steel box-girder bridges. J Bridg Eng 2012;17:470–80.

[23] Peterson J, Cashin P. Design Solutions for Steel Bridges in Milwaukee's Marquette Interchange. New Horizons Better Pract., 2007, p. 1–9.

[24] Connor RJ, Korkmaz C, Campbell LE, Bonachera Martin FJ, Lloyd JB. A Simplified Approach for Designing SRMs in Composite Continuous Twin-Tub Girder Bridges 2020.

[25] Ghosn M, Moses F, Frangopol DM. Redundancy and robustness of highway bridge superstructures and substructures. Struct Infrastruct Eng 2010;6:257–78.

[26] Frangopol DM, Nakib R. Redundancy in highway bridges. Eng J 1991;28.

[27] Hendawi S, Frangopol DM. System reliability and redundancy in structural design and evaluation. Struct Saf 1994;16:47–71.

[28] Ghosn M, Moses F. Redundancy in highway bridge superstructures. vol. 406. Transportation Research Board; 1998.

[29] Frangopol DM, Zhu B, Sabatino S. System Reliability in Special Steel and Concrete Bridge Systems: Identification of Redundancy Factor Modifiers 2018.

[30] Strauss A, Mandić Ivanković A, Matos JC, Casas JR. Performance indicators for road bridges—Overview of findings and future progress. Proc Value Struct Heal Monit Reliab Bridg Manag Zagreb Croat 2017:2–3.

[31] Fiorillo G, Miao F, Ghosn M. Direct Redundancy Evaluation of Bridges Designated as Fracture-Critical. J Perform Constr Facil 2016;30:4015045.

[32] Ghosn M, Yang J, Beal D, Sivakumar B. Bridge system safety and redundancy. 2014.

[33] Nowak AS. Calibration of LRFD bridge design code. 1999.

[34] FDOT. Index 20350 series: Prestressed Slab Unit. FDOT Des Stand Florida, USA 2009.

[35] Huckelbridge Jr AA, El-Esnawi H, Moses F. Shear key performance in multibeam box girder bridges. J Perform Constr Facil 1995;9:271–85.

[36] Alampalli S. Performance of full-depth shear keys in adjacent prestressed box beam bridges. PCI J 1998;43:72–9.

[37] Miller RA, Hlavacs GM, Long T, Greuel A. Full-scale testing of shear keys for adjacent box girder bridges. PCI J 1999;44.

[38] Riccitelli F, Mehrabi A, Abedin M, Farhangdoust S, Khedmatgozar Dolati SS. Performance of Existing Abc Projects : Inspection Case Studies. Accel Bridg Constr Univ Transp Cent Miami, FL, USA 2020.

[39] Attanayake U, Aktan H. Reflective Cracking between Precast Prestressed Box Girders. Wisconsin. Dept. of Transportation. Research and Library Unit; 2017.

[40] PCI. The state of the art of precast/prestressed adjacent box beam bridges 2012.

[41] Russell HG. Adjacent precast concrete box beam bridges: Connection details. vol. 393. Transportation Research Board; 2009.

[42] Attanayake U, Aktan H. First-generation ABC system, evolving design, and half a century of performance: Michigan side-by-side box-beam bridges. J Perform Constr Facil 2015;29:4014090.

[43] Grace NF, Jensen EA, Matsagar VA, Bebawy M, Soliman E, Hanson J. Use of unbonded CFCC for transverse post-tensioning of side-by-side box-beam bridges. 2008.

[44] Hussein HH, Sargand SM, Al-Jhayyish AK, Khoury I. Contribution of transverse tie bars to load transfer in adjacent prestressed box-girder bridges with partial depth shear key. J Perform Constr Facil 2017;31:4016100.

[45] Ulku E, Attanayake U, Aktan HM. Rationally designed staged posttensioning to abate reflective cracking on side-by-side box-beam bridge decks. Transp Res Rec 2010;2172:87–95.

[46] Jaberi Jahromi A, Valikhani A, Mantawy IM, Azizinamini A. Service Life Design of Deck Closure Joints in ABC Bridges: Guidelines and Practical Implementation. Front Built Environ 2019;5:152.

[47] Naeimi N, Moustafa MA. Numerical modeling and design sensitivity of structural and seismic behavior of UHPC bridge piers. Eng Struct 2020;219:110792.

[48] Hanna KE, Morcous G, Tadros MK. Adjacent box girders without internal diaphragms or posttensioned joints. PCI J 2011;56.

[49] Li B, Ou J. Optimal sensor placement for structural health monitoring based on K-L divergence. Safety, Reliab Risk Life-Cycle Perform Struct Infrastructures 2014;20:2535–42. https://doi.org/10.1201/b16387-366.

[50] Yuen K, Kuok S. Efficient Bayesian sensor placement algorithm for structural identification: a general approach for multi-type sensory systems. Earthq Eng Struct Dyn 2015;44:757–74.

[51] Huang H Bin, Yi TH, Li HN. Canonical correlation analysis based fault diagnosis method for structural monitoring sensor networks. Smart Struct Syst 2016;17:1031–53. https://doi.org/10.12989/sss.2016.17.6.1031.

[52] Sohn H. Noncontact laser sensing technology for structural health monitoring and nondestructive testing (presentation video). Bioinspiration, Biomimetics, Bioreplication 2014, vol. 9055, International Society for Optics and Photonics; 2014, p. 90550W.

[53] Ebrahimkhanlou A, Salamone S, Ebrahimkhanlou A, Ghiami Azad AR, Kreitman K, Helwig T, et al. Acoustic emission monitoring of strengthened steel bridges: Inferring the mechanical behavior of post-installed shear connectors. SpiedigitallibraryOrg 2019:16. https://doi.org/10.1117/12.2514231.

[54] Antunes P, Lima H, Varum H, André P. Optical fiber sensors for static and dynamic health monitoring of civil engineering infrastructures: Abode wall case study. Measurement 2012;45:1695–705.

[55] Ding Y-L, Zhao H-W, Li A-Q. Temperature effects on strain influence lines and dynamic load factors in a steel-truss arch railway bridge using adaptive FIR filtering. J Perform Constr Facil 2017;31:4017024.

[56]   Moschas F, Stiros S. Noise characteristics of high-frequency, short-duration GPS records from analysis of identical, collocated instruments. Measurement 2013;46:1488–506.

[57]   Elvin NG, Lajnef N, Elvin AA. Feasibility of structural monitoring with vibration powered sensors. Smart Mater Struct 2006;15:977.

[58]   Alavi AH, Hasni H, Jiao P, Borchani W, Lajnef N. Fatigue cracking detection in steel bridge girders through a self-powered sensing concept. J Constr Steel Res 2017;128:19–38. https://doi.org/10.1016/j.jcsr.2016.08.002.

[59]   Chatti K, Faridazar F, Hasni H, Lajnef N, Alavi AH. An intelligent structural damage detection approach based on self-powered wireless sensor data. Autom Constr 2015;62:24–44. https://doi.org/10.1016/j.autcon.2015.10.001.

[60]   Olaszek P, Łagoda M, Casas JR. Diagnostic load testing and assessment of existing bridges: examples of application. Struct Infrastruct Eng 2014;10:834–42.

[61]   Lantsoght EOL, van der Veen C, de Boer A, Hordijk DA. State-of-the-art on load testing of concrete bridges. Eng Struct 2017;150:231–41.

[62]   Schulz JL, Commander B, Goble GG, Frangopol DM. Efficient field testing and load rating of short-and medium-span bridges. Struct Eng Rev 1995;3:181–94.

[63]   Chajes MJ, Mertz DR, Commander B. Experimental load rating of a posted bridge. J Bridg Eng 1997;2:1–10.

[64]   Cai CS, Shahawy M. Understanding capacity rating of bridges from load tests. Pract Period Struct Des Constr 2003;8:209–16.

[65]   Wang N, O'Malley C, Ellingwood BR, Zureick A-H. Bridge rating using system reliability assessment. I: Assessment and verification by load testing. J Bridg Eng 2011;16:854–62.

[66]   Amer A, Arockiasamy M, Shahawy M. Load distribution of existing solid slab bridges based on field tests. J Bridg Eng 1999;4:189–93.

[67]   Breña SF, Jeffrey AE, Civjan SA. Evaluation of a noncomposite steel girder bridge through live-load field testing. J Bridg Eng 2013;18:690–9.

[68]   Ma Y, Wang L, Zhang J, Xiang Y, Liu Y. Bridge remaining strength prediction integrated with Bayesian network and in situ load testing. J Bridg Eng 2014;19:4014037.

[69]   Harris DK, Civitillo JM, Gheitasi A. Performance and behavior of hybrid composite beam bridge in Virginia: Live load testing. J Bridg Eng 2016;21:4016022.

[70] Salawu OS. Detection of structural damage through changes in frequency: a review. Eng Struct 1997;19:718–23.

[71] Kim J-T, Stubbs N. Crack detection in beam-type structures using frequency data. J Sound Vib 2003;259:145–60.

[72] Curadelli RO, Riera JD, Ambrosini D, Amani MG. Damage detection by means of structural damping identification. Eng Struct 2008;30:3497–504.

[73] Williams C, Salawu OS. Damping as a damage indication parameter. Proc. 15th Int. modal Anal. Conf., vol. 3089, 1997, p. 1531.

[74] Kim J-T, Ryu Y-S, Cho H-M, Stubbs N. Damage identification in beam-type structures: frequency-based method vs mode-shape-based method. Eng Struct 2003;25:57–67.

[75] Ewins DJ. Modal testing: theory, practice and application. John Wiley & Sons; 2009.

[76] Abedin M, Mehrabi AB. Health monitoring of steel box girder bridges using non-contact sensors. Structures, vol. 34, Elsevier; 2021, p. 4012–24.

[77] Lauzon RG, DeWolf JT. Full-scale bridge test to monitor vibrational signatures. Struct. Eng. Nat. Hazards Mitig., ASCE; 1993, p. 1089–94.

[78] Heo G, Wang ML, Satpathi D. Optimal transducer placement for health monitoring of long span bridge. Soil Dyn Earthq Eng 1997;16:495–502.

[79] Hsieh KH, Halling MW, Barr PJ. Overview of vibrational structural health monitoring with representative case studies. J Bridg Eng 2006;11:707–15.

[80] Xu YL, Chen B, Ng CL, Wong KY, Chan WY. Monitoring temperature effect on a long suspension bridge. Struct Control Heal Monit 2010;17:632–53.

[81] Abedin M, Farhangdoust S, Mehrabi AB. Fracture detection in steel girder bridges using self-powered wireless sensors. Risk-Based Bridg. Eng. Proc. 10th New York City Bridg. Conf. August 26-27, 2019, New York City, USA: CRC Press; 2019, p. 216.

[82] Zhao J, DeWolf JT. Dynamic monitoring of steel girder highway bridge. J Bridg Eng 2002;7:350–6.

[83] Khedmatgozar Dolati SS, Caluk N, Mehrabi A, Khedmatgozar Dolati SS. Non-Destructive Testing Applications for Steel Bridges. Appl Sci 2021;11:9757.

[84] Abedin M, Mehrabi AB. Novel Approaches for Fracture Detection in Steel Girder Bridges. Infrastructures 2019;4:42. https://doi.org/10.3390/infrastructures4030042.

[85] Abedin M, Mehrabi AB. Bridge damage identification through frequency changes. Sensors Smart Struct. Technol. Civil, Mech. Aerosp. Syst. 2021, vol. 11591, International Society for Optics and Photonics; 2021, p. 1159109.

[86] Abedin M, Mokhtari S, Mehrabi AB. Bridge damage detection using machine learning algorithms. Heal. Monit. Struct. Biol. Syst. XV, vol. 11593, International Society for Optics and Photonics; 2021, p. 115932P.

[87] Mehrabi AB, Tabatabai H, Lotfi HR. Damage detection in structures using Precursor Transformation Method. J Intell Mater Syst Struct 1998;9:808–17. https://doi.org/10.1177/1045389X9800901004.

[88] Hua XG, Ni YQ, Chen ZQ, Ko JM. Structural damage detection of cable-stayed bridges using changes in cable forces and model updating. J Struct Eng 2009;135:1093–106.

[89] Chen C-C, Wu W-H, Liu C-Y, Lai G. Diagnosis of instant and long-term damages in cable-stayed bridges based on the variation of cable forces. Struct Infrastruct Eng 2018;14:565–79.

[90] Domaneschi M, Limongelli MP, Martinelli L. Damage detection and localization on a benchmark cable-stayed bridge. Earthq Struct 2015;8:1113–26.

[91] Sanayei M, Onipede O. Damage assessment of structures using static test data. AIAA J 1991;29:1174–9.

[92] Sanayei M, Saletnik MJ. Parameter estimation of structures from static strain measurements. I: Formulation. J Struct Eng 1996;122:555–62.

[93] Sanayei M, Saletnik MJ. Parameter estimation of structures from static strain measurements. II: Error sensitivity analysis. J Struct Eng 1996;122:563–72.

[94] Fritzen C-P, Jennewein D, Kiefer T. Damage detection based on model updating methods. Mech Syst Signal Process 1998;12:163–86.

[95] Titurus B, Friswell MI, Starek L. Damage detection using generic elements: Part I. Model updating. Comput Struct 2003;81:2273–86.

[96] Wu JR, Li QS. Structural parameter identification and damage detection for a steel structure using a two-stage finite element model updating method. J Constr Steel Res 2006;62:231–9.

[97] Jaishi B, Ren W-X. Damage detection by finite element model updating using modal flexibility residual. J Sound Vib 2006;290:369–87.

[98] (ASCE) AS of CE. A Comprehensive Assessment of America's Infrastructure. 2021.

[99]   Daniels JH, Kim W, Wilson JL. Guidelines for redundancy design and rating of two-girder steel bridges, Final Report, November 1988, 365p. 1988.

[100]   Hovell CG. Evaluation of Redundancy in Trapezoidal Box-Girder Bridges Using Finite Element Analysis. University of Texas at Austin (Doctoral dissertation), TX, USA, 2007.

[101]   Idriss RL, White KR, Woodward CB, Jauregui D V. After-fracture redundancy of two-girder bridge: Testing I-40 bridges over Rio Grande. Proc. Fourth Int. Bridg. Eng. Conf., 1995, p. 316–26.

[102]   Williamson EB, Kim J, Frank KH. Redundancy evaluation of twin steel box-girder bridges using finite element analyses. Struct. Congr. 2010, 2010, p. 2793–802.

[103]   Nowak AS, Collins KR. Reliability of structures. CRC press; 2012.

[104]   Sivakumar B, Ghosn M, Moses F. Protocols for collecting and using traffic data in bridge design. vol. 683. Transportation Research Board; 2011.

[105]   Kulicki JM, Wasser WG, Mertz DR, Nowak AS. Bridges for Service Life Beyond 100 Years: Service Limit State Design 2015.

[106]   Federal Highway Administration. Traffic Monitoring Guide. Fhwa 2016.

[107]   Ramesh Babu A. Quantifying the Fatigue Damage Accumulation in Bridges 2019.

[108]   Documentation DA. ABAQUS/CAE Doc. Simulia Provid RI, USA 2016.

[109]   Kathol S, Azizinamini A, Luedke J. Strength Capacity of Steel Girder Bridges. Final Report. Washington, DC: Transportation Research Board; 1995.

[110]   Pham H V. Evaluation of Redundancy of Twin Steel Box-Girder Bridges. Florida International University (Doctoral dissertation), FL, USA, 2016.

[111]   Abedin M, Mehrabi AB. Effect of Cross-Frames on Load Distribution of Steel Bridges with Fractured Girder. Infrastructures 2020;5:32.

[112]   Abedin M, Maleki S, Kiani N, Shahrokhinasab E. Shear lag effects in angles welded at both legs. Adv Civ Eng 2019;2019. https://doi.org/10.1155/2019/8041767.

[113]   Lubliner J, Oliver J, Oller S, Onate E. A plastic-damage model for concrete. Int J Solids Struct 1989;25:299–326.

[114]   ACI Committee. 318, Building Code Requirements for Structural Concrete (ACI 318–14) and Commentary (ACI 318R–14). Am Concr Institute, Farmingt Hills, MI 2014:519.

[115] Lantsoght EOL, de Boer A, van der Veen C, Walraven JC. Effective shear width of concrete slab bridges. Proc Inst Civ Eng - Bridg Eng 2015;168:287–98. https://doi.org/10.1680/bren.13.00027.

[116] Topkaya C, Williamson EB, Frank KH. Behavior of curved steel trapezoidal box-girders during construction. Eng Struct 2004;26:721–33. https://doi.org/10.1016/j.engstruct.2003.12.012.

[117] Sutton JP, Mouras JM, Samaras VA, Williamson EB, Frank KH. Strength and ductility of shear studs under tensile loading. J Bridg Eng 2014;19:245–53.

[118] Hognestad E. A Study of Combined Bending and Axial Load in Reinforced Concrete Members. University of Illinois at Urbana Champaign, College of Engineering …; 1951. https://doi.org/10.14359/7785.

[119] Ghosn M, Sivakumar B, Miao F. Development of state-specific load and resistance factor rating method. J Bridg Eng 2013;18:351–61.

[120] Sivakumar B, Ghosn M. Recalibration of LRFR live load factors in the AASHTO manual for bridge evaluation. NCHRP Proj 2011.

[121] Moses F. Calibration of load factors for LRFR bridge evaluation. 2001.

[122] Cawley P, Adams RD. The location of defects in structures from measurements of natural frequencies. J Strain Anal Eng Des 1979;14:49–57.

[123] Kim J-T, Stubbs N. Model-uncertainty impact and damage-detection accuracy in plate girder. J Struct Eng 1995;121:1409–17.

[124] Stubbs N, Osegueda R. Global non-destructive damage evaluation in solids. Int J Anal Exp Modal Anal 1990;5:67–79.

[125] Abedin M, De Caso y Basalo FJ, Kiani N, Mehrabi AB, Nanni A. Bridge load testing and damage evaluation using model updating method. Eng Struct 2022;252:113648. https://doi.org/https://doi.org/10.1016/j.engstruct.2021.113648.

[126] ASTM C. Standard test method for compressive strength of cylindrical concrete specimens. Chủ Biên 2012.

[127] Wu J-J. Free vibration characteristics of a rectangular plate carrying multiple three-degree-of-freedom spring–mass systems using equivalent mass method. Int J Solids Struct 2006;43:727–46.

[128] Abedin M, Mehrabi A. Structural joint damage detector tool. U.S. Patent 11,120,181, 2021.

[129] MathWorks, App Designer Matlab and Simulink Mathworks 2017.

VITA

MOHAMMAD ABEDIN

Born, Isfahan, Iran

2007-2011	B.S., Civil Engineering University of Isfahan Isfahan, Iran
2011-2013	M.S., Structural Engineering Sharif University of Technology Tehran, Iran
2018-2021	M.S., Civil Engineering Florida International University Miami, Florida
2018 -2021	Ph.D., Civil Engineering Florida International University Miami, Florida

PUBLICATIONS AND PRESENTATIONS

Abedin, M., & Mehrabi, A. (2021). *U.S. Patent No. 11,120,181*. Washington, DC: U.S. Patent and Trademark Office.

Abedin, M., De Caso y Basalo, F. J., Kiani, N., Mehrabi, A. B., & Nanni, A. (2022). Bridge load testing and damage evaluation using model updating method. In *Engineering Structures* (252:113648). Elsevier.

Abedin, M., & Mehrabi, A. B. (2021, December). Health monitoring of steel box girder bridges using non-contact sensors. In *Structures* (Vol. 34, pp. 4012-4024). Elsevier.

Abedin, M., & Mehrabi, A. B. (2021, March). Bridge damage identification through frequency changes. In *Sensors and Smart Structures Technologies for Civil, Mechanical, and Aerospace Systems 2021* (Vol. 11591, p. 1159109). International Society for Optics and Photonics.

Abedin, M., Mokhtari, S., & Mehrabi, A. B. (2021, March). Bridge damage detection using machine learning algorithms. In *Health Monitoring of Structural and Biological Systems XV* (Vol. 11593, p. 115932P). International Society for Optics and Photonics.

Abedin, M., Mehrabi, A. B., Azizinamini, A., Ghosn, M., Nowak, A., & Babu, A. R. (2021). Redundancy of Twin Steel Box Girder Bridges. *Florida Department of Transportation, Research Center.*

Mehrabi, A., Riccitelli, F., Abedin, M., Farhangdoust, S., & Khedmatgozar Dolati, S. (2021). Performance of Existing ABC Projects: Inspection Case Studies. No. ABC-UTC-2016-2-FIU02. *Accelerated Bridge Construction University Transportation Center (ABC-UTC).*

Mehrabi, A., Torrealba Sotillo, A., & Abedin, M. (2020). Available ABC Bridge Systems for Short Span Bridges – Course Module. No. ABC-UTC-2016-C2-FIU04. *Accelerated Bridge Construction University Transportation Center (ABC-UTC).*

Abedin, M., & Mehrabi, A. B. (2020). Effect of Cross-Frames on Load Distribution of Steel Bridges with Fractured Girder. *Infrastructures*, *5*(4), 32. http://dx.doi.org/10.3390/infrastructures5040032.

Abedin, M., Kiani, N., Shahrokhinasab, E., & Mokhtari, S. (2020). Net Section Fracture Assessment of Welded Rectangular Hollow Structural Sections. *Civil Engineering Journal, 6(7), 1243–1254*. doi:10.28991/cej-2020-03091544

Abedin, M., & Mehrabi, A. B. (2019). Novel approaches for fracture detection in steel girder bridges. *Infrastructures*, *4*(3), 42. https://doi.org/10.3390/infrastructures4030042.

Abedin, M., Farhangdoust, S., & Mehrabi, A. B. (2019, August). Fracture detection in steel girder bridges using self-powered wireless sensors. In *Proceedings of the In Risk-Based Bridge Engineering: Proceedings of the 10th New York City Bridge Conference* (p. 216).

Abedin, M., Maleki, S., Kiani, N., & Shahrokhinasab, E. (2019). Shear Lag Effects in Angles Welded at Both Legs. *Advances in Civil Engineering*, *2019*. https://doi.org/10.1155/2019/8041767.

Ghoddousi, P., Abbasi, A. M., Shahrokhinasab, E., & Abedin, M. (2019). Prediction of Plastic Shrinkage Cracking of Self-Compacting Concrete. *Advances in Civil Engineering*, *2019*. https://doi.org/10.1155/2019/1296248.